DTIC FILE COPY

AD-A197 601

1

DTIC
S AUG 3 0 1988
D

DISTRIBUTION STATEMENT A
Approved for public release;
Distribution Unlimited

REPORT DOCUMENTATION PAGE

AD-A197601

1a REPORT SECURITY CLASSIFICATION Unclassified	1b RESTRICTIVE MARKINGS
2a SECURITY CLASSIFICATION AUTHORITY	3 DISTRIBUTION / AVAILABILITY OF REPORT Approved for public release; Distribution unlimited
2b DECLASSIFICATION / DOWNGRADING SCHEDULE	
4. PERFORMING ORGANIZATION REPORT NUMBER(S)	5. MONITORING ORGANIZATION REPORT NUMBER(S) AFOSR-TR- 88-0865
6a. NAME OF PERFORMING ORGANIZATION Optical Society of America 6b OFFICE SYMBOL (If applicable)	7a NAME OF MONITORING ORGANIZATION AFOSR/NC
6c. ADDRESS (City, State, and ZIP Code) 1816 Jefferson Place, N.W. Washington, D.C. 20036	7b ADDRESS (City, State, and ZIP Code) Bldg. 410 Bolling AFB, Washington, D.C. 20332-6448
8a. NAME OF FUNDING / SPONSORING ORGANIZATION AFOSR 8b OFFICE SYMBOL (If applicable) NC	9 PROCUREMENT INSTRUMENT IDENTIFICATION NUMBER AFOSR-87-0109
8c. ADDRESS (City, State, and ZIP Code) Bldg. 410 Bolling AFB, Washington, D.C. 20332-6448	10 SOURCE OF FUNDING NUMBERS PROGRAM ELEMENT NO: 61102F PROJECT NO: 2303 TASK NO: A2 WORK UNIT ACCESSION NO:

11 TITLE (Include Security Classification)
~~Organization of the~~ Second Topical Meeting on Microphysics of Surfaces, Beams, and Adsorbates

12 PERSONAL AUTHOR(S)
Jarus W. Quinn

13a TYPE OF REPORT	13b TIME COVERED	14 DATE OF REPORT (Year, Month, Day)	15 PAGE COUNT
Final	FROM 87/2/01 TO 87/10/31	87/10/31	

16 SUPPLEMENTARY NOTATION

17 COSATI CODES			18 SUBJECT TERMS (Continue on reverse if necessary and identify by block number)
FIELD	GROUP	SUB-GROUP	Microphysics of Surfaces, Beams, and Adsorbates,

19 ABSTRACT (Continue on reverse if necessary and identify by block number)

This meeting was organized within the interdisciplinary area of molecule/surface interactions induced, or studied by laser, ion or electron beam techniques. Especially to be emphasized will be the molecular physics and electromagnetism of beam-activated chemical reactions for applications in fabrication of semiconductor devices, in photocatalysis, in optical recording, and optical thin films. Emphasis was also placed on laser spectroscopy of molecular collison and reaction processes on surfaces, new sensitive or high-resolution spectroscopies for studies of adsorbated, and optical methods applied to surface characterization. The intent was to provide an informal working environment for a group not otherwise convened at any of the large meetings of broad coverage.

20 DISTRIBUTION / AVAILABILITY OF ABSTRACT	21 ABSTRACT SECURITY CLASSIFICATION	
☒ UNCLASSIFIED/UNLIMITED ☐ SAME AS RPT ☐ DTIC USERS	Unclassified	
22a. NAME OF RESPONSIBLE INDIVIDUAL Lt. Col. Larry W. Burggraf, USAF	22b. TELEPHONE (Include Area Code) 202/767-4960	22c. OFFICE SYMBOL NC

DD FORM 1473, 84 MAR 83 APR edition may be used until exhausted
All other editions are obsolete.

SECURITY CLASSIFICATION OF THIS PAGE
Unclassified

Proceedings of the
Second Topical Meeting on the Microphysics of Surfaces, Beams, and Adsorbates

1ST. AD-A170 797

16–18 February 1987
La Fonda Hotel
Santa Fe, New Mexico

Cosponsored by:
Air Force Office of Scientific Research
American Vacuum Society
Optical Society of America

Editors for the Proceedings:
T. M. Mayer
D. J. Ehrlich
T. J. Chuang

Published for the American Vacuum Society by
the American Institute of Physics, New York 1987

ORGANIZING COMMITTEE

D. J. Ehrlich, General Chair
MIT Lincoln Laboratory

T. J. Chuang, Program Co-chair
IBM Research Laboratory

T. M. Mayer, Program Co-chair
University of North Carolina

D. E. Aspnes
Bell Communications Research

D. Bauerle
Johannes Kepler University

J. Dieleman
Philips Research Laboratory

J. E. Greene
University of Illinois

R. B. Hall
Exxon Research and Engineering

M. Hanabusa
Toyohashi University of Technology

I. Hayashi
Optoelectronics Joint Research Laboratory

M. Hirose
Hiroshima University

S. J. C. Irvine
Royal Signals and Radar Establishment

P. F. Liao
Bell Communications Research

V. T. Nguyen
CNET-Grenoble

Accesion For
NTIS CRA&I
DTIC TAB
Unannounced
Justification
By
Distribution /
Availability Codes
Dist | Avail and / or Special
A-1

Proceedings of the
Second Topical Meeting on the
Microphysics of Surfaces, Beams, and Adsorbates

Preface 1385

The reaction of Si(100) 2×1 with NO and NH_3: The role of surface dangling bonds
Ph. Avouris, F. Bozso, and R. J. Hamers 1387

Molecular-dynamics simulation of low-energy beam deposition of silicon
Brian W. Dodson 1393

Summary Abstract: Chemical etching of silicon by CO_2 laser-induced dissociation of NF_3
James H. Brannon 1399

Visible-laser etching of refractory metals by surface modification
M. Rothschild, J. H. C. Sedlacek, and D. J. Ehrlich 1400

Modulated molecular-beam studies of the surface chemistry of silicon reaction with reactive gases
D. R. Olander, M. Balooch, J. Abrefah, and W. J. Siekhaus 1404

Effects of Ar^+ angle of incidence on the etching of Si with Cl_2 and low-energy Ar^+ ions
J. van Zwol, J. van Laar, A. W. Kolfschoten, and J. Dieleman 1410

Multiphoton-induced desorption of positive ions from barium fluoride
E. Matthias, H. B. Nielsen, J. Reif, A. Rosén, and E. Westin 1415

Excited-atom production by electron and ion bombardment of alkali halides
R. E. Walkup, Ph. Avouris, and A. P. Ghosh 1423

Selective area deposition of metals using low-energy electron beams
R. R. Kunz, T. E. Allen, and T. M. Mayer 1427

Summary Abstract: Role of ions in carbon-film deposition by a windowless hydrogen lamp
M. Hanabusa and T. Kaneoka 1432

Summary Abstract: Ion-beam-induced deposition of gold by focused and broad-beam sources
A. D. Dubner, G. M. Shedd, H. Lezec, and J. Melngailis 1434

Synchrotron radiation-excited chemical-vapor deposition and etching
Tsuneo Urisu and Hakaru Kyuragi 1436

Summary Abstract: Nucleation considerations in the wavelength-dependent activation selectivity of aluminum chemical-vapor deposition
G. S. Higashi, G. E. Blonder, C. G. Fleming, V. R. McCrary, and V. M. Donnelly 1441

Chemiluminescence from F and XeF_2 etching reactions with silicon
M. J. Mitchell, M. Suto, L. C. Lee, and T. J. Chuang 1444

An *in situ* infrared study on the interaction of oxygen plasmas with Si and fluorine plasmas with SiO_2 surfaces
W. C. M. Claassen and J. Dieleman 1450

Ultraviolet-assisted growth of GaAs
P. Balk, M. Fischer, D. Grundmann, R. Lückerath, H. Lüth, and W. Richter 1453

Atomic-layer growth of GaAs by modulated-continuous-wave laser metal-organic vapor-phase epitaxy
Yoshinobu Aoyagi, Atsutoshi Doi, Souhachi Iwai, and Susumu Namba 1460

Summary Abstract: Mass spectral identification of ultraviolet-laser photoablation products from polymers
R. C. Estler and N. S. Nogar 1465

Sum-frequency generation on dye-coated surfaces using collinear and noncollinear excitation geometries
R. E. Muenchausen, D. C. Nguyen, R. A. Keller, and N. S. Nogar 1466

Surface diffusion measured by laser-induced desorption: Monte Carlo simulation of effects of surface defects on diffusion
Richard B. Hall, Thomas H. Upton, and Eric Herbolzheimer 1470

Ion and neutral atomic and cluster sputtering yields of molybdenum
M. J. Pellin, W. Husinsky, W. F. Calaway, J. W. Burnett, E. L. Schweitzer, C. E. Young, B. Jørgensen, and D. M. Gruen 1477

(continued)

Molecular-beam epitaxy growth mechanisms on GaAs(100) surfaces
H. H. Farrell, J. P. Harbison, and L. D. Peterson **1482**

A study of the mechanism of metal deposition by the laser-induced forward transfer process
F. J. Adrian, J. Bohandy, B. F. Kim, A. N. Jette, and P. Thompson **1490**

Chemical processes involved in the etching of silicon by xenon difluoride
J. A. Dagata, D. W. Squire, C. S. Dulcey, D. S. Y. Hsu, and M. C. Lin **1495**

Summary Abstract: Adsorbate interactions and poisoning on Cr(110)
Neal D. Shinn **1501**

Formation of TiN on Si and SiO_2 by rapid processing using a large area electron beam
Die-chi Sun, Zeng-qi Yu, Fu-ming Li, Yuan-cheng Du, Hai Wang, and Guo-bao Jiang **1504**

Tunneling spectroscopy study of aniline adsorbed on aluminum oxide
R. J. Graves, C. B. Wallace, R. Ellialtioglu, and H. W. White **1508**

The role of Farben centers in electron- and photon-stimulated desorption from alkali halides
G. M. Loubriel, T. A. Green, N. H. Tolk, and R. F. Haglund, Jr. **1514**

Summary Abstract: Laser etching and evaporation of CaF_2 studied by mass spectrometry
R. C. Estler, J. E. Anderson, E. C. Apel, and N. S. Nogar **1519**

Energy deposition at insulator surfaces below the ultraviolet photoablation threshold
R. W. Dreyfus, F. A. McDonald, and R. J. von Gutfeld **1521**

Summary Abstract: Imaging of surface atoms and their wave functions with the scanning tunneling microscope
J. E. Demuth, R. J. Hamers, and R. M. Tromp **1528**

Pulsed-laser atom-probe and field-ion microscope study of solid surfaces
T. T. Tsong, H. M. Liu, Q. J. Gao, D. M. Ren, and Y. Liou **1530**

Proceedings Author Index **1535**

PREFACE

The Second Topical Meeting on the Microphysics of Surfaces, Beams, and Adsorbates was held at the La Fonda Hotel in Santa Fe, New Mexico, 16–18 February 1987. The interdisciplinary nature of the First Topical Meeting, held in 1985, was maintained with a broad emphasis on fundamental science of surface reactions stimulated by photon, electron, and ion beam irradiation, interactions of beams with surfaces and adsorbates, and methods of characterization and observation of surface phenomena. The format of the meeting was a three day program of single morning and evening sessions that consisted of a combination of invited and contributed papers, and an early evening poster session on the final day. Afternoons were unscheduled to allow informal interaction among the participants, and indulgence in the healthful New Mexico winter climate. General chairman for the meeting was D. J. Ehrlich, while T. J. Chuang and T. M. Mayer served as program co-chairmen.

The meeting was attended by 79 scientists from 9 countries and a total of 48 papers were given as either oral or poster presentations. An award was given for the paper which stimulated the most discussion during the meeting. By ballot of the participants, Gregg Higashi of AT&T Bell Laboratories was selected for the award, which consisted of an engraved metal plate from the Nambe Indian pueblo. Suggestions solicited from the participants recommended that the Third Microphysics Meeting be held in 1989.

Many people contributed to the success of the meeting particularly Laura Hughes, Barbara Hicks, Jane Trimmer, and Jarus Quinn of the Optical Society of America. Their expertise and efficiency of organization and execution of the many details of running a meeting were indispensible to its success. The international program committee, listed at the beginning of these Proceedings, all made many critical suggestions regarding the technical content of the meeting and recommendations of invited speakers. The session presiders, including D. Aspnes, W. Claassen, V. Donnelly, M. Hanabusa, J. Greene, G. Fisanick, and E. Yablonovich, were outstanding in their role of stimulating and moderating discussion throughout the meeting.

Many of the participants served a much appreciated role long after the meeting by refereeing papers for these Proceedings, and we gratefully acknowledge their efforts. Becky Gates of the JVST Editorial Office provided her usual efficient handling of manuscripts. Finally we wish to acknowledge the continuing guidance and financial support of Howard Schlossberg and the Air Force Office of Scientific Research.

T. M. Mayer
D. J. Ehrlich
T. J. Chuang
Proceedings Editors

The reaction of Si(100) 2×1 with NO and NH_3: The role of surface dangling bonds

Ph. Avouris, F. Bozso, and R. J. Hamers
IBM Watson Research Center, Yorktown Heights, New York 10598

(Received 27 February 1987; accepted 7 May 1987)

We present the results of a detailed study of the reactions of Si(100) 2×1 with NO and NH_3. We use several electron spectroscopies and ion scattering to study the reactivity of the surface and to determine the nature of the rate limiting steps of the above reactions over a wide temperature range (90–1200 K). We find that the Si(100) 2×1 surface is quite reactive and can dissociate NO or NH_3 even at 90 K. The reactions are, however, self-limiting. The released O or H atoms tie up the surface dangling bonds and passivate the surface. The N atoms, on the other hand, occupy mostly subsurface sites. Sustained reactivity and thin film growth occurs only at temperatures sufficiently high enough to desorb the surface oxygen or hydrogen and regenerate the surface dangling bonds. We find, however, that electron-stimulated desorption of the hydrogen can be used to nonthermally regenerate the surface dangling bonds and allow silicon nitride thin film growth even at 90 K. Because of the crucial role the top layer plays in the film growth mechanism we investigate its nature using the new technique of scanning tunneling microscopy (STM). This is the first *in situ* study of a surface chemical reaction by STM. The STM topographs indicate that the 2×1 reconstruction is preserved after exposure of the Si(100) 2×1 surface to NH_3. The topographs and the tunneling current versus voltage curves suggest the formation of a Si(100) 2×1 monohydride-like surface layer.

I. INTRODUCTION

Atoms at semiconductor surfaces have unsaturated valence (dangling bonds). For example, the bulklike terminated Si(100) surface has two dangling bonds per surface Si atom. Surface reconstruction reduces the high surface energy through nuclear displacements and a reduction of the number of dangling bonds. Nevertheless, surface dangling bonds may still exist on the reconstructed surfaces. In the case of Si(100) 2×1 surface the number of dangling bonds is reduced by approximately a factor of 2. The existence of dangling bonds should render semiconductor surfaces highly reactive. In practice however, it is often found that unusually high temperatures are needed to carry out semiconductor surface chemistry. Thus, the reactions of Si(100) with NH_3 or hydrocarbons to give silicon nitride or silicon carbide require temperatures in the range of 800–1200 °C.[1] Explanation of the high activation barriers requires the understanding of the mechanism of the surface reaction, in particular the nature of the rate-determining step. Since high reaction temperatures are often undesirable because they can also enhance the rates of unwanted side processes such as dopant diffusion, there is a strong interest in finding nonthermal reaction activation schemes.[2]

Here we present the results of a study of two prototype reactions: the reactions of Si(100) 2×1 with NO and NH_3. We use a wide variety of techniques, including x ray and ultraviolet (UV)-photoemission and Auger electron spectroscopies and ion scattering spectroscopy to study the reactivity and to determine the nature of the rate-limiting steps of the above reactions over a wide temperature range (90–1200 K). We also explore nonthermal schemes for reaction activation and demonstrate that electron-stimulated desorption can be used to induce sustained reactivity and to allow thin-film growth at very low temperatures. Finally, the nature of the surface produced by the reaction of Si(100) and NH_3, a crucial factor in the film growth process, is investigated using the new technique of scanning tunneling microscopy.

II. EXPERIMENT

The experiments were carried out in a UHV system with a base pressure of 7×10^{-11} Torr. This system was equipped for x-ray photoelectron spectroscopy (XPS), ultraviolet photoelectron spectroscopy (UPS), Auger electron spectroscopy (AES), low-energy electron diffraction (LEED), ion scattering spectroscopy (ISS), thermal desorption spectroscopy (TDS), and electron-stimulated desorption (ESD). The Si(100) crystal was of *n*-type, 10 Ω cm, phosphorous-doped material. The Si crystal was mounted on a specially designed liquid-nitrogen cooled sample holder which could be heated resistively. The crystal mounting technique ensured that no significant outgassing occurred during high temperature treatments. The pressure did not exceed 4×10^{-10} Torr at a sample temperature as high as 1200 K, preventing the formation of even small amounts of surface and subsurface contaminations during the reaction time. The sample was cleaned by 2 keV low angle Ar^+ sputtering, followed by annealing to 1150 K and rapid cooling to ~90 K. This treatment reliably produced a clean Si(100) 2×1 surface. The cleanliness of the sample was monitored by He(II) UPS with a sensitivity exceeding that of XPS or AES. The construction of the scanning tunneling microscope (STM) used in this study has been described in detail in Ref. 3.

III. RESULTS AND DISCUSSION

A. The reaction of Si(100) with NO

In Fig. 1 we show N(1*s*) XPS spectra obtained after exposing the Si(100) 2×1 surface at 90 K to NO. Two main

 0734-211X/87/051387-06$01.00 © 1987 American Vacuum Society

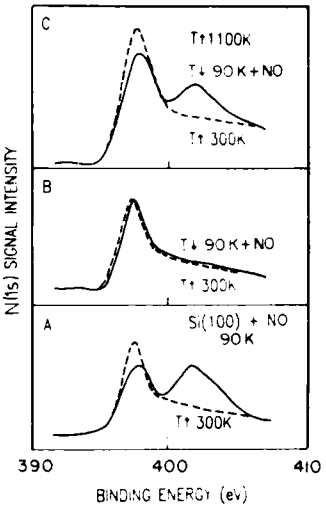

FIG. 1. (A) Solid line: N(1s) XPS spectrum obtained after exposure of the Si(100) 2 × 1 surface to 10 L NO at 90 K. Dashed line: the spectrum after anealing to 300 K. (B) Solid line: XPS spectrum obtained by cooling the annealed surface (dashed line) to 90 K, re-exposing to NO and then annealing to 300 K. No reaction is observed, the surface has been passivated. (C) Solid line: XPS spectrum obtained by heating the surface from (B) to 1100 K, cooling down to 90 K and exposing it to NO. Dashed line: after annealing to 300 K. The surface is active again.

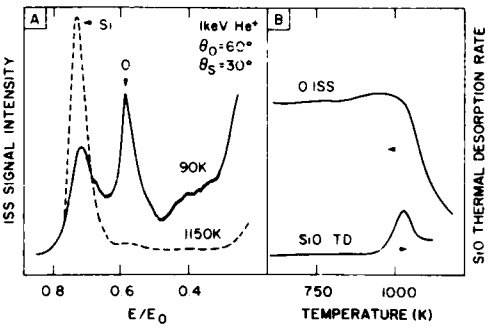

FIG. 2. (A) Solid line: He^+ ISS spectra obtained after exposure of the Si(100) 2 × 1 surface to 10 L NO at 90 K. Dashed line: after annealing to 1150 K. (B) The peak intensity of the oxygen ISS signal as a function of temperature and thermal desorption of SiO molecules.

peaks are observed: a low-binding energy peak at 397.7 eV which is characteristic of N in silicon nitride[4] and a high-binding energy peak at 401.9 eV. Upon gentle annealing of the sample to 300 K we observe the disappearance of the 401.9 eV peak with a simultaneous increase of the intensity of the 397.7 eV peak. Electron-stimulated desorption from the NO-exposed surface at 90 K[5] shows strong NO^+ desorption which however, is completely eliminated when the surface temperature is raised to 300 K. We thus conclude that the NO exists on the Si(100) surface at 90 K in both a dissociated and in a weakly adsorbed molecular form which is responsible for the 401.9-eV peak. Heating leads to the partial dissociation and partial desorption of the molecular form. Cooling the annealed surface to 90 K and re-exposing it to NO does not lead to any further increase of the XPS peak corresponding to dissociatively adsorbed NO. The surface shows a passivation towards any further reaction. The surface reactivity is restored only after heating to temperatures higher than ~1000 K.

To obtain information about the composition of the surface layer we used the highly surface sensitive technique of ion scattering spectroscopy (ISS). In our ISS experiments we used a 1 keV He^+ at a fixed 90° scattering angle. The results are shown in Fig. 2(a). Upon NO exposure the Si ISS signal decreases with the simultaneous appearance of a strong O ISS peak. No N could be detected by ISS except for a weak shoulder on the O ISS peak which was eliminated upon annealing. No further change of the ISS spectrum was detected with increasing temperature until about 900 K, where thermal desorption spectroscopy showed the desorption of SiO molecules [Fig. 2(b)]. Above this temperature the O ISS peak intensity decreases sharply while the Si intensity increases.

At ~1150 K the ISS spectrum shows no evidence of oxygen or nitrogen while the Si signal is as strong as that from the initial clean Si(100) surface. XPS studies, on the other hand, show no decrease in the N(1s) signal as a result of this heat treatment. From the above results we conclude that when NO dissociates on the Si(100) surface the O atom stays on the Si surface, while the N atom occupies mostly subsurface sites and is thus shielded from the incident He^+ ions used in ISS.

B. The reaction of Si(100) with NH_3

The behavior of the Si(100) + NH_3 reaction is in many respects similar to that of the Si(100) + NO reaction. Exposure of the Si(100) 2 × 1 surface to NH_3 at 90 K yields the N(1s) XPS spectrum shown in Fig. 3(a). Again, two main N(1s) peaks are observed: a peak at a binding energy of 399.7 eV and a second one at 397.7 eV. The 399.7 eV peak is ascribed to molecularly adsorbed NH_3. Heating the sample to 300 K leads to NH_3 desorption and to the disappearance of the 399.7 eV peak. Cooling the surface back down to 90 K and re-exposing the NH_3 regenerates the XPS peak characteristic of molecularly adsorbed NH_3. Again however, no further NH_3 dissociation takes place, the surface having been rendered inactive. He^+ ISS [Fig. 3(b)] shows that exposure of the Si(100) to NH_3 at 90 K leads to a fast decrease of the Si ISS signal. The ISS spectrum of the mixed nitride-molecularly adsorbed NH_3 phase at 90 K shows weak Si and N signals and a background at low energies. Annealing of this phase to 220 K and desorption of the molecularly adsorbed NH_3 leads to the increase of the Si ISS signal, which now has recovered approximately one-half of its original intensity, and the total elimination of the N ISS signal. No further significant change of the ISS spectrum is observed until the temperature is raised above ~600 K. At 1000 K [Fig. 3(b)] the Si ISS signal is as strong as that from the clean surface. The background at low energies has been eliminated, but no surface nitrogen is detected. XPS measurements, on the other hand, show no decrease in the N(1s) signal as a result of heating to 1000 K. We conclude that the nitrogen resulting from the dissociation of NH_3 resides mostly in subsurface sites and is thus shielded from the incident He^+ ions. The hydrogen of NH_3 could shield the Si atoms and give rise to the background at small E/E_0. However, the fact that after NH_3 desorption the Si ISS signal has only about one-half of its original intensity and that there is still significant background indicates the presence of surface hydrogen directly bonded to silicon. This surface hydrogen may inhibit further NH_3 dissociation and, thus, lead to the

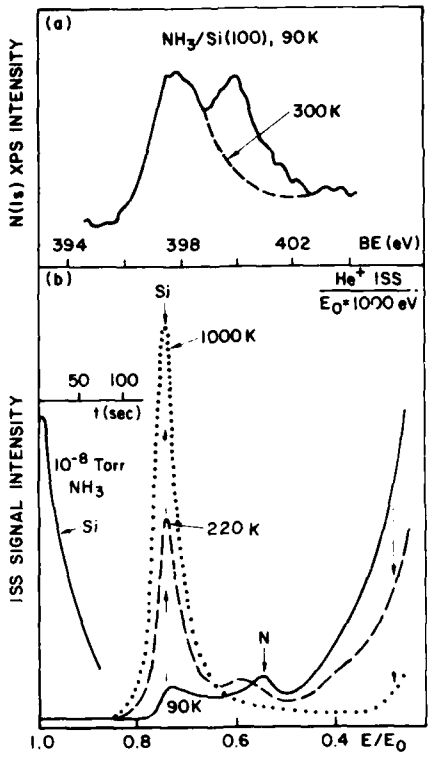

FIG. 3. (a) Solid line: N(1s) XPS spectrum obtained after exposure of the Si(100) 2×1 surface to 10 L NH_3 at 90 K. Dashed line: after annealing to 300 K. (b) Solid line: He^+ ISS spectrum of the NH_3-exposed surface at 90 K. Dashed line: after annealing to 220 K. Dotted line: after annealing to 1000 K. Inset: Si ISS peak intensity decrease in the course of a 10 L NH_3 exposure at 90 K.

observed self-limiting behavior. Strong support for this hypothesis has been provided by XPS studies of nitrogen uptake by the Si(100) surface exposed to NH_3 at increasing temperatures.[6] In those studies we found that nitrogen uptake is indeed strongly correlated with the hydrogen thermal desorption. If the hydrogen is desorbed at high temperatures and the sample is cooled back down to 90 K, the surface exhibits reactivity towards NH_3 very similar to the original clean Si(100) surface, despite the fact that XPS shows the formation of silicon nitride. The surface produced by the reaction of Si(100) with NO and subsequent thermal desorption of the oxygen is, similarly, reactive. From the above experiments we can conclude that the clean Si(100) 2×1 surface is quite reactive and can dissociate both NO and NH_3 even at 90 K. The observed passivation behavior must be due to the fact that the surface H or O tie up the Si(100) surface dangling bonds.

Direct information on the effect of surface H or O atoms and of thermal annealing on the Si dangling bonds is provided by UPS spectroscopy. In Fig. 4 we show He(II) UPS spectra of clean and ND_3-exposed Si(100) 2×1. The lowest binding energy peak (~1 eV) in the clean surface spectrum is due to photoemission from the dangling bond surface state.[7] Upon ND_3-exposure the dangling bond state is eliminated, as is seen best in the B–A difference UPS spectrum. Annealing to 825 K leads to deuterium desorption and the reappearance of the dangling bond state. (Note also the presence of new bands at about 4 and 7 eV due to overlapping Si–H and N $2p_\pi$ and $2p_\sigma$ photoemission.) The nature of dangling bond state of Si(100) 2×1 will be discussed in Sec. III D.

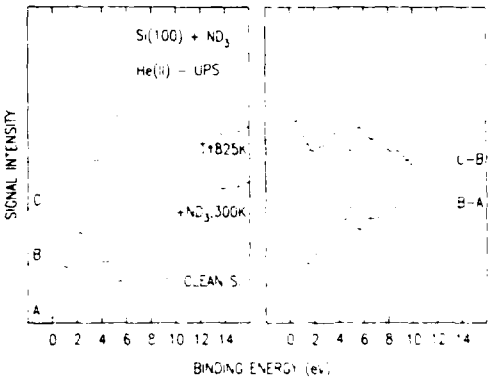

FIG. 4. Left-hand side: He(II) UPS spectra. (A) Clean Si(100) 2×1; (B) after exposure to ND_3 at 300 K, and (C) after annealing to 825 K. Right-hand side: Difference UPS spectra. Note the disappearance of the dangling bond band at ~0.5 eV (B–A spectrum) and its reappearance upon annealing (C–B spectrum).

C. Electron-beam stimulation of the Si(100)–NH_3 reaction

Having understood the cause of the surface passivation we sought to enhance the thin film growth processes by nonthermal means.[6] One such approach is to use electron-stimulated desorption (ESD) of the surface hydrogen as a nonthermal means for regeneration of surface dangling bonds. The ESD cross section for hydrogen is particularly high mainly because of its small mass which allows it to escape from the surface region before the repulsive electronic excitation is quenched.

In Fig. 5 we show the influence of electron irradiation on the reaction of Si(100) with NH_3 using as probes the Si *LVV* and N *KLL* Auger spectra excited by 1-keV electrons. In this study we use the same electron-beam to induce the reaction and also excite the Auger process. This is done in order to avoid the problems associated with the different sizes of the x-ray (XPS) and electron-beams on the sample. Curve (a) shows the Auger spectrum of the surface after exposure to 10 L NH_3 at 90 K. As can be seen, the N Auger signal is very small, corresponding to submonolayer nitride, while the Si Auger spectrum is the same as that of clean Si. Curve (b) shows the Si *LVV* spectrum obtained after raising the sample temperature to 900 K and exposing it to 10^{-7} Torr of NH_3 for 5 min. The spectrum shows the thermal growth of silicon nitride which gives the characteristic Si Auger peak at ~84 eV.[8] In addition, satellites displaced by about 11 and 21 eV from this peak are observed. The energies of these satellites coincide with the excitation energies of silicon surface plasmons[9] and silicon nitride bulk plasmons,[10] respectively. Curve (c) shows the Si *LVV* spectra obtained when the sample from step (b) is cooled back down to 90 K and exposed for 10 min simultaneously to 10^{-7} Torr NH_3 and the 20 μA, 1 keV electron-beam. We see that even at 90 K the electron-

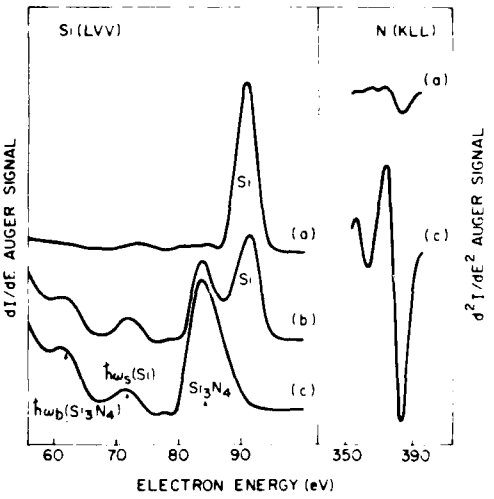

FIG. 5. Si(LVV) and N(KLL) Auger spectra of the Si(100) 2 × 1 surface. (a) After exposure to NH_3 at 90 K. (b) After partial thermal nitridization at 900 K. (c) After simultaneous exposure to NH_3 and an electron-beam (20 μA, 1 keV) at 90 K. Note that the Si(LVV) and N(KLL) Auger spectra were recorded in dI/dE and d^2I/dE^2 mode, respectively.

beam converts all silicon that can be probed by the Auger process to silicon nitride. The intensity of the N KLL Auger signal is approximately 10 times stronger than the corresponding signal from the surface not irradiated by the electron-beam. Assuming a layer-by-layer growth mechanism[11] for the silicon nitride film we estimate its thickness to be 20 ± 5 Å.

Thus, we see that through the electronic excitation induced by the electron-beam we have achieved controlled silicon nitride film growth even at 90 K. Our studies suggest that the main role of the electron-beam is to induce hydrogen desorption and thus help maintain a hydrogen-free Si surface which can then dissociate NH_3. Although, in principle, electron-beam induced dissociation of adsorbed NH_3 and the possible introduction of Si defects could further enhance the film growth process, neither seems to be essential. This is deduced from the fact that no measurable enhancement of the growth rate is observed on going from incident-electron energies below the N(1s) threshold to energies above this threshold. Also, after heating the irradiated surface to ~1000 K and cooling it back down to 90 K we find that it can readily dissociate NH_3, although this process should have annealed most of the possible radiation-induced defects.

D. The nature of the surface layer: STM study

The ISS spectra of Fig. 3, the Auger spectra of Fig. 5 and depth profiling studies using SIMS of the Si_2N^+ ion (not shown) indicate the presence of silicon on top of the nitride film. Since the nature of the surface layer(s) of thin films is a crucial factor in the film growth process, we have decided to investigate it using scanning tunneling microscopy.[12] Here we present preliminary results in this first *in situ* study of a surface chemical reaction in the STM. Before we discuss the STM results however, we need to review what is currently known about the clean Si(100) 2 × 1 surface. The bulk-like terminated Si(100) surface has two dangling bonds per surface Si atom. In the original model of Schlier and Farnsworth[13] the 2 × 1 reconstruction of this surface results when alternate rows of surface Si atoms move towards each other to form dimers, thereby rebonding one-half of the broken bonds.

The remaining dangling bonds interact with each other to form bonding and antibonding π-symmetry levels (π_b and π_a, respectively).[14] The interaction is however weak as can be seen by comparing the surface gap of ~0.5 eV[7] to the average bonding–antibonding splitting of 4.4–4.8 eV in bulk Si. Thus, on the basis of this dimer model the Si(100) 2 × 1 surface should be quite reactive. More recent theoretical work has focused on both refinements of the dimer model, i.e., possible distortions of the dimer (buckling)[15,16] and subsurface strain,[17] along with the proposal of completely new reconstruction models. Recent STM work has been decisive in establishing the correct reconstruction model for the 2 × 1 surface.[18] It showed that at room temperature, defect-free areas of the Si(100) 2 × 1 surface are composed of symmetric dimers while buckled dimers appear next to defect sites.[18] It is not clear at this point if the observed dimers represent a static configuration, or are time-averaged configurations of two interconverting buckled dimer forms. In either case we do not expect a large chemical effect since the predicted promotion energies are small (of the order of 100 meV) on the chemical bond energy scale.

In Fig. 6 (left-hand side) we show a STM picture of the Si(100) 2 × 1 surface before exposure to NH_3. This topograph is taken with the sample biased at − 2 V. Under these bias conditions, tunneling occurs out of the occupied levels

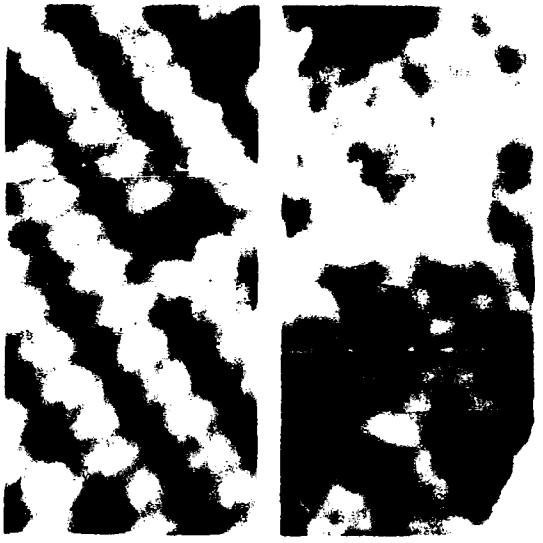

FIG. 6. Left-hand side: STM topograph of the Si(100) 2 × 1 surface obtained with the sample biased at − 2 V. White areas are surface protrusions and black areas are depressions, with a total gray-scale range of 1.0 Å. Right-hand side: STM topograph obtained after *in situ* exposure of a Si(100) 2 × 1 surface to NH_3. Sample biased at − 2 V.

of the surface. The image shows rows of oblong protrusions with a separation between rows of 7.7 Å, and a separation between protrusions within each row of 3.85 Å, producing an overall 2×1 local symmetry. Previous STM studies[18] have demonstrated that each of these protrusions represents a spatial map of the electrons in the Si–Si dimer bond. The corrugation along the ⟨110⟩ direction (perpendicular to the dimer rows) shows a minimum between the dimer rows and maximum along the center of the dimer rows with a total corrugation of 0.6 Å. In Fig. 6 (right-hand side) we show the STM picture obtained after *in situ* exposure to NH_3. Two important conclusions can be reached by inspection of this picture: (a) The reacted surface preserves the 2×1 reconstruction, and (b) while on the clean surface the center of the Si–Si bond was the strongest STM feature, on the reacted surface the tunneling is concentrated around the ends of the dimers. On this surface translation along the ⟨110⟩ direction reveals a strong minimum with a period of 7.7 Å and a second shallower minimum midway between these. The corrugation amplitude is roughly 50% larger than that of the clean Si(100) surface. In fact, the topograph of the reacted surface at -2 V looks very similar to the topograph of the clean surface[20] obtained under conditions ($+2$ V) where the tunneling takes place from the tip into the empty dangling bond states of the clean surface. This observation suggests that on the reacted surface, tunneling (Fig. 6, right-hand side) occurs out of states derived from the formerly empty states of the Si(100)-(2×1) surface. In addition to the topographs we have obtained the *I–V* characteristics of the two surfaces which are shown in Fig. 7. The most interesting feature is the enhancement of tunneling into the reacted surface observed at ~0.8 eV above the Fermi energy.

Based on the results of the other spectroscopies discussed above we offer the following tentative interpretation of the STM features: The reaction of Si(100) 2×1 with NH_3 does not break the Si–Si dimer bond. This is reflected in the fact that the 2×1 structure is for the most part preserved (which we also see by LEED). The H released attaches itself to the dangling bonds to form a surface monohydride-like phase, Si(100) 2×1:H, while the N atoms occupy mostly subsurface sites. The diminished charge density between the Si atoms forming the dimer in the STM topograph we ascribe to the formation of the Si(100) 2×1:H-like phase. The H removes intensity from the region around 1 eV below the top of the VB (see Fig. 4). According to the symmetric dimer description, this band is due to the occupied π_b-dangling bond level. The π_b level mixes with the hydrogen levels and becomes a Si–H bonding level whose DOS is peaked at -5 eV. This is clearly seen in the UPS difference spectra of Fig. 4. As a result of the formation of the Si–H bond, charge density is removed from the region between the two Si atoms forming the dimer bond, and any double bond character imparted to the dimer bond by the occupied π_b level is lost. In addition, the unoccupied π_a-dangling bonding level is pulled below the top of the VB, is mixed with the hydrogen levels and contributes to the Si–H bonding. We place this level tentatively at about 2–3 eV below the top of the VB (see again Fig. 4). This energy is in good agreement with the calculations of Appelbaum *et al.*[19] on the Si monohydride phase. The charge density of this level is concentrated along the Si–H bonds at the end of the Si–Si bond, and tunneling out of this level also should result in a topograph such as that seen in Fig. 6 (right-hand side). Thus, we believe that under the bias conditions used here (-2 V), Fig. 6 (right-hand side) images the modified Si dimers present in the Si(100)-(2×1): H phase. Finally, the enhanced tunneling into the surface at ~0.8 eV above the CB edge is most likely due to a hydrogen chemisorption-induced $(Si–H)_a$ unoccupied state. This could be the same state as that populated by the ~8 eV electronic transition observed by ELS of the Si(100) 2×1 monohydride phase.[21] This ELS transition is assumed to originate from $(Si–H)_b$ levels in the region of 6–8 eV below the top of the VB.

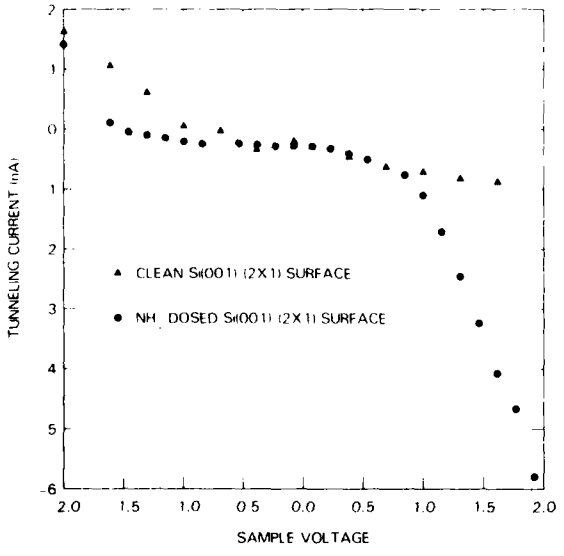

FIG. 7. Tunneling current vs voltage measurements for the clean (triangles) and NH_3-exposed (circles) Si(100) 2×1 surfaces. The samples are *n*-type (P-doped) Si(100) with a conductivity of 6 mΩ cm. The *I–V* curves are spatial averages of a low defect ~400 Å^2 area.

IV. SUMMARY AND CONCLUSIONS

We find that the Si(100) 2×1 surface can dissociate NO or NH_3 even at low temperatures (90 K). In both cases however, the reactions are self-limiting to less than a monolayer of product. ISS of the NH_3 or NO-exposed Si(100) surfaces does not detect N atoms while these are clearly seen by photoemission and Auger spectroscopies, thus indicating that the N atoms reside mostly in subsurface sites. On the other hand, surface oxygen from NO and, indirectly, H atoms from NH_3 are detected by ISS. These atoms tie up the Si surface dangling bonds, as is proven by the disappearance of the characteristic surface state in UPS. Sustained reactivity can be achieved only at temperatures sufficiently high enough to desorb the surface hydrogen or oxygen atoms and regenerate the surface dangling bonds. We find, however, that in the reaction of Si(100) with NH_3, electron-stimulated desorption can be used to nonthermally desorb the sur-

face hydrogen, regenerate the surface dangling bonds, and thus allow silicon nitride thin film growth even at 90 K.

Another important issue involves the nature of the surface layers(s) of the thin nitride films thus formed, ISS, SIMS, and Auger studies suggest there is always a thin Si layer on top of the nitride film irrespective of the mode of its preparation. Surface topographs obtained by the STM show that the 2×1 surface reconstruction is maintained on the reacted surface. The observed topographic features and I–V tunneling curves can be accounted for in terms of Si(100) 2×1 monohydride-like surface layer.

[1]M. M. Moslehi and K. C. Saraswat, IEEE J. Solid-State Circuits **20**, 6 (1985); J. A. Nemetz and R. E. Tressler, Solid State Technol. **26**, 209 (1983).

[2]For reviews, see: *Nanometer Structure Electronics*, edited by Y. Yamamura, T. Fujisava and S. Nambs (North-Holland, Amsterdam, 1985); *Laser and Electron Beam Processing of Materials*, edited by C. W. White and P. S. Peercy (Academic, New York, 1980).

[3]J. E. Demuth, R. J. Hamers, R. M. Tromp, and M. E. Welland, IBM J. Res. Dev. **30**, 396 (1986).

[4]J. A. Taylor, G. M. Lanchaster, A. Ignatiev, and J.W. Rabalais, J. Chem. Phys. **68**, 1776 (1978); D. Hackleman, Y. G. Vlasov, and R. B. Buck, Electrochem. Soc. **125**, 1875 (1978).

[5]Ph. Avouris, F. Bozso, and A. R. Rossi, in *Photon, Beam and Plasma Stimulated Chemical Processes at Surfaces, Materials Research Society Symposium Proceedings*, edited by V. M. Donnelly, I. P. Herman, and M.Hirose (to be published).

[6]F. Bozso and Ph. Avouris, Phys. Rev. Lett. **57**, 1185 (1986).

[7]F. J. Himpsel and D. E. Eastman, J. Vac. Sci. Technol. **16**, 1297 (1979).

[8]J. F. Delord, A. G.Schrott, and S. C. Fain, J. Vac. Sci. Technol. **17**, 517 (1980).

[9]H. Raether, *Excitation of Plasmons and Interband Transitions by Electrons* (Springer, Berlin, 1980).

[10]R. Kärcher, L. Ley, and R. L. Johnson, Phys. Rev. B **30**, 1896 (1984); N. Lieske and R. Hezel, Thin Solid Films **61**, 217 (1979).

[11]T. A. Gallon, Surf. Sci. **17**, 486 (1969).

[12]G. Binnig, H. Rohrer, C. Gerber, and E. Weibel, Phys. Rev. Lett. **50**, 120 (1983).

[13]R. E. Schlier and H. E. Farnsworth, J. Chem. Phys. **30**, 917 (1959).

[14]J. A. Appelbaum, G. A. Baraff, and D. A. Hamann, Phys. Rev. B **14**, 588 (1976).

[15]D. J. Chadi, Phys. Rev. Lett. **43**, 43 (1979).

[16]J. Ihm, M. L. Cohen, and D. J. Chadi, Phys. Rev. B **21**, 4592 (1980).

[17]J. A. Appelbaum and D. R. Hamann, Surf. Sci. **74**, 21 (1978).

[18]R. J. Hamers, R. M. Tromp, and J. E. Demuth, Phys. Rev. B **34**, 5343 (1986).

[19]J. A. Appelbaum, G. A. Baraff, D. R. Hamann, H. D. Hagstrum, and T. Sakurai, Surf. Sci. **70**, 654 (1978).

[20]R. J. Hamers, R. M. Tromp, and J. E. Demuth, Surf. Sci. (to be published).

[21]S. Maruno, H. Iwasaki, K. Horioka, S.-T. Li, and S. Nakamura, Phys. Rev. B **27**, 4110 (1983).

Molecular-dynamics simulation of low-energy beam deposition of silicon

Brian W. Dodson
Sandia National Laboratories, Albuquerque, New Mexico 87185

(Received 27 February 1987; accepted 7 May 1987)

The mechanisms controlling low-energy (10–100 eV) beam deposition of silicon onto a relaxed (111) silicon substrate have been studied using a molecular dynamics technique. The atomic interaction was modeled using a many-body empirical potential so that the effects of the covalent Si–Si bonding could be accurately included. Silicon atoms (10 eV) with near-perpendicular incidence were studied to determine the energy-loss mechanism resulting in capture and the local lattice excitation near and subsequent diffusion of excess vibrational energy away from the impact point. Shallow angles of incidence (5°–30°) were studied for beam energies of 20–100 eV. For incidence angles less than an energy- and orientation-dependent critical value, a new phenomenon of "surface channeling" is observed, in which the trajectory of the incoming particle is steered parallel to, and roughly 2 Å above, the surface of the substrate by inelastic interaction with the surface atoms. The phenomena observed in low energy beam deposition offer considerable promise for precision control of the growth of nonequilibrium semiconductor structures.

I. INTRODUCTION

Devices with a more critical dependence on physical structure than had previously been required are currently of great interest. Examples of such structures include superlattices, strained-layer systems, devices with ultrathin layers, such as single quantum wells, and so on. The performance of such devices can be very sensitive to the presence of defect structures produced during the growth phase. Since defects often correlate with substrate temperature, one approach to reducing defect density is to optimize the growth temperature. However, this optimization involves balancing competing processes: If the temperature is too low, defects associated with unannealed configurations will remain, whereas if the temperature is too high, thermally induced defects will appear. For some systems an adequate window of temperatures exists between these two limits, but this is not always the case.

A nonequilibrium approach to reducing defects in the growth process is to keep the bulk of the structure relatively cool during deposition while supplying the additional excitation needed to grow high-quality material through some specific interaction with the surface. One proposed technique is low-energy ion-beam deposition, in which experimental studies have recently begun.[1] As the beam energy must be larger than the energy of adsorption of a silicon atom onto a silicon surface (a few eV) to significantly change the adsorption dynamics from those of thermal deposition, the perpendicular and near-perpendicular atomic beam deposition of 10 eV silicon atoms onto, and the grazing incidence interaction of 20–100 eV silicon atoms with, a silicon (111) surface has been simulated.

II. SIMULATION METHOD AND INTERACTION POTENTIAL

Molecular dynamics techniques have been used with considerable success to simulate the microscopic response of atomistic systems to a given set of conditions.[2] In molecular dynamics the classical equations of motion for an assembly of interacting particles are integrated numerically, resulting in a complete classical description of the system over the integration period. In the current simulations, we are generally concerned with length scales of < 10 nm, several hundred atoms, and time scales < 1 ps. These restrictions make the problem easily accessible to conventional molecular dynamics techniques.

Proper description of the Si–Si bonding interactions is an important factor in these low-energy simulations. In the simulation of high energy (many keV) ion–substrate interactions, the ion–atom potential is taken as spherically symmetric and purely repulsive, since the kinetic energy scale is so much larger than that of binding energies.[3] These approximations cannot properly be applied in the very-low energy regime with which we are currently concerned, especially when concerned with materials which form highly directional covalent bonds. Several many-body empirical potentials which describe, with various regimes of applicability, the bonding of silicon have recently been introduced.[4–7] The qualitative (and even semiquantitative) nature of these results should not depend strongly on the details of the silicon potential used. The potential recently introduced by Dodson,[7] which provides a useful and accurate global description of the structural energetics of silicon, is used here.

In the Dodson potential, the structural energy is the sum over the asymmetric potential Φ_{ij}:

$$E = 0.5 \sum_{i,j} \Phi_{ij}, \tag{1}$$

where the pairwise potential Φ_{ij} has a form similar to a Morse potential, but contains a many-body interference term B_{ij}:

$$\Phi_{ij} = f_{ij}(A\, e^{-\lambda_1 r_{ij}} - B_{ij}\, e^{-\lambda_2 r_{ij}}), \tag{2}$$

where A, λ_1, and λ_2 are fitting parameters, and f_{ij} is a radial cutoff term active near 3 Å. The influence of neighboring

 0734-211X/87/051393-06$01.00 © 1987 American Vacuum Society

atoms on the bonding interaction is embedded in the many-body interference term B_{ij}, which contains four additional fitting parameters. The parameters of the potential were fit, using a simulated annealing technique, to the lattice constant and cohesive energy of various high-density phases of silicon, the bulk modulus of bulk silicon, and the bond length and binding energy of the Si_2 dimer. The resulting potential accurately describes the structural energetics of silicon over a broad range of configurations.[7]

The kinetic energies used in the present simulation are large enough that suspicion may be raised concerning the behavior of the potential at small r, since it is based on a data set primarily concerned with deformation of the outer electron shell. As the momentum transfer in an individual scattering event rises, the inner shell structure will produce harder core behavior than predicted by the Dodson potential. The error resulting from this factor must be evaluated in two different regimes, near-perpendicular beam deposition and the predicted surface channeling of more grazing incidence angles. In the first case, there will be large momentum transfer in individual scattering events. In this regime, the resulting errors are rendered acceptable by limiting the beam energy to 10 eV. When considering grazing angles of incidence, the accuracy of the potential at small r is unimportant, since the trajectories of interest result from glancing interactions with the surface in which the vertical momentum is absorbed by gentle inelastic interactions with many surface atoms. We therefore have reasonable confidence in the present use of the Dodson potential, but emphasize that (at least) an additional hard-core repulsive term would be needed to extend the description to problems requiring treatment of larger momentum transfers.

The most time-consuming step in the molecular dynamics integration scheme is the determination of the forces acting on each particle by differentiation of the many-body potential. In order to limit the difficulty of computation, we have chosen the Schofield method,[8] a simple, although stable, low-order integration routine requiring only one force calculation per time step. The resulting algorithm, using a time step of 0.5 femtoseconds (fs), has proven quite satisfactory on the class of problems considered here.

III. ATOMIC BEAM DEPOSITION OF SILICON

In considering the adsorption phenomena which may affect the atomic beam deposition of silicon, two dynamical properties are of particular interest. The first is the simple description of adsorption dynamics of the incident atom, including such factors as sticking coefficient, depth of penetration, location of adsorbed atom (surface, interstitial site, etc.), and sputtering of substrate atoms. These quantities allow one to describe the direct consequences of atomic beam growth. In addition, however, the excess kinetic energy and momentum of the atomic beam must be carried away by substrate lattice excitation if the incoming particle is to stick. This excess energy provides a local and short-lived region of vibrational excitation which may serve to selectively anneal nearby metastable configurations which arise during the process of growth. It is therefore important to determine the characteristic time, length, and energy scales driving this nonequilibrium annealing process.

A. Near-perpendicular beam incidence: Adsorption

The incoming atoms from normal or near-normal 10 eV silicon beams adsorbed into a single site very quickly (perhaps 0.05–0.1 ps). Since lattice vibrations will travel no more than a few angstroms in this period, the adsorption sites of the incident atoms could be determined through studies on a small substrate. Thus, the substrate used for this portion of the study was a 4×4 cell on the (111) surface six atomic layers thick (96 atoms total). The silicon atom from the incoming beam is assigned a random initial position above the (111) surface, and the evolution of the system is then calculated using the molecular dynamics procedure described above. Sets of 30 trajectories were analyzed to determine trends in the deposition of atoms directed perpendicular to the surface, with a 60° angle of incidence and surface projection parallel to the (110) surface vector, and with a 60° angle of incidence and surface projection parallel to the $(1\bar{2}0)$ surface vector. [The first of the 60° beams is directed along a bulk channeling direction for the (111) silicon surface whereas the second is not.] For normal incidence, 70% of the incident atoms either come to rest in an interstitial position between the first and second double atomic layers or substitute for an atom in the first double layer by knocking the substrate atom into an interstitial location; the other 30% come to rest on the surface. For the 60° $(1\bar{2}0)$ case, 50% of the incident atoms become interstitials between the first two double atomic layers. The other 50% come to rest on the surface, usually after skipping perhaps 10 Å from the initial impact point along the surface. For a 60° angle of incidence parallel to a bulk channeling direction, the results are similar (60% penetrate, 40% surface). In this case, however, the incident atoms do not travel across the surface before they stop. It appears that the bulk channeling directions have little influence on the penetration of incident silicon atoms in this energy range. All incident atoms stick to the substrate, and no substrate atoms sputter off, indicating a sticking coefficient of one, within the limitations inherent in examining a finite number of trajectories.

B. Near-perpendicular beam incidence: Surface excitation

Propagation of excess vibrational energy away from the impact point is now considered. A larger substrate is used for these relaxation studies so that longer time scales can be considered. The silicon substrate used consists of a 6×8 cell eight atomic layers in thickness on an unreconstructed but relaxed (111) free surface, with a total of 384 atoms. This structure is large enough that reflected phonons cannot disturb the dynamics of the incoming beam atom in the 0.2 ps duration of the calculation. All other features of the calculation are identical with those described earlier.

The kinetic energy and momentum of an incident atom is almost entirely transferred to the substrate lattice within 0.02 ps of the initial interaction. The energy and momentum are first coupled to substrate atoms near the impact point by

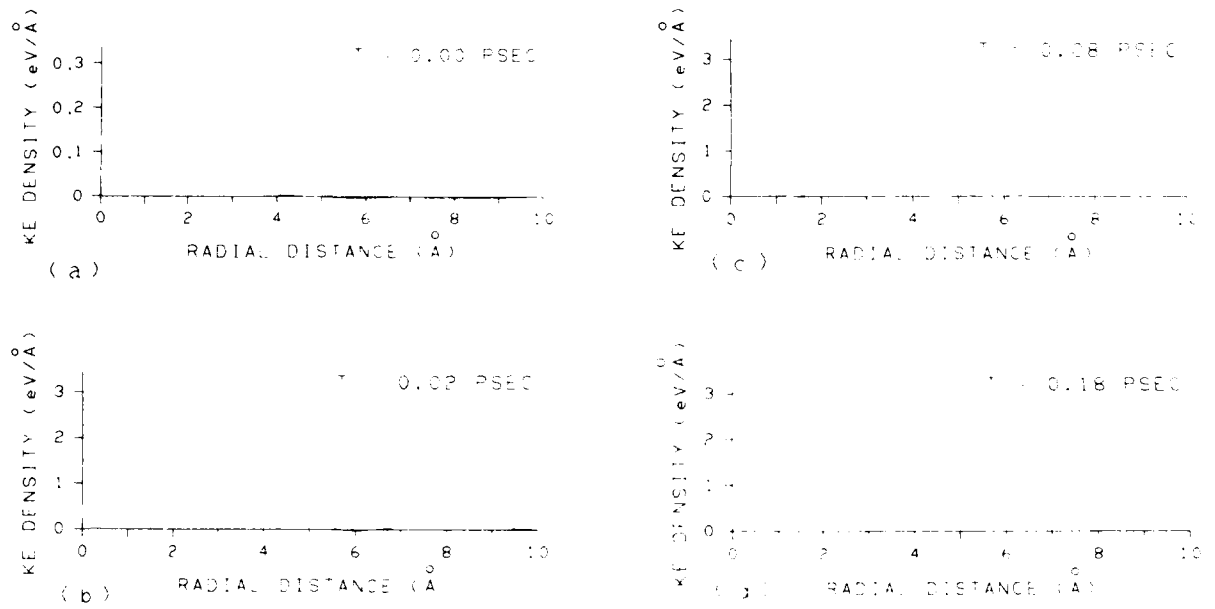

FIG. 1. Time evolution of the radial kinetic energy density as a function of distance from the impact point of a perpendicularly directed 10 eV silicon atom incident on a silicon (111) surface. The kinetic energy in a spherical shell is calculated and normalized to units of eV/Å. (a) At $t = 0$; (b) at 0.02 ps; (c) at 0.08 ps, and (d) at $t = 0.18$ ps. The excess energy resulting from the initial collision radiates from the impact site at near-sonic velocity.

collision-induced momentum transfer, and are then transported away from the impact point by phonons. This process results in a transient spike of high-vibrational excitation near the impact point, which may serve to activate modifications of the atomic configuration near the impact point. In order to evaluate this possibility, characteristic time, length, and energy scales of the transient spike were determined by calculating the radial (relative to the impact point) kinetic energy density and radial dependence of the average kinetic energy per substrate atom (local "temperature") as a function of time after impact.

A typical set of results are presented in Figs. 1 and 2,

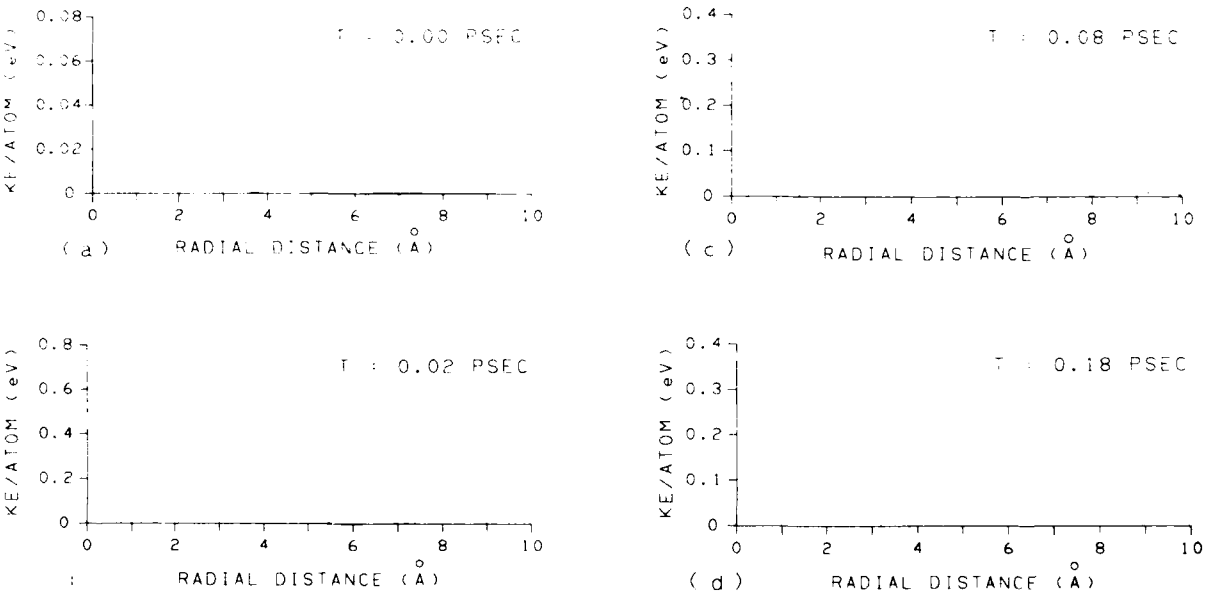

FIG. 2. Time evolution of the average kinetic energy per atom resulting from the impact of a perpendicularly directed 10 eV silicon atom on a silicon (111) surface as a function of distance from the impact point. (a) At $t = 0$; (b) at 0.02 ps; (c) at 0.08 ps, and (d) at $t = 0.18$ ps. The large residual kinetic energies at small (2–4 Å) radius are due to a local breathing mode with a time constant of 0.08 ps.

which show the time evolution of, respectively, the radial kinetic energy density and the local "temperature" for the first 0.2 ps of the simulation. The 10 eV atom has normal incidence. It begins to interact with the substrate atoms at $t = 0$ [Figs. 1(a) and 2(a)]. At 0.02 ps, 80% of the initial kinetic energy of the incident atom has been transferred to the substrate, divided almost evenly between kinetic and potential lattice energy. At this time the excitation has only affected atoms surrounding the impact site; the radius of the excitation front is roughly 4 Å [Fig. 1(b)] and the average kinetic energy per atom in this region is about 0.3 eV [Fig. 2(b)]. The next set of graphs [Figs. 1(c) and 2(c)] describe the system at 0.08 ps. Here the excitation front has advanced to nearly 9 Å radius. This corresponds to a front velocity of 83 ± 20 Å/ps, which is remarkably (and, to some extent, coincidently) similar to the sound velocity of 83 Å/ps. The large peak near 4.5 Å is a signature of a relatively long-lived local mode which slowly radiates energy into the substrate. Detailed analysis of the time evolution of this mode reveals that the initial amplitude corresponds to an excitation of several eV, and that the local mode radiates its energy to the rest of the lattice with a time constant of about 0.08 ps. Finally [Fig. 1(d)] at 0.18 ps, the radial kinetic energy density, save for the diminishing influence of the small radius local mode, is nearly constant at 0.5 eV/Å past 15 Å radius. Consistent with this, the average kinetic energy per atom [Fig. 2(d)] continues to decrease roughly as r^{-2} beyond the immediate neighborhood of the impact point.

C. Grazing incidence: Trajectories of 20–100 eV Si atoms

We next considered the case of grazing beam incidence (3°–30°) with energies of 20–100 eV. For these grazing angles, the principal interaction with the substrate takes place by interaction with many substrate atoms, rather than through one major collision. The generic results in this regime of incidence angle and beam energy are rapid adsorption, trajectories which bounce off of the substrate, or long-range surface transport (denoted surface channeling). We consider grazing beam incidence onto a long thin silicon substrate which has an unreconstructed but relaxed (111) surface, about 12 Å wide and 80 Å long (in the 100 direction), is 4 atomic layers in thickness, and totals 320 atoms. This is large enough that reflected phonons do not disturb the dynamics of atoms from the incoming beam as they move rapidly enough to leave the disturbance behind. The silicon atom incident from the atomic beam is assigned an initial position, direction, and velocity. In all cases, the initial trajectory is oriented with the projection of the velocity onto the surface collinear with the surface (110) vector, so that the particle travels primarily along the long direction of the substrate. The evolution of the resulting system of 321 atoms is then calculated as before. The simulation is continued until the incoming particle bounces from the surface, is adsorbed onto the substrate, or falls off the edge of the substrate through surface channeling (typically a few tenths of a picosecond).

Results of a typical simulation run appear in Fig. 3. The

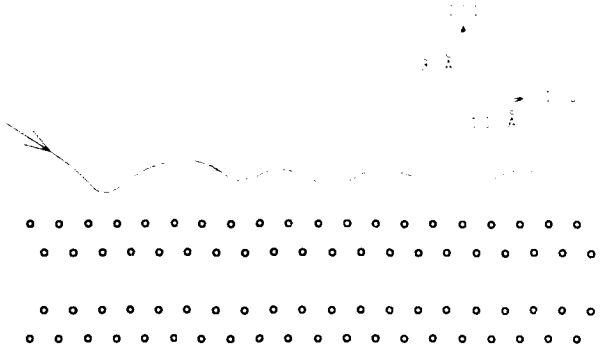

FIG. 3. The surface channeling trajectory of an energetic silicon atom interacting with an unreconstructed silicon (111) surface. The incoming atom initially has a kinetic energy of 40 eV and an angle of incidence of 10°. The perpendicular momentum of the incoming atom is lost to the substrate through inelastic interactions, and the resulting trajectory is essentially parallel to, and about 2 Å above, the surface of the substrate. Evaluation of the rate of energy loss indicates that the total range along the surface for this 40 eV atom is several thousand angstroms.

incoming silicon atom had a kinetic energy of 40 eV and an initial angle of incidence of 10° relative to the surface of the substrate. In the figure, the response of the substrate to the impact of the atom is ignored, and the substrate atomic positions are simply the initial positions. (The substrate response is of course included in the molecular dynamics simulation.) As the particle approaches the substrate, it begins to interact with the surface atoms. The kinetic energy increases slightly as the atom is attracted to the surface, but the interaction quickly turns repulsive and the particle bounces from the surface. However, the interaction with the surface atoms is sufficiently inelastic (because of phonons removing momentum from the impact site) that the rebounding particle does not escape from the lattice, but rather is trapped between the attractive and repulsive interactions with the surface of the substrate. The vertical oscillations in these competing fields damp out quickly as the atom undergoes further inelastic interaction with the substrate, and eventually settles down to motion nearly parallel to and about 2 Å above the surface of the substrate. In this mode, further loss of kinetic energy is extremely slow, and ranges of thousands of angstroms (on perfect surfaces) are possible.

D. Surface channeling trajectories

The behavior seen in Fig. 3 and described above is a general feature of low-angle beam–surface interactions in this energy range. We call this phenomenon surface channeling, in analogy to the more conventional bulk channeling. In bulk channeling, a high energy ion is steered along the symmetry directions of a lattice by the combined effect of the repulsive potentials of the atoms making up the lattice. The analogy in surface channeling is that the competition between the long-range attractive potential and short-range repulsive potential generated by the surface of the substrate serves to produce a potential well which guides the incoming atom along the surface, once the vertical momentum is lost to the substrate. The (110) direction seems particularly fa-

vorable on the (111) silicon surface, but surface channeling should also occur along other surface symmetry directions at more glancing angles.

The phenomenon called surface channeling described above must not be confused with the low-angle trajectory focusing surface scattering described by Thompson and coworkers,[9,10] or with the near-surface channeling mechanism proposed by Sizmann and Varelas.[11] In both cases these effects require high-beam energies (keV–MeV), the principal interaction with the substrate takes place below the surface layer, and transport does not take place along the surface. By contrast, in the surface channeling mechanism proposed here, very low energy atoms exhibit the effect, the principal interaction generates bulk phonons through excitation of the surface atoms, and transport occurs *above* the substrate surface, which is never penetrated.

It is interesting to consider the effect of different initial conditions on the trajectories of incoming atoms. The initial location of the particle does not have a strong influence on the surface channeling phenomenon. We cannot rule out the possibility that there may be impact points on the surface which are particularly unfavorable for surface channeling, but such points were not found in the current work, in which roughly 100 trajectories were studied. It is clearly safe to say that, at a given beam orientation and kinetic energy, the appearance (or not) of surface channeling is a generic behavior, occasional special cases notwithstanding.

For a given initial beam energy, there is a critical angle Θ_c below which we see surface channeling and above which either the particle bounces off or rapidly absorbs onto the surface (see sample trajectories in Fig. 4). Surface channeling quickly vanishes when the critical angle is exceeded. Note that, as the critical angle is exceeded, the lowest energy atoms (20 eV) always undergo abrupt adsorption [Fig. 4(a)], whereas higher energy (40 and 100 eV) atoms always bounce off [Fig. 4(b)]. The higher energy atoms are expected to stick or penetrate for sufficiently steep angles, which suggests that there is a second critical angle ψ_c separating scattering off the surface from deposition onto the substrate (see Fig. 5).

The dependence of the critical angle on the initial energy of the beam is described next. We have performed a large number of simulations at 20, 40, and 100 eV in order to identify the critical angles (respectively, 18°, 10°, and 5°) for each initial energy. These figures tell us that the perpendicular momentum, which must be carried away via inelastic interaction with the substrate, is only a weak function of beam energy. More precisely, the critical perpendicular velocity is

$$V_p = 20.5 + 336/E_b, \tag{3}$$

where V_p is in Å/ps and E_b is the beam energy in eV. This relation implies that the initial inelastic interaction with the surface removes similar amounts of perpendicular momentum regardless of the total kinetic energy of the incoming atom, which allows extrapolation of the critical conditions to higher energies. The above information is summarized in an incidence angle versus beam energy phase diagram (Fig. 5).

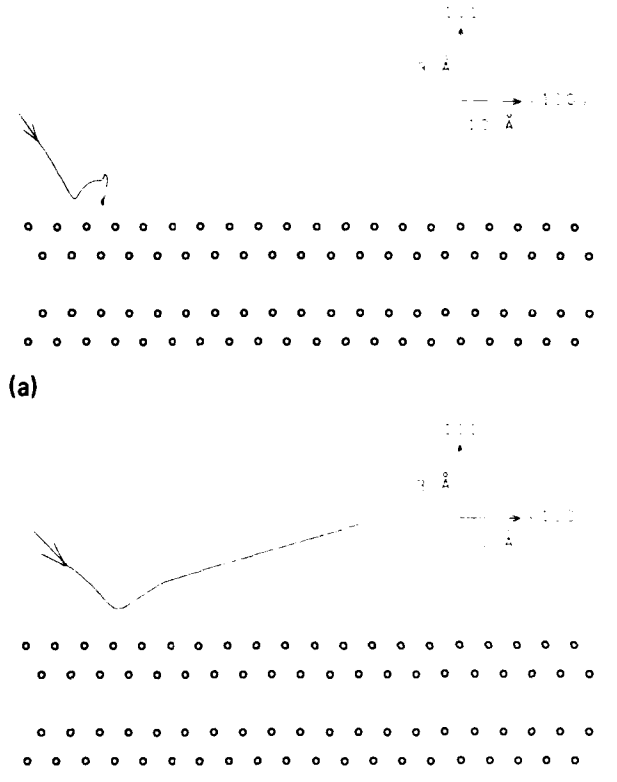

FIG. 4. Atomic trajectories not resulting in surface channeling. (a) Initial kinetic energy of 20 eV, angle of incidence of 20°. Adsorption occurs immediately following the first collision with the surface. (b) Initial kinetic energy of 40 eV, angle of incidence of 12°. The incoming particle scatters immediately from the surface.

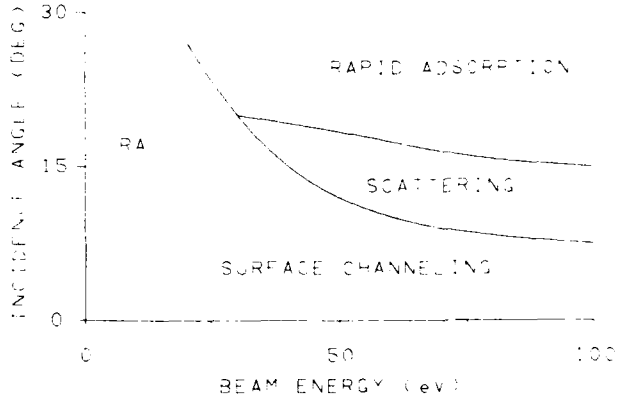

FIG. 5. Incidence angle vs beam energy phase plane for Si atoms incident on the Si(111) surface. Incoming atoms with either low-kinetic energy or large angle of incidence will quickly become localized and adsorb at the surface (this region is marked RA for rapid adsorption). If the energy is above roughly 20 eV and the angle of incidence is sufficiently small, the atom will be steered into a surface channeling trajectory. At somewhat higher energies and intermediate incidence angles, the incoming atom scatters off the surface and does not stick.

Finally, the rate of energy loss experienced by a particle in the surface channeling mode is of interest. This can be evaluated directly from the computed trajectories by numerical differentiation. Upon doing so, the rate of energy loss is found to be nearly linear in kinetic energy of the surface channeling atom; in this energy range,

$$\frac{\partial E}{\partial X} = 0.000\,154E - 0.0193, \tag{4}$$

where E is in eV and X is in Å. Clearly, this relation cannot be extrapolated far outside of this energy range, but it does allow estimation of the total surface channeling range along the surface as a function of initial beam energy. Crude estimates reveal that the surface channeling ranges will be thousands of Å for the higher energy atoms. Direct calculation for the 20 eV atoms show that the linearity of the energy loss relation fails badly for smaller energies, and a surface channeling range of around 40 Å is found before adsorption for these atoms, compared to perhaps 1000 Å as predicted by Eq. (4).

IV. DISCUSSION

Let us first summarize the case of perpendicular or near-perpendicular incidence of 10 eV Si atoms on the unreconstructed Si(111) surface. In normal incidence, 30% of the incident atoms come to rest on top of the surface, whereas 70% penetrate into the top double layer and stop in interstitial sites. At an incidence angle of 60°, 50%–60% of the incident atoms penetrate and stop in interstitial sites, while the remainder form a new layer on the surface. Thermal diffusion should eventually bring the interstitials to the surface, but this requires long times compared to our current simulation. When the beam orientation is parallel to a $(1\bar{2}0)$ surface vector, the incident atoms which remain on the surface first skip perhaps 10 Å along the surface from the initial impact point. When the orientation is along a (110) surface vector (the bulk channeling direction), those atoms remaining on the surface do not skip before adsorption. A small region near the impact point experiences very strong excitation and forms a short-lived ($\tau \simeq 0.08$ ps) local mode which radiates the energy of the incident atom to the rest of the lattice as phonons. The lattice excitation (and accompanying distortion) beyond about 10 Å from the impact site will be insufficient to anneal metastable states. In no case were incident atoms seen to bounce off the substrate, nor were substrate atoms sputtered off.

In the case of grazing incidence, the most interesting result is prediction of surface channeling trajectories. In surface channeling the competition between the long-range attractive potential and short-range repulsive potential generated by the surface of the substrate serves to produce a potential well which guides the incoming atom along the surface. For a given initial beam energy, there is a critical angle Θ_c below which we see surface channeling and above which either the particle bounces off or rapidly absorbs onto the surface. The (110) direction seems particularly favorable for surface channeling on the relaxed Si(111) surface, but it should occur along other surface vectors at more glancing angles. In a surface channeling trajectory on this idealized surface, loss of kinetic energy is extremely slow, and ranges of thousands of angstroms (on perfect surfaces) are possible.

The atomic beam adsorption processes described here thus offer several mechanisms which may lead to high-quality epitaxial growth. One is the formation and subsequent thermal annealing of near-surface interstitials. This produces a dense and locally distorted near-surface region which is likely to heal into a perfect epitaxial layer through thermal migration of the interstitial atoms. Since these interstitial atoms need not diffuse long distances to reach the surface, the healing suggested above should be a quick process, allowing high rates of deposition. Another mechanism is strong vibrational excitation in the region near the impact of the incident atom, which will provide a nonthermal mechanism through which metastable defect structures may be eliminated. Finally, the surface channeling trajectories offer the possibility of preferentially transferring energy into badly placed surface atoms, resulting in benign growth on good crystal combined with selective removal of physisorbed impurities and improperly placed adatoms. Extending our current studies into actual simulations of crystal growth has not been possible because of the long time scales involved. However, it seems clear that low-energy atomic beam deposition offers several nonthermal mechanisms for influencing the quality of epitaxial crystal growth. Either simple low-energy beam deposition or a combination of beam deposition with more conventional molecular beam epitaxy seem to be reasonable possibilities for high-quality epitaxial film growth in semiconductors.

ACKNOWLEDGMENTS

Many discussions with Paul Taylor are acknowledged. This work was performed at Sandia National Laboratories and was supported by U.S. DOE Contract No. DE-ACO4-76DP00789.

[1] N. Herbots, B. R. Appleton, T. S. Noggle, S. J. Pennycook, R. A. Zuhr, and D. M. Zehner, in *Semiconductor-Based Heterojunctions*, edited by M. L. Green *et al.* (The Metallurgical Society, Warrendale, PA, 1986).
[2] See J. J. Erpenbeck and W. W. Wood, in *Statistical Mechanics-Part B*, edited by B. J. Berne (Plenum, New York, 1977), Chap. 1; J. Kushick and B. J. Berne, *ibid.* Chap. 2.
[3] L. C. Feldman, J. W. Mayer, and S. T. Picraux, *Materials Analysis by Ion Channeling* (Academic, New York, 1982).
[4] F. H. Stillinger and T. A. Weber, Phys. Rev. B **31**, 5262 (1985).
[5] R. Biswas and D. R. Hamann, Phys. Rev. Lett. **55**, 2001 (1985).
[6] J. Tersoff, Phys. Rev. Lett. **56**, 632 (1986).
[7] B. W. Dodson, Phys. Rev. B **35**, 2795 (1987).
[8] P. Schofield, Comput. Phys. Commun. **5**, 17 (1973).
[9] A. D. Marwick, M. W. Thompson, B. W. Farmery, and G. S. Harbinson, Radiat. Eff. **15**, 195 (1972).
[10] M. W. Thompson and H. J. Pabst, Radiat. Eff. **37**, 105 (1978).
[11] R. Sizmann and C. Varelas, Nucl. Instrum. Methods **132**, 633 (1976).

Summary Abstract: Chemical etching of silicon by CO_2 laser-induced dissociation of NF_3

James H. Brannon
IBM East Fishkill Development Laboratory, Route 52, Z-340, Hopewell Jct., New York 12533

(Received 27 February 1987; accepted 7 May 1987)

Studies have established that radicals frequently react with surfaces which are inert to the parent molecule. Dissociation of the parent molecule provides a surface reaction channel which avoids the often large activation barrier inherent in parent molecule–surface interactions. The interaction of gaseous NF_3 with amorphous silicon is an excellent example of this type of behavior.[1] While NF_3 does not measurably chemically react with silicon at ambient temperatures, the fluorine containing radicals produced from laser-dissociated NF_3 readily do so. Some fraction of the fluorosilyl reaction products spontaneously desorb, resulting in silicon removal (etching). In this study parallel and focused dissociating radiation did not contact the silicon surface, indicating that the observed etching reactions result from purely chemical effects. Effects due to transient heating or ablation were not present.

The ν_3 nonsymmetric stretching mode of NF_3 is resonant with several CO_2 laser lines in the P branch of the 10.6 μm band. Because of this, it appeared likely that an intense pulse would induce gas-phase dissociation. Nevertheless, prior to this study the CO_2 laser induced dissociation of NF_3 had not been reported. At 922.8 cm^{-1} the absorption cross section is found to decrease with increasing pulse energy—evidence supporting a multiple-photon excitation process. Due to the laser pulse length (1.2 μs) and gas pressure ($\leqslant$250 Torr) however, the dissociation process is collisionally (thermally) assisted. Infrared absorption analysis of the irradiated gas shows peaks due to N_2F_4. The presence of N_2F_4 suggests that NF_3 decomposition produces an NF_2 intermediate, and hence F atoms, according to the following: $NF_3 \rightarrow NF_2 + F$. The reaction of two NF_2 species will produce the observed N_2F_4.

Once formed, fluorine-containing radicals diffuse the minimum 3 mm distance to the silicon surface and react, causing etching. Etching was monitored using a quartz-crystal microbalance upon which a thin layer of silicon had been deposited.[2] For a surface with no previous exposure to the dissociation products, the data demonstrate the formation of a fluorosilyl surface layer prior to the onset of etching.[3] In contrast, a surface already thickly fluorinated does not form a thicker layer once laser pulsing commences. In that case etching starts immediately with the first pulse. The etch yield dependence on several parameters was examined for the case of a thickly fluorinated silicon surface. These variables were laser energy and wave number, NF_3 pressure, argon buffer gas pressure for a fixed NF_3 pressure, and perpendicular distance from the laser focal volume to the surface. The etch yield is found to linearly increase as the gas incident laser energy is increased. Similarly, as the laser wave number is tuned to NF_3 rotational bands of increasing absorption, the etch yield increases. In examining pressure variation, no etching is observed until 35 Torr. From there, the etch yield rises sharply toward its maximum near 110 Torr. As the pressure is further increased toward 250 Torr, the etch yields drops off linearly. For a fixed NF_3 pressure of 70 Torr, increasing partial pressures of argon buffer gas result in a decreasing etch yield. This is interpreted as a drop in the laser dissociation yield due to increasing competition with collisional relaxation. Finally, the etch yield varies inversely with increasing distance from the focal volume to the surface. This is consistent with a simple radical diffusion model.

Reaction product analysis has clearly shown that NF_3 dissociation occurs, and that resultant fluorine interacts with the silicon. Most informative are the results from x-ray photoelectron spectroscopy (XPS) analysis of the silicon surface. The pre-etch analysis of a Si sample with no exposure to NF_3, only air, shows the main Si(2p) peak near 100.5 eV, and a smaller, broader peak near 104.5 eV. This latter peak indicates the expected presence of a native oxide layer. The oxide layer is consistent with the strong O(1s) spectrum. Small amounts of carbon were also observed. The Si sample was then inserted into the gas chamber and etching was performed. During transfer from the etching chamber to the XPS spectrometer, the etched sample was briefly exposed to air ($\sim$1 s). The postetch analysis showed the O(1s) intensity to significantly decrease. No carbon or nitrogen peaks were detected. In contrast to the pre-etch spectrum, a strong F(1s) peak was present. Again, the Si(2p) spectrum showed two peaks—the main peak at 100.5 eV, and another chemically shifted 5.3 eV higher. This new peak is different from the residual Si–O peak at 104.5 eV, and represents the Si–F bonding in the fluorosilyl reaction layer. The magnitude of the chemical shift indicates significant concentrations of SiF_3 and SiF_4. SiF_4 in the fluorosilyl reaction layer has been observed previously.[4]

[1] J. H. Brannon, Appl. Phys. A (to be published).
[2] T. J. Chuang, J. Chem. Phys. **74**, 1453 (1981).
[3] F. A. Houle, J. Appl. Phys. **60**, 3018 (1986).
[4] F. R. McFeeley, J. F. Morar, and F. J. Himpsel, Surf. Sci. **165**, 277 (1986).

 0734-211X/87/051399-01$01.00 © 1987 American Vacuum Society

Visible-laser etching of refractory metals by surface modification[a)]

M. Rothschild, J. H. C. Sedlacek, and D. J. Ehrlich
Massachusetts Institute of Technology Lincoln Laboratory, Lexington, Massachusetts 02173

(Received 1 May 1987; accepted 4 June 1987)

A two-step laser etching technique for Mo and W films is described. In the first step, the laser modifies the chemical composition of the metal surface; in the second, deep etching of the pre-exposed areas is by broad-area heating in a reactive ambient. The surface modification takes place in the presence of Cl_2, which etches the native-metal oxide and replaces it with a more volatile metal halide. Deep etching is performed with NF_3. Since the native oxide is resistant toward etching with NF_3, the second step is selective with respect to the laser-halogenated area and is, in effect, a chemical amplification of the surface modification. Well-delineated, high-contrast patterns are obtained with this method.

I. INTRODUCTION

In recent years, electronic materials processing by laser-controlled chemistry has been developed rapidly. Early industrial applications are now appearing. The role of the laser radiation in these processes varies from case to case, but usually involves one or more of the following mechanisms: localized heating, electronic or vibrational excitation of an external phase (vapor or adsorbed layers), or generation of electron–hole pairs.[1] Within this wide range of laser-induced processes one powerful special class employs laser-induced surface modifications to obtain efficient utilization of the typically expensive laser photons. A process in this class consists of two steps. The laser is used in the first step only to reactively cause a localized change in surface chemical properties, while a more conventional nonlaser-based technique is used in the second step for "chemical amplification." If properly configured, this reaction will proceed at much greater rates on the laser-pretreated areas than on those previously unexposed to the laser. The term chemical amplification arises from the great increase in pattern depth achieved in the second step. Such a two-step process is similar to the expose–develop sequence in patterning photoresists, with one important difference: in photoresists the photons are used to change the bulk properties of the resist, whereas in "surface modification" the photons are used to modify a thin surface layer.

The scheme of laser-induced surface modification followed by chemical amplification has been demonstrated to date in several systems. These include (1) room-temperature polymerization of organic vapors on a laser-deposited thin film of a compound similar to a Ziegler–Natta catalyst,[2] and (2) laser-chemical-vapor deposition of aluminum from trimethylaluminum (TMA) and triisobutylaluminum (TIBA).[3,4] The former materials are deposited by photolysis of mixed adsorbates of $TiCl_4$ and TMA; amplification is by vapor-phase polymerization. In the second example the laser-modification stage consists of "photonucleation," i.e., deposition of a ~5-nm-thick aluminum-containing film, while the chemical amplification is by thermal chemical-vapor deposition (CVD), which proceeds autocatalytically at elevated temperatures. The increased temperatures have been generated by conventional heating or irradiation with a weakly focused infrared laser.

In this paper we describe a new laser surface modification/chemical amplification system, used for etching of refractory metals by laser surface halogenation. In this process, the laser is employed in the area-selective removal of an existing surface layer, the "native" oxide commonly present on metals exposed to air. The "chemical amplification" consists of etching the metal itself in a heated, halogen containing ambient. Under appropriate conditions, the native-metal oxide in the unexposed areas impedes etching of the metal in the second stage, and thus the chemical amplification is selective towards the laser preirradiated pattern.

II. EXPERIMENTAL AND DISCUSSION

The experimental setup to demonstrate the technique consists of a cw, line-tunable Ar^+-laser operated at 488 nm which is focused through a microscope objective onto a 30-nm-thick sputter-deposited Mo or W thin film on a fused silica substrate. The surface modification step is carried out in a flowing Cl_2 ambient, with a moderately tight focus (~5 μm diameter) at 10–30 mW power, corresponding to an estimated surface temperature of 230–700 °C. The chemical amplification takes place in a NF_3 ambient, where the required heating is obtained by intentionally defocusing the laser beam to a ~250-μm-diam spot. Other heat sources, such as a lamp, could be effective substitutes to the laser in this step. For patterning purposes, the substrate is placed on a computer-controlled translation stage. The gas-handling manifold is an all stainless-steel system, pumped by a liquid-nitrogen-trapped diffusion pump. The gas-flow rate is adjusted to ~4 sccm with a mass flow controller.

In previous publications[5,6] we discussed the mechanism of etching Mo and W thin films in a similar configuration but in one step only, i.e., when the laser is tightly focused throughout the etching process and the ambient gas is either Cl_2 or NF_3. Briefly, the etching is due to the generation of volatile metal halides, such as $MoCl_5$ and WF_6, formed in a surface chemical reaction which is promoted by the local laser-induced decomposition of the ambient molecules into reactive halogen-containing radicals. This decomposition is either a pyrolytic (NF_3) or a thermally enhanced photolytic process (Cl_2). The temporal evolution of the one-step etch process was observed by monitoring the self-transmission of the laser through the film being etched. Since these observa-

 0734-211X/87/051400-04$01.00 © 1987 American Vacuum Society

tions are key in the design of the modification/amplification sequence, we discuss them in some detail.

Typical transmission curves are shown in Fig. 1. There are marked differences between the Cl_2 and NF_3 reactions. Etching with Cl_2 is observed to start instantaneously within the resolution of our experiment (~ 1 ms) as evidenced by the instantaneous rise in transmitted laser power. The point of inflection of the Cl_2 curve in Fig. 1 (at $t \simeq 0.3$ s) corresponds to etch through in the center of the laser focus. At $t > 0.3$ s, the transmitted power increases due to further etching over a wide halo, whose size is determined by gas-phase diffusion and recombination kinetics of the Cl atoms, generated photochemically above the surface. The NF_3 curve (Fig. 1) exhibits a very different behavior. In particular, there is an induction time, t_0 (~ 50 ms under the experimental conditions of Fig. 1) where no change in optical transmission is observed. The value of t_0 depends on laser power and NF_3 pressure, and can be varied in the range 10 ms to 10 s. At $t > t_0$, however, the etch rate is faster with NF_3 than with Cl_2, as seen from the steeper initial slopes in Fig. 1. The saturation level with NF_3 is somewhat lower than that with Cl_2 because no "halo" is etched, as the etching mechanism is solely pyrolytic with no gas-phase photolysis. In the following we will concentrate on the initial stages of the etching, specifically on the induction time, t_0.

In one experiment the conditions were adjusted so that $t_0 = 250$ ms, (laser power = 50 mW, NF_3 pressure = 300 Torr). A previously untreated area was briefly (20 ms) exposed to 200 Torr Cl_2 at 24 mW. The exposure was too short to induce appreciable etching, and no changes in transmission were observed. Following this exposure the Cl_2 was pumped out and a 300 Torr NF_3 was introduced into the cell. When the laser was turned on (50 mW) the transmission started increasing immediately. The behavior is qualitatively similar to that of NF_3 in Fig. 1, except the induction time is reduced to 10 ms. This dramatic reduction in t_0 due to a brief pre-exposure to Cl_2, as well as the different behavior of the NF_3 and Cl_2 curves in Fig. 1, are interpreted as due to a thin layer near the surface of the Mo film, which is resistant towards laser etching with NF_3, but is easily removed by laser/Cl_2. The induction time, t_0, is the time necessary for NF_3 to remove this layer. After this the bulk of the Mo is etched rapidly. In contrast, Cl_2 etches the top layer rapidly, but the etch rate of the Mo bulk is slower with Cl_2 than with NF_3.

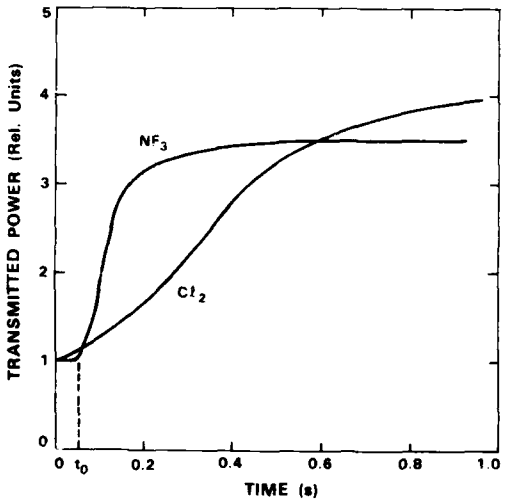

FIG. 1. The temporal evolution of the self-transmission of the laser through initially 30-nm-thick Mo film on fused silica. The pressure of Cl_2 or NF_3 is 300 Torr, and the laser power is 70 mW on a 6-μm-diam spot. With Cl_2, etching starts instantaneously, while with NF_3 there is an induction time, t_0. Following t_0, the etch rate with NF_3 is faster than the etch rate with Cl_2.

The elemental composition of this surface layer is revealed by Auger electron spectroscopy (AES) of the Mo film. Auger depth profiling of the 30-nm-thick film shows a large amount ($> 30\%$) of oxygen incorporated in the top ~ 4 nm, corresponding to the native oxide of the Mo film. This oxide acts as a barrier towards laser etching of Mo with NF_3. We confirmed this interpretation of the AES results in the following experiments. Under conditions for which $t_0 = 250$ ms, the surface was exposed to laser/NF_3 for t_0, during which no changes in transmission were noted. Then the NF_3 was pumped out and the same area was irradiated in vacuum at 20 mW for 300 s. Still there was no change in transmission. Then the laser was turned off, and the sample was exposed to air for 300 s. Following this a laser etch with NF_3 was attempted again. A renewed induction time of $t_0 = 250$ ms was observed, followed by rapid etching of the Mo. It should be stressed that if either the low-power irradiation in vacuum or the exposure to air were omitted in the above sequence, t_0 was zero in the second laser/NF_3 etch, and the transmission was seen to rise immediately. This experiment demonstrated that, following the removal of the resistive layer in the first laser/NF_3 exposure this layer was regrown in the presence of oxygen. Its identity as Mo oxide, suggested by AES, was thus supported. We would also like to comment on the necessity of the low-power irradiation in vacuum, prior to reoxidizing the Mo. This step is apparently required in order to volatilize the metal fluoride layer which is generated in the first laser/NF_3 exposure. Following removal of the oxide by generation of volatile oxyfluorides, the active sites on the bare metal are occupied by fluorine atoms, which form a thin-MoF_x layer. The halide layer must be removed before oxidation can take place, for example by heating it with the laser in vacuum.

The studies described above have shown that the thin refractory metal films of our studies, are in fact composed of two films; a thin (4–5 nm) oxide, and the bulk metal. The oxide is easily etched with a laser in a Cl_2 ambient, but not with NF_3. The reasons for this are not obvious. The vapor pressure of the etch products is apparently not the determining factor, since the sublimation energies of the best-known tungsten oxyfluorides are lower than those of the tungsten oxychlorides. However, a possible source for the higher effectiveness of Cl_2 is its higher surface coverage. In separate studies with a quartz crystal microbalance, we determined the adsorption isotherms of Cl_2 and NF_3 vapors on Mo and W films. At equal pressures, the mass of adsorbed Cl_2 was 10–30 times higher than that of adsorbed NF_3. The isotherm for Cl_2 saturates only weakly and multiple monolayers are certainly adsorbed at the higher pressures. On the other

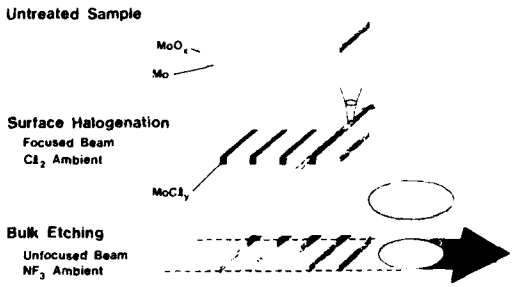

FIG. 2. Schematic diagram of the two-step laser etching of a Mo film by patterned surface modification (Cl_2 ambient) followed by chemical amplification (NF_3 ambient).

hand, the bulk metal is more rapidly etched with NF_3 than with Cl_2. These differences suggest a laser-induced chemically amplified etching process. This two-step patterned etching is shown schematically in Fig. 2. The laser-induced surface modification step consists of etching the metal oxide layer with a focused laser in a 200 Torr Cl_2 ambient, and its replacement with a more volatile metal chloride. This step is performed in a rapid scanning geometry (30 mW power, 0.25 mm/s scan speed in our studies) and it does not affect the bulk optical and electrical properties of the metal film. The chemical amplification step is the deep etching of the halogenated metal with NF_3. This step requires broad-area heating in order to induce the required pyrolysis of NF_3, the

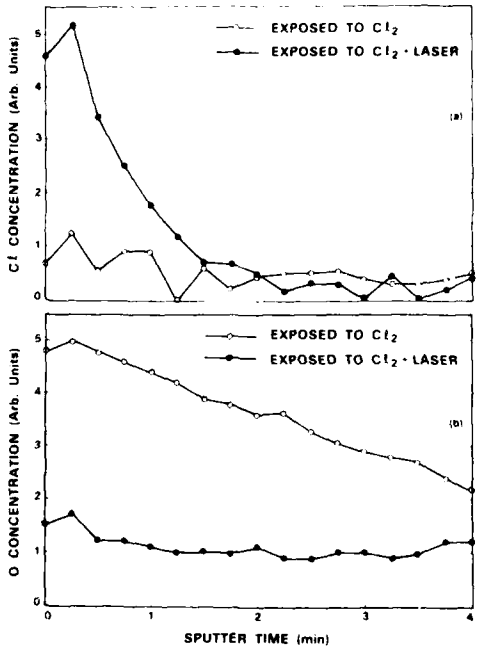

FIG. 3. Auger depth profiles of chlorine and oxygen near the surface of a Mo film. One minute of sputter time corresponds to ~1 nm. The open circles represent concentrations after the sample was exposed to 200 Torr Cl_2 but with the laser off. No significant subsurface chlorination is detected, while the oxide is 4–5 nm deep. The filled circles represent concentrations after laser halogenation. The oxygen is replaced with a thin (~1 nm) layer of chlorine.

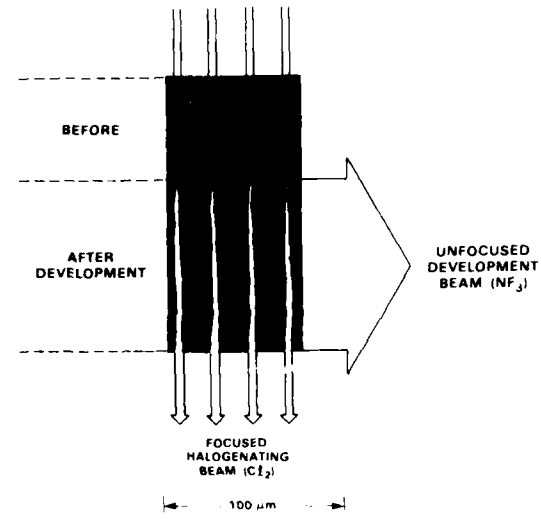

FIG. 4. Optical transmission micrograph of a 30-nm-thick Mo film patterned in the fashion described in the text and shown schematically in Fig. 2. The tapering is due to the nonuniform intensity profile of the defocused developing beam. Note the high contrast achievable with this technique.

subsequent fluorination reactions, as well as the temperature necessary for vaporization of the metal fluorides. In our studies we used a weakly focused laser (300 mW over a 250 μm spot) for ~30 s, although other alternatives may be as effective. The changes in elemental composition induced by the laser in the first step are shown in Fig. 3, which is the result of Auger depth profiling before and after laser irradiation (1 min of sputter time corresponds to ~1 nm in depth). In Fig. 3(a) the oxygen concentration which originally extended ~4 nm below the surface, is seen to be effectively removed by the laser/Cl_2, and Fig. 3(b) shows its replacement with a ~1-nm-deep chlorine-containing layer. Incidentally, no subsurface Cl was observed in untreated areas, indicating that "dark" halogenation of Mo or W is not a significant process. Finally, Fig. 4 is a transmission optical micrograph of the sample after the chemical amplification step. The 30-nm-thick Mo film is completely removed along the surface-halogenated lines "drawn" in the first step. Under our experimental conditions the optical transmission of the Mo film is not affected by either the "write" or "development" stages alone, but the combination of the two generates the high-contrast features shown in Fig. 4.

Based on our observations, the metal halide layer is quite stable and the chemical amplification does not have to be performed immediately after laser halogenation. In fact, we exposed one sample to laboratory air for several days before developing the "latent image," without any noticeable adverse effects on the rate of development or final contrast. The spatial resolution attainable with this two-step etching technique is ultimately limited by the depth of the etched features. Similarly to the polymerization and laser deposition examples mentioned in the Introduction,[2–4] the chemical amplification in etching is an isotropic process, therefore undercutting will become significant when the required etch depth is comparable to or larger than the etch width.

III. CONCLUSIONS

In conclusion, we have demonstrated a new laser-based surface modification process, similar to the UV-laser modification for polymerization and metal CVD. The present process was applied to the etching of refractory metal films. The surface modification involves replacing (by halogenation) of the native-metal-oxide layer, by laser reaction in Cl_2. A conventional large-area heating process is used for chemical amplification in a second vapor ambient (NF_3).

[a]This work was sponsored by the Department of the Air Force, in part under a specific program supported by the Air Force Office of Scientific Research, by the Defense Advanced Research Projects Agency and by the Army Research Office.

[1]D. J. Ehrlich and J. Y. Tsao, J. Vac. Sci. Technol. B **1**, 696 (1983).
[2]D. J. Ehrlich and J. Y. Tsao, Appl. Phys. Lett. **46**, 198 (1985).
[3]J. Y. Tsao and D. J. Ehrlich, Appl. Phys. Lett. **45**, 617 (1984); J. Cryst. Growth **68**, 176 (1984).
[4]G. E. Blonder, G. S. Higashi, and C. G. Fleming, Appl. Phys. Lett. **50**, 766 (1987).
[5]M. Rothschild, J. H. C. Sedlacek, and D. J. Ehrlich, Appl. Phys. Lett. **49**, 1554 (1986).
[6]M. Rothschild, J. H. C. Sedlacek, J. G. Black, and D. J. Ehrlich, J. Vac. Sci. Technol. B **5**, 414 (1987).

Modulated molecular-beam studies of the surface chemistry of silicon reaction with reactive gases

D. R. Olander, M. Balooch, and J. Abrefah
Materials and Chemical Sciences Division, Lawrence Berkeley Laboratory and Department of Nuclear Engineering, University of California, Berkeley, California 94720

W. J. Siekhaus
Materials and Chemistry Department, Lawrence Livermore Laboratory, Livermore, California 94550

(Received 27 February 1987; accepted 7 May 1987)

The method of studying the kinetics of gas–solid surface reactions using modulated molecular beams and mass-spectrometric detection is described. Results obtained for Si(111) etching by H(g) and deposition from SiH_4 are presented.

I. INTRODUCTION

In commercial practice, single-crystal semiconductors are etched using reactive gases in plasma discharges. Rational design of such processes requires quantitative models of the kinetics of the surface reactions by which substrate atoms are removed as volatile species. Because of the complexity of plasma etching, single-effect experiments, in which only the chemistry of the surface reactions are investigated, are very useful. An important feature of such experiments is the capability of separating the effects of the purely thermal reaction from the enhancement due to simultaneous exposure of the reacting surface to the gaseous reactant and to laser or ion beams. Preliminary studies of the thermal reaction which lead to an understanding of the basic mechanism of the surface chemistry then permit subsequent investigation of the beam-enhanced reaction to be better understood. It is often possible to determine which elementary steps of the reaction are affected by the energetic beam. In this paper, an experimental system with this two-step capability is described. Application of the method to the investigation of thermal etching and deposition reactions on silicon are also presented.

The technique of supplying the gaseous reactant in the form of a collisionless molecular beam to the surface under high-vacuum conditions and sampling the reaction products with an *in situ* mass spectrometer can provide mechanistic and kinetic information on the surface processes.[1] The incident reactant molecular beam is modulated (i.e., synchronously chopped), both to improve the signal-to-noise ratio of the detection system as well as to provide a measure of the reaction residence time on the surface. The latter is contained in the *phase lag* between the first Fourier component of the output signal from the reaction product and that from the portion of the reactant which simply scatters from the surface without reacting. The *reaction probability* is the ratio of the magnitudes of these two signals. By measuring this conjugate pair as a function of incident reactant beam intensity, substrate temperature, and modulation frequency, a model of the surface reaction can be deduced. Reaction models are based on combinations of elementary steps such as sticking of the gaseous reactants, surface reaction of the Langmuir–Hinshelwood or the Eley–Rideal types, product desorption, and surface or bulk diffusion of reaction intermediates.

The broad utility of the modulated-beam technique has been described in detail in a number of review papers.[2–9] The major advantages and drawbacks of the modulated molecular-beam method for studying surface chemical kinetics are summarized below. The positive features of the technique include the following:

Because of the high-vacuum environment in which the experiments are conducted, the surfaces can be well-cleaned and characterized; different faces of single crystal specimens can be studied.

Because of the low-background gas pressure in the apparatus, no gas-phase reactions occur; only the pure heterogeneous gas–surface processes are involved.

Reactions with walls of the apparatus or in sampling lines are avoided by the direct-flight mass-spectrometric detection method; molecules which make several collisons with chamber walls are out-of-phase and not detected by the ac detection method.

Reverse reactions are absent because the reaction products are pumped away before they can return to the reacting surface.

Mass spectrometric detection makes product identification unambiguous (except for difficulties in interpreting mass spectra).

In addition to providing kinetic information on the surface processes, modulation of the primary beam coupled with phase-sensitive detection improves the signal-to-noise ratio of the detection system by at least a factor of 1000 relative to dc detection; it also permits velocities of the species emitted from the surface to be measured.

Because the data obtained in the experiment include both reaction probability and reaction phase lag, modeling of the reaction can be detailed and quantitative.

Most mechanisms containing nonlinear elementary processes are adequately treated by the linearized analysis.[10]

Processes with multiple reaction channels (i.e., branch mechanisms) can be analyzed as readily as single-channel mechanisms. Section IV gives an example of such a reaction model.

On the other hand, the molecular-beam method has a

 0734-211X/87/051404-06$01.00 © 1987 American Vacuum Society

number of disadvantages when compared to conventional techniques for investigating surface reactions. Most notable are:

The sensitivity is low because only the consequences of single molecular collisions with the surface are detectable; in practice, reactions which occur with a probability $< \sim 10^{-4}$ per collision cannot be measured.

Very fast reactions (reaction times $< \sim 10\,\mu s$) are detectable but all kinetic information on the reactions is lost; this limitation arises from the effects of time spreading during transit of the molecular beams between the surface and the detector.

Because only low-pressure reactions (i.e., incident fluxes equivalent to gas pressures $p_{eq} \leqslant 10^{-4}$ Torr) can be studied, relating the results of molecular-beam experiments to those obtained for the same reaction conducted at atmospheric pressure by conventional methods is problematic.

The angular distribution of the scattered reactant molecules or the emitted reaction products are usually not measured; moreover, with a fixed angle of detection (usually specular), interpretation of the data relies on the assumption of a cosine distribution of all molecules leaving the surface.

Modeling of the reactions is complex and uniqueness of the models deduced from molecular-beam data is not assured.

Despite these shortcomings, the modulated molecular-beam method can provide kinetic and mechanistic information on surface chemical reactions unattainable by other techniques. However, reaction modeling based on such data is greatly enhanced if complementary techniques, such as temperature-ramp thermal desorption, surface spectroscopy, or gravimetric rate experiments, can be brought to bear on the same reaction.

II. EXPERIMENTAL TECHNIQUE

The basic working parts of the apparatus (Fig. 1) are contained in three individually pumped vacuum chambers connected by small orifices through which the molecular beams pass. The source chamber contains the primary beam source, which is a tube terminated by a hole through which the reactant gas effuses into a vacuum, and a rotating toothed disk which mechanically modulates the gas flow. A small part of this modulated gas flow is collimated by an orifice in the vacuum chamber wall and enters the target chamber. This chamber houses the solid surface (target) upon which the reactant beam impinges; any surface heating, cleaning or analysis equipment is located in this chamber. Scattered reactant and desorbed products leaving the surface are collimated by a second orifice which leads to the detection chamber. A quadrupole mass spectrometer is located in this chamber for measurement of the species in the beam arriving from the solid surface. The system is completed by phase-sensitive amplification equipment, which is usually a lock-in amplifier.

Options to the basic model described above can extend the analytic power of the method.

A digital pulse counting device coupled to a multiscaler permits acquisition of the entire waveform of the modulated signals produced by the mass spectrometer instead of just the fundamental mode provided by the lock-in amplifier. Occasionally, the ability to see an entire oddly shaped waveform provides insight on the surface reaction not obtainable from just the fundamental mode of the same signal. However, the numerical output of the lock-in amplifier is generally sufficient for quantitative reaction modeling.

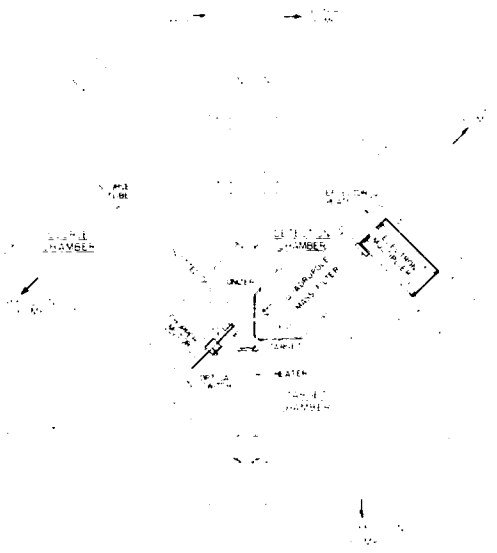

FIG. 1. Modulated molecular-beam apparatus with mass spectrometric detection and ion-bombardment capabilities.

The target chamber can be augmented with an Auger electron spectrometer to permit detection of surface species during reaction[11] or simply for verification of surface cleanliness.

The quartz source tube used for generating beams of most gaseous reactants can be replaced by a high-temperature oven for production of atomic beams (e.g., hydrogen and fluorine).

A small tube mounted close to and pointed at the target can be added to supply a steady reactant beam to the same spot on the target struck by the primary modulated beam. This feature is essential for isotope exchange tests.

A second mass spectrometer can be placed along the axis of the primary molecular beam behind the target so that with the target withdrawn, the primary beam is detected. This option is needed to calibrate the mass spectrometer when mixed atomic-molecular beams are utilized.

An ion gun can be installed to bombard the target with keV-energy ions simultaneously with impingement of the modulated-molecular beam (Fig. 1). This feature permits investigation of ion-assisted reactions, which are often important in semiconductor etching. Otherwise, the ion beam is useful simply for surface cleaning.

A second mass spectrometer located behind the primary product mass spectrometer in the detection chamber permits the velocity of the products emitted from the reacting surface to be measured.

III. DATA ANALYSIS

A basic set of molecular-beam data for a surface reaction consists of reaction probability (ϵ) and phase lag (Φ) measurements for each reaction product as functions of incident beam intensity (I), surface temperature (T), and modulation frequency (f).

Reaction modeling consists of comparing these data with predictions based on a postulated reaction mechanism consisting of a sequence of elementary steps. The modeling process involves selecting the elementary steps and the phenomenological laws governing their rates. These are then used in mass balances written for all distinct surface species. The surface balances are then Fourier analyzed to provide the fundamental modes of the emission rates, which are then used to formulate the observable quantities ϵ and Φ. Details of this procedure are given in Ref. 1.

The phase lag Φ is a particularly valuable measurement and is unique to the modulated molecular-beam technique. Its meaning can be understood by means of a very simple example. Suppose a gaseous atom strikes the surface of a solid and a fraction η stick to the surface and react to form a product, spending a time τ in so doing. Modulation of the incident beam is analogous to the movement of the hand of a clock at a frequency of f Hz. The delay time τ between incidence of the reactant and re-emission of the product results in sweeping out by the hand of the clock of an angle $\Phi = 2\pi f\tau$ between the times of these two events. The reaction phase lag is thus a direct measure of the lifetime on the surface, or, equivalently, of the surface reaction rate constant $k = \tau^{-1}$.

For this simple illustration, the reaction probability ϵ is equal to the sticking probability η.

IV. SILANE CRACKING ON Si (111)

To illustrate some of the capabilities of the molecular-beam method, the study reported in Ref. 12 is reviewed. The overall reaction is:

$$SiH_4(g) \rightarrow Si(111) + 2H_2(g).$$

The reaction product detected by the mass spectrometer is H_2. Reflected SiH_4 is also measured. A room-temperature silane beam strikes the surface with intensities in the range 10^{15}–10^{16} molecules/cm^2 s and modulation frequencies between 20 and 900 Hz. The target on which deposition occurred is an 0.6 μm thick epitaxial layer on Si(111) held at temperatures between 1000 and 1440 K in a vacuum of 10^{-8} Torr.

The effect of temperature on the reaction probability and reaction phase lag is shown in Fig. 2. The reaction probability is relatively constant above ~1130 K but drops abruptly by a factor of about 5 at lower temperatures. This discontinuity coincides with a known transition in the Si(111) surface from a low-temperature (7×7) structure to a (1×1) stable structure at high temperature. The reaction phase lag is low (~15 deg) at high temperature but increases as the phase transition is approached and exhibits a discontinuity at this point.

Data similar to those shown in Fig. 2 were obtained for

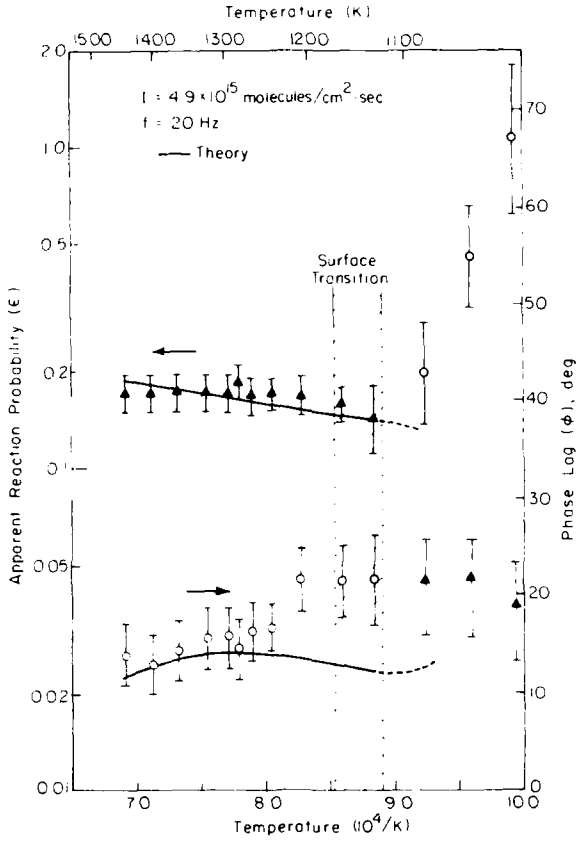

FIG. 2. Temperature effect on the silane cracking reaction.

variation in beam intensity at constant temperature and frequency and for a frequency scan at constant incident beam intensity and surface temperature.

In order to provide additional information on the processes occurring during the reaction, an attempt was made to measure the surface lifetime of SiH_4 on Si(111). This involved impinging a mixed beam of silane and an inert gas on the target and measuring the phase difference between the reflected signals from these two species. A silane phase angle larger than that of the inert gas would indicate that the former spent some time on the surface before re-emission. However, the phase difference was found to be zero, which indicated either that the lifetime of SiH_4(ads) on the surface is too small to measure (i.e., $< 10\,\mu$s) or that the gaseous molecule has a very small probability of purely physically adsorbing on Si(111) (i.e., it either reflects without interaction or adsorbs and decomposes).

An isotope mixing experiment was conducted by impinging a steady beam of SiD_4 on the surface at the same time as the modulated SiH_4 beam and searching for the reaction product HD(g). None was found, which means that adsorbed atomic hydrogen is not involved in the surface reaction mechanism.

These two auxiliary experiments, even though providing null results, were valuable in constraining the nature of the important steps in the mechanism. The model which fits the molecular-beam data for temperatures above the transition

temperature consisted of two parallel channels for product formation:

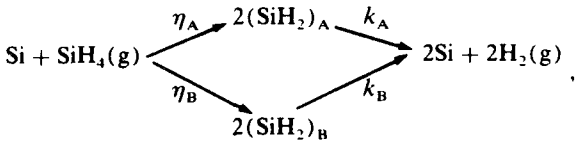

where η_A and η_B are the sticking probabilities on sites A and B and k_A and k_B are the rate constants for their decomposition. In the absence of surface spectroscopic evidence, the existence of the two sites during reaction could not be verified. However, the SiH_2 group has been identified on the room-temperature silicon surface doped with hydrogen. The two channels are active in an approximately 2:1 ratio and the rate of one is a factor of ~ 100 different from the other. However, the activation energies for the decomposition steps of both channels are nearly equal and agree well with that measured earlier by conventional kinetic methods.[12]

V. ETCHING OF Si(111) BY ATOMIC HYDROGEN

Gasification of silicon by hydrogen atoms is nearly the reverse of the silane cracking reaction discussed in the preceding section. However, silicon is not etched by molecular hydrogen, even at elevated temperatures. Contrary to reactive metals (e.g., tungsten), the silicon surface is not capable of breaking the hydrogen–hydrogen bond and chemisorbing the atomic fragments. However, if H_2 dissociation is performed prior to reaction, atomic hydrogen interacts strongly with silicon and in addition produces volatile SiH_4.

The most notable feature of the interaction is the "capping" of the dangling bonds exposed at the surface of Si(111). The binding energy of this β_1 state [relative to $H_2(g)$] has been estimated from thermal desorption spectra (TDS) to lie between 50 and 80 kcal/mol.[13] There is also evidence of a less strongly bound state of hydrogen (the β_2 state) which binds to the silicon surface with an energy between 40 and 50 kcal/mol.[13,14] This second state has been attributed to H atoms attached to silicon atoms just beneath the uppermost layer where dangling bonds have been capped by hydrogen.[12] Alternatively, the origin of the second TDS peak may be decomposition of an SiH_2 surface complex, the existence of which has been demonstrated by electron-energy loss spectroscopy (EELS)[15,16] and by high-resolution infrared spectroscopy.[17]

The studies cited above dealt with the states of hydrogen on Si(111) observed (either by TDS, or EELS) following dosing with atomic hydrogen. In the present work silane vaporization was observed during bombardment of the surface with atomic hydrogen at temperatures well below those at which the β_1 and β_2 states evaporate.

The atomic hydrogen beam was produced by thermal dissociation of H_2 in a 2500 K tungsten oven, which replaced the source tube shown in Fig. 1. This source delivers a mixed H/H_2 beam with an H atom flux adjustable in the range of 10^{16}–10^{17} cm^{-2} s^{-1}. The target was the same epitaxial layer grown on a Si(111) substrate as used in the deposition experiments. The temperature of the surface during reaction was varied from 300 to 1250 K.

A significant fraction of the incident H atoms recombined on the surface and were re-emitted as H_2. The molecular hydrogen from this source could not be measured directly by the mass spectrometer in the system because it was mixed with the H_2 portion of the partially dissociated hydrogen beam striking the target, which simply reflects from the surface. However, use of a second mass spectrometer on the axis of the primary beam permitted the $H:H_2$ ratio of the incident flux to be measured. The beam produced by the high-temperature oven was found to be ~ 30% dissociated. The corresponding ratio in the hydrogen emitted from the target at 300 K was ~ 10%.

Only one reaction product, SiH_4, was observed. Figures 3 and 4 show the dependences of the silane reaction probability and reaction phase lag (both with respect to the incident H-atom flux on the surface) on the temperature of the surface. Two features of these data are worthy of note.

First, the largest reaction probability occurs when the silicon surface is at room temperature and decreases with increasing temperature. The corresponding silane phase lag is smallest at room temperature and increases as the target is heated. This behavior is diametrically opposite that observed in the silane deposition reaction (Fig. 2) and for that matter, in most gas–surface reactions; usually the rates of chemical reactions increase with increasing temperature. The reaction probability at room temperature approaches 3% and the reaction time is a few milliseconds.

Second, at temperatures above that at which the silicon surface transforms from the common (7×7) structure to a (1×1) structure (shown hatched in Fig. 3) ϵ increases sharply, demonstrating a strong structural sensitivity of the surface reaction.

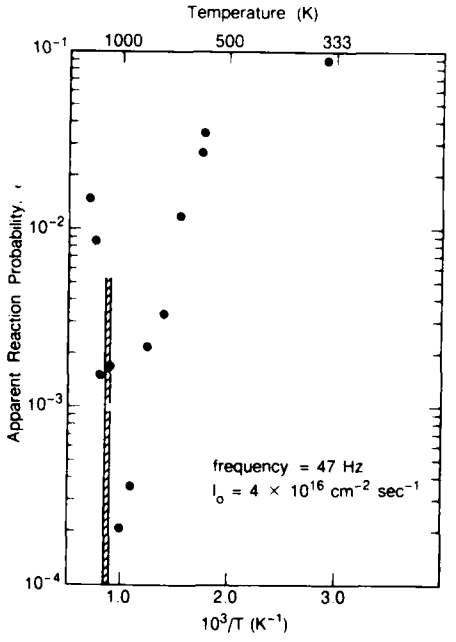

FIG. 3. Temperature effect on the reaction probability of atomic hydrogen etching of Si(111). The true reaction probability is about a factor of 3 lower than the ordinate values, which are based on the ratio of the signals for SiH_4 and *reflected* atomic hydrogen. This correction arises because the H atom sticking probability is 0.7, so that only $\frac{1}{3}$ of the incident hydrogen is reflected from the surface.

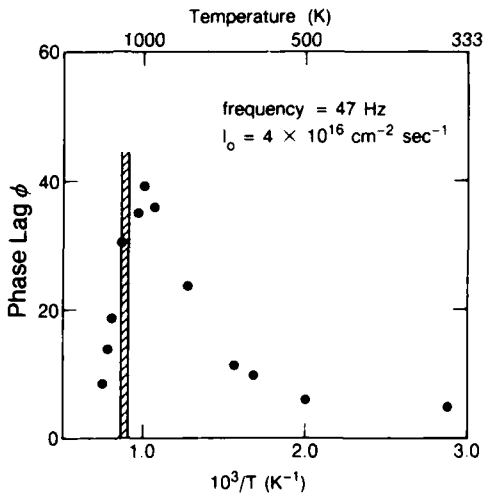

FIG. 4. Temperature effect on the reaction phase lag of atomic hydrogen etching of Si(111).

Except for the dramatic change in reactivity which accompanies the surface rearrangement, the forward and reverse reactions in the silicon–hydrogen–silane system have little in common, nor, being very far from equilibrium in both cases, is there any reason they should have. The etching reaction appears to be the more complicated of the two, and its description in terms of a simple set of elementary steps is not yet possible. However, a qualitative picture of the overall etching reaction can be gleaned from the combination of the TDS, EELS, and molecular-beam data.

The primary sink for hydrogen atoms delivered to the Si(111) surface is the dangling bonds of the uppermost layer of silicon atoms. Only when these are ~50% saturated can the second (β_2) state of hydrogen begin to be occupied.[13] These two states are quite stable and evaporate as H_2 only at temperatures of ~700 K (for the β_2 state) and ~825 K (for the β_1 state). Consequently, these states are saturated during the molecular-beam experiments at temperatures < 500 K, where substantial SiH_4 production is observed (Fig. 3). Moreover, the very fact that TDS and EELS studies could be conducted after the supply of atomic hydrogen to the surface had been shut off shows that the bound states of hydrogen do not react with the substrate to form SiH_4 at low temperature; a continuous supply of gas-phase H atoms is required to accomplish this. The mechanism for low temperature gasification may be by an Ely–Rideal step whereby an impinging H atom directly picks off an SiH_3 surface complex. However, analysis of models incorporating this elementary step require unacceptably large cross sections for the H(g)–SiH_3 reaction in order to fit the data. A more likely mechanism involves the existence of a third type of surface hydrogen, weakly bound and sustained only by virtue of the constant supply from the atomic beam. This weakly bound surface hydrogen is presumably mobile, and by reacting with the SiH_2 complexes on the surface, eventually leads to SiH_4. The possibility of this process occurring was first suggested by Wagner *et al.*[15] When the H atom beam is turned off, the weakly bound hydrogen is quickly returned to the gas phase (either as H_2 or as SiH_4), leaving behind the tightly bound forms which are observed in the TDS and EELS experiments. These forms of surface hydrogen appear to be stable for long periods in vacuum up to ~500 K.[15]

Recombination of the weakly bound adlayer to form H_2 could occur by reaction of two of these species or by reaction of one with another H atom in one of the more tightly bound layers. In addition, when a hydrogen atom from the β_1 or β_2 states is removed in the process of forming an SiH_4 molecule, the mobile adlayer provides a source for rapidly replacing the H atoms lost from these sites.

The most likely mechanism for production of silane during H atom bombardment is by reaction of the weakly bound hydrogen with the SiH_2 complex:

$$H(ads) + SiH_2 \rightarrow SiH_3$$

followed by:

$$H(ads) + SiH_3 \rightarrow SiH_4(g).$$

Part of the reason for the decrease in the silane reaction probability with increasing temperature (as shown in Fig. 3) can be found from the EELS data. The ratio of the loss peak representing the Si–H stretching mode to that of the SiH_2 scissor mode increases with increasing temperature.[15] This observation can be interpreted as the result of the temperature effect on the equilibrium $SiH_2(\beta_2)$: $SiH(\beta_1)$ ratio, where $SiH_2(\beta_2)$ represents the hydrogen associated with the β_2 TDS peak and Si–H(β_1) is the very strongly bound form of hydrogen which gives rise to the β_1 TDS peak. The EELS data from Ref. 15 indicate that the above ratio decreases as temperature increases. As the population of the SiH_2 complex decreases, the rate of production of SiH_4 via this intermediate would also be expected to decrease.

Two other factors may contribute to the dramatic drop in reaction probability with increasing temperature seen in Fig. 3. First, the rate of the recombination process, which is likely to be represented by the reaction:

$$H(ads) + Si\text{–}H \rightarrow Si + H_2(g)$$

was observed to increase with temperature. Second, in addition to the temperature-dependent shift in the SiH_2/Si–H ratio noted above, the TDS data of Refs. 13 and 14 show that the strongly bound states begin to depopulate above ~600 K.

The increase in the silane phase lag with increasing temperature (Fig. 4) often indicates that some form of bulk solution-diffusion process is active in the overall surface reaction. Spectroscopic evidence of the bulk solution is shown by a broadband centered at 1970 cm^{-1}, which only appears on the 7×7 surface.[17] When the solid becomes permeable to one of the surface intermediates (H atoms in this case), the bulk sorption and diffusion provides a "flywheel" effect on the reaction, preventing rapid response of the surface concentrations to incident beam modulation. Bulk diffusion coefficients increase with temperature; the migration energy of hydrogen in silicon is ~11 kcal/mol[18] which tends to render the solution-diffusion process more important as the temperature is increased. When this process dominates the temporal behavior of the overall reaction, the phase lag approaches 45°. This behavior is consistent with the data shown in Fig. 4.

VI. CONCLUSIONS

The modulated molecular-beam technique permits mechanistic study of gas–solid reactions which exhibit characteristic reaction times between 10 ms to 10 μs.

In situ direct-flight mass spectrometric detection allows for determination of individual reaction product species.

Use of the method is greatly enhanced if related techniques, such as isotopic exchange, temperature-ramp thermal desorption and surface spectroscopies are brought to bear on the same reaction.

Low-pressure thermal cracking of silane on Si(111) proceeds along two parallel channels, neither of which involves atomic hydrogen as a surface intermediate.

Etching of Si(111) by atomic hydrogen gas exhibits a $\sim 5\%$ reaction probability at room temperature and may be rate-controlled by the reaction of a loosely bound hydrogen adlayer with surface SiH_x complexes, competing processes of recombination to produce H_2 and bulk solution-diffusion of surface adsorbed H atoms becoming more important as the temperature is increased.

ACKNOWLEDGMENTS

This work was supported by the Director, Office of Energy Research, Office of Basic Energy Sciences, Materials Sciences Division of the U.S. Department of Energy under Contract No. DE-AC03-76SF00098 and the Lawrence Livermore National Laboratory under Contract No. W7405-ENG-48.

[1]D. R. Olander, W. Siekhaus, J. A. Schwarz, and R. Jones, J. Vac. Sci. Technol. **9**, 1429 (1972).
[2]C. T. Foxon, M. R. Boudry, and B. A. Joyce, Surf. Sci. **44**, 69 (1974).
[3]J. A. Schwarz and R. J. Madix, Surf. Sci. **46**, 317 (1974).
[4]R. J. Madix, in *Physical Chemistry of Fast Reactions*, edited by D. O. Hayward (Plenum, New York, 1975), Vol. 2.
[5]R. L. Palmer and J. N. Smith, Jr., Catal. Rev. **12**, 279 (1975).
[6]W. H. Weinberg, Adv. Colloid Interface Sci. **4**, 301 (1975).
[7]G. A. Somorjai, J. Colloid Interface Sci. **58**, 150 (1977).
[8]S. T. Ceyer and G. A. Somorjai, Annu. Rev. Phys. Chem. **28**, 477 (1977).
[9]M. J. Cardillo, Annu. Rev. Phys. Chem. **32**, 331 (1981).
[10]A. Ullman and D. R. Olander, Int. J. Chem. Kinet. **8**, 625 (1976).
[11]M. Balooch, D. R. Olander, W. Siekhaus, and J. Abrefah, Surf. Sci. **149**, 285 (1985).
[12]M. Farnaam and D. R. Olander, Surf. Sci. **145**, 390 (1984).
[13]G. Schulze and M. Henzler, Surf. Sci. **124**, 336 (1983).
[14]S. Gates (personal communication, 1986).
[15]W. Wagner, R. Butz, U. Backes, and D. Bruchmann, Solid State Commun. **138**, 1155 (1981).
[16]J. A. Schaefer, F. Stucki, D. J. Frankel, W. Gopel, and G. J. Lapeyre, J. Vac. Sci. Technol. B 3, 399 (1984).
[17]Y. J. Chabal, G. S. Higashi, and S. B. Christman, Phys. Rev. B **28**, 4472 (1983).
[18]A. van Wieringen and N. Warmoltz, Physica **22**, 849 (1956).

Effects of Ar^+ angle of incidence on the etching of Si with Cl_2 and low-energy Ar^+ ions

J. van Zwol, J. van Laar, A. W. Kolfschoten, and J. Dieleman
Philips Research Laboratories, P.O. Box 80000, 5600 JA Eindhoven, The Netherlands

(Received 27 February 1987; accepted 6 July 1987)

Experiments have been performed in a beam apparatus where an Ar^+ beam and a Cl_2 beam are directed simultaneously at a Si target. The apparatus allows independent variation of the ion angle-of-incidence and the detection angle. Time-of-flight (TOF) distributions of the reaction product SiCl are measured for various Cl_2 to Ar^+ flux ratios and various angles-of-incidence. These distributions can for the larger part well be fitted with collision cascade distributions, showing that at the parameter values chosen, the etch process in $Si(Cl_2,Ar^+)$ is a chemically enhanced physical sputtering process. The observed variations of the binding energy U_0 obtained from the TOF distributions support this mechanism. A discussion in relation to similar studies on the etch rate and the composition of the surface and the altered layer leads to a consistent picture in support of the above model.

I. INTRODUCTION

During the last few years fundamental aspects of processes involved in plasma etching have been studied by concurrently exposing a solid surface to a low-energy (< 5 keV) noble gas ion beam and a reactive gas beam in ultrahigh vacuum and measuring properties, like composition and kinetic energy distribution, of the etch products leaving the surface. The results of such studies for some gas-ion–solid combinations have been reviewed recently by Zalm.[1] The effect of this concurrent exposure (crossed beams exposure) on the etch rate of the surface for quite a few combinations has been dealt with in a review by Winters, Coburn, and Chuang.[2] The latter review shows that sometimes only ion-influenced etching is observed while in other cases additional spontaneous etching (i.e., by the reactive gas and temperature alone) occurs. In some cases the simultaneous exposure to a reactive gas beam enhances the ion-beam etching, sometimes to a level higher than the sum of the separate spontaneous etch rate and the ion etch rate, whereas in other cases the ion etch rate is reduced.

Three models have been proposed to explain the effects of the above-mentioned concurrent exposure. The first suggests that surface damage produced by the ion bombardment enhances the reaction with reactive gases.[3,4] The second proposes that activation energy for reactions of the reactive gas beam with the surface is supplied from the collision cascade induced by the ion bombardment; if the resulting molecular reaction products are weakly bound to the surface, they will subsequently be desorbed thermally into the gas phase, possibly at the elevated temperatures produced during ion impact.[2,5] The third model states that the ion-bombardment-induced part of the etching involves mainly physical sputtering, but from a chemically and structurally altered surface layer. This alteration is produced by a number of effects. One of these effects is adsorption of reactive gas, in some cases followed by indiffusion of the adsorbates. Another is ion-bombardment-induced damage and sometimes amorphization. A third effect is ion beam mixing of the adsorbates from the surface into the top atomic layers producing additional compound formation including trapped molecules. While the main etch effect is due to physical sputtering from this altered layer, a second, but minor, contribution is produced by ion-bombardment-enhanced outdiffusion. Due to this alteration the binding energies of the atoms (molecules) in this layer will have changed. As the sputtering yield of these atoms (molecules) is inversely proportional to the binding energies, similar, but inverse, changes are expected in the etch rate. The idea of adsorbate-induced altered physical sputtering has been derived from modeling of Si etching by a CF_4 plasma by Mauer *et al.*,[6] whereas the more complete model has been formulated on the basis of the measurements of surface modification of Si under the action of concurrent beams of low-energy Ar^+ ions and Cl_2 molecules by Mayer *et al.*,[7] and of mass and kinetic energy distributions for the etching products of the same system by Dieleman *et al.*[8]

As illustrated, for example, by the results of Ref. 8, one can experimentally distinguish between the above-mentioned models by determining the mass, energy, and angular distributions of the etch products. Mass spectroscopy (MS) combined with time-of-flight (TOF) measurements (MS–TOF) gives direct information about these distributions. The addition of the TOF feature is essential in several ways. To name a few: 1° TOF allows the determination of the various neutral precursors (etch products) contributing to a certain m/e signal measured by the MS, 2° one can correct for the velocity dependent ionization probability in the ionizer of the MS (which is imperative in quantifying the contributions of the various etch products), and 3° TOF distributions contain indispensable information about the etch mechanism. For these and other reasons MS–TOF has been chosen for the present study of plasma etching mechanisms.

Attention will be focused on certain aspects of the etching of Si under concurrent exposure to an Ar^+-ion beam and a Cl_2 beam, a rather well-studied model system for plasma etching [indicated by $Si(Cl_2,Ar^+)$]. For this system several previous MS-TOF studies have been published.[8–14] It is the object of the present paper to extend these earlier studies on

 0734-211X/87/051410-05$01.00 © 1987 American Vacuum Society

the Si(Cl_2, Ar^+) system by investigating and discussing the effects of the Cl_2 flux to Ar^+ flux ratio ($\phi_{Cl_2}/\phi_{Ar^+} = R$) and the Ar^+ angle-of-incidence (θ_{inc}) on the TOF distributions of the etch product SiCl. Furthermore, the results of these MS–TOF investigations are compared with results of similar studies on etch rates[15–17] and on Cl removal rates.[18]

II. EXPERIMENT

A schematic representation of the crossed beams apparatus in which the experiments are performed is given in Fig. 1. Briefly, the apparatus consists of a main vacuum chamber with the target placed in the center. The target can be rotated about a vertical axis. In the present experiments an ion beam and a thermal reactive gas beam, the axes of which are both lying in the same vertical plane through the target rotation axis, are directed at the target at angles of 115° and 135°, respectively, to the target rotation axis. For the product detection a differentially pumpe ' MS–TOF unit is used, which can be rotated about the same (vertical) axis as the target. Thus the angle-of-incidence of the Ar^+ ions θ_{inc} and that of Cl_2 molecules θ'_{inc} can be varied independently from the detection angle θ_{det}. The main improvements as compared to the equipment used in our previous MS–TOF studies[8–10] are this possibility of investigating angular effects and a lower background pressure of 3×10^{-7} Pa (without bakeout) in the main chamber. The Ar^+-ion energy E_{inc} used here is fixed at 3 keV and the flux of Ar^+ ions ϕ_{Ar^+} is about 5×10^{13} Ar^+ $cm^{-2}s^{-1}$. The Ar^+-ion beam is chopped with a pseudorandom code[19] to provide discrimination against a possibly spontaneous reaction. ϕ_{Cl_2} is chosen in the range 10^{15} to 5×10^{16} Cl_2 $cm^{-2}s^{-1}$. This leads to a range of values of $\phi_{Cl_2}/\phi_{Ar^+} = R$ between 20 and 10^3. The highest ϕ_{Cl_2} gives rise to a background pressure in the main chamber of 10^{-4} Pa, which means that the Cl_2 background contributes $<1\%$ to the ϕ_{Cl_2} at the Si target. This beam quality factor of about 100 holds for the whole range of ϕ_{Cl_2} values. It also holds for the reaction products. The highest value of the background pressure corresponds to a mean free path of several tens of a meter. Since the flight path has a length of a few tens of a centimeter, no interference from gas phase collisions is expected in the TOF spectra. All experiments described in this paper are conducted at 300 K.

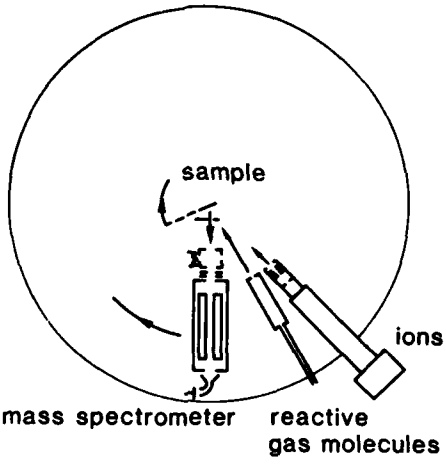

FIG. 1. Schematic drawing of the crossed beams reactor.

III. RESULTS

First the effect is investigated of varying the value of ϕ_{Cl_2} on the TOF distributions of one of the main etch products, viz., SiCl, at constant ϕ_{Ar^+} and at constant $\theta_{inc} = 50°$ from the surface normal. The value of ϕ_{Cl_2} is taken in the range of 10^{15} to 5×10^{16} Cl_2 $cm^{-2}s^{-1}$ and thus $R = 20$ to 10^3. At the $\theta_{inc} = 50°$ for Ar^+ the incidence angle for Cl_2 is $\theta'_{inc} = 60°$. The detection angle for the etch products is kept fixed along the Si surface normal, i.e. $\theta_{det} = 0°$. For all values of R the TOF distributions of SiCl can be fitted quite well with a combination of a large contribution of a collision cascade (CC) distribution, typical of physical sputtering, and a small contribution of a Maxwell–Boltzmann (MB) distribution, typical of thermal desorption, at 300 K. The contribution of the MB distribution increases continuously with increasing value of R but never exceeds 20% of the total number of SiCl molecules leaving the target. No indications have been found that the $m/e = 63$ signal measured by the MS contains contributions from neutral products other than SiCl; this should have been visible as an extra peak or a broadening of the peak in the TOF distribution due to SiCl. An example of a measured TOF distribution and the fitted curves is given in Fig. 2 for $R = 40$. As shown by this figure, a combination of 90% of a CC distribution with $U_0 = 0.28$ eV and 10% of an MB distribution at $T = 300$ K fits the data quite well. The signal has been corrected for the $1/v$ dependence of the ionization probability in the ionizer of the MS (v is precursor velocity). As shown by Fig. 3 the values of the binding energy U_0 of the CC distributions decrease with increasing values of R from $U_0 = 0.57$ eV at $R = 20$ to $U_0 = 0.17$ eV at $R = 10^3$. The rate of the decrease of U_0 with increasing R is particularly large between $R = 20$ and 40, whereas between $R = 10^2$ and 10^3 this rate is much smaller

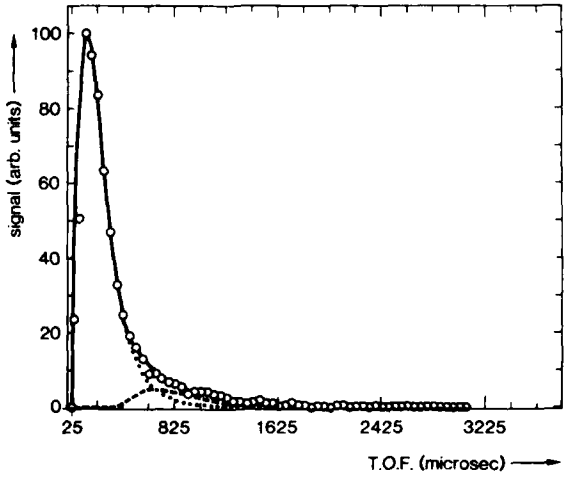

FIG. 2. Time-of-flight distribution of the product SiCl for $\phi_{Cl_2}/\phi_{Ar^+} = 40$, $\theta_{inc} = 50°$, $\theta_{det} = 0°$. As demonstrated, a combination of 90% of a collision cascade distribution and of 10% of a Maxwell–Boltzmann distribution at $T = 300$ K fits the data quite well.

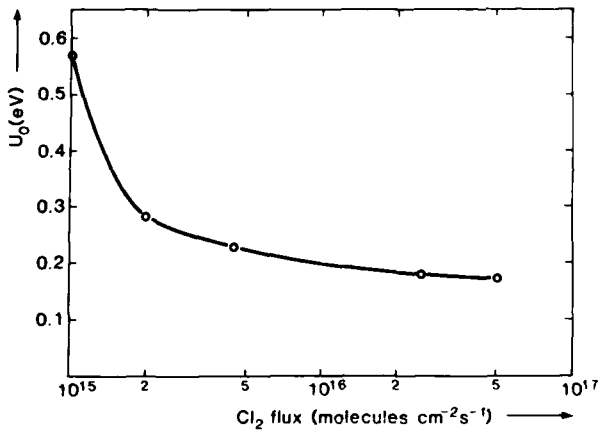

FIG. 3. Variation of U_0 as a function of ϕ_{Cl_2}. $\phi_{Ar^+} = 5 \times 10^{13}$ Ar^+ cm^{-2} s^{-1}.

and an asymptotic value seems to be reached at high values of R. The signal intensity of SiCl also increases with R and saturates at high R values.

In the second series of experiments, θ_{inc} is varied at an intermediate value of $R = 40$. TOF distributions are measured at $\theta_{inc} = 30°$, 50°, and 70°, respectively ($\theta'_{inc} = 47°$, 60°, and 75°, respectively). Again $\theta_{det} = 0°$ is used. Also in these cases the TOF distributions of SiCl can be fitted quite well with a combination of CC and MB distributions. The MB contribution decreases continuously with increasing value of θ_{inc}. The CC supplies again the main contribution to the total SiCl yield. As shown by Fig. 4 the value of U_0 increases significantly with increasing value of θ_{inc}. The signal intensity of SiCl does not change significantly with θ_{inc}.

IV. DISCUSSION

In the following first the main results of previous, related work will be discussed to provide a contextual framework for the treatment of the present results. After that some attention will be paid to TOF studies on the same system $Si(Cl_2, Ar^+)$ by two other groups. In one of the first crossed beams studies on the $Si(Cl_2, Ar^+)$ system Coburn and Winters[20] observed that addition of Cl_2 exposure to Ar^+ bombardment of Si at $\theta_{inc} = 0°$ for a flow ratio of 10^3 first gives rise to a weight increase, the rate of which levels off to zero after about 30 s. Evidently this weight increase corresponds to chlorine adsorption to the Si surface, which saturates after 30 s. This weight increase is followed by a period of about 200 s in which the etch rate increases to a steady-state level a few times higher than for physical sputtering of Si by Ar^+ bombardment alone. That this enhanced etch rate is only obtained after a relatively long time of 200 s instead of during the chlorine adsorption period suggests that an altered layer is gradually building up till a steady-state composition distribution has been reached. So the mere adsorption of chlorine on the Si is not sufficient to cause etch rate enhancement. Ion-beam mixing of the chlorine into the Si to form an altered layer seems imperative for getting the enhanced etch rate. Indications that this ion-beam mixing of adsorbed chlorine into the Si occurs indeed, have been provided by Mayer *et al.*[7] Although their samples were exposed to the atmosphere between crossed beams etching and analysis by Rutherford backscattering, the RBS analysis suggests that chlorine is mixed into the Si and that the mixing decreases with increasing value of θ_{inc}. Retention of implanted Ar and depth of damage decreased similarly. This etch rate enhancement for $Si(Cl_2, He^+/Ne^+/Ar^+)$ at ion energies between 400 eV and 2.5 keV and $\theta_{inc} = 0°$ has been confirmed several times.[15,21-23] Another important observation made, is that the enhancement of the etch rate increases from a factor of 1 at $R = 0$ to a saturation value at $R = 10^2$ to 10^3 of a few times higher than at $R = 0$.[15-17] It has been shown[16-18] that the steady-state surface concentration of chlorine for $R = 1$ corresponds to at most a few percent of a monolayer, while steady-state coverages of the order of one monolayer are reached only when $R = 10^2$ to 10^3. These results are due for one part to the low sticking coefficient of Cl_2 on Si of about 10%[24] and for another part to the resputtering of the adsorbed chlorine.[18] So, the more the surface is covered with chlorine, the higher the effect on the sputtering behavior is. A further interesting observation made[21,22] is that the dependence of the etch rate on θ_{inc} changes when the Si surface is exposed simultaneously to Cl_2 and that this change becomes more profound the higher the value of R. At $R = 10^2$ to 10^3 and $\theta_{inc} = 0°$ the etch rate has increased a few times as compared to the situation at $R = 0$. This etch rate enhancement decreases with increasing θ_{inc} such that even the pronounced etch rate maximum observed for $R = 0$ at θ_{inc} is about 60° has disappeared. This again illustrates the drastic effect of chlorine adsorption on the sputtering behavior. The effect of θ_{inc} may be related to the observation that the cross section for removal of Cl from Si by 1-keV-Ne^+ bombardment increases from 3×10^{-16} cm^2 at $\theta_{inc} = 0°$ to about 200×10^{-16} cm^2 at $\theta_{inc} = 70°$.[18] There is good reason to expect a similar behavior for Ar^+ bombardment. This means that for equal values of R, the effective chlorine coverage will be the lower the larger θ_{inc}.

In what form and with what mechanism the chlorine and Si are removed from the surface cannot be derived from these publications. To shed more light onto this intriguing

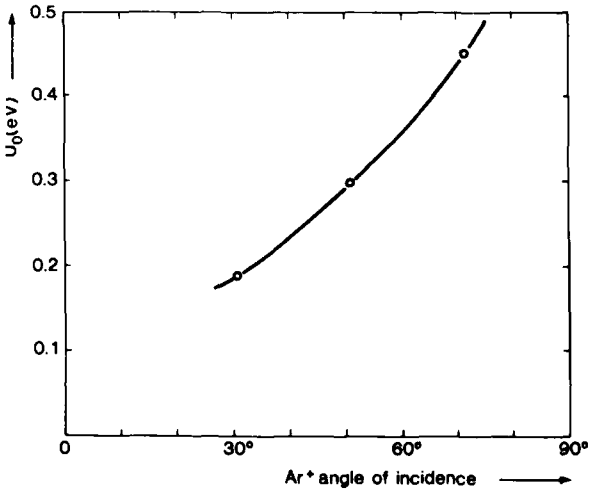

FIG. 4. Variation of U_0 as a function of the Ar^+ angle-of-incidence.

and useful enhancement of the sputter etch rate in the $Si(Cl_2, Ar^+)$ case, but also in other etch systems, a diagnostic tool, allowing the unequivocal determination of the masses and kinetic energy distributions of the etch products, would be of help. Such a diagnostic, viz., MS–TOF, has been introduced into this area recently.[25] As has been illustrated above, since then several other groups have also started to follow this line. Our group has started cooperation with the authors of Ref. 25 soon after this publication. This has resulted in a number of crossed-beam studies using MS–TOF. Some of the results of such studies on the $Si(Cl_2,Ar^+)$ system, which have been published during the last three years[8-10,26-28] will be summarized below as an introduction to the discussion of the present results. The previous results to be summarized have been obtained for $\theta_{inc} = 60°$, $\theta_{det} = 0°$, $\phi_{Ar^+} = 2$ to 5×10^{14} Ar^+ cm^{-2} s^{-1}, $E_{inc} = 0.25$–6 keV, $\phi_{Cl_2} = 5\times10^{14}$–$5\times10^{16}$ Cl_2 cm^{-2} s^{-1} and $T = 300$–625 K.

First of all the species emitted from the Si surface under the above conditions have been divided up into major and minor products by, e.g., taking a mass spectrum using 10-Hz square-wave modulation and lock-in detection techniques.[9] As compared to the mass spectrum of $SiCl_4$ gas the peaks in the mass spectrum of the $Si(Cl_2,Ar^+)$ system at m/e values corresponding to $SiCl_4^+$ and $SiCl_3^+$ are one to two orders of magnitude lower. Except if $SiCl_4$ or $SiCl_3$ should leave the surface after excessively long residence times, it may be concluded that $SiCl_4$ and $SiCl_3$ contribute a minor fraction to the etch products over the whole range of parameter values specified above, even at the highest R values. The results of these previous MS–TOF studies are that

(i) the main etch products appear to be Ar (implanted and subsequently sputtered), atomic Si, and Cl and molecular SiCl and $SiCl_2$. The yield of ionized etch products is at most 1% of the neutrals.

(ii) The main contribution, viz., over 80%, to the kinetic energy distributions of the molecular products SiCl and $SiCl_2$ can be simulated well with a collison cascade. The atomic products Si and Cl have kinetic energy distributions at mean energies far above 1 eV.

(iii) A minor contribution, viz., $<20\%$, to the kinetic energy distributions of SiCl and $SiCl_2$ can be simulated with a Maxwell–Boltzmann distribution at target temperature.

(iv) The *mean* kinetic energies of the various products vary widely, from values of 0.1 eV for Ar, of the order of 1 eV for SiCl and $SiCl_2$, and much larger than 1 eV for Cl and Si.

These results may be summarized in the conclusion that: The main products SiCl and $SiCl_2$ are removed for more than 80% by physical sputtering, and for less than 20% by bombardment-induced diffusion and evaporation at the surface; and the main products Si and Cl are, in all probability, removed by physical sputtering.

Because of the low binding energies corresponding to the CC distributions of SiCl and $SiCl_2$ and the MB contribution at target temperature, it has been suggested that these molecules are formed immediately after the ion impact and are partly "locked" in voids from where they are subsequently sputtered.[8,26] At first sight, it seems difficult to understand why such a large fraction of molecular products can be sputtered from voids without being dissociated. However, as can be found in the theoretical work of Harrison[29] the impact of an important fraction of the ions does not result in sputtered products, whereas another fraction of the impacting ions removes many atoms per impacting ion. If this notion is combined with the high sputtering yield in the $Si(Cl_2,Ar^+)$ system the above suggestion becomes more reasonable. Furthermore, that product molecules, like SiF_4, may be trapped in the reaction layer has been proven for the thermal reaction of Si with XeF_2 by McFeely *et al.*[30] So, it seems allowed to suggest a similar possibility for less halogenated molecules in the system $Si(Cl_2, Ar^+)$.

Let us now turn to the discussion of the experimental results of this paper in relation to the previous work of our group and that of the groups of Coburn *et al.* and of Mayer *et al.* It has been shown in physical sputtering, that alloying of metals may give rise to a reduction of the binding energy of both partners.[31,32] Furthermore, in general the binding energy of the various particles physically sputtered from an alloy or from a compound are found to be different for different particles.[33] So there is reason enough to conclude that the binding energies of the various sputtered products of $Si(Cl_2, Ar^+)$ may be different, as observed in our previous work. The above literature also suffices to support the idea that the mixing of chlorine into the Si by the combined effect of chlorine adsorption on the surface and the Ar^+ ion bombardment will change the binding energies U_0 and correspondingly the TOF distributions of the sputtered particles. Since the results of Gerlach–Meyer *et al.*[15] and those of Mayer *et al.*[16,17] show that the etch yield increases with increasing R and since Mayer *et al.*[16-18] have shown that this is directly related to the surface coverage and probably the amount of chlorine mixed into the altered layer it has to be expected that the binding energy U_0 of the sputtered species, which is inversely proportional to the sputtering yield, decreases with increasing R. And that is just what Fig. 3 shows for one of the main etch products, viz., SiCl. An interesting point of Fig. 3 is the behavior of U_0 at low R values. It is worthwhile to investigate whether U_0 will show a further rapid increase to even lower values of R, since hopefully this will provide additional data for testing the hypothesis of void molecules.

As discussed above, the results of Mayer *et al.*[18] have shown that the cross section for removal of adsorbed chlorine increases drastically with increasing value of θ_{inc} and this and other work of this group[7] indicates a corresponding decrease in steady-state chlorine surface coverage and in the amount of chlorine mixed into the altered layer. This is clearly reflected in the etch yield as a function of θ_{inc}, viz., a relative decrease with θ_{inc} instead of an increase up to $\theta_{inc} = 60°$ found for Ar^+ sputtering of pure Si. Because of this decrease in the amount of chlorine mixed into the altered layer it is expected that also the binding energy of the sputtered species, and thus of SiCl, will increase with increasing value of θ_{inc}. As Fig. 4 shows this is observed indeed. Extrapolation of U_0 to $\theta_{inc} = 0°$ suggests a value of U_0 of about 0.1 eV. Since this number is obtained for the relatively low value of $R = 40$ it will be interesting to investigate the system $Si(Cl_2,Ar^+)$ at $\theta_{inc} = 0°$ and for $R = 10^2$ to 10^3, to see whether the mechanism of etching is going to change.

When comparing the present and previous[8-10] results of

our group on the $Si(Cl_2,Ar^+)$ system with those of McNevin and Becker[14] and of Rossen and Sawin[11-13] there seems to be partial to total disagreement about what the main etching products are and about their kinetic energy distributions. A direct comparison with the results of McNevin and Becker[14] is impossible because they used R values from as low as 10^{-2} up to about 1 and applied the Cl_2 in the form of a Cl_2 atmosphere, whereas in our studies R values range from about 10 up to about 10^3 and the Cl_2 is applied in the form of a beam. In addition, their experimental method and interpretation are open to criticism. To mention just one point, they did not apply the $1/v$ correction for the ionization probability, which is inter alia necessary for proper quantification of the contribution of the various neutral etch products. This leads to an underestimation of the contribution of high velocity particles like, e.g., Si atoms of about two orders of magnitude as compared to thermal 300 K $SiCl_4$ molecules. Even if this correction is applied, the contribution of $SiCl_4$ for $R = 10^{-2}$ is far too high to be the result of Ar^+-ion-induced etching of Si. Reaction of Si atoms physically sputtered from the Si target with chlorine adsorbed on the chamber walls, followed by desorption and detection by the MS might explain the observation of these authors better. Also the comparison with the results of Rossen and Sawin[11-13] gives rise to difficulties. In their first two publications[11,12] a value of $R = 3$ is used, which is at the low end outside of the range of R values applied in our studies. The comparison with their more recent study,[13] in which $R = 500$, is seriously hampered by the limited amount of information given in this extended abstract. For example, the abstract does not indicate what the major etch products are. In addition, their claim that SiCl and $SiCl_2$ are emitted by a combination of evaporation and sputtering and that their results are consistent with those of Kolfschoten *et al.*[9] is inconsistent with their remark that the TOF spectra of SiCl is reasonably well-fitted by a MB distribution at 450 K.

V. CONCLUSION

The observation that the binding energy U_0 of the etch product SiCl in the $Si(Cl_2, Ar^+)$ system increases with decreasing Cl_2 to Ar^+ flux ratio and with increasing value of the angle-of-incidence of the Ar^+ ions is discussed in relation to similar studies on the etch rates in this system and to an analysis of the altered layer. A satisfying consistency between the various results is found. This is further support of the "chemically enhanced sputtering" model for the $Si(Cl_2, Ar^+)$ system for the parameter value ranges investigated thus far. Future research has to show if this model also applies for other parameter values, particularly for normal incidence of the Ar^+ ions at high Cl_2 to Ar^+ flux ratios.

[1] P. C. Zalm, Vacuum **36**, 787 (1986).
[2] H. F. Winters, J. W. Coburn, and T. J. Chuang, J. Vac. Sci. Technol. B **1**, 469 (1983).
[3] J. W. Coburn, H. F. Winters, and T. J. Chuang, J. Appl. Phys. **48**, 3532 (1977).
[4] D. L. Flamm and V. M. Donnelly, Plasma. Chem. Plasma Process. **1**, 317 (1981).
[5] J. W. Coburn and H. F. Winters, Appl. Surf. Sci. **22/23**, 63 (1985).
[6] J. L. Mauer, J. S. Logan, L. B. Zielinski, and G. C. Schwartz, J. Vac. Sci. Technol. **15**, 1734 (1978).
[7] T. Mizutani, C. J. Dale, W. K. Chu, and T. M. Mayer, Nucl. Instrum. Methods B **7/8**, 825 (1985).
[8] J. Dieleman, F. H. M. Sanders, A. W. Kolfschoten, P. C. Zalm, A. E. de Vries, and A. Haring, J. Vac. Sci. Technol. B **3**, 1384 (1985).
[9] A. W. Kolfschoten, R. A. Haring, A. Haring, and A. E. de Vries, J. Appl. Phys. **55**, 3813 (1984).
[10] F. H. M. Sanders, A. W. Kolfschoten, J. Dieleman, R. A. Haring, A. Haring, and A. E. de Vries, J. Vac. Sci. Technol. A **2**, 487 (1984).
[11] R. A. Rossen and H. H. Sawin, Appl. Phys. Lett. **45**, 860 (1984).
[12] R. A. Rossen and H. H. Sawin, Appl. Phys. Lett. **46**, 613 (1985).
[13] R. A. Rossen and H. H. Sawin, J. Vac. Sci. Technol. A **3**, 881 (1985).
[14] S. C. McNevin and G. E. Becker, J. Vac. Sci. Technol. B **3**, 485 (1985).
[15] U. Gerlach-Meyer, J. W. Coburn, and E. Kay, Surf. Sci. **103**, 177 (1981).
[16] R. A. Barker, T. M. Mayer, and W. C. Pearson, J. Vac. Sci. Technol. B **1**, 37 (1983).
[17] T. M. Mayer and R. A. Barker, J. Vac. Sci. Technol. **21**, 757 (1982).
[18] E. L. Barish, D. J. Vitkavage, and T. M. Mayer, J. Appl. Phys. **57**, 1336 (1985).
[19] G. Comsa, R. David, and B. J. Schumacher, Rev. Sci. Instrum. **52**, 789 (1981).
[20] J. W. Coburn and H. F. Winters, J. Appl. Phys. **50**, 3189 (1979).
[21] T. M. Mayer, R. A. Barker, and L. J. Whitman, J. Vac. Sci. Technol. **18**, 349 (1981).
[22] H. Okano and Y. Horiike, Jpn. J. Appl. Phys. **20**, 2429 (1981).
[23] P. C. Zalm, A. W. Kolfschoten, F. H. M. Sanders, and P. Vischer, Nucl. Instrum. Methods B **18**, 625 (1987).
[24] J. V. Florio and W. D. Robertson, Surf. Sci. **18**, 398 (1969).
[25] R. A. Haring, A. Haring, F. W. Saris, and A. E. de Vries, Appl. Phys. Lett. **41**, 174 (1982).
[26] J. Dieleman, Le Vide—Les Couches Minces, Suppl. **218**, 3 (1983).
[27] R. A. Haring, A. W. Kolfschoten, and A. E. de Vries, Nucl. Instrum. Methods B **2**, 544 (1984).
[28] J. Dieleman, F. H. M. Sanders, and P. C. Zalm, Nucl. Instrum. Methods B **2**, 1384 (1985).
[29] D. E. Harrison, Radiat. Eff. **70**, 1 (1983).
[30] F. R. McFeely, J. F. Morar, and F. J. Himpsel, Surf. Sci. **165**, 277 (1986).
[31] A. E. de Vries, in *Proceedings of the Symposium on Sputtering I, Perchtolsdorf-Wien, Austria*, edited by P. Varga, G. Betz, and F. P. Viehbock (Institut für Allgemeine Physik, Techn. Univ. Wien, Austria, 1980).
[32] M. Szymonski, Appl. Phys. **23**, 89 (1980).
[33] G. Betz and G. K. Wehner, in *Sputtering by Particle Bombardment II* edited by R. Behrisch (Springer, Berlin, 1983), p. 11.

Multiphoton-induced desorption of positive ions from barium fluoride

E. Matthias, H. B. Nielsen, and J. Reif
Freie Universität Berlin, Fachbereich Physik, Arnimallee 14, D-1000 Berlin 33, Federal Republic of Germany

A. Rosén and E. Westin
Chalmers University of Technology, Institute of Physics, S-41296 Göteborg, Sweden

(Received 13 March 1987; accepted 4 June 1987)

Subject of this paper is the interaction between laser radiation and surfaces of optically transparent ionic crystals at low-power densities of the order of 10^6–10^7 W/cm^2. By studying the wavelength and intensity dependencies of electron and ion-emission yields, it is shown that surface states play a decisive role for photon absorption at surfaces of divalent ionic crystals. They resonantly enhance multiphoton processes which leads to a strong-wavelength dependence of both photoemission and ion desorption. Cluster calculations confirm the existence of occupied surface states in the middle of the band gap and of unoccupied states in its upper half as well as above the ionization limit. The dependence on laser intensity reveals both two- and five-photon processes for photoemission, and ten-photon processes for the desorption of positive ions. The latter is interpreted as the creation of two holes, each by five-photon absorption, with subsequent Coulomb repulsion of a positive ion.

I. INTRODUCTION

Nonthermal desorption of atoms and ions from clean surfaces of ionic materials exposed to electron or photon irradiation has been the subject of many investigations.[1-15] From both electron- and photon-stimulated desorption studies (ESD and PSD) the general picture evolved that the absorbed energy excites localized defects which migrate to the surface and lead to the ejection of particles. The precise knowledge of the energy absorption mechanism is a fundamental requirement for any detailed understanding of the desorption mechanism. In ESD inelastic collisions caused the excitation of defect centers. For PSD the initial excited electronic state is well-defined as long as we are concerned with inner-shell excitations by synchrotron radiation.[3,16] Nonthermal PSD with *optical radiation* can, for ionic materials, only proceed by multiphoton absorption because of the large band gap. Desorption induced by multiphoton excitation has been reported by several authors.[14,15,17-19] In most cases, however, the initial and final states involved in the process were unknown and subject to speculation. Schmid *et al.*[14] detected neutral halogen atoms and a small fraction of negative ions when irradiating alkali–halide crystals with pulsed ruby-laser light at fluxes one order of magnitude below the surface breakdown threshold. No alkali emission was observed. The halogen emission was shown to originate from a four-photon absorption, which in case of KBr started from the valence band and in case of NaCl and KCl from impurity states in the band gap. Sesselman *et al.*[17] found for solid CuCl surfaces a desorption yield proportional to the fifth power of the laser intensity, indicating a five-photon excitation process. Chuang and Hussla[18] showed that two-photon absorption in the infrared caused desorption of adsorbates due to excitation of vibrational states of the adsorbate. Multiphoton processes are also held responsible for the plasma generation which leads to optical damage of surfaces.[19] Recently Siekhaus *et al.*[15] reported multiphoton-induced electron emission from insulator and semiconductor surfaces at wavelengths of 1.06 μm and 355 nm. From the dependence of the photoemission on laser-beam fluence the authors concluded that they observed a multiphoton excitation across the band gap. They also mentioned the possibility of multistep excitation involving defects, impurities or surface states. In their measurements, however, they only detected the total negative charge which may have included negative ions. In fact, they specifically mention that also positively charged particles were emitted from ZnS and SiO_2 samples.

The purpose of this paper is to study multiphoton processes induced by radiation in the green and blue spectral ranges. Specifically we want to raise the question to what extent *surface states* can affect multiphoton absorption. Our goal is to prove that surface states which are energetically located in the middle and upper half of the band gap can either be the origin of photon absorption (if they are filled), or (if they are empty) they can resonantly enhance multiphoton absorption from deeper-bound states. In this paper we present both theoretical and experimental results. The theoretical results come from cluster calculations which were performed in order to gain some qualitative information about surface states on $BaF_2(111)$ that can guide the interpretation of the experimental data. In the experimental part we present results on the intensity and wavelength dependence of both electron and positive-ion emission from $BaF_2(111)$. We selected divalent ionic crystals since we expect the second valence electron of the metal atom to form occupied surface states as well as excitonic resonances at the surface. BaF_2 was chosen as a prototype for divalent ionic crystals among others for spectral reasons. We speculated that excitations of the second valence electron might have some reminiscence to the excitation scheme of the free BaF, as long as the electron remains localized at the barium ion.

II. CLUSTER CALCULATIONS

Surface states of monovalent ionic crystals have received some attention in the past, and for NaCl(100) and

 0734-211X/87/051415-08$01.00 © 1987 American Vacuum Society

KCl(100) surfaces cleaved in vacuum Ernst[20] reported a surprisingly high density of filled extrinsic surface states up to the middle of the band gap. In contrast, little seems to be known about surface states of divalent ionic crystals, in particular the alkaline-earth halides. Cluster calculations should be appropriate to obtain reasonable estimates of the electronic surface structure, since to a first approximation any surface can be modeled as a planar cluster embedded in a crystal potential. To describe the $BaF_2(111)$ surface we have chosen a 10-atom cluster in C_{3v} symmetry, where a central barium atom is surrounded by three fluorine atoms, positioned slightly beneath the barium plane, and six more barium atoms, as shown in Fig. 1. This corresponds to a Ba-rich surface, otherwise three more fluorine atoms would have to be added on top, as is illustrated in Fig. 1 of Ref. 21. Here, we go on the assumption that fluorine deficient defects (F centers) exist on the surface and that they act as kernels for photon absorption. We also have evidence that under laser irradiation some of the outermost fluorine atoms desorb thermally with the result that the upper surface layer becomes increasingly barium enriched.[22]

We use the discrete variational embedded cluster approach to describe the molecular electronic structure.[23–25] The potentials were constructed within the local-density approximation, using the form of exchange correlation potential proposed by von Barth and Hedin.[26] The influence of the surrounding crystal lattice was approximated by the ionic potential of a number of Ba^{2+} and F^- ions contained in a half-sphere of certain radius. The choice of the radius was dictated by the requirement that the total charge of cluster and crystal must approach zero. This resulted in including 21 Ba^{2+} and 41 F^- ions for the calculation of the crystal potential. Also, the crystal potential was truncated slightly above the Fermi level in order to prevent electron transfer from the cluster into states of the crystal potential well. The molecular wave functions were found as linear combinations of atomic orbitals of the cluster constituents with the addition of some empty orbitals like $Ba[(Xe)6s^26p^05d^0]$ and $F(1s^22s^22p^53s^0)$. The reliability of our calculations was checked by comparing the energies of the F(2*p*) and Ba(5*p*) bands with experimental data.[27]

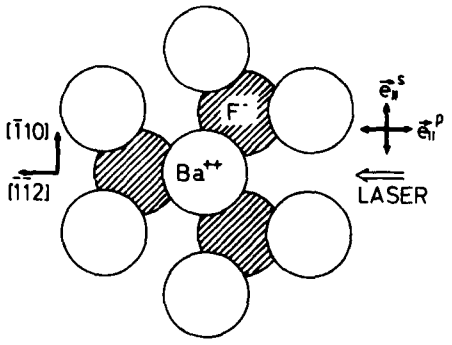

FIG. 1. View of the 10-atom cluster used for the calculations. The projections of the electric vector $\mathbf{e}_{\parallel}$ onto the surface are indicated for *s*- and *p*-polarized light for the case that the plane of incidence is parallel to the [1̄12] direction.

The results of the calculations for a 10-atom cluster are shown in Fig. 2 in form of density of states plots. These curves were obtained by arbitrarily broadening the energy levels with a Lorentzian line shape of 0.02 eV width. Also, the relaxation shift for ionization from the F 2*p* band is taken into account. In Fig. 2(a) the total density of states for the whole 10-atom cluster is shown, while Fig. 2(b) displays the partial density of states localized at the center barium atom of the cluster. In Fig. 2(a) the position of the upper F 2*p* valence-band edge as determined by the experiment[27] is indicated for comparison. The calculations predict the existence of *occupied surface states* near the middle of the band gap up to a Fermi level of about -2.7 eV. Starting from those states electron emission should be possible by the absorption of only two optical photons, as indicated by the solid arrows. In addition, strong *excitonic resonance structures* appear in the upper half of the band gap as well as above the ionization threshold. The partial density of states analysis in Fig. 2(b) shows that these states originate mainly from the Ba atomic orbitals and that they still possess some 5*d*, 6*s*, or 6*p* character. From this density of states it becomes clear that multiphoton absorption will be resonantly enhanced for certain photon energies corresponding to the energy difference between two resonances. In this way it is conceivable that a five-photon absorption from the F 2*p* band and a two-photon absorption from the occupied surface states exhibit the same wavelength dependence when they have at least two states in common.

We have also carried out calculations for other cluster sizes (see Ref. 21) to check the convergence towards the F 2*p* and Ba 5*p* bands and to study the dependence of the occupied surface states on cluster configuration and nature of the

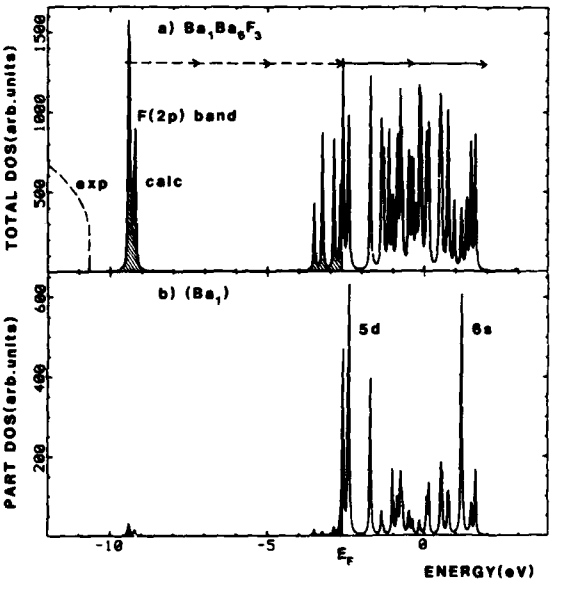

FIG. 2. Density-of-states (DOS) as obtained from the cluster calculations. Part (a) shows the total DOS for the 10-atom cluster, and (b) displays the partial DOS at the center Ba atom. The energy levels have been broadened by a Lorentzian of 0.02 eV width. The arrows indicate possible two- and five-photon absorption leading to photoemission.

upper surface layer. For example the calculation for a 13-atom cluster ($Ba_1Ba_6F_3F_3$) gives qualitatively the same result as for a bulk cluster, i.e., no occupied states in the band gap. This is to be expected since the three outer-fluorine atoms bind the second valence electron of the barium. We want to emphasize, however, that at this stage the results of the calculations can only be a *qualitative guide* in that they predict certain electronic properties of the surfaces of divalent crystals. Quantitative results can only be obtained by parameter adjustments based on precise experimental data as to the location of the surface states involved in the multiphoton absorption.

III. EXPERIMENTAL DETAILS

The experimental setup is sketched in Fig. 3. The frequency-tripled output of a Nd:YAG laser pumped a tunable dye laser which was operated either in the green (coumarine 152) or in the blue (stilbene 420) spectral range. The pulse length was about 8 ns and the maximum pulse energy 5 mJ. The laser-beam intensity could be varied using the combination of a Fresnel rhomb and a Glan linear polarizer. A small fraction of the laser light was reflected onto an artificially blackened diode to monitor the light intensity during the experiments. The laser beam was focused onto a spot of about 0.5 mm^2 at the crystal surface measured at normal incidence. All measurements were carried out with an angle of incidence of approximately 70°, with the plane of incidence oriented either parallel with the $[\bar{1}10]$ or the $[\bar{1}\bar{1}2]$ direction (cf., Fig. 1). The crystal was mounted in an ultrahigh vacuum (UHV) chamber on an *xyz* manipulator and could be rotated around the *z* axis. Using a combination of a turbopump and a cryopump, an ultimate pressure of about 3×10^{-10} mbar was reached. At this pressure the BaF_2 crystal was cleaved to expose the (111) plane. No additional surface preparation was carried out. For the green spectral range where we used low-power densities ($\leq 5\times10^6$ W/cm^2) spectra from a cleaved surface did not change noticeably within 24 h after cleavage and most of the spots behaved similarly. Nevertheless, a fresh surface was prepared for each day of experiments. In the blue spectral range the measurements were carried out at significantly higher power densities ($3\text{–}5\times10^7$ W/cm^2), and here the spots usually bleached out after 5 min[28] with only few exceptions that remained active longer.

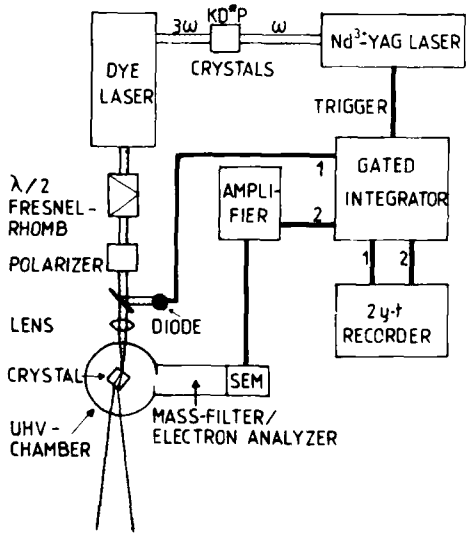

FIG. 3. Experimental setup for measuring electron and ion emission from laser-irradiated BaF_2. The ion detection could be done using a quadrupole mass filter or, alternatively, a grid-multiplier combination.

Emitted particles were detected alternatively with a quadrupole mass spectrometer (where the ionization current was turned off when detecting ions) or with a grid-multiplier combination that was only charge selective (ions and electrons). The latter was mounted close to the crystal with an acceptance angle of about 5% of the half-space. The grid in front of the secondary electron multiplier was held at 4–5 V for electron detection and at ground potential for ion detection. All signals from the monitor diode, from the grid-multiplier detector, or from the mass spectrometer were processed by gated integrators time correlated to the laser pulse. Although the grid-multiplier detector was not capable of mass selection, the gated integrators had sufficient time resolution to distinguish between electrons and negative ions by their different flight times.

IV. EXPERIMENTAL RESULTS

In the *green* spectral range we have up to now only performed measurements of the photoelectron and of the positive-ion emission, without any mass selectivity. We could not detect any negative ions. We have not yet studied the emission yield of neutrals for this photon energy, instead we focused our attention on the wavelength and the intensity dependence of both electron and ion emission yields. As reported earlier[29] laser irradiation of BaF_2(111) in the *blue* wavelength range leads to the emission of abundant neutral fluorine and the positive ions Ba^+, Ba^{2+}, BaF^+, and F^+. Also for this photon energy no negative ions were recorded. With blue laser light we again see a strong wavelength dependence of the emission yield and in addition we find evidence that the desorption takes place layer-by-layer.[28]

A. Wavelength and polarization dependence

Experimental results on the wavelength and polarization dependence of the electron and the positive-ion emission in the green spectral range are presented in Figs. 4(a)–4(d). The upper part of the figure [Figs. 4(a) and 4(c)] shows the positive ion yields, while the lower part [Figs. 4(b) and 4(d)] displays the electron yields. We notice that the spectral dependence of both is identical which leads to the conclusion that ion and electron emission must originate from the same photoabsorption process. This suggests that the hole formed by the photoionization of electrons is the forerunner for ion desorption. The intensity ratios of the peaks in Figs. 4(a) and 4(b) differ somewhat, which remains unexplained at the present time. The left- and the right-hand parts of Fig. 4 differ by the relative polarization of the incident laser radiation. It is obvious that the emission yields are highly polarization dependent. The spectra in Figs. 4(a) and 4(b) result from *p*-polarized light and the ones in Figs. 4(c)

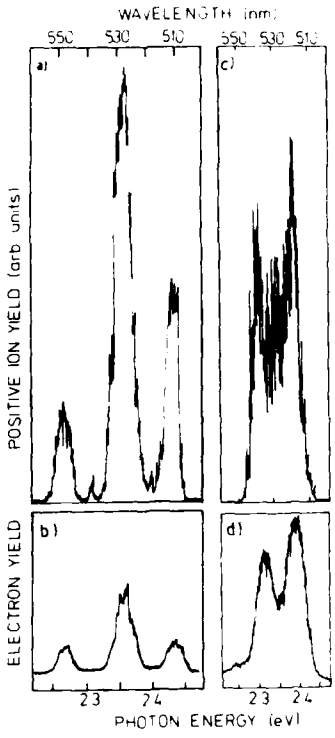

FIG. 4. Wavelength and polarization dependence of ion (a), (c) and electron (b), (d) emission from $BaF_2(111)$ in the green spectral range at laser intensities of about 5×10^6 W/cm^2. The yield spectra (a) and (b) result when the projection of the electric field vector **e** is parallel to the $[\bar{1}\bar{1}2]$ direction, (c) and (b) when **e** is parallel to the $[\bar{1}10]$ direction (cf., Fig. 1).

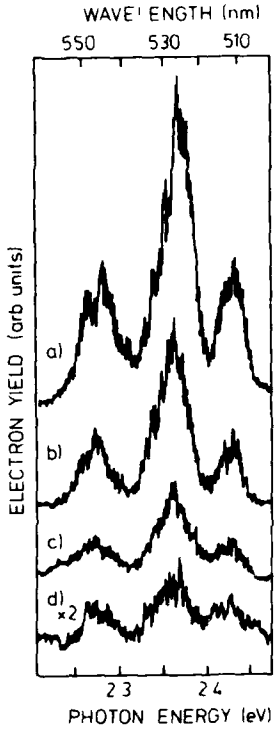

FIG. 5. Spectral dependence of photoemission for the following laser intensities: (a) 3.2×10^6 W/cm^2; (b) 2.8×10^6 W/cm^2; (c) 2.2×10^6 W/cm^2; (d) 1.7×10^6 W/cm^2. The polarization was chosen in such a way that the projection of the electric field vector, **e**, was parallel to the $[\bar{1}\bar{1}2]$ direction, like in Figs. 4(a) and 4(b).

and 4(d) from *s*-polarized light provided the plane of incidence coincides with the $[\bar{1}\bar{1}2]$ direction. Hence in case of *p*-polarized light the projection $\mathbf{e}_{\parallel}$ of the electric field vector onto the surface is along the $[\bar{1}\bar{1}2]$ direction, while for *s*-polarized light $\mathbf{e}_{\parallel}$ is along the $[\bar{1}10]$ direction. In case the plane of incidence lies in the $[\bar{1}10]$ direction the polarization dependence is reversed. We note at this point that the polarization dependence reflects the symmetries of the electronic states involved and that it is uniquely associated with the crystal directions.

Another observation is that the spectral dependence of the emission yields is independent of laser intensity. This is shown in Figs. 5 and 6 for electron emission induced by *p*- and *s*-polarized light. In Fig. 5 the incident-laser intensity was varied from 1.7×10^6 to 3.2×10^6 W/cm^2 and the spectral shape can be seen to be preserved. The same is valid for *s*-polarized light, and is illustrated in Fig. 6 for two intensities that differ by a factor of 8. The fact that the peaks remain in position and that only their amplitudes vary with laser intensity enables us to measure the intensity dependence for the various peaks in Fig. 4, in order to obtain information about the order of the multiphoton process involved.

B. Intensity dependence

The dependence of emission yield on laser intensity is shown in Fig. 7 for both electrons and positive ions. These points were measured at 518 nm with *s*-polarized light, corresponding to the peak at the right-hand side in Figs. 4(c) and 4(d). Similar data were obtained for the other peaks in Fig. 4. As a precaution against possible changes of the surface under irradiation with high intensities, the yield at a given intensity was integrated over 30-laser pulses only.

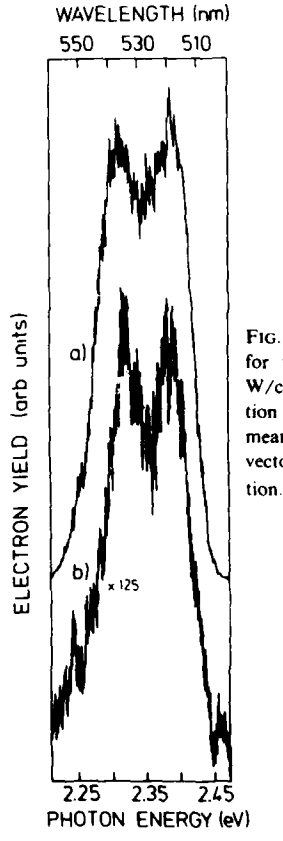

FIG. 6. Spectral dependence of photoemission for the two laser intensities: (a) 5×10^6 W/cm^2 and (b) 6×10^5 W/cm^2. The polarization was like in Figs. 4(c) and 4(d), which means that the projection of the electric field vector, **e**, was oriented along the $[\bar{1}10]$ direction.

Thereafter the laser beam was interrupted until the next point was to be measured. Nevertheless, repeated measurements at different spots were necessary to establish a reliable intensity dependence like the one shown in Fig. 7. The slope of the double logarithmic plot in Fig. 7 should give the order of the multiphoton absorption if the yield Y obeys the relation $Y \propto I^n$, where I is the laser intensity and n the number of photons required for the process.

In Fig. 7 the slope for the electron yield at low intensities ($\sim 1\times 10^6$ W/cm^2) is 1.9 ± 0.2, which means that two photons are necessary to ionize one electron. We take this as proof for the existence of occupied surface states near the middle of the band gap, as predicted by the cluster calculations (cf., Fig. 2). At intensities above 1.5×10^6 W/cm^2 the slope becomes 4.8 ± 0.5 and the electron emission apparently turns into a five-photon process. This corresponds to about 12 eV energy deposition which is more than sufficient to ionize electrons from the $2p$ valence band. Since the crystal surface is a highly complex multielectron system, collective effects may account for the fact that the probability for a five-photon process is comparable to the one for a two-photon process at such moderate laser intensity. Furthermore, in view of the estimates given by Bräunlich *et al.*[30] it does not seem unreasonable that the transition from a two- to a five-photon absorption takes place at the intensities used here, especially, when resonant stages are involved. It should be emphasized, however, that the exact position of these resonances is not known at present.

The ion emission sets in at only slightly higher laser intensities and shows a slope of 10 ± 1. However, for several reasons it seems highly unlikely that we are dealing here with a true 10-photon process. First of all, no such power dependence is observed for electrons, yet the energy absorption can only occur by excitation of electrons. Secondly, a ten-photon absorption would amount to an energy of 24 eV, about 5 eV (approximately two photons) more than the binding energy of the Ba $5p$ band.[27] Furthermore, since the yield spectra are similar for ions and electrons, additional intermediate resonances can be ruled out and therefore a ten-photon process involving deeper-bound electrons is expected only to occur at much higher laser intensities. It must be mentioned here that these considerations are based on the assumption that one can identify the measured exponent with the order of the multiphoton process. That this is strictly true only outside sharp atomic resonances has been shown by Morellec *et al.*[31] However, since the structures observed in Figs. 4–6 are extremely broad by any atomic standards, we believe that our conclusions about the order of the multiphoton process involved here are correct. The clear break between the slopes $n = 2$ and $n = 5$ is an additional argument supporting our interpretation.

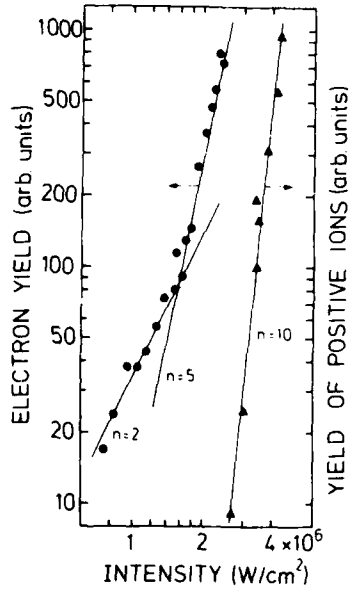

FIG. 7. Intensity dependence of electron and ion yields measured at a wavelength of 518 nm (cf., Fig. 6). The solid lines correspond to the slopes given by the integers and indicate the order of the multiphoton process. The results of least-squares fits to the data are given in the text.

C. Layer-selective laser sputtering

In the blue spectral range we studied[28,29] the desorption of positive ions mass selectively at considerably higher power densities (5×10^7 W/cm^2), yet well-below the damage threshold of about 5×10^8 W/cm^2 quoted for crystals in air.[32] Again we find a marked wavelength dependence of the ion yield, as is demonstrated in Fig. 8 for Ba^+ ions. Repeated scans of the same spot [Figs. 8(a)–8(c)], however, reveal a change of the yield spectrum from scan to scan. We interpret this as desorption of Ba^+ from different chemical environ-

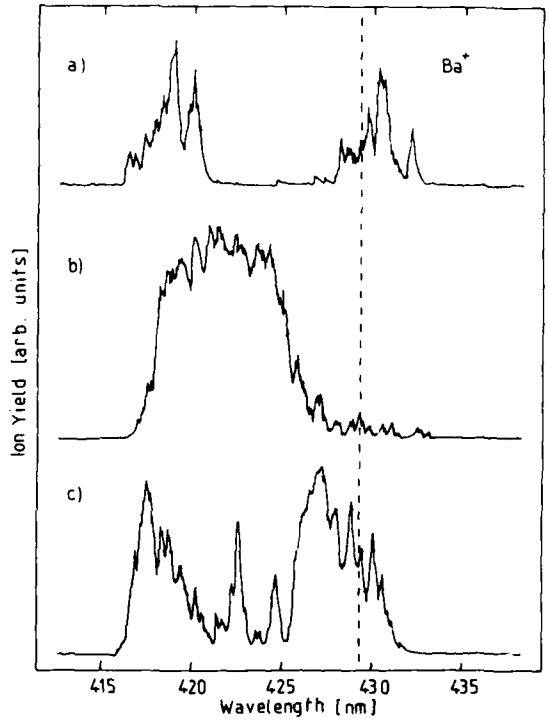

FIG. 8. Spectral dependence of the Ba^+ desorption yield from $BaF_2(111)$ in the blue spectral range at an intensity of about 5×10^7 W/cm^2. The three scans (a), (b), and (c) were carried out successively at the same surface spot. The dashed line indicates the wavelength at which the data in Fig. 9 were recorded.

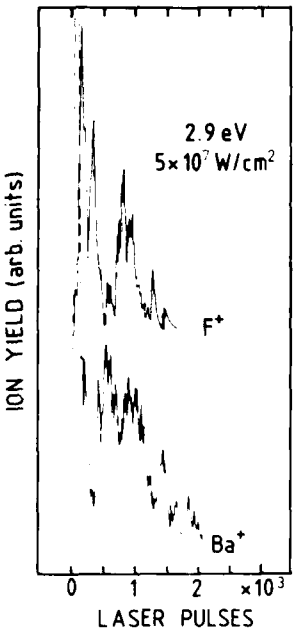

FIG. 9. Anticorrelation of the Ba^+ and F^+ desorption yields measured at the wavelength indicated by the dashed line in Fig. 8. To distinguish the large emission peak of Ba^+ in the beginning from the F^+ yield it is drawn by dashed lines. The dashed–dotted lines are meant to illustrate the anticorrelation of the Ba^+ and F^+ yields.

ments. Based on the results presented in Fig. 9 we suggest that the yield spectrum in Fig. 8(a) is characteristic for Ba^+ emission out of a Ba-rich layer, while the scan in Fig. 8(b) reflects Ba^+ emission from a F-rich environment. The yield spectrum in Fig. 8(c) again shows some similarities to the one in Fig. 8(a). Keeping in mind that in the [111] direction BaF_2 has the layer sequence Ba–F–F–Ba, the three scans in Fig. 8 seem to indicate that we are indeed observing a layer-by-layer ablation. To observe this layer sequence, however, it needs a favorable combination of power density, scanning time, and spot characteristics. Site-to-site variations of the spot characteristics make measurements like the ones shown in Fig. 8 rather difficult, in particular, since the spots must remain active during the scanning time and not bleach out too rapidly.

The interpretation in terms of layer-by-layer ablation is supported by the anticorrelation of the Ba^+ and F^+ yields as a function of irradiation time (the laser repetition frequency was 10 Hz) for one spot at a fixed wavelength, as shown in Fig. 9. Marked by the dot–dashed lines we can clearly see that a maximum of the desorption yield of F^+ correlates with a minimum of the desorption yield of Ba^+, and vice versa. This is indeed what one would expect for an ablation of a Ba–F–F–Ba layer sequence. The anticorrelation of the desorption yields of Ba^+ and F^+ can be related to the emission spectra shown in Fig. 8. As indicated by the dashed line in Fig. 8 one can understand that for a fixed wavelength the oscillation of the Ba^+ yield is actually caused by a different spectral absorption, depending on whether the ion is situated in a barium- or in a fluorine-rich environment. The fact that laser-induced desorption is layer selective may be of interest for some applications, since by the right number of laser pulses with a certain intensity one can prepare the upper surface layer to be either barium or fluorine enriched. There is no doubt that this concept can be applied to other materials as well. The other feature in Fig. 9 is the rapid bleaching out of a spot, that is the desorption usually ceases at these intensities within minutes. We speculate that this might be caused by metallization which quenches the surface states discussed above and leads to different optical properties of the surface.

V. DISCUSSION

In this chapter we will discuss the experimental results presented in Secs. IV A and IV B in view of the predictions of the cluster calculations and try to extract a reasonable model for the laser-induced desorption mechanism. The key question is: are the observed wavelength and intensity dependencies indeed caused by surface states? Can we rule out contributions from bulk defects? After all, the five-photon absorption can create holes in the bulk, and further the excitation of existing defects might also provide for wavelength-dependent absorption. The following arguments combined speak against bulk-defect excitations: (1) The observation is time-resolved. The ions arrive at the detector in $< 50\ \mu s$ which is the estimated flight time for a kinetic energy of a few tenths of an eV. This time interval rules it unlikely that we are dealing with migration of defects to the surface, which is expected to take milliseconds or longer at room temperature.[9,33] (2) The spectral dependence of the electron emission is identical for two- and five-photon processes. A two-photon ionization, however, can with significant intensity only originate from occupied surface states in the band gap. Therefore, the five-photon ionization must also occur at the surface and must proceed via the same excitonic resonances as the two-photon ionization, as indicated by the dashed and solid arrows in Fig. 2. (3) The alternating yields of F^+ and Ba^+ together with the wavelength dependence of the Ba^+ desorption indicate that surface states are involved in the photoabsorption process. The change of the Ba^+-emission spectra, depending on whether Ba^+ is desorbed from a Ba-rich or a F-rich layer, can be taken as evidence that the surface states vary with their chemical environment. In this connection the question of how localized these surface states really are is of importance but must be left to future investigations.

Next we want to consider the role of surface states for the desorption process. First of all it is evident that unfilled states can resonantly absorb energy at the proper wavelength. Hence the existence of occupied surface states makes resonant *single photon absorption* of a few eV possible, and we suggest that this is the dominant process at very low intensities ($\ll 10^6$ W/cm^2). In this case the excited state will quickly relax radiationless and transfer the absorbed energy into the heat bath of the crystal. *Multiphoton absorption*, on the other hand, leads to electron emission (Figs. 4–6) and hence creates holes. Among other positive ions we observe F^+ which requires two electrons to be removed from the F^- ion in the lattice, and we showed that the ion yield is proportional to the square of the electron yield. Thus a plausible ion desorption mechanism to consider is the analog of the Knotek–Feibelman mechanism,[16] except that in our case the holes are generated by the ionization of valence rather than inner-shell electrons.

It seems reasonable to distinguish between two cases. One is when two holes are generated near one barium or fluorine ion, with the result that the chemical bond is broken and one positive ion is ejected by Coulomb repulsion.[6] The probability for creation of two adjacent holes is difficult to estimate since the cross sections for the multiphoton ionization are unknown. If we use a typical cross section for two-photon ionization of free atoms ($\sigma^{(2)} \simeq 10^{-50}$ cm^4 s), we arrive at a probability of about 3×10^{-12} for generating two $2p$ holes per atom for one laser pulse of an intensity of 5×10^6 W/cm^2. With about 10^{13} irradiated atoms in the surface layer this would amount to about 30 paired holes per laser pulse. The objection has been raised[34] that the shielding of the first hole would shift all surface states to such an extent that the multiphoton ionization would require either more photons, or at least be no longer resonantly enhanced. This objection cannot at present be dismissed. However in our model the emission of two electrons is necessary to trigger one ion emission, and if only the emission of the first electron proceeds via the resonances discussed above, the spectral dependence of the electron and ion yield would still be similar. What would be affected is the probability for multiphoton ionization of the second electron and thus the peak intensities in the yield spectra.

The other and more likely case is when the holes are generated apart from each other well outside their Coulomb interaction range and must meet by diffusion during their lifetime. If we for an estimate again invoke the cross section for atomic two-photon ionization, we arrive at a probability of 10^{-8} for creating one $2p$ hole per atom per pulse at 5×10^6 W/cm^2, i.e., one hole for about 10^5 surface atoms. For a rigorous model the lifetime of the holes and their surface diffusion rate at room temperature must be known. If we speculate that two diffusing holes indeed can meet, then we expect them with a certain probability to combine and form a localized two-hole state which can lead to emission of positive ions.[10,35] Nevertheless, the precise ion desorption mechanism remains to be determined.

Recently, Walkup *et al.*[4,36] showed that gas phase ionization of ground-state atoms by secondary electrons might account for most of the positive ions detected in ESD and PSD (with high-energy photons) studies with alkali–halide crystals. We have to examine whether this might also apply to laser-induced desorption of positive ions. The collisional cross sections, on which the authors base their arguments, are for barium atoms certainly comparable to the ones for alkali atoms. It is unlikely, however, that gas-phase ionization occurs in our case, simply because the energy of the incident photons is orders of magnitude smaller compared to the energy of the electrons in ESD and of the photons in PSD. As a result, the kinetic energy of the electrons released by multiphoton processes is considerably smaller and probably amounts to less than the energy of one photon (2.3 eV), which is much below the threshold energy required to ionize neutral barium (5.1 eV). Furthermore, we never reliably observed neutral barium atoms. At this stage it is not known whether this is because no barium atoms are emitted and the surface will become enriched with barium[22] (metallization), or whether neutral barium condenses at the surrounding surfaces, metal screens, and grids because of its low-vapor pressure.

VI. CONCLUSION

To summarize, we have shown that surface states play an important role for the energy absorption by optically transparent BaF_2 samples. They account for the resonant single or multiphoton absorption. It was proven by two-photon photoemission that occupied surface states exist in the middle of the band gap, and we suggest that similar results are to be expected for all divalent ionic crystals. The most encouraging result was that at the low intensities used here reproducible emission spectra for electrons and ions could be obtained from freshly cleaved crystal surfaces during the course of many hours. This holds good promise for future spectroscopy of surface states using tunable dye lasers. At higher intensities, yet well below the dielectric breakdown, it was shown that the desorption proceeds layer-by-layer which, when carried out in a well-controlled manner might be of interest for applications.

Our results indicate that for the desorption of positive ions two holes in the $2p$ valence band of BaF_2 are required. However, more data are needed to confirm this clue. In order to understand the exact mechanism for laser-induced ion desorption, it will be necessary to measure the kinetic energies and angular distributions of both photoelectrons and ions. Also, the ratio of neutral fluorine to ion yield must be determined together with a more careful search for neutral barium. Last but not least these type of investigations should be carried out with other divalent ionic crystals as well, in order to establish the general character of the conclusions reached in this paper for $BaF_2(111)$.

ACKNOWLEDGMENTS

This work was supported by the Deutsche Forschungsgemeinschaft, Sonderforschungsbereich 6, the Swedish Natural Science Research Council, and the Swedish Board of Technical Development. One of us (E. M.) acknowledges the hospitality of Rolf M. Steffen and his wife, Tesuque, NM, and of Norman H. Tolk, Vanderbilt University, Nashville, TN, during the preparation of this manuscript.

[1] *Desorption Induced by Electronic Transitions, DIET I*, Vol. 24 in Springer Series in Chemical Physics, edited by N. H. Tolk, M. M. Traum, J. C. Tully, and T. E. Madey (Springer, Heidelberg, 1983).
[2] *Desorption Induced by Electronic Transitions, DIET II*, Vol. 4 in Springer Series in Surface Sciences, edited by W. Brenig and D. Menzel (Springer, Heidelberg, 1985).
[3] M. L. Knotek, Rep. Progr. Phys. **47**, 1499 (1984).
[4] Ph. Avouris, F. Bozso, and R.E. Walkup, Nucl. Instrum. Methods B **27**, 136 (1987).
[5] R. E. Walkup and Ph. Avouris, Phys. Rev. Lett. **56**, 524 (1986).
[6] P. Williams and G. Gillen, Surf. Sci. **180**, L109 (1987).
[7] H. Overeijnder, M. Szymonski, A. Haring, and A. E. deVries, Radiat. Eff. **36**, 63 (1978).
[8] R. F. Haglund, Jr., R. G. Albridge, D. W. Cherry, R. K. Cole, M. H. Mendenhall, W. C. B. Peatman, N. H. Tolk, D. Niles, G. Margaritondo, N. G. Stoffel, and E. Taglauer, Nucl. Instrum. Methods B **13**, 525 (1986).
[9] G. M. Loubriel, T. A. Green, P. M. Richards, R. G. Albridge, D. W. Cherry, R. K. Cole, R. F. Haglund, Jr., L. T. Hudson, M. H. Mendenhall,

D. M. Newns, P. M. Savundararaj, K. J. Snowdon, and N. H. Tolk, Phys. Rev. Lett. **57**, 1781 (1986).
[10]N. Itoh and T. Nakayama, Phys. Lett. A **92**, 471 (1982).
[11]N. Itoh, T. Nakayama, and T. A. Tombrello, Phys. Lett. A **108**, 480 (1985).
[12]T. Yasue, T. Gotoh, A. Ichimiya, Y. Kawaguchi, M. Kotani, S. Ohtani, Y. Shigeta, S. Takagi, Y. Tazawa, and G. Tominaga, Jpn. J. Appl. Phys. **25**, L363 (1986).
[13]P. D. Townsend, R. Browning, D. J. Garlant, J. C. Kelly, A. Mahjoobi, A. J. Michael, and M. Saidoh, Radiat. Eff. **30**, 55 (1976).
[14]A. Schmid, P. Bräunlich, and P. K. Rol, Phys. Rev. Lett. **35**, 1382 (1975).
[15]W. J. Siekhaus, J. H. Kinney, D. Milam, and L. L. Chase, Appl. Phys. A **39**, 163 (1986).
[16]M. L. Knotek and P. J. Feibelman, Phys. Rev. Lett. **40**, 964 (1978).
[17]W. Sesselmann, E. E. Marinero, and T. J. Chuang, Appl. Phys. A **41**, 209 (1986).
[18]T. J. Chuang and I. Hussla, Phys. Rev. Lett. **52**, 2045 (1984).
[19]T. W. Walker, A. H. Guenther, and P. E. Nielsen, IEEE J. Quantum. Electron. **17**, 2041, 2053 (1981).
[20]L. Ernst, Surf. Sci. **176**, L825 (1986).
[21]J. Reif, H. B. Nielsen, O. Semmler, E. Matthias, E. Westin, and A. Rosén, Phys. Scripta **35**, 532 (1987).
[22]R. Kelly, Surf. Sci. **90**, 280 (1979).
[23]D. E. Ellis, G. A. Benesh, and E. Byrom, Phys. Rev. B **20**, 1198 (1979).
[24]A. Rosén, D. E. Ellis, H. Adachi, and F. W. Averill, J. Chem. Phys. **65**, 3629 (1976).
[25]B. Delley and D. E. Ellis, J. Chem. Phys. **76**, 1949 (1982).
[26]U. von Barth and L. Hedin, J. Phys. C **5**, 1629 (1972).
[27]W. Pong, C. S. Inouye, and S. K. Okada, Phys. Rev. B **18**, 4422 (1978).
[28]J. Reif, H. Fallgren, H. B. Nielsen, and E. Matthias, Appl. Phys. Lett. **49**, 930 (1986).
[29]J. Reif, H. Fallgren, W. E. Cooke, and E. Matthias, Appl. Phys. Lett. **49**, 770 (1986).
[30]P. Bräunlich, A. Schmid, and P. Kelly, Appl. Phys. Lett. **26**, 150 (1975).
[31]J. Morellec, D. Normand, and G. Petite, Phys. Rev. A **14**, 300 (1976).
[32]F. Rainer, W. H. Lowdermilk, and D. Milam, NBS Spec. Publ. **669**, 157 (1984).
[33]H. Overeijnder, R. R. Tol, and A. E. deVries, Surf. Sci. **90**, 265 (1979).
[34]This question was asked by G. M. Loubriel.
[35]D. R. Jennison and D. Emin, Phys. Rev. Lett. **51**, 1390 (1983).
[36]R. E. Walkup, Ph. Avouris, and A. P. Ghosh, Phys. Rev. Lett. **57**, 2227 (1986).

Excited-atom production by electron and ion bombardment of alkali halides

R. E. Walkup, Ph. Avouris, and A. P. Ghosh
IBM Thomas J. Watson Research Center, P. O. Box 218, Yorktown Heights, New York 10598

(Received 27 February 1987; accepted 7 May 1987)

We present experimental results on the production of excited atoms by electron and ion bombardment of alkali halides. For the case of electron bombardment, Doppler shift measurements show that the electronically excited atoms have a thermal velocity distribution in equilibrium with the surface temperature. Measurements of the absolute yield of excited atoms, the distribution of population among the excited states, and the systematic dependence on incident electron current and sample temperature support a model in which the excited atoms are produced by gas-phase collisions between desorbed ground-state atoms and secondary electrons. In contrast, for the case of ion bombardment, the excited atoms are directly sputtered from the surface, with velocity distributions characteristic of a collision cascade, and with typical energies of ~ 10 eV.

Bombardment of solids by energetic beams of electrons, photons, or ions is generally accompanied by the ejection of particles from the surface. For bombardment with ions, particle ejection can be caused by a sequence of momentum transfer collisions.[1] However, for electron or photon bombardment, direct momentum transfer is usually negligible, and particle ejection is due to electronic excitations induced by the incident electron or photon.[2] An understanding of the basic mechanisms responsible for this electron- or photon-stimulated desorption (ESD or PSD) is of substantial current interest. In this paper we present experimental results on the production of *electronically excited* atoms by electron and ion bombardment of alkali halides. The alkali halides are particularly interesting substrates because these materials have relatively simple geometric and electronic structures, and because they exhibit an interesting variety of desorption phenomena. Moreover, the alkali halides may be regarded as useful prototypes for understanding the interactions of electron, photon, and ion beams with ionic insulators.

The alkali halides have some remarkable properties which need to be kept in mind. In particular, when alkali halides are bombarded by any ionizing radiation, electron–hole pairs are generated which lead to an extremely efficient mechanism for neutral desorption.[3–10] The holes, i.e., neutral halogen atoms, are trapped in stable defects called H centers, which diffuse to the surface region. Holes produced in the bulk can thus be transported to the surface layer, where the neutral halogen atoms can thermally desorb. In addition, there are directional "focused collision" sequences which occur along the halogen sublattice, in ⟨110⟩ directions, which result in nonthermal, directional ejection of neutral halogen atoms. The loss of halogen leaves excess electrons and halogen vacancies in the material. The excess electrons can trap in halogen vacancies to form stable F centers. The F centers diffuse to the surface[11] where electrons can recombine with alkali ions to form neutral alkali atoms, which thermally desorb. For some of the alkali halides, such as NaCl, the net rate of halogen loss is balanced by alkali evaporation, and the material remains stoichiometric, provided that the temperature is sufficiently high.[12] However, at low temperatures, the net rate of alkali evaporation does not make up for the halogen loss, and the material becomes alkali enriched.[12] The absolute yield of atoms desorbed by this bulk-defect mediated process is remarkably large. For example when NaCl is bombarded by 1 keV electrons at $T = 300$ °C, ~ 10 neutral atoms desorb per incident electron.[12,13] Now we turn to the consideration of the production of *electronically excited* atoms.

The experimental apparatus is briefly outlined below. Alkali halide crystals were cleaved in air, and cleaned by heating to 300 °C in ultrahigh vacuum ($\simeq 5\times10^{-10}$ Torr) overnight. The samples could be bombarded either by an electron beam of 200–2000 eV and 0.1–10 μA mm^{-2}, or an Ar^+ ion beam of 1–5 keV and 0.1–10 μA mm^{-2}. The area of each beam was $\simeq 1\times2$ mm on the substrate surface. The stainless-steel sample holder could be resistively heated, and the sample temperature was monitored with a thermocouple. The electron and ion beams were incident on the cleaved (100) surfaces at 45 deg from the surface normal. Optical windows were mounted in the plane containing the (100) surface, providing line-of-sight to the bombarded region.

Electronically excited atoms were detected both by laser-induced fluorescence (LIF) and by optical emission spectroscopy. The LIF measurements were restricted to the detection of Na*($3p$) excited atoms produced by electron bombardment of NaCl. These measurements have been reported in the literature.[13] The LIF experiments provided accurate measurements of the velocity distributions of the excited atoms, which were found to be thermal, in equilibrium with the surface temperature. We have also obtained velocity distributions of the electronically excited atoms by high-resolution optical emission spectroscopy, using a scanning Fabry–Perot interferometer. In this method, the velocity distribution along the viewing axis is obtained from the Doppler-broadened emission profile. The Fabry–Perot interferometer provides excellent spectral resolution and high optical throughput. However, the emission profiles observed are convolutions of the actual profiles with the instrument response function, and the instrument response is extremely sensitive to interferometer alignment. In practice it was necessary to place an aperture in front of the collection lens to stop the optical system down to $f/10$. This increases the

 0734-211X/87/051423-04$01.00 © 1987 American Vacuum Society

depth of focus and reduces the errors due to misalignment. It was also necessary to optimize the alignment and measure the instrument response using light scattered from a monochromatic laser beam prior to each set of scans.

For the electronically excited Na*($3p$) atoms produced by electron bombardment of NaCl, the emission profiles obtained with the Fabry–Perot interferometer were in good agreement with our earlier LIF measurements.[13] The emission profiles were observed to be Doppler broadened, with a thermal velocity distribution characterized by the surface temperature measured with a thermocouple, to within experimental error. An example of the Na* $3p \rightarrow 3s$ emission profile obtained with the Fabry–Perot is shown in Fig. 1, along with a fit to a thermal distribution, taking into account the convolution with the instrument response function. For this data, the incident electron current was $\simeq 2\,\mu A$ in a 1×2 mm beam, the electron kinetic energy was 1 keV, and the substrate temperature was 300 °C. Compared to the LIF measurements, the Fabry–Perot provided higher sensitivity, but lower spectral resolution. Due to the high sensitivity, we were able to observe Doppler broadening of the emission lines over a very wide range of experimental conditions including temperatures from 40 to 300 °C, and incident electron currents from 0.1 to 10 μA mm^{-2}. The observed profiles were thermal over the entire range of parameter space. In addition, weak emission from one of the higher excited states of Na, the $4d$ state was detected and analyzed. The Na* $4d \rightarrow 3p$ emission line was found to be Doppler broadened, with a thermal velocity distribution characterized by the surface temperature to within error. These results support our proposal[13] that the excited atoms are formed by gas-phase excitation of desorbed ground-state atoms.

With the scanning Fabry–Perot interferometer, it was possible to obtain limited measurements on Li* produced by electron bombardment of LiF. A scan of the Li* $2p \rightarrow 2s$ transition is shown in Fig. 2. For this data, the incident electron current was 20 μA in a 1×2 mm beam, the electron kinetic energy was 1 keV, and the sample temperature was 260 °C. The observed linewidth is $\simeq 5.5$ GHz (FWHM). This is consistent with the combined instrument width, $\simeq 3.0$ GHz (FWHM), and the Doppler width, $\simeq 2.8$ GHz (FWHM), at the substrate temperature. In contrast to NaCl, LiF showed strong evidence of surface modification by electron bombardment in the 200–300 °C temperature range. In order to obtain the data shown in Fig. 2, it was necessary to translate the LiF sample to bring unexposed material into the beam. Because of the beam-induced surface modification, we have not been able to obtain quantitative measurements of the Li* velocity distributions. However, from the available data it is clear that the majority of the excited atoms must have velocity components along the viewing axis $< 2(kT_s/\mathrm{m})^{1/2}$, where T_s is the substrate temperature. The available data are consistent with thermal distributions for Li* produced by electron bombardment of LiF. This suggests that gas-phase excitation is responsible for Li* production by electron bombardment of LiF as well as Na* production by electron bombardment of NaCl.

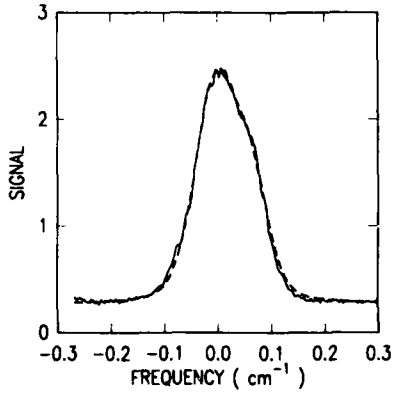

FIG. 1. Experimental Doppler-broadened profile of the sodium $3p_{3/2} \rightarrow 3s_{1/2}$ emission line measured by a scanning Fabry–Perot interferometer (solid curve). The excited atoms were produced by electron bombardment of NaCl. The dashed curve is a fit for a thermal velocity distribution with $T = 300$ °C, the substrate temperature measured with a thermocouple. The fit accounts for the convolution of the actual emission profile with the Fabry–Perot transmission function. The hyperfine structure of the emission line is clearly seen as a shoulder at $\simeq 0.06$ cm^{-1}.

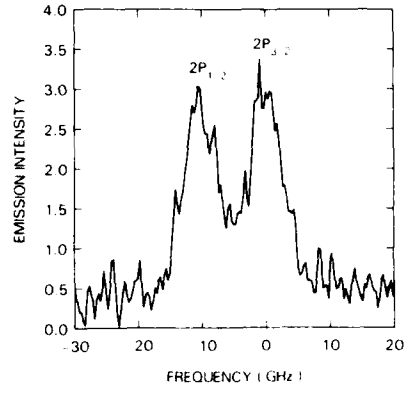

FIG. 2. Experimental Doppler-broadened profile of the lithium $2p \rightarrow 2s$ emission line measured by a scanning Fabry–Perot interferometer. The excited atoms were produced by electron bombardment of LiF. The fine structure in the excited state is clearly resolved, with separate peaks arising from the $2P_{1/2}$ and $2P_{3/2}$ levels. The observed line width, $\simeq 5.5$ GHz (FWHM), is consistent with the combined instrument width, $\simeq 3.0$ GHz (FWHM), and the Doppler width, $\simeq 2.8$ GHz (FWHM), for a thermal distribution at the substrate temperature.

Further evidence for gas-phase excitation was obtained from studies of the excited-state emission intensity as a function of incident electron current. Sample temperature and electron dose are important parameters in these studies. We have carried out systematic studies of Na* production by electron bombardment of NaCl over a wide range of conditions. At high temperatures ($T > 200$ °C), ground-state alkali evaporation keeps up with halogen loss, and the surface remains stoichiometric.[12] The ground-state alkali-atom yield is then proportional to the incident electron flux, I_e. The incident electron current and the yield of secondary electrons are also $\propto I_e$. Thus for a gas-phase electron-impact excitation mechanism, the yield of excited alkali atoms should be $\propto I_e^2$. In Fig. 3 (upper curve) we show that the dependence of emission intensity on incident electron cur-

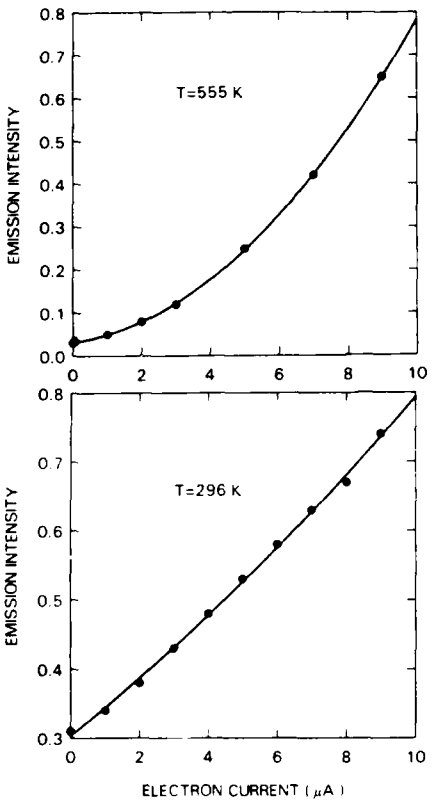

FIG. 3. The Na $3p \rightarrow 3s$ emission intensity is shown as a function of incident current for electron bombardment of NaCl. In the upper curve, the sample temperature was 555 K, and in the lower curve the sample temperature was 296 K. The quadratic behavior in the upper curve indicates a gas-phase excitation mechanism. The approximately linear trend in the lower curve is due to beam-induced modification of the surface stoichiometry, which occurs for low substrate temperatures (see the text).

rent is quadratic when the temperature is high enough ($T > 200$ °C) for the substrate to remain stoichiometric NaCl. Concurrent measurements of the ground-state Na density by laser-induced fluorescence showed a linear dependence on incident current over the same current range. In contrast, at low temperatures ($T < 370$ K) the surface becomes alkali enriched because ground-state alkali evaporation becomes rate limited. The ground-state alkali yield then becomes nearly independent of electron current (and principally dependent on temperature); and the excited alkali-atom yield takes on an approximately linear dependence on incident electron flux, as observed by previous workers.[14] This effect is illustrated in the lower curve of Fig. 3, which covers the same current (and current density) as used in the earlier studies of Tolk *et al.*[14] Emission profiles measured with the Fabry–Perot interferometer were observed to be thermal at these low temperatures where the yield versus current curves were approximately linear. We emphasize that the apparently linear excited-state yield at low temperatures is entirely due to beam-induced modification of the surface layer. Because of the extremely efficient mechanism for neutral halogen desorption, surface modification occurs when the electron dose exceeds $\sim 10^{13}$ electrons cm^{-2}. At high temperatures, where the material remains stoichiometric NaCl, the yield curves are quadratic, indicating a gas-phase excitation mechanism.

In summary, the available evidence demonstrates that the excited atoms reproduced by electron bombardment of alkali halides are formed by gas-phase excitation of desorbed ground-state atoms. The evidence includes velocity distribution measurements both by laser-induced fluorescence and by high-resolution optical emission spectroscopy; systematic studies of the yield of excited atoms versus electron current and sample temperature; quantitative agreement between the absolute excited state yield and the calculated yield for gas-phase excitation[13]; and good agreement between the experimental distribution of population over the various excited states and the population distribution expected for gas-phase electron-impact excitation.[13]

Now we turn to a brief discussion of the production of excited atoms by *ion* bombardment. For these experiments, Ar^+ ions with 1–5 keV and 0.1–10 μA mm^{-2} were incident on (100) faces of alkali-halide crystals at an angle of 45 deg from the surface normal. For ion bombardment, the excited-atom yield was always observed to be proportional to the incident ion current. In addition, the emission lines from the excited atoms were broad, reflecting kinetic energies in the ~ 10 eV range. Moreover, the emission profiles could be accurately reproduced by fitting with the velocity distribution expected for atoms sputtered by a linear collision cascade mechanism. The Thompson formula[15] gives the flux distribution for sputtered atoms. In our experiment, we observe the number of excited atoms produced per second with a given velocity component along an axis parallel to the surface. This distribution can be obtained for the Thompson formula by a simple transformation and an integration over ejection solid angle. The analytic result is $f(v_x) \propto (v_x^2 + v_B^2)^{-3/2}$, where v_x is the velocity component along the viewing axis, and the parameter v_B is related to the surface binding energy, E_B, by the relation $E_B = (1/2)\, m v_B^2$. For the sputtering of excited atoms, E_B cannot be strictly interpreted as a surface binding energy. Instead, it must be regarded only as a characteristic kinetic energy of the excited sputtered particles.

The Li* $2p \rightarrow 2s$ emission profile for 5 keV bombardment of LiF is shown in Fig. 4. The fit for a collision cascade distribution is also shown. The characteristic kinetic energy, E_B, determined from the fit is $E_B = 5.5 \pm 0.8$ eV. The best fit curve overlaps the experimental data to within error. Convolution of the collision cascade profile with the instrument response function was taken into account in the fitting procedure. Values of E_B for several sputtered excited atoms were obtained from analysis of the experimental emission profiles. The results are listed in Table I. The error bars listed in Table I indicate variations over a number of data sets combined with best estimates of remaining systematic errors.

The important findings are (1) the sputtered excited atoms are produced by relatively low energy collisions (~ 10 eV), with velocity distributions characteristic of a collision cascade; (2) the characteristic kinetic energy is greater for atoms with a greater degree of electronic excitation, and (3)

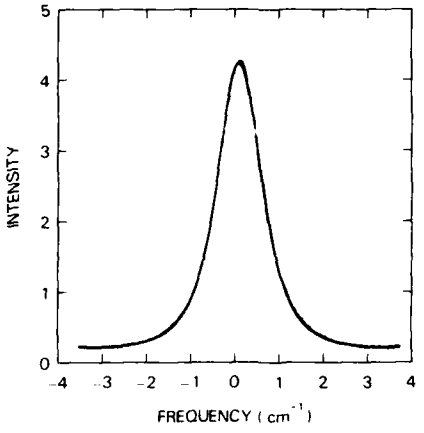

FIG. 4. Experimental Doppler-broadened profile of the lithium $2p \rightarrow 2s$ emission line measured by a scanning Fabry–Perot interferometer (solid curve). The excited atoms were produced by ion bombardment of LiF with 5 keV Ar^+. The experimental profile is compared to a fit with a collision cascade velocity distribution (dashed curve). The fit overlaps the experimental curve to within error. The characteristic kinetic energy of the Li* ($2p$) atoms is 5.5 ± 0.8 eV.

the kinetic energy for excited atoms with strong allowed transitions is very similar to the kinetic energy of sputtered metastable atoms.[16] The results for Ba* $6p \rightarrow 6s$ produced by Ar^+ bombardment of BaF_2 are in direct conflict with measurements based on the decrease of emission intensity vs. distance from the surface.[17] The light versus distance measurements lead to erroneously high kinetic energies, probably because of difficulties caused by radiative cascading from more highly excited states. The Doppler-shift measurements reported here do not suffer from such difficulties, and they unambiguously show that the sputtered excited atoms have low (~ 10 eV) kinetic energies. The correlation between electronic and kinetic energies is particularly interesting. A qualitatively similar correlation is expected according to the model of excited-atom sputtering proposed by Kelly.[18] However, the quantitative relationships between yield, kinetic energy, and electronic energy predicted by that model are not in agreement with the experimental data. Qualitatively, the observed correlation between kinetic and electronic energy suggests that the higher excited states are formed in more energetic collisional encounters. However, the precise excitation mechanisms are not known at this time.

It is interesting to note that even for the case of ion bombardment, there should be some contribution to the excited-state yield coming from gas-phase excitation of ground-state atoms. The flux of ground-state atoms is primarily due to evaporation via the bulk-defect formation mechanism, as in the case of bombardment by electron beams. Under typical conditions, the probability that a given ground-state atom will be excited by gas-phase electron impact is of order 10^{-5}–10^{-6}. However, for ion bombardment there is an efficient collisional mechanism for the direct ejection of atoms in excited states. For the alkali halides bombarded by ion beams, this direct process produces the vast majority of the excited atoms observed.

TABLE I. Characteristic energies of sputtered excited atoms obtained by high-resolution optical emission spectroscopy, using a Fabry–Perot interferometer. The excited atoms were produced by bombardment of the target material by 5 keV Ar^+ ions at an angle of incidence of 45 deg from the surface normal.

Transition	Target	E_B (eV)
Na* $3p \rightarrow 3s$	NaCl	4.0 ± 0.6
Na* $4d \rightarrow 3p$	NaCl	7.3 ± 1.1
Li* $2p \rightarrow 2s$	LiF	5.5 ± 0.8
Li* $3d \rightarrow 2p$	LiF	10.9 ± 1.5
Ba* $6p \rightarrow 6s$	BaF_2	19 ± 3
Ba* $8s \rightarrow 6p$	BaF_2	36 ± 8

In conclusion we have presented experimental data which indicate that the excited atoms produced by electron bombardment of alkali halides are formed by gas-phase electron-impact excitation of desorbed ground-state atoms. Similarly, gas-phase ionization is expected to be a major source of positive ions in experiments on ion desorption from alkali-halides stimulated by electron or photon beams. In contrast, for the case of bombardment by ion beams, excited atoms are directly ejected by a low-energy collision cascade mechanism.

[1]For a recent review see, R. Kelly, Radiat. Eff. **80**, 381 (1984).
[2]A good collection of recent work appears in *Desorption Induced by Electonic Transitions DIET 1*, edited by N. H. Tolk, M. M. Traum, J. C. Tully, and T. E. Madey (Springer, Berlin, 1983); *Desorption Induced by Electronic Transitions, DIET 2*, edited by W. Brenig and D. Menzel (Springer, Berlin, 1984).
[3]D. Pooley, Proc. Phys. Soc. **87**, 257 (1966).
[4]H. N. Hersh, Phys. Rev. **148**, 928 (1966).
[5]P. W. Palmberg and T. N. Rhodin, J. Phys. Chem. Solids **29**, 1917 (1968).
[6]D. J. Elliot and P. D. Townsend, Philos. Mag. **23**, 249 (1971).
[7]N. Itoh, Nucl. Instrum. Methods **132**, 201 (1976).
[8]H. Overeijnder, M. Szymonski, A. Haring, and A. E. deVries, Radiat. Eff. **36**, 63 (1978); **38**, 21 (1978).
[9]M. Szymonski, H. Overeijnder, and A. E. deVries, Surf. Sci. **90**, 274 (1979).
[10]M. Szymonski, Radiat. Eff. **52**, 9 (1980).
[11]G. M. Loubriel, T. A. Green, P. M. Richards, R. G. Albridge, D. W. Cherry, R. K. Cole, R. F. Haglund, Jr., L. T. Hudson, M. H. Mendenhall, D. M. Newns, P. M. Savundararaj, K. J. Snowdon, and N. H. Tolk, Phys. Rev. Lett. **57**, 1781 (1986).
[12]M. Szymonski, J. Ruthowski, A. Poradzisz, Z. Postawa, and B. Jorgensen, in Ref. 2, p. 160.
[13]R. E. Walkup, Ph. Avouris, and A. P. Ghosh, Phys. Rev. Lett. **57**, 2227 (1986).
[14]N. H. Tolk, L. C. Feldman, J. S. Kraus, R. J. Morris, M. M. Traum, and J. C. Tully, Phys. Rev. Lett. **46**, 134 (1981); N. H. Tolk, L. C. Feldman, J. S. Kraus, R. J. Morris, T. R. Pian, M. M. Traum, and J. C. Tully, *Inelastic Particle–Surface Collisions*, edited by E. Taglauer and W. Heiland (Springer, Berlin, 1981), p. 112.
[15]M. W. Thompson, Philos. Mag. **18**, 377 (1968).
[16]M. L. Yu, D. Grichkowsky, and A. C. Balant, Phys. Rev. Lett. **48**, 427 (1981); W. Husinsky, G. Betz, and I. Giris, *ibid.* **50**, 1689 (1983); C. E. Young, W. F. Calaway, M. J. Pellin, and D. M. Gruen, J. Vac. Sci. Technol. A **2**, 693 (1984).
[17]S. Dzioba and R. Kelly, Surf. Sci. **100**, 119 (1980).
[18]R. Kelly, Phys. Rev. B **25**, 700 (1982).

Selective area deposition of metals using low-energy electron beams

R. R. Kunz, T. E. Allen, and T M. Mayer
Department of Chemistry, University of North Carolina, Chapel Hill, North Carolina 27514

(Received 27 February 1987; accepted 7 May 1987)

We have investigated the use of low-energy electron beams to nucleate and stimulate the deposition and growth of thin films of metals. Selective area growth of Fe from $Fe(CO)_5$ using low-energy focused electron beams (<5 keV) has been deomnstrated. Low-energy electron-beam irradiation (0.5–3.0 keV) can be used to nucleate growth of Fe on a Si surface. Subsequent thermal decomposition of $Fe(CO)_5$ on Fe is ~ 900 times faster than on Si at 125 °C resulting in thick, polycrystalline Fe films deposited only in areas irradiated by the electron beam. We have demonstrated nucleation and growth of 150 nm Fe features using 3 keV, 100-nm-diam electron beam. Fluxes and energies of low-energy electrons passing through the surface (primaries, secondaries, backscatters) are calculated by a Monte Carlo technique using an accurate scattering cross section for low-energy electrons. Spatial distributions of backscatters and secondaries at primary energies <3000 eV are seen to be confined primarily to a radius of <10 nm from the point of impact, and it appears that scattering contributes little to the spatial distribution of deposited film. Minimal electron scattering at low-energy makes this regime attractive for direct write, selective area processing.

I. INTRODUCTION

Deposition and growth of thin films by nonthermal means is well-established in electronic material applications. Restrictions on material compatibility and total thermal budget has led to the acceptance of low temperature, plasma-enhanced chemical-vapor deposition for formation of many dielectric, semiconductor, and metal films.[1,2] Photochemical processes have also been investigated for low-temperature oxide growth as well as for deposition of a variety of films from gaseous precursors.[3] Activation energies usually associated with chemical processes are overcome in the nonthermal cases by energy deposition to the starting material by gas-phase electron impact (in the case of plasma processing) or photon absorption (in the photochemical case).

In addition to the need for low-temperature processing there has been recent emphasis on selective area processing using focused beams of radiation, for applications in circuit repair, custom wiring, and *in situ* processing where the usual lithographic pattern transfer procedure is either not possible or not desirable. Most activity in selective area processing has emphasized photochemical or photothermal means using focused lasers[3] but recently applications using focused particle beams have appeared.[4]

We have chosen to investigate selective area processing using low-energy focused electron beams for a number of reasons. First, electron-beam technology is well-advanced through the development of electron microscopy and electron-beam lithography. Second, the absence of diffraction limitations inherent in photon processing give the promise of decreased feature sizes. Third, for nonthermal processes, energy deposition by electron impact is less selective than photon absorption and potentially more widely applicable. Cross sections for inelastic scattering of electrons leading to chemical activation (dissociation, ionization) usually exhibit maxima at fairly low energy (<500 eV). Thus from a chemical point of view low-energy electrons are the most interesting.

In order to obtain minimum feature sizes and maximum rates in selective area film growth using electron beams a number of conditions must be met. First, the flux of activating particles through the reactive medium must be maximized. In the case of electron beams incident on a solid surface this flux includes the primary beam as well as electrons backscattered from the solid, and secondary electrons generated in the solid. Typically the secondary electron yield for most materials possesses a maximum at 200–2000 eV, while the backscatter yield is relatively constant over this range.[5] Second, activation must take place in a restricted area of the surface, or volume of gas above the surface. For electron-beam irradiation, the primary concern is the scattering of the electrons into large angles by the solid, leading to exposure over a much larger area than the beam diameter. While scattering is a major problem at tens of keV, as in electron-beam lithography,[6] it is expected to be much less severe at low-primary energies, which also makes the low-energy regime attractive. Third, mobility of activated particles must be minimal, also to avoid deposition outside the irradiated area. This is usually associated with gas phase activation and diffusion away from the irradiated volume of gas, and can be circumvented by activation only of surface adsorbed species. Fourth, deposition yields must be high ($\gg 1$ atom deposited per incident electron) in order for deposition to proceed at useful rates. Deposition yields >1 usually imply some sort of catalytic process that leads to chemical amplification of the deposition rate.

We have previously demonstrated that low-energy electrons, primary as well as secondary and backscatters, can lead to deposition and growth of films from gaseous precursors.[7–9] In particular we have demonstrated selective area growth using low-energy focused-electron beams in the case of deposition of Fe films from gaseous $Fe(CO)_5$.[9] This sys-

 0734-211X/87/051427-05$01.00 © 1987 American Vacuum Society

tem also exhibits a catalytic enhancement of growth rate due to selective thermal decomposition on freshly deposited Fe surfaces. Selective area nucleation by electron irradiation in combination with selective decomposition leads to deposition yields in excess of 20 atoms per electron for beam energy of < 1000 eV.

In this paper we investigate the limitations to feature size obtainable in selective area deposition of Fe by low-energy electron-beam irradiation. Nucleation and growth of Fe from $Fe(CO)_5$ is performed for electron-beam energy < 3 keV in a modified scanning electron microscope. These measurements are compared to calculations of fluxes of low-energy electrons through the surface plane. Fluxes are calculated using a Monte Carlo technique considering elastic scattering of incident electrons leading to backscatter emission, and inelastic scattering leading to secondary-electron emission. In particular the spatial distribution of backscatters and secondaries is of primary interest in selective area deposition using low-energy electrons.

II. EXPERIMENTAL PROCEDURES

Low-energy electron-bombardment-induced film deposition was carried out in two different machines. A high density, unfocused broad beam was generated from a modified Kaufman type ion source.[10] Current densities up to 1 mA/cm^2 were obtained over a range of 50–1500 eV. This source was mounted in a high-vacuum chamber and was used to investigate quantitative aspects of electron-stimulated film growth and secondary electron emission. This system has been described in detail previously.[8] Selective area growth studies using focused beams were carried out in a modified ISI DS-130 scanning electron microscope (SEM). This system is shown schematically in Fig. 1. The electron beam was generated from a W filament. Beam energy could be varied down to 500 eV, and beam current was measured with a Faraday cup mounted on the sample stage. Beam diameter was estimated by scanning across the edge of the 200 μm entrance aperture to the Faraday cup, and measuring the secondary electron intensity profile. This measurement of beam diameter is not wholly adequate, since measurement of secondary intensity in this manner includes scattering effects of the beam on the Faraday cup. Measured beam diameter also appears to change from experiment to experiment depending on cleanliness of the aperture in the beam column. Typical beam diameters were 100 nm at 3 keV and 300 nm at 1 keV. Relative backscatter and secondary electron yields could be made by combinations of current measurements with the Faraday cup versus a flat surface, and use of a backscatter detector (not shown). Silicon samples were mounted on a precision stage which could be heated to 250 °C. The scan coils on the beam column were digitally controlled by a PDP 11 minicomputer with rudimentary pattern generation from a Tracor Northern TN-5500 image analysis software package. Electron dose and dwell time on a particular spot were controlled by beam size, current, and scan rate. $Fe(CO)_5$ was admitted to the SEM sample chamber via a leak valve to a pressure of 10^{-6} to 10^{-4} Torr. To prevent excessive contamination of the beam column liquid-nitrogen cooled surfaces were incorporated into the beam column and down stream of the sample chamber.

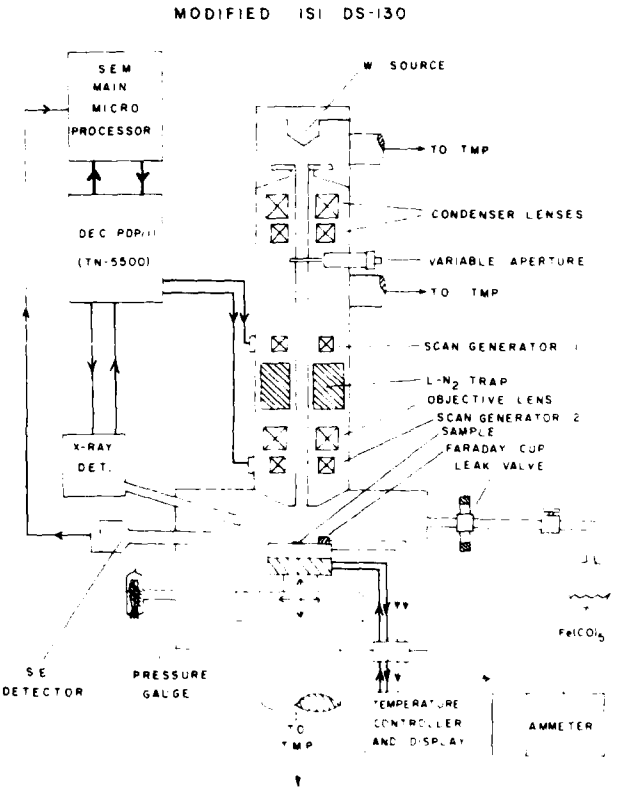

FIG. 1. Schematic diagram of the modified ISI DS-130 scanning electron microscope.

III. RESULTS AND DISCUSSION

A. Selective area growth of Fe films

Our previous work has demonstrated that low-energy electron irradiation is effective at nucleating and stimulating growth of Fe from $Fe(CO)_5$ at temperatures of ~ 125 °C.[9] Under these conditions thermal decomposition of $Fe(CO)_5$ on Fe is roughly 900 times more probable than decomposition on Si. The electron beam was used to form nucleation sites on the surface, presumably by electron-impact-induced dissociation of adsorbed $Fe(CO)_5$. Following this nucleation Fe was observed to deposit spontaneously and selectively on the nucleated area. Thus only a relatively small dose of electrons is necessary to stimulate film growth.

Figure 2 displays evidence for the localized nucleation and initial stages of Fe growth on Si. In this case a 1 keV electron beam, 70 pA, ~ 300 nm diameter was scanned across the surface at 3.2 μm/s, with a $Fe(CO)_5$ pressure of $\sim 10^{-5}$ Torr. Notice the thin-Fe film that has been deposited on the surface and the larger crystallites that have begun to grow spontaneously. No nucleation or Fe growth was observed in unirradiated areas at this temperature. The average feature width in the thin nucleation layer is about 300 nm. Similar features produced with 100-nm-diam beams at 3 keV produced nucleation layer width of ~ 150 nm. The features produced at 1 keV are equal to the apparent beam diameter, indicating that scattering effects of the beam contribute

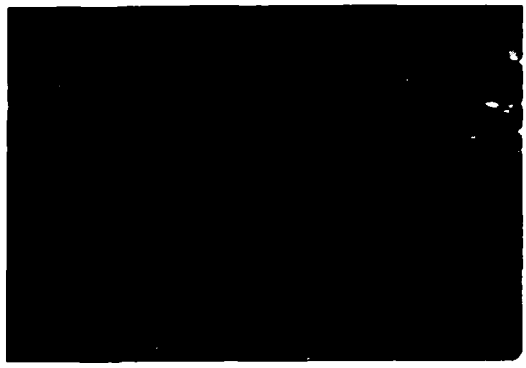

FIG. 2. Nucleated Fe feature produced at 1-keV-electron energy, $\sim 1\times10^{-5}$ Torr $Fe(CO)_5$. Beam diameter was ~ 300 nm. Larger crystallites are the result of spontaneous growth of Fe on the nucleated layer.

minimally to the size of the features produced. Spatial distributions of backscatter and secondary electron emission will be discussed in the next section.

Thermal decomposition of $Fe(CO)_5$ on the nucleated layer leads to rapid Fe growth as shown in Fig. 3. The isotropic nature of film growth over the nucleated layer leads to further broadening of the feature by an amount comparable to the film thickness. This is evident in the center of Fig. 3, where the $Fe(CO)_5$ pressure was suddenly decreased from 2×10^{-4} to 4×10^{-5} Torr. The decrease in feature width corresponds to an equivalent decrease in film thickness.

Low-energy electrons appear to be the most effective at producing a nucleated layer. Previous measurements have shown an overall increase in deposition yield with decreasing electron energy to 100 eV, the lowest we have measured. We have not yet attempted localized deposition below 1 keV, but at increasing electron energy nucleation fails to occur. No nucleation and growth was observed for primary energy of 19 keV.

It is not clear at the moment whether nucleation involves dissociation of adsorbed or gas phase $Fe(CO)_5$. Ford *et al.*[1] report that $Fe(CO)_5$ does not adsorb to clean Si, suggesting that the initial dissociation event may be in the gas phase, above the sample. However we observe no apparent spreading of the deposition profile due to the isotropic flux of dissociated species from the irradiated gas volume. In addition, no nucleation was observed when the beam was passed through the gas without striking the sample in the broad beam apparatus at the same pressure and temperature. It is possible that nucleation is occurring via adsorption of $Fe(CO)_5$ on the native SiO_2 film or on a contamination layer deposited by the electron beam. Indeed, Phillips *et al.*[12] have observed adsorption and decomposition of $Fe(CO)_5$ on graphite at 125 °C. In any case, we think it improbable that formation of the nucleated layer occurs by gas phase dissociation.

FIG. 3. Fe feature deposited at 3 keV. $Fe(CO)_5$ pressure was decreased from 2×10^{-4} to 4×10^{-5} Torr in the middle of the scan.

Aspects of Fe nucleation and growth that have not been fully explored as of yet are the enhancement of the spontaneous film growth by simultaneous electron bombardment leading to anisotropic growth of the deposit on the nucleated layer, and the possibility of a threshold electron dose for efficient nucleation. We have observed that an increase in the scan rate at constant current density and gas pressure results in smaller feature width. This perhaps indicates nucleation in the wings of the Gaussian beam profile above some threshold electron dose. These studies are continuing and will be reported in more detail later.

B. Modeling of low-energy electron scattering

Formation of the nucleated layer presumably occurs by electron-impact dissociation of $Fe(CO)_5$ adsorbed on or in the near vicinity of the surface. The rate of these dissociation events is given by Eq. (1):

$$\text{Rate}(x) = \int_0^\infty f(E,x)\sigma(E)N\,dE, \tag{1}$$

where $f(E,x)$ is the flux distribution of electrons passing through the surface plane as a function of their kinetic energy and position; (E) is the cross section for the dissociation event, and N is the density of $Fe(CO)_5$ adsorbed on the surface (or in the gas immediately above the surface). Contributions to the electron flux include the incident primary electrons as well as backscattered and secondary electrons emitted from the surface. Since dissociation cross sections typically have maxima at $\leqslant 100$ eV, it is likely that the major contribution to the dissociation rate will be the flux of low-energy backscatters and secondaries, rather than the relatively high energy primaries. The spatial and energy distribution of backscatters and secondaries are determined by the scattering characteristics of the primary electron in the solid. In order to estimate the limits to selective area processing using electron beams we must understand the scattering phenomena.

The purpose of the calculations presented here is to provide detailed information about the spatial and kinetic energy distributions of secondary and backscattered electrons produced at low primary electron energy. Convolution of the spatial profile with the measured beam diameters will yield electron flux profiles that can be used with Eq. (1) to give calculated film deposition profiles that can be compared to the above experiments. We address the electron flux profiles here.

Calculation of electron scattering in solids has been pursued vigorously in the context of electron microscopy, electron-beam lithography, and Auger electron spectroscopy.

The usual approach is to calculate scattering trajectories in the solid by a Monte Carlo technique using an electron interaction potential appropriate to the energy regime and some model of inelastic energy loss in the solid that causes the electron to eventually slow down. Backscattered electrons are simply those primaries that have undergone one or more large angle deflections in the solid and pass back through the surface plane. Secondaries are produced via inelastic impact ionization of valence shell electrons of the solid. Secondaries produced near the surface may eventually pass through the surface plane and be emitted.

Kotera *et al.*[13] have shown that at low-primary energies (<5 keV) the screened Rutherford cross section normally employed in electron scattering problems is no longer valid. In particular Monte Carlo models based on the Rutherford cross section show an increase in backscatter yield with decreasing primary energy, while experiment and calculations based on the Mott cross section show a decrease. Calculations by Goto *et al.*[14] show that backscattered electrons are especially productive in generating secondary electrons. Because of the importance of backscatters directly in the dissociation process and indirectly in the production of secondaries, an accurate model for elastic scattering at low energies is crucial for this problem.

We have developed a Monte Carlo program for scattering of low-energy primaries which employs the Mott scattering cross section,[15] and inelastic secondary electron generation using the Streitwolf excitation function.[16] Spatial, angular, and energy distributions of backscatter electrons are obtained straightforwardly by examination of the trajectories that re-emerge from the surface. The same parameters for secondary electrons are obtained via a detailed calculation of the secondary cascade, in the manner of Koshikawa *et al.*[17] Full details of the model calculations will be presented in a separate publication. Our intention here is to present illustrative results that can be used to evaluate the actual and potential performance of our selective area deposition experiments.

A qualitative feel for the extent of electron scattering in Si at low energy can be obtained by examination of the elastic scattering trajectories in Fig. 4, calculated at 250 and 2000 eV. In these calculations all primaries impact at normal incidence at a point in the center of the graph. The range of the 250 eV electrons in the solid is obviously quite small and scattering is confined to a volume very near the impact point. At 2000 eV the trajectories fill a much larger volume due to the greatly increased range. We are interested only in those electrons that pass through the surface plane. Trajectories that end in the solid, and energy loss in the solid, are presumably not important to the process of film nucleation on the surface. Qualitative examination of Fig. 4 shows that backscattered electrons at 250 eV are emitted only within a few nm from the impact site, while at 2000 eV the lateral spreading extends to approximately 40 nm.

More detailed radial distributions of backscattered and secondary emission (in yield/area) are shown in Fig. 5 for a primary energy of 3000 eV. The total secondary electron yield calculated for these conditions was 0.34 per incident electron. If we convolve the Gaussian primary-beam profile

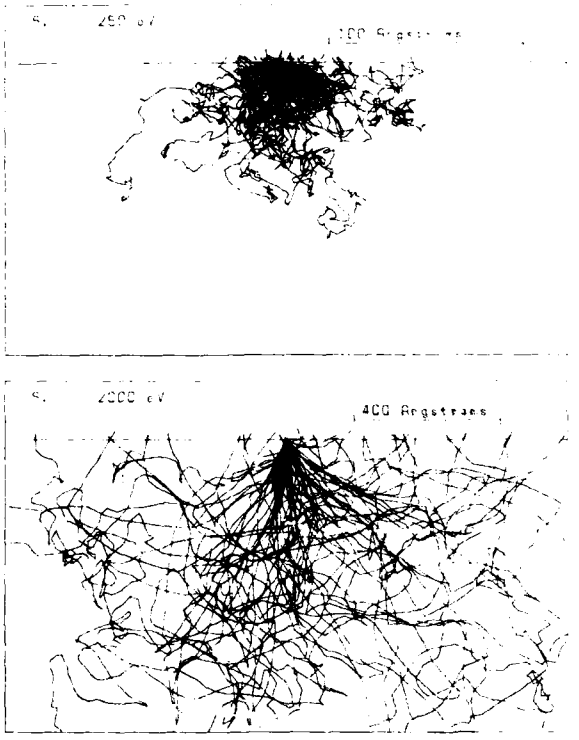

FIG. 4. Scattering trajectories for 250 and 2000 eV electrons in Si. Backscattered electrons are those trajectories that re-emerge from the surface.

with the calculated secondary radial distributions we obtain the radial flux distributions of low-energy electrons passing back through the surface. This convolution is shown in Fig. 6 at 3000 eV for nominal-beam diameter of 100 nm and a beam current of 50 pA. From this figure one can see that lateral spreading of the electron flux profile due to primary scattering is small. Beyond a radius of 70 nm the secondary electron flux is greater than the primary flux, and may play a

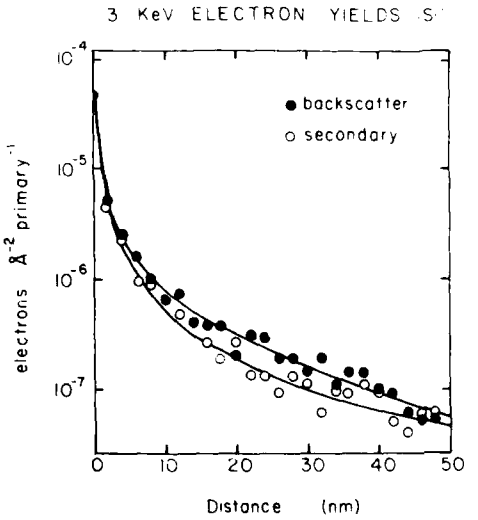

FIG. 5. Calculated backscatter and secondary yields per unit area as a function of distance from the primary impact for primary energy of 3000 eV. Total secondary yield is 0.34 per incident electron.

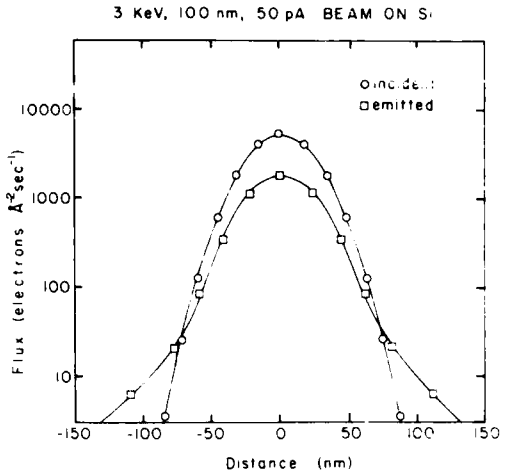

FIG. 6. Primary and calculated secondary electron flux per unit area as a function of distance from the center of the beam at primary energy of 3000 eV obtained by convolving the yield distribution of Fig. 5 with a nominal Gaussian beam diameter of 100 nm and current of 50 pA.

significant role out to > 100 nm. We do not know the probability of a nucleation event occurring per secondary electron. The experimental results show, however that a feature width of 150–180 nm is obtained for a beam diameter of 100 nm, suggesting that nucleation may indeed be effected by the low flux of secondaries in the wings of the emission profile. At energies < 3000 eV spatial broadening of the secondary emission profile is even less than demonstrated here and minimal broadening of the deposited feature is expected.

In order to complete the problem by integration of Eq. (1) to obtain the nucleation rate we need also to know the energy distributions of the backscattered and secondary electrons, and the energy dependence of the cross section for the nucleation event. Although the energy distributions of the backscatter and secondary electrons are obtained directly from the scattering model, we do not know the precise nature of the nucleation event, so this exercise is not warranted at the moment.

The results of these model calculations support our hypothesis that local-area deposition by low-energy electrons will not be severely limited by electron scattering. Chemical reactions that are driven by low-energy electron impact will proceed most efficiently at energies where the secondary emission coefficient is high and the spatial density of backscattered and secondary electrons is high. These conditions are satisfied at primary energies in the keV range. These advantages of low-primary energy are offset by the difficulty of producing high current, small spot beams at keV energy. High-brightness field-emission sources and high-numerical aperture objective lenses[18] for low-energy electron-beam lithography have been produced however, which should result in much better performance than we have been able to achieve in a standard (SEM).

Selective area deposition by focused ion beams has also been reported recently, which may have a direct relation to the electron-stimulated processes we have demonstrated. Shedd *et al.*, have demonstrated very high deposition yields of Au from gaseous organogold compounds using 15-keV-Ga^+ ion bombardment.[4] While high-energy ion impact is not expected to deposit significant energy to an adsorbed layer, the secondary electron yield resulting from inelastic energy loss can be as high as 10 per incident ion in this energy regime. If, indeed, surface reactions can be stimulated by low-energy secondary electrons, this may be the activating force for ion-beam deposition as well. We are currently investigating secondary electron emission from high-energy ion impact.

IV. SUMMARY

We have demonstrated selective area growth of Fe films from surface decomposition of $Fe(CO)_5$. Nucleation of a deposit is efficiently brought about by a low-energy electron-beam incident on the surface at moderate-gas pressure and electron dose. Spontaneous growth of Fe occurs on the nucleated layer at a temperature of ~ 125 °C, with no deposition occurring in unirradiated areas. Deposited feature widths are close to the measured beam diameters, apparently showing little if any effect of gas-phase decomposition or electron scattering in the solid. We have also developed a scattering program to model backscatter and secondary emission spatial profiles for low-energy electron impact. These calculations confirm that spatial spreading of deposition profiles due to scattering should be minimal in the keV energy range.

ACKNOWLEDGMENT

This work was supported by the National Science Foundation Grant No. DMR-851132.

[1]D. W. Hess, *VLSI-Electronics: Microstructure Science*, edited by N. Einspruch and D. M. Brown (Academic, New York, 1984), Vol. 8.
[2]T. B. Gorszyca and B. Gorowitz, *VLSI Electronics: Microstructure Science*, edited by N. Einspruch and D. M. Brown (Academic, New York, 1984), Vol. 8.
[3]D. J. Ehrlich and J. W. Tsao, J. Vac. Sci. Technol. B **1**, 969 (1983).
[4]G. M. Shedd, R. Lezec, A. D. Dubner, and J. Melngailis, Appl. Phys. Lett. **49**, 1584 (1986).
[5]J. I. Goldstein, D. E. Newbury, P. Echlin, D. C. Joy, C. Fiori, and E. Lifshin, *Scanning Electron Microscopy and X-ray Microanalysis* (Plenum, New York, 1981).
[6]L. F. Thompson and M. J. Bowden, *Introduction to Microlithography*, edited by L. F. Thompson, C. G. Willson, and M. J. Bowden (American Chemical Society, Washington, D.C., 1983).
[7]R. R. Kunz and T. M. Mayer, J. Vac. Sci. Technol. B **5**, 427 (1987).
[8]R. R. Kunz and T. M. Mayer, Mater. Res. Soc. Proc. (to be published).
[9]R. R. Kunz and T. M. Mayer, Appl. Phys. Lett. (to be published).
[10]H. R. Kaufmann and R. S. Robinson, J. Vac. Sci. Technol. A **3**, 1774 (1985).
[11]J. S. Foord and R. B. Jackman, Chem. Phys. Lett. **112**, 190 (1984).
[12]J. Phillips, B. Clausen, and J. A. Dumesic, J. Phys. Chem. **84**, 1814 (1980).
[13]M. Kotera, K. Murata, and K. Nagami, J. Appl. Phys. **52**, 997 (1981).
[14]K. Goto, K. Ishikawa, T. Koshikawa, and R. Shimizu, Surf. Sci. **47**, 477 (1975).
[15]A. C. Yates, Comput. Phys. Commun. **2**, 175 (1971).
[16]H. W. Streitwolf, Ann. Phys. Lpz. **3**, 183 (1959).
[17]T. Koshikawa and R. Shimizu, J. Phys. D **7**, 1303 (1974).
[18]Y. W. You, R. F. W. Pease, A. A Iranamesh, and K. J. Polasko, J. Vac. Sci. Technol. **19**, 1048 (1981).

Summary Abstract: Role of ions in carbon-film deposition by a windowless hydrogen lamp

M. Hanabusa and T. Kaneoka
Department of Electrical and Electronic Engineering, Toyohashi University of Technology, Tenpaku, Toyohashi 440, Japan

(Received 27 February 1987; accepted 7 May 1987)

Carbon films, either amorphous or crystalline, are attracting a great deal of attention recently. They are characterized by optical transparency, high electrical resistivity, chemical inertness, great hardness, and other favorable properties suitable for various applications. We have been interested in producing such films using photochemical-vapor deposition (photo-CVD), and in a previous work, a low-pressure mercury lamp was used to deposit carbon films from acetylene source gas.[1] The deposited films were soft and scratches were made easily with a pointed object like a needle. Comparing with the films prepared by other methods, in particular ionized deposition[2] and rf plasma CVD,[3] the inferior properties were attributed to the lack of accelerated ions.

The objective of the present work is to produce and make use of accelerated ions in photo-CVD and examine whether the same kinds of the favorable effects are produced on film properties as with the other deposition methods. Ions can be generated by photoionization in this photoinduced deposition method. Then, they can be accelerated simply by applying a proper bias to the substrate.

Acetylene is a good choice as the source gas for photo-CVD of carbon films. It can be photodissociated by light below 200 nm, and therefore the low pressure mercury lamp with its emission at 185 nm was good enough for deposition. For photoionization we need light below 108 nm. This explains why the films produced by the mercury lamp were soft. Therefore, we chose a hydrogen lamp in this experiment because it generates vacuum ultraviolet (VUV) light below 160 nm and emission is observed even at 90 nm. The apparatus is shown in Fig. 1. Hydrogen gas is excited by 2.45 GHz microwave power and continues to flow into a reaction chamber. Normally an optical window is used in photo-CVD to separate the light source from the reaction chamber. However, in the present work photons with short wavelengths are important, which cannot be transmitted through any window material without intensity reduction. The best choice of the material is LiF, but the transmission is reduced appreciably below 120 nm. Besides, the window surface is quickly covered by unwanted deposits in the chamber, and the amount of transmitted light is cut appreciably in a relatively short time. Therefore, we used the windowless method. It is to be cautioned that radicals are generated in discharge and they are transported into a reaction zone. Therefore, deposition may occur as the result of reactions induced by these radicals. However, it is known that the products of hydrogen dissociation give rise to favorable effects on deposition of carbon films. For amorphous films, hydrogenated films are as good as purely carbon films, and for diamond films, such radicals are known to selectively remove graphite in the deposit. Actually it turned out that light, rather than the radicals, plays a major role in the reactions in the present experiment, as described later.

Figure 2 shows the dependence of deposition rates on the bias voltage. They increase rapidly with the bias. We observed that ion currents originated from acetylene increased in a similar way with the bias. It means that accelerated ions are importantly involved in deposition. In this experiment,

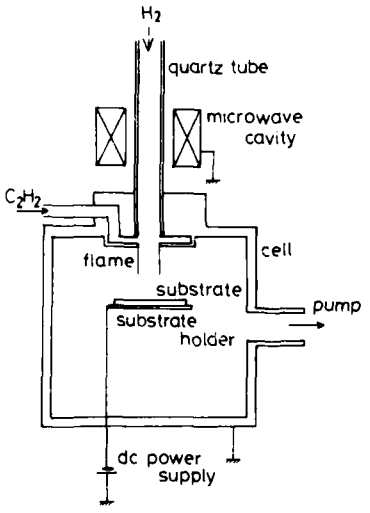

FIG. 1. Apparatus used for deposition of amorphous carbon films.

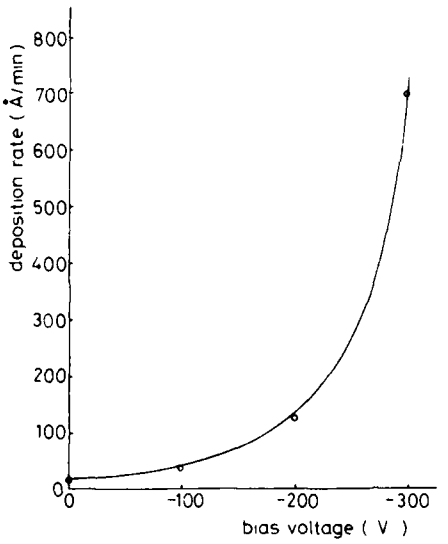

FIG. 2. Dependence of deposition rates on bias voltage.

 0734-211X/87/051432-02$01.00 © 1987 American Vacuum Society

the microwave input power was 200 W. The hydrogen flow rate was 120 ml/min. While the reaction chamber was evacuated with a 60 l/min rotary pump, the gas pressure in the chamber was 400 Pa. Acetylene was fed from the ring around the exit end of the quartz discharge tube at a flow rate of 5 ml/min. The silicon substrate, placed on a metal holder, was located 20 mm from the tube end or 45 mm from the lower end of the cavity. A negative bias voltage was applied to the substrate holder against the grounded stainless reaction chamber. The substrate was kept at room temperature.

The properties of the deposited films changed also with the bias. The films were soft without the bias, but when prepared with a bias of -300 V, they could hardly be scratched by the needle. Unfortunately, the films were too thin to be tested with a hardness meter. The refractive indices increased from 1.6 to 2.1. Also the chemical inertness was different; the hard films resisted a $HF-HNO_3$ (1–1) solution, while the soft films dissolved immediately in such a solution. The Raman spectra for the hard films were measured, which showed a broad peak centered around 1550 cm^{-1}. This peak is commonly observed in the so-called *i* carbons prepared by ion deposition or rf plasma CVD.

For comparison we reversed the polarity of the bias to examine the effect of accelerated electrons. No increase in deposition rates was observed, and the films remained soft. Unlike ions, electrons are useless to produce hard amorphous carbon films.

A question remains as to whether dissociation and ionization have been induced by photons or radicals. To answer this question, we used a hydrogen tube with a LiF window and deposited carbon films. On the other hand, when the discharge tube was bent between the microwave cavity and the reaction chamber so that light could not reach the chamber, deposition did not occur. From these experiments and others we conclude that light plays a major role in the reactions.

[1]M. Danno and M. Hanabusa, Mater. Lett. **4**, 261 (1986).
[2]T. Mori and Y. Namba, J. Appl. Phys. **55**, 3276 (1984).
[3]A. Bubenzer, B. Dischler, G. Brandt, and P. Koidl, J. Appl. Phys. **54**, 4590 (1983).

Summary Abstract: Ion-beam-induced deposition of gold by focused and broad-beam sources

A. D. Dubner, G. M. Shedd,[a] H. Lezec, and J. Melngailis
Research Laboratory of Electronics, Massachusetts Institute of Technology, Cambridge, Massachusetts 02139

(Received 20 April 1987; accepted 7 May 1987)

Ion-beam-induced deposition is a novel method of film growth in which an ion, incident on a substrate, decomposes a gas molecule, for example, an organometallic, leaving the metal atom on the substrate. Deposition of a film, which was a mixture of Al/C/O from a gas of $Al(CH_3)_3$ was first reported in 1984,[1] subsequently deposition of a Ta/C/O film from $Ta(OC_2H_5)_5$ and a W/O film from WF_6 were reported.[2] Some of these impurities are thought to be due to the background gas in the vacuum system. There is currently interest in depositing carbon from hydrocarbon gases because it can be used to repair clear defects in optical masks.[3–5] (See Table I for a summary of recent work.) Our experiments have used a capillary gas feed of dimethyl gold hexafluoroacetylacetonate ($C_7H_7F_6O_2Au$) and have induced gold deposition, on silicon and SiO_2, using a focused 15 KeV Ga^+ ion beam[6] as well as broad beams of 70 KeV Ar^+, 50 KeV Si^+ and 0.75 KeV Ar^+ (see Fig. 1).

Using the focused-ion beam (15 KeV Ga^+, 0.5 μm diameter) deposition patterns with width equal to the beam diameter were obtained. The yield observed was four to five atoms deposited per incident ion, however, the yield was found to be dependent on the scan rate.[3] Too low a scan rate led to depletion of the adsorbed gas and a drop in the yield. With the present focused-ion beam, deposition occurs at a rate of 1 μm^3 in 20 s. The films are 75% gold, 20% gallium, and $< 5\%$ carbon and oxygen. The gallium level is expected from the yield. The resistivity of this film was comparable to that of polysilicon i.e., 500 to 1300 $\mu\ \Omega$ cm (bulk gold is 2.4 $\mu\ \Omega$ cm). The alloying with gallium accounts for only part of this increase, i.e., from alloying we would predict a resistivity of 25 $\mu\ \Omega$ cm.

For the 70 KeV Ar^+ broad-beam experiments a differentially pumped chamber was placed in the end station of a low-current ion implanter. Yields of 100 atoms per ion were

TABLE I. Ion-induced deposition.

Gas (Reference)	Ion, Energy	Current Density (A/cm^2)	Yield (atoms/ion)	Deposit composition	Resistivity ($\mu\ \Omega$ cm)
$Al(CH_3)_3$ (1)	Ar^+ 50 KeV Au^+ 50 KeV		13	Al 20% O 16% C 64%	
$Ta(OC_2H_5)_5$ (2)	Ar^+ 50 KeV		27	Ta 56% O 27% C 17%	
WF_6 (RT) (2)	Ar^+ 50 KeV		31	W 75% O 25%	
WF_6 (80 K) (2)	Ar^+ 50 KeV		3800	high-oxygen content	
WF_6 (H. Lezec)	Ar^+ 750 eV	4×10^{-4}	5	W 90% O 5% C 5%	350 Bulk W = 4.6
Hydrocarbon (3–5)	Ga^+ 30 KeV		10	only carbon	
$C_7H_7F_6O_2Au$ (6)	Ga^+ 15 KeV (Focused ion beam)	0.05 scanned	4–5	Au 75% Ga 20% O < 5% C < 5%	500 to 1300 Bulk Au = 2.4
$C_7H_7F_6O_2Au$	Ar^+ 70KeV (Implanter)	7×10^{-6}	100	Au 60% O 5% C 35%	10 000
$C_7H_7F_6O_2Au$	Ar^+ 750 eV (Ion Miller)	4×10^{-4}	~ 1	Au 95% other < 4%	20
$C_7H_7F_6O_2Au$	Si^+ 50 KeV (Implanter)	7×10^{-6}	8–16	Au 75% O 10% C 10%	130

 0734-211X/87/051434-02$01.00 © 1987 American Vacuum Society

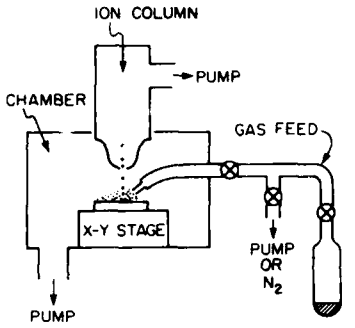

FIG. 1. Schematic of apparatus for focused-ion-beam-induced deposition.

obtained. The thickness of the deposited films varied linearly with dose (see Fig. 2), and the yield was found to be dependent on gas pressure. The composition of these films was 60% gold, 35% carbon, and 5% oxygen. The resistivity was correspondingly high: 10 000 $\mu\,\Omega$ cm. We have also deposited gold using 50 KeV Si^+ and 750 eV Ar^+. The results are summarized in Table I. The film deposited with 750 eV Ar^+ showed a composition of 95% gold and a resistivity of 20 $\mu\,\Omega$ cm. Future work will aim at combining the high yields of the broad-beam depositions with the resistivity of the focused and lower-energy ion-beam depositions, and on reducing the impurity content (O and C) by depositing in an ultrahigh vacuum system. The main applications of ion-beam-induced deposition are photomask or x-ray lithography mask repair, and circuit restructuring, customization, or repair. In addition, it appears to be a promising technique for deposition of both metals and insulators with submicrometer resolution.

Acknowledgments: This work was supported by Draper Laboratory, by the Defense Advanced Research Projects Agency/Office of Naval Research (Contract No. N00014-84-K-0073), and by Nippon Telegraph and Telephone.

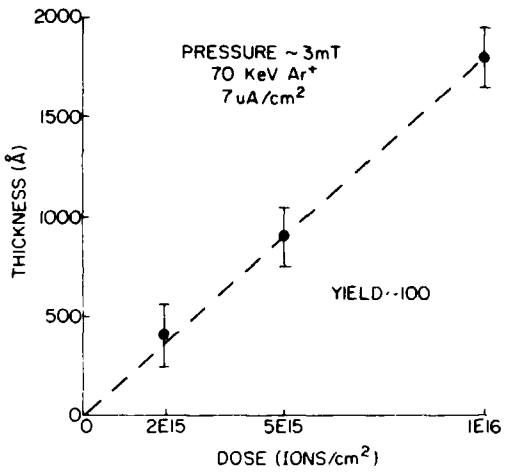

FIG. 2. Plot showing gold film thickness as a function of dose. The gas used was $C_7H_7F_6O_2Au$. Depositions were done with 70 KeV Ar^+ ions from an ion implanter.

[a] Present address: Dept. of Material Engineering, North Carolina State University, Raleigh, NC 27695.

[1] K. Gamo, N. Takakura, N. Samoto, R. Shimizu, and S. Namba, Jpn. J. Appl. Phys. **23**, L293 (1984).
[2] K. Gamo, D. Takehara, Y. Hamamura, M. Tomita, and S. Namba, Microelectron. Eng. **5**, 163 (1986).
[3] J. R. A. Cleaver, H. Ahmed, P. J. Heard, P. D. Prewett, G. J. Dunn, and H. Kaufman, Microelectron. Eng. **3**, 253 (1985).
[4] N. Economou, D. Shaver, and B. Ward, in Proceedings of the SPIE Conference, Santa Clara, March 1987 (to be published).
[5] M. Yamamoto, M. Sato, H. Kyogoku, K. Aita, Y. Nakagawa, A. Yasaka, R. Takasawa, and O. Hattori, SPIE **632**, 97 (1986).
[6] G. M. Shedd, H. Lexec, A. D. Dubner, and J. Melngailis, Appl. Phys. Lett. **49**, 1584 (1986).

Synchrotron radiation-excited chemical-vapor deposition and etching

Tsuneo Urisu and Hakaru Kyuragi
NTT Electrical Communications Laboratories, 3-1, Morinosato Wakamiya, Atsugi-shi, Kanagawa Pref., 243-01 Japan

(Received 12 March 1987; accepted 26 May 1987)

Photoexcited chemical-vapor deposition (CVD) and etching using synchrotron radiation as an exciting light source were experimentally demonstrated. CVD of silicon nitride film and etching of Si and SiO_2 by $SF_6 + O_2$ gases are described in detail. In several reaction systems, it was found that the surface photoexcitation was an important mechanism. Reaction models for gas-phase excitation and surface excitation were proposed.

I. INTRODUCTION

In recent years, research on photoexcited semiconductor processes[1-8] has been conducted actively in many places, with a view to their use as new processing techniques which have the characteristics of low temperature, low damage, low contamination, and high controllability. These characteristics are becoming increasingly necessary as the dimensions of large-scale integrated circuits (LSIs) and microdevices decrease. An important problem with photoexcited semiconductor processes is the matching of the photon energy and the molecular absorption energy. There are two approaches to solving it. One is to design the absorption energy of reaction molecules to match the photon energy of efficient light sources such as lasers.

The other approach is to control the photon energy of the light source to match the molecular absorptions. Most gas molecules commonly used in the conventional semiconductor processes have strong absorptions in the VUV (vacuum ultraviolet) range.[9] Accordingly to these facts, photochemical vapor deposition experiments using VUV discharge lamps[10] have been conducted.

In these experiments, however, the intensity of the light source seems to be rather insufficient. On the other hand, synchrotron radiation is a unique light source in the range from x-ray to VUV, having such excellent characteristics as strong intensity, good directivity, and wavelength continuity. Owing to recent technical developments in this type of apparatus, the intensity, lifetime, and stability have become high enough for its applications to the light source for photoexcited processes.

In the present work, several experiments of photoexcited CVD and etching using synchrotron radiation have been conducted and its feasibility as a light source to the photoexcited semiconductor processes has been examined.

II. EXPERIMENTAL SETUP

Experiments were conducted using the 2.5-GeV-storage ring at the photon factory of the National Laboratory for High Energy Physics. Figure 1 shows a schematic diagram of the beam line and the reaction chamber. In the VUV range, there is no transparent material, which can be used as a window for the reaction chamber. So, the difference between the high vacuum of the beam line, and the high pressure of the reaction chamber was maintained by differential vacuum pumping. At the entrance port of the reaction chamber, the vacuum gradient is about two orders of magnitude over a distance of about 18 cm. A fast closing valve and a number of pneumatic valves and pressure gauges are set in the beam line, and these are controlled by an interlock system. The emitted beam is reflected by a toroidal mirror with a grazing incident angle of 4 deg and focused in the reaction chamber at about 30 m from the emitting source. Inside of the reaction chamber, a molybdenum block holding the substrate is placed in a small heating furnace, which controls the temperature of the block. The substrate and molybdenum block are inserted into the reaction chamber using an airlock system. Monochromater was not used in the beam line and the spectrum distribution of the radiation beam was from about 10 A to a thousand few hundred A with a peak at about 30 A. The cross section of the beam at the reaction chamber was about 5×10 mm and the total power of the incident beam was about 2W.

III. DEPOSITION AND ETCHING

Table I shows the reaction systems we have examined up to now and their deposition or etching rates.

With the silane and silane plus nitrogen systems, the deposition of amorphous silicon film was observed.[11] With the hydrogen chloride systems, it has been reported that laser excitation induces etching.[1] However, very slow deposition was observed in the irradiation with synchrotron radiation. In the SF_6 and SF_6 plus O_2 systems, the etching of Si and SiO_2 was observed. Carbon film was observed to be etched in

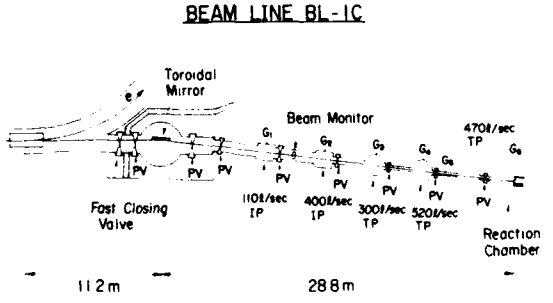

FIG. 1. Schematic diagram of the beam line and the reaction chamber. PV: pneumatic valve; IP: ion pump; TP: turbomolecular pump; G: vacuum gauge

 0734-211X/87/051436-05$01.00 © 1987 American Vacuum Society

TABLE I. Reaction systems and results.

Reaction Gases (Pressure, Torr)	Substrate (Temperature)	Results (Deposition or Etching Rate/100 mA)
SiH_4 (0.1)	Si, SiO_2 (100~400 °C)	Depo. Si: H film (~2 Å/min)
$SiH_4 + N_2$ (0.02/0.1)	Si, SiO_2 (100~400 °C)	Depo. $Si_xN_yH_z$ film (~4 Å/min)
HCl (0.1)	Si, SiO_2 (RT)	Depo. Cl containing film (~0.5 Å/min)
$HCl + O_2$ (0.1/0.02)	Si, SiO_2 (RT)	Depo. Cl containing film (~0.5 Å/min)
SF_6 (0.1)	Si, SiO_2 (RT)	Etching (Si: ~15 Å/min, SiO_2: ~15 Å/min)
$SF_6 + O_2$ (0.1/0.01)	Si, SiO_2 (RT)	Etching (Si: ~0 Å/min, SiO_2: ~14 Å/min)
O_2 (0.1)	C (RT)	Etching (~18 Å/min)

oxygen.[12] In the following, the silicon nitride film deposition and the etching by the SF_6 systems will be described in some detail.

A. Deposition of $Si_xN_yH_z$ Films

Hydrogen containing silicon nitride film is used as a passivation film in metal-organic semiconductor field-effect transistors (MOSFETs). In this application, it has been reported that the hydrogen contained in the film causes some degradation of the transistors.[13] In laser or mercury lamp excited CVD, a gas mixture of disilane or silane and ammonia is used as the reaction gas.[14,15] But with synchrotron radiation, a mixture of silane and nitrogen can be used, since VUV photons from the synchrotron can decompose or ionize molecules of these gases, efficiently. The use of nitrogen instead of ammonia should reduce the hydrogen content.

Figure 2(a) shows the pattern profile of a deposited silicon nitride film. The incident beam had a diameter of 1 mm limited by the orifice set 1 cm above the substrate and was perpendicular to the substrate surface. It is clear that deposition occurs preferentially on the irradiated area. In order to find out how the deposition occurs, the intensity distribution of the incident beam, which determines the profile in the case of surface excitation, and also the deposition pattern for gas phase excitation were calculated and compared to the observed profile in Fig. 2(b). The intensity distribution of the incident beam was calculated and based on the Fresnel diffraction equation considering the spectrum distribution. The deposition pattern for the gas-phase excitation mechanism was numerically calculated based on the idea given in Ref. 16. It is obvious that the observed profile corresponds quite closely to the surface excitation curve, although the reason for the disagreement with the fine oscillation profile is not clear.

From these data, it is concluded that surface excitation plays an important role in deposition. In this reaction system, deposition can also be attributed in part to gas phase excitation mechanisms, since it was observed even when the incident beam was parallel to the substrate surface, although the rate was slower than for the perpendicular arrangement. The hydrogen content of the deposited film was determined from the infrared absorption spectrum.[17] The composition of the source gas was changed in order to see how the hydrogen content varies with the composition of nitrogen and silicon in the film. As shown in Fig. 3, the hydrogen content decreased with increasing nitrogen content. For comparison, reported values of the hydrogen content in mercury lamp excited CVD film[15] and in plasma CVD film[18] are given in the same figure. This shows that silicon nitride films with a relatively low-hydrogen content can be obtained with synchrotron radiation CVD. Our analysis at present is insufficient to pinpoint the exact reason for this. But it is speculat-

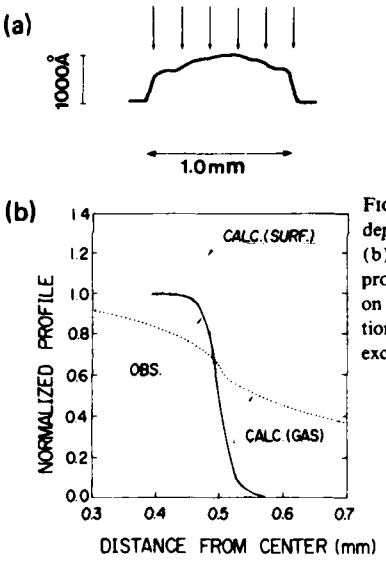

FIG. 2. (a) Pattern profile of deposited silicon nitride film. (b) Comparison of observed profile with profiles calculated on the basis of surface-excitation mechanism and gas-phase excitation mechanism.

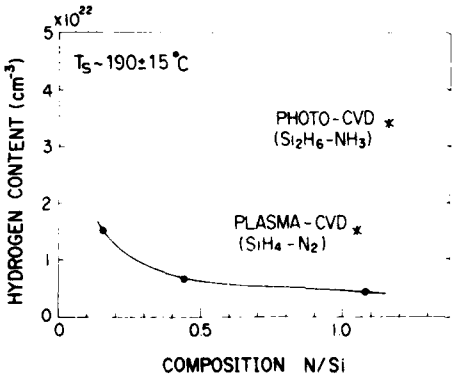

FIG. 3. Dependence of hydrogen content on N/Si composition of deposited $Si_xN_yH_z$ film. T_s is substrate temperature.

ed that one reason might be the use of nitrogen instead of ammonia, and another reason might be the desorption of hydrogen from the film due to irradiation during deposition.

B. Etching on Si and SiO_2

The etching systems, $SF_6 + O_2$/Si or SiO_2, are important because they are commonly used in plasma etching.[19] Our main interest in them is a comparison with plasma etching.

The experimental setup was the same as that for CVD. The substrate was mounted on the molybdenum block and the radiation beam impinged perpendicularly on to the substrate surface.

Figure 4 shows the observed dependence of the etching rate on the oxygen content. The pressure of SF_6 was 0.1 Torr. Without oxygen, both silicon and SiO_2 were etched at an almost equal rate. The etching rate of the SiO_2 decreased slightly with the addition of oxygen, but the etching rate of Si drops rapidly to zero with the addition of just a slight amount of oxygen. This phenomenon is very interesting especially when it is compared with the results for plasma etching.[19]

In the $SF_6 + O_2$ plasma etching system, the etching rate of Si is a few tens of times larger than that of SiO_2 and it increases even more when oxygen is added. This tendency is completely different from synchrotron radiation etching.

Another important feature is found in the profiles of an etched pattern. Figure 5 shows the observed depth profiles of patterns etched on SiO_2 and Si without oxygen. In the case of SiO_2, etching occurs only in the irradiated area, which means that etching proceeds only by means of surface photoexcitation. The sampe profile was obtained when oxygen was added. On the other hand, in the case of Si, the etching occurs over a broad area, which means that gas phase excitation is dominant.

Figure 6 shows a pattern etched on SiO_2 observed with scanning-electron microscope (SEM). Polysilicon film with a thickness of about 1600 A was deposited on SiO_2 as an etching mask. For surface photoexcitation reactions, the etching rate depends on the surface density of the adsorbed molecules and the intensity distribution of the photon flux. In this photograph, the side wall of the pattern clearly shows no undercutting, which reflects the good directivity and short wavelength nature of the synchrotron-radiation beam.

Furthermore, it should be pointed out that the irregular fine structure of the polysilicon mask pattern has been transferred to the silicon dioxide below with a resolution of less than a few hundred angstroms. This indicates that the diffusion of the photon energy absorbed by the surface is negligible.

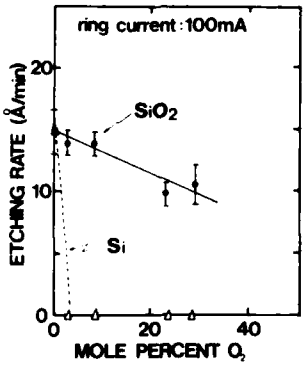

FIG. 4. Observed dependence of etching rate on oxygen content $[O_2]/([SF_6] + [O_2])$. The pressure of SF_6 was 0.1 Torr.

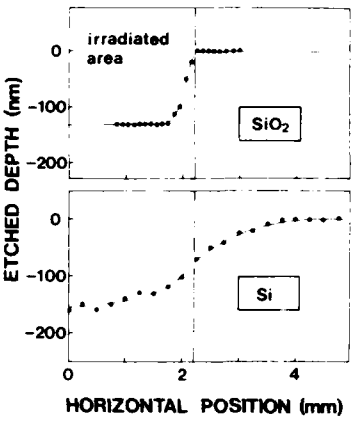

FIG. 5. Observed etched-depth profile. The pressure of SF_6 was 0.1 Torr.

It has been reported that fluorine atoms or ions are the key species in plasma etching. However, the results obtained here indicate that the etching mechanisms for synchrotron radiation excitation are quite different. We speculate that a photoinduced reaction between SiO_2 and chemisorbed-sulfur–fluoride molecules plays an important role in this SiO_2 etching.

IV. REACTION MODELS

The reaction mechanisms are extremely complex both for etching and for deposition, since many kinds of fragment radicals, atoms, and ions are produced by excitation, and there are a large number of possible chemical reactions. Therefore, here, instead of making a detailed analysis of the mechanisms, some reaction models are presented.

The possible excitation mechanisms can be categorized as (1) gas-phase excitation; (2) surface excitation, and (3)

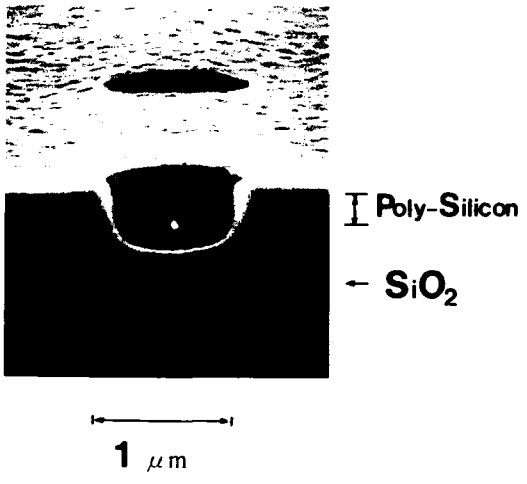

FIG. 6. Etched pattern on SiO_2 observed with SEM. The etching mask was polysilicon film deposited on SiO_2.

thermal excitation. In the present case, the incident power density was only about 4 W/cm^2, so the thermal-decomposition mechanism can be ignored. Contribution of photoelectrons to the excitation is discussed later.

The reaction model for gas-phase excitation shown in Fig. 7 is relatively simple. For etching, gas molecules are decomposed by synchrotron radiation. The fragment active species arrive at the substrate surface and react with the substrate atoms. Then the resulting compound evaporates. Therefore, the etched pattern is rather broad in the case of gas-phase excitation. The same reaction model is applicable to CVD except that the resulting compound remains on the surface.

The reaction model for surface excitation shown in Fig. 7 is as follows: Since the Van der Waals adsorption is negligible in the present temperature range, it can reasonably be assumed that the adsorbed layer is formed by chemisorption, which implies that excitation occurs in a surface-adsorbed monolayer or in a substrate-surface layer. The etching proceeds through photoinduced chemical reactions between adsorbed molecules and substrate molecules.

A similar model explains deposition. In this case, stable gas-phase molecules are chemisorbed to active sites on the surface. Then the chemisorbed molecules are decomposed by the VUV radiation, and an active site is generated again.

So, the reaction model for surface excitation is characterized by chemisorption and photostimulated chemical reactions in the adsorbed monolayer on the surface.

According to these reaction models, equations giving deposition or etching rates are derived in the following for the most simple cases ignoring effects of secondary reactions between fragment species and stable molecules and effects of photoelectrons.

The rate of excitation γ (1/s,cm^3 for gas-phase excitation and 1/s,cm^2 for surface excitation) is given by

$$\gamma = N \int P(\lambda)\sigma(\lambda)/S d\lambda,$$
$$= \mu N, \qquad (1)$$

where N is the density of gas-phase molecules in the case of gas-phase excitation and the surface density of the adsorbed molecules in the case of surface excitation, $P(\lambda)$ (photons/s,cm) is the total photon flux at wavelength $\lambda \sim \lambda + d\lambda$ $\sigma(\lambda)$ is the excitation cross section of the active species and S is the cross sectional area of the photon beam. Here, we name a new term $\mu = \int P(\lambda)\sigma(\lambda)/S d\lambda$ excitation efficiency.

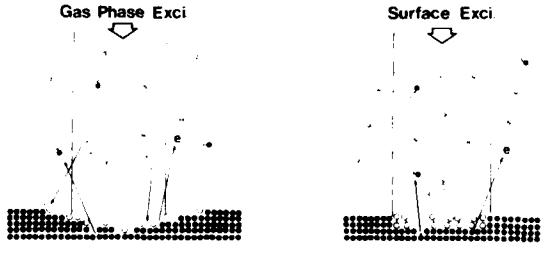

FIG. 7. Reaction models for gas-phase excitation and surface excitation.

The number f (1/s,cm^2) of fragment species arriving at the center unit area of the beam on the surface, expressed by a cylindrical coordinate (r,z,ϕ), is[16]

$$f = \int \frac{\gamma z}{4\pi(r^2 + z^2)^{3/2}} r\, dr\, dz\, d\phi \quad . \qquad (2)$$

Therefore, the etching or deposition rate R_g for the gas-phase excitation at the beam center ($r = 0$) is

$$R_g = \eta(\mu N r_0/2N_f), \qquad (3)$$

where η is the reaction yield of the active species, r_0 is the beam radius and N_f is the density of atoms for the deposited film or for the etched substrate.

The rate of etching or deposition R_s for the surface excitation is given by

$$R_s = \theta\gamma a_0/N_s = \theta\mu a_0, \qquad (4)$$

where N_s is the surface atom or molecule density of the etched substrate or the depositing film and a_0 is the thickness of the surface monolayer of the deposited film or of the etched substrate.

Using Eqs. (3) and (4), the etching rates corresponding to the present experiments of SF_6/SiO_2, Si systems ($N = 3.5 \times 10^{15}$/cm^3, $r_0 = 0.4$ cm, $N_f = 5.2 \times 10^{22}$/cm^3, $a_0 = 3 \times 10^{-8}$ cm and $S = 0.5$ cm^2) were calculated.

Photon flux $P(\lambda)$ was calculated based on the equation derived by Schwinger,[20] considering the reflectivity of toroidal mirror and effects of absorption by the reaction gases. Since the active species have not as yet been identified and their partial cross sections of the excitation have not been measured, the rates have been calculated using the reported values for the total ionization cross section,[9] and assuming that $\eta = 1.0$ and $\theta = 1.0$. Furthermore, it has been assumed in the calculation that the total ionization cross section values for the gas phase molecules SF_6[9] are valid for the chemisorbed species.

In truth, the chemisorbed species may not have the form SF_6. It is also possible that incident photon is absorbed not by the chemisorbed species but by the substrate molecules (SiO_2). However, the above assumption may be allowed as an order of magnitude estimates, since total absorption cross section values in VUV do not differ so much among many simple gas molecules.

The calculated values are given in Table II (storage ring current is 100 mA). Taking into consideration the fact that these calculated values are only order of magnitude estimates, the agreement between the calculated and the ob-

TABLE II. Comparison of calculated and observed etching rates.

Reaction system		Calc.	Obs.
Si by SF_6 (Gas phase exc.)	$\mu = 0.24$ /s ($\mu_{valence} = 0.16$)	19.3 Å/min	15 Å/min
SiO_2 by SF_6 (Surface Exc.)	($\mu_{core} = 0.08$)	43.2 Å/min	15 Å/min

served values is rather good. So, the reaction model described above seems to give a fairly accurate picture of the actual reaction mechanisms involved.

The ionization-cross-section spectrum can be roughly separated to two parts, one is due to excitation of valence electrons and another is due to core electrons.[9] So, excitation efficiency corresponding to valence electrons, μ_{valence} and that correspond to core electrons, μ_{core} can be evaluated separately. The values of μ_{valence} and μ_{core} shown in Table II, indicate that not only the excitation of the valence electrons but also the core electrons possibly contribute to the etching.

Photoelectrons emitted from the substrate can excite the gas phase and adsorbed molecules. The excitation efficiency μ_e for the excitation by photoelectrons is also defined by replacing $P(\lambda)$ by a flux of photoelectrons and σ by the excitation cross section with electrons. The flux of the photoelectrons is calculated from the incident photon flux, the ionization cross section of the substrate atoms and the escape depth of the photoelectrons. The calculated value of μ_e was about an order of magnitude smaller than μ shown in Table II, indicating minor contribution of photoelectrons. In these calculations, however, contributions of secondary electrons and negative ion formations were not considered. So, more detailed investigations are required to evaluate the contribution of photoelectrons precisely.

V. CONCLUSIONS

The feasibility of synchrotron radiation excited CVD and etching was experimentally demonstrated. The results obtained were quite different from those for other methods. In the CVD of silicon nitride film, it was found that the hydrogen content in the film was fairly low. In the etching of Si and SiO_2 by $SF_6 + O_2$ gas, the etching selectivity was completely different from that of conventional plasma etching.

In several reaction systems, it was found that surface photoexcitation was an important mechanism, and the reaction model characterized by chemisorption and photostimulated chemical reaction in the chemisorbed monolayer was proposed to explain the results. Fairly good agreement was obtained between the calculated and observed etching rates.

ACKNOWLEDGMENTS

The authors would like to thank Mamoru Kondo, Norihiko Ohwada, Toyoki Kitayama, and Akira Yoshikawa for their encouragement and discussions. Thanks are also given to the staff of the Photon Factory of the National Laboratory for High Energy Physics for their help in experiments and discussions.

[1] D. J. Ehrlich, R. M. Osgood, Jr., and T. F. Deutsch, Appl. Phys. Lett. **38**, 1018 (1981).
[2] T. J. Chuang, J. Vac. Sci. Technol. **18**, 638 (1981).
[3] D. J. Ehrich and J. Y. Tsao, J. Vac. Sci. Technol. B **1**, 969 (1983).
[4] P. D. Brewer, D. McClure, and R. M. Osgood, Jr., Appl. Phys. Lett. **47**, 310 (1985).
[5] S. Yokoyama, Y. Yamakage, and M. Hirose, Appl. Phys. Lett. **47**, 389 (1985).
[6] T. J. Chuang, J. Vac. Sci. Technol. B **3**, 1408 (1985).
[7] G. M. Reksten, W. Holber, and R. M. Osgood, Jr., Appl. Phys. Lett. **48**, 551 (1986).
[8] S. Higashi, G. E. Blonder, and C. G. Fleming, in *Proceedings of the 8th Symposium on Dry Process* (The Institute of Electrical Engineers of Japan, Tokyo, 1986), p. 120.
[9] J. Berkowitz, *Photoabsorption, Photoionization, and Photoelectron Spectroscopy* (Academic, New York, 1979).
[10] G. G. A. Perkins, E. R. Austin, and F. W. Lampe, J. Am. Chem. Soc. **101**, 1109 (1979).
[11] H. Kyuragi and T. Urisu, *Late News Abstract of the 18th International Conference on Solid State Devices and Materials* (The Japan Society of Applied Physics, Tokyo, 1986), p. 727.
[12] H. Kyuragi and T. Urisu, Appl. Phys. Lett. **50**, 1254 (1987).
[13] R. B. Fair and R. C. Sun, IEEE Trans. Electron Devices, **28**, 83 (1981).
[14] P. K. Boyer, G. A. Roche, W. H. Ritchie, and G. J. Collins, Appl. Phys. Lett. **40**, 716 (1982).
[15] H. Okuhira and A. Shintani, in *Proceedings of the 87th Meeting of Crystal Technology Session in the Japan Society of Applied Physics* (in Japanese) (The Japan Society of Applied Physics, Tokyo, 1986), p. 23.
[16] T. H. Wood, J. C. White, and B. A. Thacker, Appl. Phys. Lett. **42**, 408 (1983).
[17] W. A. Lanford and M. J. Rand, J. Appl. Phys. **49**, 2473 (1978).
[18] S. Fujita, N -S. Zhou, and A. Sasaki, Jpn. J. Appl. Phys. **22**, L100 (1983).
[19] R. d'Agostino and D. L. Flamm, J. Appl. Phys. **52**, 162 (1981).
[20] J. Schwinger, Phys. Rev. **75**, 1912 (1949).

Summary Abstract: Nucleation considerations in the wavelength-dependent activation selectivity of aluminum chemical-vapor deposition

G. S. Higashi, G. E. Blonder, C. G. Fleming, V. R. McCrary, and V. M. Donnelly
AT&T Bell Laboratories, Murray Hill, New Jersey 07974

(Received 10 April 1987; accepted 8 June 1987)

Projection-patterned-laser deposition is an alternative to focused-beam writing in the growth of patterned films for microelectronic applications. Focused-beam writing has the advantage of extreme flexibility because it allows discretionary patterning, while the projection-patterned-deposition technique offers high throughput for the repetitive processes encountered in mass production.

However, projection-patterned-laser deposition processes are more difficult to implement because all photoreactions are necessarily confined to surface species.[1,2] Only in this way can high-resolution patterns with good spatial selectivity be maintained. Otherwise, gas-phase diffusion of reaction products cause unwanted depositions to occur.

Building on the original ideas of Tsao and Ehrlich,[3] we have recently developed a technique where patterned-laser illumination is used to photochemically activate the growth of high-quality Al-thin films (resistivities $\sim 5\ \mu\ \Omega$ cm) via pyrolysis of triisobutylaluminum (TIBA).[1,2] The laser-activation step is performed at a substrate temperature of 250 °C under an ambient of flowing TIBA at ~ 100 mTorr. Immediately following the laser exposure (20 mJ/cm^2 at 100 Hz for 600 s), no visible deposit is apparent on the wafer. The deposited pattern only becomes apparent after several minutes of sitting at this elevated temperature under vapors of TIBA. Once initiated, the film grows indefinitely at a rate of ~ 2 Å/s via thermal decomposition of the TIBA molecule. Thus, films on the order of a micron in thickness can be produced in a period of about an hour. We have achieved pattern resolutions of 2 μm and extremely high-spatial selectivities ($\gtrsim 10\,000{:}1$), using radiation at 248 nm. An example of such a deposit on a glass substrate is shown in Fig. 1. Since the laser-activation step is performed under a pressure of ~ 100 mTorr of TIBA, gas-phase mean-free paths for photoproducts are $\sim 300\ \mu$m. Thus, one clearly sees that adlayer photoreactions must be dominating the activation process since features are reproduced which are much smaller than any gas-phase-diffusion lengths. In addition, since surface transient temperature rises are limited to < 10 °C on transparent substrates, the laser-induced reactions we observe must be nonthermal in nature.

Thus we see that surface photolysis plays the major role in the growth activation process at 248 nm. Under identical circumstances (e.g., reactor pressure, substrate temperature, laser fluence) using 193-nm radiation, the deposit shown in Fig. 2 is obtained. Here, a great deal of our spatial control of over the growth of Al is lost. It is apparent that gas-phase photolysis leads to random deposits capable of nucleating growth. These deposits appear hundreds of microns away from the laser-irradiated area, resulting from vapor-phase diffusion and transport of reactive species.

A clearer understanding of this result is obtained by studying the gas-phase absorption cross section of this molecule, shown in Fig. 3. Plotted is the optical density [i.e., log(base 10) of the absorptance] of 400 mTorr of TIBA in a 7.5-cm long-fused silica absorption cell. As can clearly be seen, although the absorption cross section is large at 193 nm ($\sim 2\times 10^{-17}$ cm^2), the cross section at 248 nm is negligibly small. We place an upper limit on the TIBA cross section at 248 nm of 10^{-19} cm^2. Thus, the flux of photoproducts raining down from the gas phase must be at least 100 times greater at 193 nm than at 248 nm. Consequently, the selectivity degradation can be understood simply, as arising from the difference in the flux of photoproducts arriving at the surface. This result can be analyzed more quantitatively by comparing our observations with classical nucleation theory.

In classical nucleation theory,[3-5] where one considers the nucleation of stable clusters of atoms from the vapor phase, the nucleation rate is found to be extremely superlinear with the incoming flux or supersaturation ratio (the ratio between the pressure of atoms in the vapor-phase P and the equilibirum vapor pressure of these atoms P_0). This nonlinearity occurs because the supersaturation ratio, appears in the free energy ΔG_c to create clusters of critical size. Recall, that this free energy is calculated by considering the competition between the bulk-free energy of a cluster, scaling as r^3, and the surface-free energy or surface tension of a cluster, scaling as r^2, where r is the radius of the cluster. The free energy of such a cluster peaks at a critical size, above which, the cluster is stable and grows indefinitely, below which, the cluster is unstable and vaporizes. This critically sized cluster has an energy given by Eq. (1),

FIG. 1. Scanning-electron micrograph of KrF (248 nm) laser-activated patterned-Al film.

 0734-211X/87/051441-03$01.00 © 1987 American Vacuum Society

FIG. 2. Scanning-electron micrograph of ArF (193 nm) laser-activated patterned-Al film.

$$\Delta G_c = \frac{16\pi}{3}\frac{\sigma^3 v^2}{(kT)^2 \ln(P/P_0)^2} C. \tag{1}$$

Here, σ is the free energy per unit area of surface, v is the volume occupied by an atom in the bulk, k is Boltzmann's constant, and T is the absolute temperature in Kelvin. The term $(kT)\ln(P/P_0)$ is simply the free energy for removing an atom from the bulk and placing it in the gas phase. C is a correction factor, which accounts for the interfacial energy between the cluster and the surface, and if a spherical cap nucleus is assumed, varies between 0 and 1 depending upon whether the nucleus wets or does not wet the surface. Thus, clusters must surmount ΔG_c in order to be stable. Clearly, the rate of formation R of stable clusters must be proportional to a Boltzmann factor of ΔG_c. Then, since the supersaturation ratio appears in ΔG_c, one sees why the nucleation rate R varies so strongly with the flux. The full expression for the nucleation rate during the initial stage of nucleation is written in Eq. (2),

$$R = \left(\frac{F}{\nu_0} e^{\Delta G_{\rm des}/kT} a_0 \nu_0 e^{-\Delta G_{\rm diff}/kT} \sigma_{\rm lin}\right) \times \left(\frac{F}{\nu_0} e^{\Delta G_{\rm des}/kT} e^{-\Delta G_c/kT}\right), \tag{2}$$

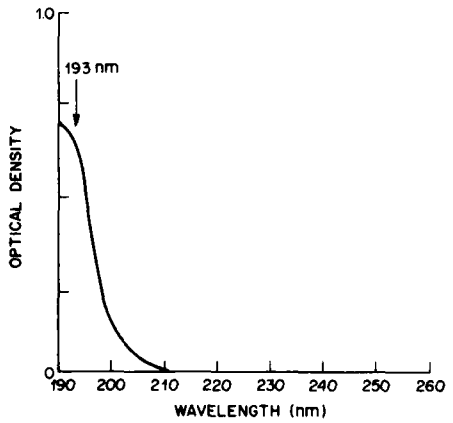

FIG. 3. Ultraviolet-absorption spectrum of triisobutylaluminum.

where $\Delta G_{\rm des}$ and $\Delta G_{\rm diff}$ are the free energies for desorption and diffusion on the initial surface, respectively. F is the flux of atoms incident on the surface ($P/\sqrt{2mkT}$ for an ideal gas), ν_0 is the vibrational frequency of an atom on the surface and $\sigma_{\rm lin}$ is the linear cross section of the critically sized cluster. The flux incident on the surface divided by the vaporization rate gives the surface coverage in steady state. Thus, the second term in Eq. (2) represents the coverage multiplied by a Boltzmann factor of ΔG_c, or the number density of critically sized nuclei. The first term is simply the rate at which atoms on the surface collide with critical nuclei to produce stable nuclei.

If classical nucleation theory was in fact applicable to this system, it would also predict an increase in the nucleation rate from gas-phase photoproducts at lower-substrate temperatures. This occurs because the supersaturation ratio increases dramatically as one decreases the temperature. We have checked this prediction experimentally by lowering the substrate temperature to 200 °C during the 248-nm laser-activation step and then raising it back to 250 °C again to grow. This results in such a high degree of nucleation from gas-phase photoproducts that no pattern can be discerned in the deposit. A dot 300 μm in diameter is deposited instead. Before trying to evaluate this result, one should note that for a chemically activated surface reaction, rates always decrease with decreasing temperature. Thus, the aggregate-nucelation model apparently gives a favorable description of our observations. There is one caveat, however; although the model correctly predicts the selectivity loss at both 193 nm (250 °C) and 200 °C (248 nm), it would have predicted the loss at 193 nm (250 °C) should have been much more severe than the loss at 200 °C (248 nm). This result should not be overinterpreted, however, since the classical theory of nucleation, as applied here, deals with Al atoms impinging from vapor phase and Al-cluster formation, whereas formation of Al atoms by single-photon photolysis of TIBA is energetically unfeasible. Al hydrides or partially reacted TIBA are the more likely photoproducts participating in the nucleation process.

We have yet to identify the mechanism for the surface activation at 248 nm and 250 °C. If the gas-phase driven reaction is related to the formation of critically sized nuclei, it is likely the surface-activation mechanism is the same. One would postulate that surface photolysis of these adsorbed layers lead to some kind of aggregate formation. Previous studies of the photolysis of adsorbed trimethylaluminum have indicated that metal-cluster formation may indeed be occurring.[6] If this were the correct interpretation, one would also have to postulate an enhancement in the photodissociation cross section for surface adsorbed TIBA at 248 nm over that in the gas phase, as observed by Ehrlich and Osgood[7] for trimethylaluminum, to explain the extremely high-growth selectivities achieved. Experiments to verify this speculation are underway.

It appears that the nucleation of clusters on the surface may be playing an important role in activating the growth of Al on our surfaces. It should be stressed, however, that the chemistry involved with this surface nucleation phenomenon is sufficiently complicated that an unambigious identifi-

cation of a mechanism is difficult. The fact that the model, only correctly predicts the sign and not the magnitude of the nucleation selectivity in going from 248 to 193 nm, at 250 °C, as compared to going from 250 to 200 °C, at 248 nm, may already be an indication that chemical changes need to be included in this simple model in order to describe the phenomena observed. In particular, one might postulate changes in surface-wetting properties or chemical changes which affect the free energies used in the calculation to explain the dramatic increase in nucleation from gas phase photoproducts in going from 250 to 200 °C, at 248 nm.

[1]G. S. Higashi and C. G. Fleming, Appl. Phys. Lett. **48**, 1051 (1986).
[2]G. S. Higashi, G. E. Blonder, and C. G. Fleming, in Proceedings of the Symposium on Photon, Beam and Plasma Stimulated Chemical Processes as Surfaces at the 1986 Fall Meeting of the Materials Research Society, Boston, MA. (to be published).
[3]J. Y. Tsao and D. J. Ehrlich, J. Cryst. Growth **68**, 176 (1984).
[4]C. A. Neugebauer, in *Handbook of Thin Film Technology*, edited by L. I. Maissel and R. Glang (McGraw–Hill, New York, 1970), Chap. 8.
[5]J. W. Christian, *The Theory of Transformation in Metals and Alloys*, 2nd ed. (Pergamon, Oxford, 1975) Part 1, Chap. 10.
[6]G. S. Higashi and L. J. Rothberg, Appl. Phys. Lett. **47**, 1288 (1985).
[7]D. J. Ehrlich and R. M. Osgood, Jr., Chem. Phys. Lett. **79**, 381 (1981).

Chemiluminescence from F and XeF_2 etching reactions with silicon

M. J. Mitchell, M. Suto, and L. C. Lee[a)]
Department of Electrical & Computer Engineering, San Diego State University, San Diego, California 92182

T. J. Chuang
IBM Almaden Research Center, San Jose, California 95120-6099

(Received 27 February 1987; accepted 7 May 1987)

The ultraviolet-visible chemiluminescence spectra from the etching reactions of silicon with atomic fluorine and xenon difluoride were observed. In both reactions, the visible chemiluminescence arises mainly from excited SiF_3^*, which is produced from the reaction of $SiF_2 + F$ in the gas phase. The XeF_2 etching reaction yields additional bands from excited XeF and possibly from a second excited state of SiF_3 which may be produced from the reaction of SiF_2 with a hot F atom. When an inert gas is added to the XeF_2 etching system, the SiF_3^* emission is quenched and new emission bands appear. The mechanism for the production of chemiluminescence is discussed in accord with the chemiluminescence spectra and polarization observed.

I. INTRODUCTION

Plasma and dry chemical etching are of increasing importance to the microelectronic fabrication industry.[1,2] A better understanding of the etching mechanism will lead to advances in fabrication technique. Fluorine atoms from electrical discharge have been used for rapid etching of crystalline and amorphous silicon,[2-4] and XeF_2 has been extensively used as a model compound for the study of the F atom etching mechanism.[5-7] In both etching systems, gaseous SiF_4 is the major reaction product, which can be simply pumped out. The reaction mechanisms for these two etching systems are not yet fully understood. In major aspects, the etching behavior of the two systems is similar. Yet in detail, they appear substantially different.[2,3,8]

The etching reactions of both fluorine atom and XeF_2 with silicon produce chemiluminescence which may be useful in understanding the etching mechanism. It has been reported[9-11] that visible chemiluminescence occurs in the gas phase when atomic fluorine or molecular fluorine is the etchant. When XeF_2 is used, infrared chemiluminescence emits from the silicon surface or near-surface region.[12] Though it has been mentioned[9,13] that ultraviolet chemiluminescence may be produced from the etching reaction of silicon, no spectra have yet been published. Clearly, the two etching systems deserve further study.

We have embarked upon a study of the visible and ultraviolet chemiluminescence produced from the fluorine atom and XeF_2 etching of silicon in order to further understand the etching mechanisms involved. We have observed that the visible emissions from the two different systems have strong similarities, but the XeF_2 etching produces additional ultraviolet emissions not exhibited in the fluorine atom etching. Furthermore, the emission from the XeF_2 etching changes dramatically when inert gases are present in the system, yielding some new, and as yet unidentified, emission bands.

II. EXPERIMENT

Both fluorine atom and XeF_2 etching experiments were carried out in the same apparatus as shown in Fig. 1. A sixway stainless steel cross was equipped with quartz or LiF observation windows. Three vacuum pumps were attached to the system: either standard mechanical pump (Sargent Welch) for the discharge–flow experiment, a turbomolecular pump (Pfeiffer TSU 170) for lower pressure evacuation of the system ($\sim 10^{-7}$ Torr), or else a cryosorption pump, alone, used for XeF_2.

Atomic fluorine was generated by a 2450 MHz microwave discharge (Opthos) of mixtures of He (MG Scientific 99.997%) and F_2 (Matheson 9.9% in He) in a 0.5 in. o.d. alumina tube; the discharge was led into the reaction chamber through a short length of Teflon or stainless steel tubing. The end of the tubing was placed 1–3 mm from the silicon surface.

Xenon difluoride (SCM Specialty Chemicals) is a solid compound with a vapor pressure of about 4.5 Torr at room temperature.[14] The compound was stored in a small stainless steel reservoir and degassed at the liquid-N_2 temperature prior to the experiment. XeF_2 was admitted into the reaction chamber through the same tubing as for the atomic fluorine etching by opening a metering valve between the reaction chamber and the XeF_2 reservoir. The XeF_2 gas could also be

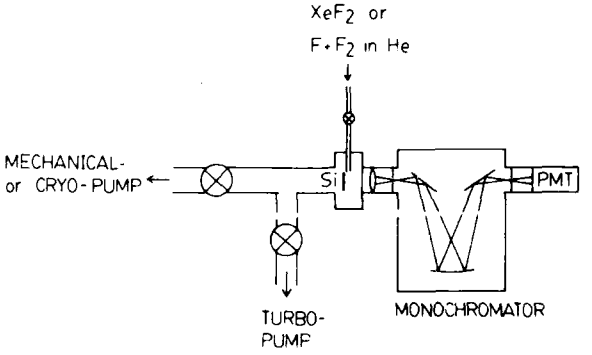

FIG. 1. Schematic diagram of experimental apparatus used for the atomic fluorine and XeF_2 etching reactions with silicon.

 0734-211X/87/051444-06$01.00 © 1987 American Vacuum Society

pressurized with inert gas and then admitted to the reaction chamber.

Silicon (111) substrates with *n*-doping 6–8 Ω cm resistivity or *p*-doping 1–3 Ω cm resistivity (both form Aurel) were held in the reaction chamber by a Teflon holder so that the surface central normal line of the sample was either coincident to or perpendicular to the axis of detection. Chemiluminescence was dispersed using either a 0.2 m (Acton Research VM-502 for vacuum UV) or 0.25 m (Kratos GMA-201) monochromator and detected via photomultiplier tube (EMI 9558QB sensitive in the 180–800 nm region or EMI B-215FV solar blind) and standard photon counting system (EG&G ORTEC).

For polarization studies, the silicon samples were mounted in a small slot at the end of a stainless steel rotary feedthrough, which allowed the sample to be turned at any angle with respect to the axis of detection. The polarizer was mounted so that its rotation axis was coincident with the axis of detection; the detection system consisted of a PMT and photon counting apparatus as described above.

The apparatus for vacuum ultraviolet (VUV) excitation of SiF_3H has been fully described previously.[15,16] Briefly, a capillary condensed discharge light source was used to produce atomic emission lines in the 40–150 nm spectral region. A single emission line was isolated by a 1 m vacuum monochromator (McPherson 225) with a grating blazed for 80 nm. The selected emission line was passed through a slit (no window) into a gas cell which was 5 cm in length and 3 in. i.d. Fluorescent light from the gas cell passed through a lithium fluoride window and was dispersed by a 0.3 m monochromator (McPherson 218). Detection was by a cooled PMT (EMI 9558QB), and signal processing was by a standard, gated photon counting system (EG&G ORTEC).

Trifluorosilane was prepared according to published methods[17] and was purified by trap-to-trap distillation. The only volatile product appeared to be SiF_3H; Infrared spectroscopy and mass spectrometry confirmed this assignment[18] and further indicated no evidence of any chlorine contaminants. The SiF_3H was transferred to a clean stainless steel cylinder and promptly used for the photolysis experiments.

III. RESULTS

A. Si+F etching

Etching of both *n*- and *p*- doped (111) silicon with fluorine atoms generated from a microwave discharge of trace F_2 in He (1–3 Torr) gives a broad emission continuum in the visible wavelength region. Figure 2 illustrates the spectra observed. The response for the detection system (Kratos GMA 200 + EMI 9558QB) was studied using a standard lamp, and it was found that the broad peaks at about 445 and 700 nm arise from either the sensitivity profile of the PMT or monochromator generated "ghost."

The chemiluminescence spectrum extends into the ultraviolet to approximately 220 nm as shown in Fig. 2. Several sharp peaks are superimposed upon the chemiluminescence continuum in the 220–280 nm region. These peaks are present even when a silicon sample is not in the chamber, and at

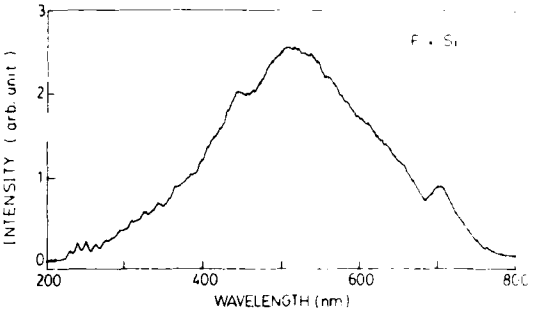

FIG. 2. Chemiluminescence spectrum produced from the etching reaction of atomic fluorine with silicon. He ~600 mTorr, F_2 ~5 mTorr, and 3.3 nm resolution.

0.33 nm resolution can be identified as arising from excited NO emission (B→X: 0,5 through 0,13; A→X: 0,0 through 0,2; C→X:0,3 through 0,6).[19] These NO emissions may be caused by impurities in the F_2/He cylinder or undetectable leak in the gas handling line. No emission was detected in the vacuum UV region (110–190 nm).

The intensity of chemiluminescence increases with increasing F_2 concentration. At a constant F_2 concentration, addition of He pressure (5–15 Torr) to the microwave discharge causes some quenching of the visible chemiluminescence. The ultraviolet portion, unfortunately, is obscured by the NO* emission which becomes far more intense than the chemiluminescence at He pressures over 10 Torr.

B. Si+XeF_2 etching

The XeF_2 etching reaction produces chemiluminescence as shown in Fig. 3. Two prominent spectral features in addition to a spectrum similar to that from the Si + F etching reaction are observed: a narrow, strong emission band centered at about 353 nm and a broad spectral continuum from 215 to 285 nm. The overall emission intensity for the XeF_2 etching is apparently much less than that for the fluorine

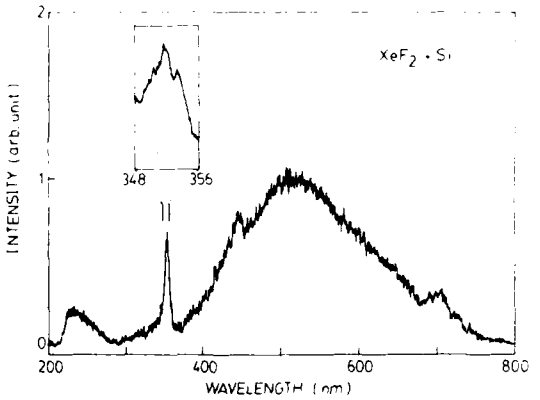

FIG. 3. Chemiluminescence spectrum produced from the etching reaction of XeF_2 with silicon; XeF_2 ~40 mTorr and 6.6 nm resolution; the insert was taken with XeF_2 ~700 mTorr and 0.33 nm resolution.

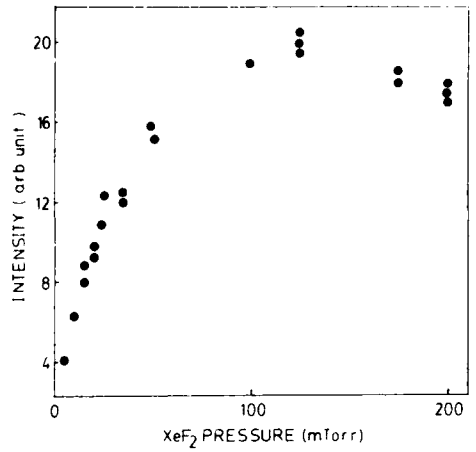

FIG. 4. Total emission intensity produced from the etching reaction of XeF_2 with silicon at varied XeF_2 pressures.

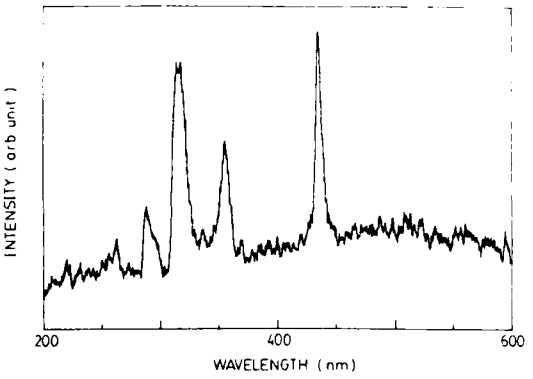

FIG. 5. Chemiluminescence spectrum produced from the etching reaction of XeF_2 with silicon in the presence of added argon gas; Ar ~4 Torr, XeF_2 ~200 mTorr, 3.3 nm resolution.

atom etching, despite XeF_2 giving a much faster etching rate (see more discussion later).

The inert in Fig. 3 illustrates the emission at 0.33 nm resolution. Readily, it can be seen that there are actually two peaks approximately 2 nm apart, indicating that they are the 351 and 353 nm bands[14] of XeF (B→X) emission.[20] The broad peak from 215 to 285 nm shows no fine structure at 1 nm resolution. This band is not observed in the fluorine atom etching reaction, suggesting that the XeF_2 + Si system involves more energetic species than the F + Si system.

The total chemiluminescence intensity as a function of XeF_2 pressure in a flowing system is illustrated in Fig. 4. The intensity increases with increasing pressure at lower pressures. But at higher XeF_2 pressures, the chemiluminescence intensity decreases, which is likely due to quenching of the excited state. Changing XeF_2 pressure does not affect the shape of chemiluminescence spectrum.

When moderate pressures (1–20 Torr) of flowing He, Ar, or N_2 are mixed with XeF_2 in the reaction chamber, there are dramatic changes in the chemiluminescence spectrum as shown in Fig. 5. Both the 215–285 and 380–780 nm continua are quenched, but the 353 nm band is still present, and new bands appear at 260, 290, 320, and 435 nm. The two continua are quenched more effectively by N_2 and Ar than He. For instance, 4 Torr of Ar or 2.2 Torr of N_2 will completely quench the continua, but a significant component of the visible continuum is still present even at 16 Torr of He, though the UV continuum is totally quenched. The UV band is more effectively quenched than the visible band by added gases. An attempt was made to observe the sharp 435 nm structure from a fluorine atom etching; however, at 5, 10, and 15 Torr of added He, no evidence could be found for the existence of the 435 nm peak.

To further characterize emissions from the etching reactions, SiF_3H was irradiated with 92.3 nm light and the resulting fluorescence was observed. Figure 6 illustrates the fluorescence which was obtained at a SiF_3H pressure of 8 mTorr. These emissions possess ultraviolet and visible, unstructured bands which closely resemble the etching emissions. Due to the low-gas pressures used in the windowless sample cell, the signal-to-noise ratio is low, but the spectrum still allows comparison with the etching emissions. The large peak centered at 320 nm is, as yet, unassigned.

C. Observation of polarization

When pure XeF_2 was used to etch silicon mounted on a rotary feedthrough at an angle θ between the surface normal and the axis of detection, there was a small increase in the intensity of *s* polarization over *p* polarization. This increase reached a maximum of about 8% at an angle $\theta = 45°$. This result indicates that the polarization is caused by the reflection of chemiluminescent light from the silicon surface.

IV. DISCUSSION

A. Fluorine atom etching

There has been some disagreement in the literature over the nature of the chemiluminescence produced from the F atom etching of silicon. The emissions have been attributed, at various times, to excited states of SiF_2,[21] and SiF_3,[11] though the bulk of spectral work seems to indicate that SiF_3^* is the probable emitting species.[9–11] The visible emission is extremely broad and unresolved, and may conceal emissions

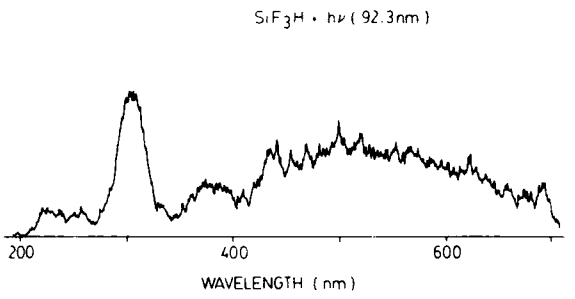

FIG. 6. Fluorescence spectrum produced from the excitation of SiF_3H gas by 92.3 nm light; SiF_3H ~8 mTorr, 5 nm resolution.

from other fluorosilicon species.[22–24] Mass spectral studies of the gas desorbing from the F atom etching of silicon indicate that substantial fractions of SiF and SiF_2 (up to 0.3) are present.[25] This observation is consistent with spectral emission studies which indicate that the visible emission results[10,26] from reaction of atomic fluorine and SiF_2.

We have now observed that the chemiluminescence from F atom etching of silicon containing just one broad, unresolved band extending from 220 to 760 nm. This emission spectrum looks remarkably like the emission spectrum obtained from the gas phase reaction of $SiF_2 + F$ in the 400–800 nm region[26] as well as the recently obtained spectrum in the entire 220–760 nm region.[27,28] In addition, VUV excitation of SiF_3H (Fig. 6), which has been shown to produce SiF_3, yields a broad UV-visible band similar to that of the Si + F etching reaction. As suggested by Donnelly and Flamm[9,10,26] we also conclude that the broad emission band arises from excited SiF_3^* species (further discussed below). Recent study[29] of the etching of silicon by the discharge medium of $CF_4 + O_2$ also supports this assignment.

The chemiluminescent reaction is likely initiated[9,10] by desorption of SiF_2 radical from the surface, then followed by,

$$SiF_2 + F(+M) \rightarrow SiF_3^*(+M) \quad (1)$$

and

$$SiF_2 + F_2 \rightarrow SiF_3^* + F. \quad (2)$$

The maximum excess energy available for reaction (1) to excite the SiF_3 radical is 136.8 kcal/mol (5.93 eV), where the heats of formation[30] for $\Delta H_f(SiF_3) = -258.7$ kcal/mol, $\Delta H_f(SiF_2) = -140.3$ kcal/mol, and $\Delta H_f(F) = 18.4$ kcal/mol are used in the calculation. With this available maximum energy, the shortest wavelength that can be emitted by the excited SiF_3^* is 209 nm, thus, it is energetically possible to produce the observed spectrum. Using $\Delta H_f(SiF_3) = -239$ kcal/mol, which is recently recommended by Walsh,[31] the ΔH for reaction (1) becomes -117.1 kcal/mol (5.08 eV), and the shortest wavelength emitted by the excited SiF_3^* be 244 nm, which is longer than the shortest wavelength observed. The current result indicates that the ΔH_f for SiF_3 lies between the two reported values.[30,31] Since reaction (1) is a three-body recombination process, the available energy may widely distribute to the excited SiF_3 state. The maximum available energy for reaction (2) is 100 kcal/mol (4.33 eV), which is not sufficient to produce emission at such short wavelengths as observed. This reaction is thus not likely to be responsible for the observed emission at wavelengths shorter than 286 nm.

B. XeF_2 Etching

The chemiluminescence spectrum from XeF_2 etching of silicon (Fig. 3) is similar to the spectrum obtained from the F atom etching (Fig. 2). Principally, the broad, unresolved, and virtually identical continua in the visible and near-ultraviolet regions are similar in both spectra, leading to a proposal that the emitter is also SiF_3^*. The lack of polarization in the chemiluminescence spectrum strongly indicates that the emission originates from the gas phase reaction. Similar to the fluorine atom etching, SiF_3^* may be produced from the gas phase reaction of $F + SiF_2$. The fluorine atom may be produced from the $SiF_2 + XeF_2$ reaction as discussed below. Although there are disagreements concerning the exact amount of SiF_2 present in the gas phase as the etching product of $Si + XeF_2$ reaction, there seems little doubt about its existence.[26,32–34] A recent study by Lin and co-workers[35] using multiphoton ionization mass spectrometry also shows the presence of SiF_2 in the gas phase above room temperature. Considering the moderately high XeF_2 pressure used in our experiment, the silicon temperature could rise above room temperature due to thermochemical energy produced by etching reactions. Thus, SiF_2 is expected to be abundant in the etching system.

The strong, sharp feature at ~353 nm in Fig. 3 is likely due to the XeF (B–X) transition.[36] The XeF (B) species could result from the reaction of unsaturated fluorosilicon species with XeF_2 such as,

$$SiF_2 + XeF_2 \rightarrow SiF_3 + Xe + F, \Delta H = -73.7(\text{or } -54.0), \quad (3)$$

$$\rightarrow SiF_3 + XeF(B)\ \Delta H = 11.0(\text{or } 30.7), \quad (4)$$

$$SiF_3 + XeF_2 \rightarrow SiF_4 + XeF(B), \Delta H = 0(\text{or } -19.7), \quad (5)$$

$$SiF + XeF_2 \rightarrow SiF_2 + XeF(B), \Delta H = -7.7, \quad (6)$$

where ΔH (in units of kcal/mol) is calculated from the dissociation energies[37] $D_0(Xe\text{–}F\text{–}F) = 63.09$ kcal/mol, $D_0(XeF\text{–}F) = 59.73$ kcal/mol, the heat of formation[37] of XeF_2 $\Delta H_f^\circ(XeF_2) = -28.0$ kcal/mol, and the electronic energy of the XeF(B) state, $T_e = 84.7$ kcal/mol (3.67 eV).[38] The ΔH values depend on the $\Delta H_f^\circ(SiF_3)$ values.[30,31] If Walsh's value[31] is used, ΔH values for reactions (3), (4), and (5) are -54, 30.7, and -19.7 kcal/mol, respectively. Reaction (3) may release chemical energy sufficient to excite SiF_3 to contribute to the visible emission, i.e., wavelength longer than 390 nm. Reaction (4) is endothermic, so it is much slower than reaction (5) for the production of XeF(B). Reaction (6) also produces XeF(B) and is exothermic; however, recent studies indicate that SiF is not present in the gas phase.[35]

The atomic fluorine from reaction (3) carries very high kinetic energy. Also the atomic fluorine released following the XeF(B $\rightarrow$X) emission in reaction (5) will be translationally hot, because the ground state of XeF is weakly bonded or repulsive.[38] This liberated fluorine atom may carry kinetic energy as high as 0.7 eV.[38] These hot F* atoms may make it possible for reaction with SiF_2 to yield SiF_3^* in the second excited state,

$$F^* + SiF_2 \rightarrow SiF_3^*. \quad (7)$$

This highly excited SiF_3^* may emit the UV band shown in Fig. 3. Excitation of SiF_3H by 92.3 nm light (13.4 eV) also gave a broad emission in the 220–280 nm region lending further credence to this supposition.

The F atom in the fluorine atom etching experiment is thermalized so that it may not have enough energy to produce the UV emitting state. To further support this assertion, He, Ar, or N_2 have been added to the XeF_2 etching system to thermalize the presumably hot F atom so that the

UV band may disappear. Our experimental result indicates that the UV band is quenched by the added gas much more efficiently than the visible band, namely, the ratio of the UV and visible emission intensities decreases with the buffer gas pressure. For instance, the ratio is reduced to one-half when 5 Torr of He or 1 Torr of either Ar or N_2 was added to the XeF_2 etching system. Although the quenching rate of the UV band by He is slower than that of Ar and N_2, they are all in the same order of magnitude. These results indicate that the quenching is a thermalization process. Generally, the quenching of electronically excited states by He is a few orders of magnitude slower than that by molecules such as N_2, in contrast to the thermalization of translationally hot species for which He is almost as effective as N_2. A similar phenomenon was observed in a previous experiment[30] where hot $O(^1S)$ atom was quenched as effectively by He as N_2O, N_2, etc. This result lends support to the assertion that the UV band possibly emits from a second excited state of SiF_3^* produced from the reaction (7).

Spectroscopic character of SiF_3 radical is not well established. The emission in the 210–260 nm region, observed in the microwave discharge of SiF_4, was assigned[32] to the SiF_3 (A–X) emission; however, this identification was not certain due to the overlap with SiF_2 emission. An attempt to detect SiF_3 by laser-multiphoton-ionization failed.[35] The absorption of SiF_3 radical in rare-gas matrix was observed[40] at 178 and 186 nm. Theoretical calculation[41] obtained the energy of $T_e = 6.1$ eV for the SiF_3 (A^2B–X^2A) transition, thus, it is possible that SiF_3^* emits in the UV region, but the UV emitting state may not be reached by laser photons in the 220–240 nm region.

Recently, it has been revealed that the spectroscopic character of SiF_4[42] is remarkably similar to that of CF_4.[43] Thus, the spectroscopic character of SiF_3^* may be similar to that of CF_3^*, for which emission spectra have been well-studied.[44–47] The CF_3 radical has two emission systems, a UV transition in the 190–320 nm and a visible transition in the 400–800 nm region. The upper states of both CF_3 emissions are bound, with energy about 6.4 eV above the ground state.

The visible chemiluminescence spectra observed in the XeF_2 and F etching system are very similar to the CF_3^* visible emission spectrum; however, the character of the transition may not be the same. For the case of CF_3, the transition occurs between the electronically excited states. On the other hand, the SiF_3 continuum emission is produced by the $SiF_2 + F$ reaction, so both the upper state and the lower state must be the bound states correlating to $SiF_2(X) + F$. Since SiF_3 is a polyatomic molecule, the transition is complicated enough to be seen as the continuum. The upper state of SiF_3^* UV emission may correlate to the $SiF_3^* + F$ or the $SiF_2 + F^*$. It is possible that the reaction between $SiF_2(X)$ and hot F^* atom can pump the SiF_3 up to such an electronically excited state through the potential surface crossing. Thus, it is reasonable to attribute both UV and visible emissions to SiF_3 at different excited states. Further study of SiF_3 emission spectrum is of interest.

The infrared chemiluminescence arising from the XeF_2 reaction with silicon is polarized (p over s by a factor of 2), leading to the conclusion that this chemiluminescence comes from the silicon surface or near surface region.[17] Our investigation of this effect in the visible and near ultraviolet regions indicates that little or no polarization is present (s over p by $< 10\%$). This result further supports the conclusion that, like fluorine atom etching, the UV-visible chemiluminescence observed in the etching of silicon by XeF_2 arises primarily from the gas phase reactions.

Addition of inert gases to the XeF_2 etching system causes quenching of the emission continua, and appearance of several new peaks in the chemiluminescence spectrum. The wavelengths of peaks at ~ 265 and ~ 290 nm correspond to the XeF (D–X) and XeF (D–A) transitions,[48] respectively. The peaks at ~ 320 and ~ 435 nm are as yet unidentified, though the appearance of a broad peak at ~ 320 nm in the fluorescence resulting from the VUV excitation of SiF_3H may aid in the identification. Attempts to generate the 435 nm peak by etching silicon with atomic fluorine at 5, 10, and 15 Torr of added He pressure failed to reveal such a peak, though the peak appears clearly in the emission spectra of XeF_2 etching at these He pressures. Further study in this area is of interest.

Quenching of the chemiluminescence from the XeF_2 etching reaction may occur even in the absence of added inert gas. Figure 4 illustrates a decrease in total chemiluminescence intensity at higher XeF_2 pressures. Such a quenching could partly be due to Xe, which is liberated by dissociation of XeF_2 during etching reactions.

As a final note, we observe that the emission intensity in the $Si + XeF_2$ etching is much weaker than that in the Si + F etching at equivalent etching rates. At a given Si etching rate, the amounts of SiF_2 generated from both F and XeF_2 etching reactions are expected to be equivalent.[5] A stronger emission observed in the Si + F etching is likely due to the fact that the F atom is readily available in the Si + F etching system, but for the $Si + XeF_2$ etching system the F atom is produced by secondary reactions such as reaction (3). Reaction (7) which we have suggested to be responsible for the emission at 215–285 nm is not expected to yield a strong UV emission either, because the required F atoms have to be produced by secondary reactions such as reaction (3) and thus, its concentration should be quite small in the $Si + XeF_2$ system. In any event, this observed difference in emission intensity further supports the assertion that the chemiluminescence is produced from gas phase reactions.

V. CONCLUSION

We have observed chemiluminescence spectra for the etching of silicon by fluorine atom and XeF_2. Both etching systems give emissions consistent with the emitter being excited SiF_3^*, however, the emission intensity in the $Si + XeF_2$ etching is much weaker than that of the Si + F etching. Excitation of SiF_3H by VUV light yields UV-visible fluorescence similar to that observed in the etching reactions. This fluorescence and the complete UV-visible chemiluminescence spectra, coupled with the results of others, points to a conclusion that SiF_3^* is the source of emission produced from gas phase reactions.

Additional peaks are observed in the ultraviolet chemilu-

minescence spectrum from the XeF_2 etching of silicon, in which a peak at 353 nm is assigned to the XeF (B–X) transition, whereas the 215–285 nm band may result from another excited state of SiF_3^*. When inert gases are added to the XeF_2 etching, both the ultraviolet and visible broad bands are quenched and new sharp bands of XeF* and other as yet unidentified species are produced.

ACKNOWLEDGMENTS

The authors wish to thank M. C. Lin (Naval Research Laboratory), H. F. Winters (IBM), and V. M. Donnelly (AT&T, Bell Laboratories) for useful discussions, M. A. Ring for synthesis of SiF_3H, and X. Wang for taking the fluorescence spectra from photoexcitation of SiF_3H. The authors also appreciate the preprint received from M. C. Lin describing study of the XeF_2 + Si etching reaction, and the spectrum received from J. Wormhoudt showing gas phase reaction of SiF_2 + F. This material is based on the work supported by the NSF under Grant No. CBT-8518555.

[a] Also, Department of Chemistry, San Diego State University.

[1] J. W. Coburn and H. F. Winters, J. Vac. Sci. Technol. **16**, 391 (1979).
[2] D. L. Flamm, D. E. Ibbotson, J. A. Mucha, and V. M. Donnelly, Solid State Technol. **26**, 117 (1983).
[3] D. E. Ibbotson, D. L. Flamm, J. A. Mucha, and V. M. Donnelly, Appl. Phys. Lett. **44**, 1129 (1984).
[4] M. Chen, V. J. Minkiewicz, and K. Lee, J. Electrochem. Soc. **126**, 1946 (1979).
[5] H. F. Winters and J. W. Coburn, Appl. Phys. Lett. **34**, 70 (1979).
[6] T. J. Chuang, J. Appl. Phys. **51**, 2614 (1980).
[7] Y. Y. Tu, T. J. Chuang, and H. F. Winters, Phys. Rev. B **23**, 823 (1981).
[8] M. J. Vasile, J. Appl. Phys. **54**, 6697 (1983).
[9] V. M. Donnelly and D. L. Flamm, J. Appl. Phys. **51**, 5273 (1980).
[10] D. L. Flamm, V. M. Donnelly, and J. A. Mucha, J. Appl. Phys. **52**, 3633 (1981).
[11] J. A. Mucha, V. M. Donnelly, D. L. Flamm, and L. M. Webb, J. Phys. Chem. **85**, 3529 (1981).
[12] T. J. Chuang, Phys. Rev. Lett. **42**, 815 (1979).
[13] T. J. Chuang, J. Vac. Sci. Technol. **21**, 798 (1982).
[14] J. H. Holloway, *Noble Gas Chemistry* (Methuen, London, 1968), p. 108.
[15] D. L. Judge and L. C. Lee, J. Chem. Phys. **57**, 455 (1972).
[16] M. Suto, X. Wang, and L. C. Lee, J. Chem. Phys. **85**, 4228 (1986).
[17] H. S. Booth and W. D. Stillwell, J. Am. Chem. Soc. **56**, 1531 (1934).
[18] C. Newman, S. R. Polo, and M. K. Wilson, Spectrochim. Acta **10**, 793 (1959).
[19] R. W. B. Pearse and A. G. Gaydon, *The Identification of Molecular Spectra, 4th ed.* (Wiley, New York, 1976), pp. 235–241.
[20] R. Sauerbrey, W. Walter, F. K. Tittel, and W. L. Wilson, Jr., J. Chem. Phys. **78**, 735 (1983).
[21] C. I. M. Beenakker, J. H. J. van Dommelen, and J. Dieleman, in *Extended Abstracts, 157th Meeting Electrochemical Society* (The Electrochemical Society, Pennington, N. J., 1980), Vol. 80-1, p. 330.
[22] J. L-F. Wang, C. N. Krishnan, and J. L. Margrave, J. Mol. Spectrosc. **48**, 346 (1973).
[23] C. P. Conner, G. W. Stewart, D. M. Lindsay, and J. L. Gole, J. Am. Chem. Soc. **99**, 2540 (1977).
[24] S. P. So, J. Mol. Struct. **39**, 133 (1977); R. A. Armstrong and S. J. Davis, J. Chem. Phys. **71**, 2433 (1979).
[25] M. J. Vasile and F. A. Stevie, J. Appl. Phys. **53**, 3799 (1982).
[26] J. A. Mucha, D. L. Flamm, and V. M. Donnelly, J. Appl. Phys. **53**, 4553 (1982).
[27] A. C. Stanton, A. Freedman, and J. Wormhoudt, and P. P. Gaspar, Chem. Phys. Lett. **122**, 190 (1985).
[28] J. Wormhoudt (private communication, 1986).
[29] Y. Matsumi, S. Toyoda, T. Hayashi, M. Miyamura, H. Yoshikawa, and S. Komiya, J. Appl. Phys. **60**, 4102 (1986).
[30] M. P. Farber and R. D. Srivastava, J. Chem. Soc. Faraday Trans. 1 **74**, 1089 (1978).
[31] R. Walsh, J. Chem. Soc. Faraday Trans. 1 **79**, 2233 (1983).
[32] H. F. Winters and F. A. Houle, J. Appl. Phys. **54**, 1218 (1983).
[33] H. F. Winters, J. Vac. Sci. Technol. B **1**, 927 (1983).
[34] H. F. Winters, J. W. Coburn, and T. J. Chuang, J. Vac. Sci. Technol. B **1**, 469 (1983).
[35] J. A. Dagata, D. W. Squire, C. S. Dulcey, D. S. Y. Hsu, and M. C. Lin, J. Vac. Sci. Technol. B **5**, 1495 (1987).
[36] J. E. Valazco, J. H. Kolts, D. W. Setser, and J. A. Coxon, Chem. Phys. Lett. **46**, 99 (1977).
[37] J. Berkowitz, W. A. Chupka, P. M. Guyon, J. H. Holloway, and R. Spohr, J. Phys. Chem. **75**, 1461 (1971).
[38] P. J. Hay and T. H. Dunning, Jr., J. Chem. Phys. **69**, 2209 (1978).
[39] L. C. Lee and M. Suto, J. Chem. Phys. **80**, 4718 (1984).
[40] D. E. Milligan, M. E. Jacox, and W. A. Guillory, J. Chem. Phys. **49**, 5330 (1968).
[41] J. W. Hastie and J. L. Margrave, J. Phys. Chem. **73**, 1105 (1969).
[42] M. Suto, X. Wang, L. C. Lee, and T. J. Chuang, J. Chem. Phys. **86**, 1152 (1987).
[43] L. C. Lee, X. Wang, and M. Suto, J. Chem. Phys. **85**, 6294 (1986).
[44] M. Suto and N. Washida, J. Chem. Phys. **78**, 1007, 1012 (1983).
[45] M. Suto, N. Washida, H. Akimoto, and M. Nakamura, J. Chem. Phys. **78**, 1019 (1983).
[46] N. Washida, M. Suto, S. Nagase, U. Nagashima, and K. Morokuma, J. Chem. Phys. **78**, 1025 (1983).
[47] M. Suto and L. C. Lee, J. Chem. Phys. **79**, 1127 (1983).

An *in situ* infrared study on the interaction of oxygen plasmas with Si and fluorine plasmas with SiO_2 surfaces

W. C. M. Claassen and J. Dieleman
Philips Research Laboratories, P.O. Box 80.000, 5600 JA Eindhoven, The Netherlands

(Received 27 February 1987; accepted 26 May 1987)

Infrared spectroscopy has been used to study *in situ* the oxidation of silicon in an oxygen plasma (10 Pa) and the etching of this silicon oxide in a He:F_2 (5%) plasma (50 Pa) by monitoring the Si–O stretch vibration. The sensitivity of the present system is 10% of a monolayer of oxide. A wave number shift is observed from 1088 to 1045 wave numbers during the first stage of the oxidation. The oxide-layer thickness is determined from the integrated-band intensity. This thickness increases with the square root of the oxygen plasma exposure time and decreases linearly with etch time in the fluorine plasma (6 nm/min).

I. INTRODUCTION

Future technology for ultralarge-scale-integrated semiconductor circuits will need low-temperature processes for growing and etching thin films. An important example is that of SiO_2 on Si. The composition and structure of this film and its interface with Si partly determines the electrical properties of the resulting devices. Detailed information about composition and structure of thin films can be obtained with the use of vibrational spectroscopy, e.g., electron-energy-loss (EELS), Raman-, or infrared-absorption spectroscopy (IRAS). EELS features high sensitivity and a large-spectral range but its disadvantages are low resolution (>40 cm^{-1}), the risk of electron-beam-induced reactions and its limitation to pressures below 10^{-4} Pa.[1] With Raman spectroscopy enough sensitivity is obtained only when using special modified metal surfaces (SERS). Since infrared spectroscopy combines high resolution with adequate sensitivity and furthermore is not limited to low-pressure environments, it is an obvious choice for the study of plasma interaction with thin films and interfaces. Its sensitivity however poses problems for frequencies below 800 cm^{-1}.

In this work infrared spectroscopy is used for the *in situ* study of the oxidation of Si and the etching of SiO_2 in a plasma-etch reactor. This is accomplished by monitoring the position and intensity of the infrared absorption band associated with the Si–O stretch vibration in SiO_2 located at about 1100 cm^{-1}.

II. EXPERIMENT

The experimental setup of the spectrometer is shown in Fig. 1. The spectrometer uses a globar source at 1500 K, a monochromator with 1:4 optics and a helium-cooled copper-doped germanium detector. To eliminate the $1/f$ noise of the detector the source is modulated at 1 kHz and the signal is detected phase sensitively with a lock-in amplifier. The signal is then averaged on a minicomputer, which also controls the wavelength scanning and filter exchanges of the monochromator. Because the spectrometer has a simple single-beam configuration care is taken to ensure wavelength reproducibility and mechanical stability. To be able to detect the small absorption signal of the thin oxide film superimposed on the strong background each spectrum is normalized to a reference spectrum taken from the clean silicon surface. This way the transmission of the oxide itself is obtained. With a scan time of 25 s over the spectral range 1300–800 cm^{-1} and a resolution of 5 cm^{-1} the signal-to-noise (S/N) ratio is 1000:1. Averaging over 10 scans results in a S/N of 3000:1. This only enables detection of the formation of an oxide film with submonolayer sensitivity if a multiple internal-reflection technique is used. Due to phonon and impurity absorption Si is insufficiently transparent in the wavelength region of interest[2] and cannot be used as an internal-reflection element (IRE). To solve this problem a thin, typically <0.1 mm, slice of silicon is applied to a germanium IRE. Germanium is chosen because it has a good transparency and its refractive index matches well with that of Si. The IRE allows for 10 reflections on the silicon side.

The reaction chamber consists of a silica tube with a diameter of 40 mm with the IRE mounted on one side. The chamber can be evacuated with a diffusion pump and a liquid-nitrogen cooled baffled to a base pressure of 10^{-4} Pa. The oxygen or fluorine plasma is generated by a 17 kHz hf-discharge in the gas inlet at a distance of 20 mm from the sample surface. The pressures of the plasma used are 10 Pa for the oxygen plasma and 50 Pa for the He:F_2 (5%) plasma. The substrate temperature during the experiments is 300 K.

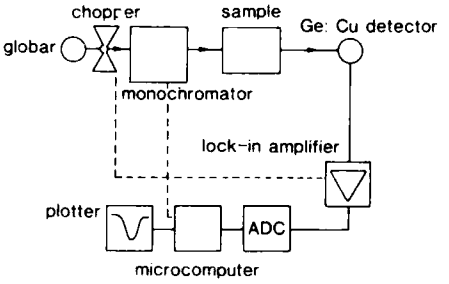

FIG. 1. Schematical drawing of the spectrometer.

 0734-211X/87/051450-03$01.00 © 1987 American Vacuum Society

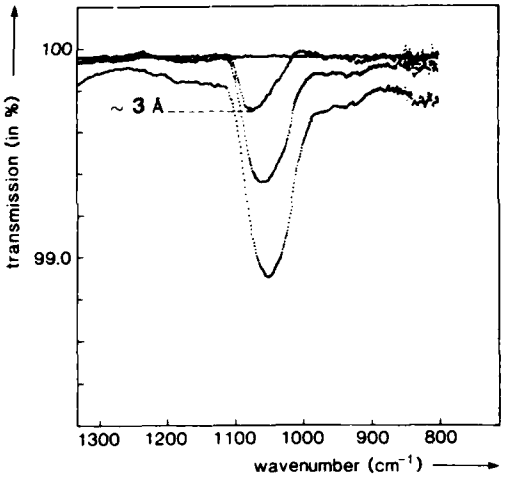

FIG. 2. Infrared absorption spectra of thin films of silicon oxide for thicknesses of 0.3, 1.0, and 1.8 nm, respectively. The Si–O stretch vibration shifts towards lower frequencies with increasing film thickness.

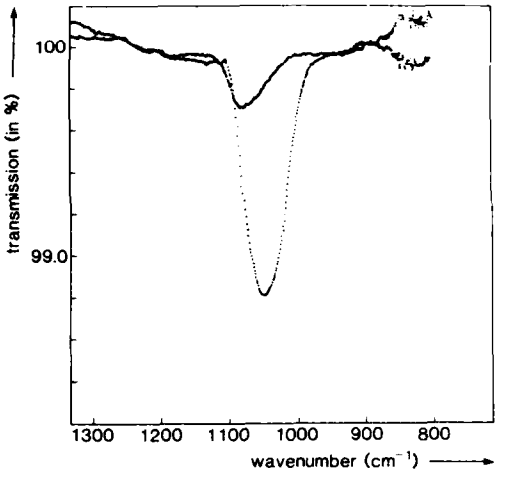

FIG. 4. The wave number shift ofthe Si–O stretch vibration during oxide removal by a He:F_2 (5%) plasma (50 Pa). The figure shows spectra of films with thicknesses of 0.3 and 1.9 nm, respectively.

III. RESULTS

In a typical experiment the silicon surface is oxidized by exposing it to the effluent of an oxygen plasma (10 Pa) for periods of 5 s. After each oxidation step the plasma is shut off and a spectrum is recorded. Some of these spectra are shown in Fig. 2. The oxide layer thickness is assumed to be proportional to the integrated band intensity of the Si–O stretch vibration. Calibration is done by growing an oxide layer of about 5 nm and measuring the thickness of that layer with ellipsometry. The absorption coefficient thus obtained of $3.0 \pm 0.5 \times 10^4$ cm^{-1} is in agreement with values found for thermally grown oxide ($3.4 \pm 0.1 \times 10^4$ cm^{-1}).[3]

Up to an oxide thickness of 0.3 nm the Si–O stretch vibration is found at 1088 cm^{-1} with a full width at half-maximum (FWHM) of 45 cm^{-1}. For thicker layers a second absorption peak evolves at 1048 cm^{-1} with a FWHM of 70 cm^{-1}. This latter absorption band is in accordance with previously published spectra for thin thermally grown oxide films.[3] If the layer thickness is plotted versus exposure time (Fig. 3) a square root dependency is found. This suggests that the plasma oxidation of silicon at room temperature is a diffusion limited process.

When a layer thickness of 5 nm is reached the oxide is etched using the effluent of a He:F_2 (5%) plasma at a pressure of 60 Pa. The same changes are observed in reversed order (Fig. 4). This indicates that the vibration at 1088 cm^{-1} must be assigned to the oxide interface with silicon and that the etching of the oxide is strictly layer by layer. As in the case of plasma oxidation the removed oxide thickness can be plotted versus etch time (Fig. 5). As might be expected a linear dependency is found. The etch rate, determined by the slope of this plot, is 6.0 ± 0.5 nm/min. In previous experiments (Ref. 4) the following relation for the etching of SiO_2 with atomic fluorine has been found:

$$R_F(SiO_2) = (6.1 \pm 0.5) \times 10^{-14} n_f T^{1/2} e^{-0.163/kT} \text{ nm/min.}$$

Even assuming a 100% dissociation for the fluorine this

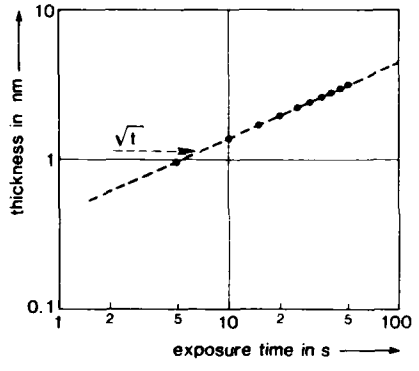

FIG. 3. Oxide-layer thickness vs oxygen plasma (10 Pa) exposure time.

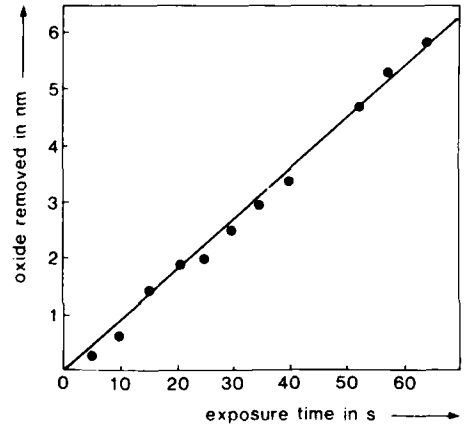

FIG. 5. The amount of silicon oxide removed by a He:F_2 (5%) plasma (50 Pa) vs etch time.

would only give an etch rate of ± 2 nm/min at room temperature. This discrepancy could be a result of the relative small discharge to sample distance (2 cm) in our experiment as compared to that of Ref. 4 (50 cm).

IV. CONCLUSION

In this experiment the feasibility is shown of infrared spectroscopy for *in situ* measurements of the interaction of plasmas with semiconductor surfaces up to a wavelength of 800 cm^{-1}. The oxidation rate and the etch rate of silicon dioxide in plasmas can be determined this way. It is even possible to detect the $Si:SiO_2$ interface.

[1]H. Ibach, in *Electron Spectroscopy for Surface Analysis*, edited by H. Ibach (Springer, Berlin, 1977), pp. 1,11.
[2]Y. J. Chabal, G. S. Higashi, and S. B. Christman, Phys. Rev. B **28**, 4472, 4479 (1983).
[3]I. W. Boyd and J. I. B. Wilson, J. Appl. Phys. **53**, 4166 (1982).
[4]D. L. Flamm, V.M. Donnelly, and J. A. Mucha, J. Appl. Phys. **52**, 3633 (1981).

Ultraviolet-assisted growth of GaAs

P. Balk, M. Fischer, D. Grundmann, R. Lückerath, H. Lüth, and W. Richter
Institute of Semiconductor Electronics and Institute of Physics, Aachen Technical University, D-5100 Aachen, Federal Republic of Germany

(Received 27 February 1987; accepted 26 May 1987)

This paper presents results of a comparative study of the UV-assisted epitaxial growth of GaAs from metal-organic Ga compounds and AsH_3 at 0.1 bar total pressure using a low-pressure-Hg lamp ($\lambda = 254$ nm) or an excimer laser ($\lambda = 193$ or 351 nm). Since effective stimulation only takes place for reaction-limited growth conditions these were defined first. It is shown that at 0.1 bar only the Ga compound, no AsH_3, is involved in the rate-limiting step. The rate increase upon illumination becomes larger with increasing stability of the metal-organic compound, i.e., in the order tri-isobutyl to triethyl to trimethyl gallium. Experiments with UV of 351 nm, a wavelength at which radiation is not absorbed by the reactants, indicate that in this case growth enhancement is absent. Thus, heating effects do not play a significant role in the stimulation process. The other wavelengths are both absorbed by the metal-organic compounds and consequently their use leads to larger growth rates. The attenuation of the incident radiation by absorption in the bulk of the gas phase determines the photon density reaching the substrate surface. Since the absorption depends on the wavelength, the photon energy and wavelength are important factors governing the rate of growth. Although the present data show that the photostimulation takes place very close to the surface, it is not possible to determine whether the stimulation process takes place at the surface, in the gas phase near the surface or in both locations.

I. INTRODUCTION

For a number of years persistent efforts have been made to enable epitaxial growth of III–V films at reduced substrate temperatures using plasma[1–5] or UV stimulation.[6–12] One reason for this approach is the desire to avoid the smearout of compositional and dopant profiles. However, UV-assisted growth at reduced-substrate temperatures additionally opens up the possibility of localized deposition without masking, i.e., writing of patterns directly on the substrate. Localized etching[13] and localized deposition of metal[14–18] and insulator films[18–22] have also been shown to be feasible using UV stimulation. This suggests a novel approach towards the fabrication of devices and circuits, for example for application in integrated optics.

The present study is concerned with a comparison of the effect of UV irradiation at different wavelengths on the deposition process of GaAs in the metal-organic vapor-phase epitaxy (MOVPE) approach. In our experiments we used a low-pressure mercury lamp ($\lambda = 254$ nm) and an excimer laser ($\lambda = 193$ or 351 nm). We also compared the effect of the nature of the alkyl group in the group III–alkyl compound on the deposition process. Since the main interest of this approach is directed towards writing of patterns on the surface we used perpendicular incidence of the UV radiation at the substrate surface.

II. EXPERIMENT

The growth studies using a low-pressure-Hg lamp (dominant UV output at $\lambda = 254$ nm) and an excimer laser ($\lambda = 193$ or 351 nm) were performed in very similar reactors. In the low-pressure-Hg lamp system, which was described earlier,[7,23] the samples were placed on a graphite substrate holder (area 2×2 cm^2) in a rectangular quartz reactor with rectangular liner (3×5.5 cm^2). The average linear flow velocity v (cm s^{-1}) during a given experiment has been indicated in the corresponding figure. The excimer-laser experiments were performed in a cylindrical-quartz reactor (Fig. 1) with rectangular liner (3.5×7 cm^2) provided with a 3-mm-diam opening for the laser beam and a graphite substrate holder (area 7×8 cm^2). Heating of the graphite was performed with IR quartz halogen lamps. The output of the Hg lamp was 0.6 mW per cm^2 substrate area; the excimer laser (Lambda–Physik EMG 101 MSC) provided 17 ns pulses of 2.8 MW/cm^2 at 10 Hz for $\lambda = 193$ nm, 20 ns pulses of 2.4 MW/cm^2 at 10 Hz for $\lambda = 351$ nm.

As substrates semi-insulating (100) GaAs wafers misoriented 2° towards the (110) plane were used. The carrier gas was Pd-diffused H_2. Reactants were AsH_3 (supplier Matheson; grade: Phoenix Plus); the metal-organic compounds TMG (trimethyl-Ga), TEG (triethyl-Ga), and TIBG (triisobutyl-Ga) were from Alfa-Ventron. The vapor pressures quoted in this study are based on data measured in our laboratory.[24] In some cases they differ considerably from published values.

Film thicknesses were determined optically, from scanning electron microscope (SEM) pictures or gravimetrically, as indicated in the figures. This led to some systematic differences between different sets of measurements. Since we were only interested in relative changes we have not attempted to apply corrections in cases where only one method per curve was used.

III. CONDITIONS FOR STIMULATED GROWTH

A. Kinetic limitations in MOVPE of GaAs

UV stimulation of the deposition process, particularly for the selective growth of patterns without the use of masking

 0734-211X/87/051453-07$01.00 © 1987 American Vacuum Society

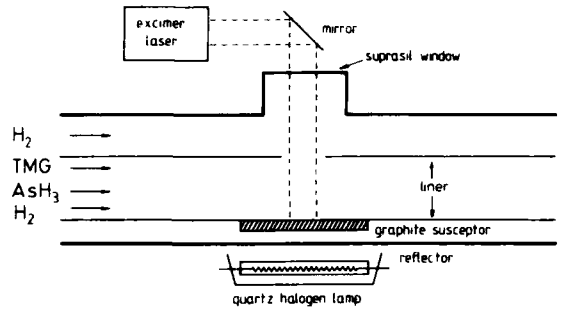

FIG. 1. Schematic of reactor for laser-assisted growth of GaAs.

films, requires conditions where without stimulation the rate is low or zero. This implies that conditions should be selected where the rate is, at least to a considerable extent, reaction limited. The data in Fig. 2 [3,7,24] depicting the temperature dependence of the rate of GaAs deposition at a total pressure of 0.1 bar for three metal-organic compounds are helpful in defining the appropriate range of experimental parameters. The three curves in this figure [for trimethyl gallium (TMG), triethyl gallium (TEG), and tri-isobutyl gallium (TIBG)] are all of basically the same shape. They show an intermediate region where the rate changes only slowly (TEG, TIBG) or not at all (TMG) with temperature. It may be seen that the maximum values are different. However, when correcting for the differences in vapor pressure of the group III alkyls used in the experiments of Fig. 2 (the rate depends linearly on this pressure) the maximum values, normalized to the same pressure of the metal-organic compound, are found to be comparable for the three cases. This confirms that the amount of Ga available at the surface determines the rate, as expected. At lower temperatures the rate drops off rather steeply. In the latter region the reaction limitation dominates the overall process, in contrast to the intermediate region, where diffusive transport processes play a rate controlling role. Towards higher temperatures the rate decreases again, probably because of depletion of the

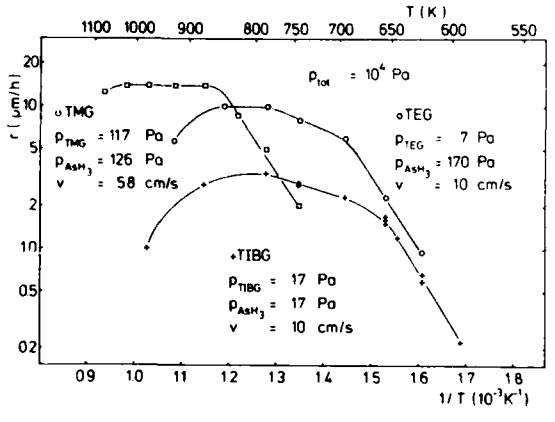

FIG. 2. Temperature dependence of growth rate of GaAs comparing TMG, TEG, and TIBG as Ga sources; data obtained in reactor used for Hg-lamp experiments taken from Refs. 3, 7, and 24; thickness data for TMG from optical measurements, for TEG from optical and weight measurements, for TIBG from weight measurements.

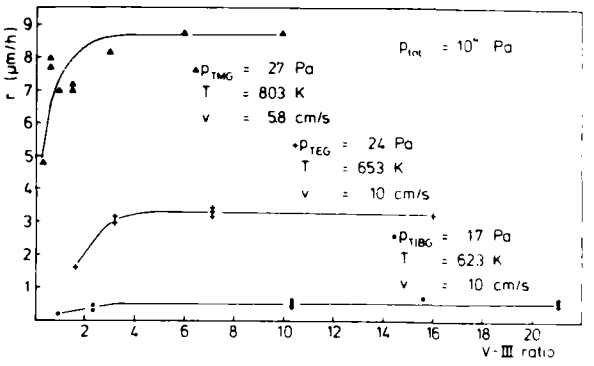

FIG. 3. Dependence of growth rate on V/III ratio for three different Ga sources; at the temperatures selected growth takes place at reaction limited conditions; experiments were performed in same reactor as used in Fig. 2; data were taken from Refs. 3 and 24 but using corrected vapor pressures from Ref. 24; thickness data for TMG from optical measurements, for TEG from optical and weight measurements, for TIBG from weight measurements.

gas phase by deposition on the quartz walls or on the substrate holder.

It may be seen that the temperature below which the reaction kinetic limitation dominates shifts to lower temperature from TMG to TEG to TIBG. Indeed, this is the order of decreasing stability of the metal organic compounds, i.e., of the metal to carbon bonds. It thus can be concluded from the data that the metal alkyl compound plays a role in the rate limiting step. The problem of breaking the metal to carbon bond in the metal-organic compound is also illustrated by the tendency to incorporate carbon in the deposited film, which is particularly pronounced in metal-organic molecular-beam epitaxy (MOMBE).[25] The dissociation of the AsH_3 apparently does not present any difficulties, at least at a total pressure of 0.1 bar. As shown in Fig. 3, [3,24] as long as there is an excess of AsH_3 (V/III ratio above 2), the rate in the temperature region where the process is kinetically limited is essentially independent of the AsH_3 pressure for all three metal alkyl compounds. It may be remarked that at lower overall pressures (0.01 bar and below) the rate is also dependent on the AsH_3 pressure.[2] However, the experiments described in the following were all carried out at conditions where AsH_3 apparently does not contribute significantly to the rate limitation.

B. Absorption spectra

From the above it appears logical to select wavelengths absorbed by the group III alkyl compound for optical stimulation by UV radiation. Figure 4 shows the absorption spectrum of trimethyl gallium measured in our laboratory. Some other versions of this spectrum have also been published[26–28]; our own measurements strongly support the data of Ref. 26. It may be seen, that the 193 nm radiation produced by the ArF-excimer laser falls in the region of maximum absorption of TMG. On the other hand, at 351 nm (XeF) no measurable absorption is observed. The 254-nm-Hg line is situated at a shoulder in the flank of the spectrum. The spectra for the Ga compounds with higher alkyl groups

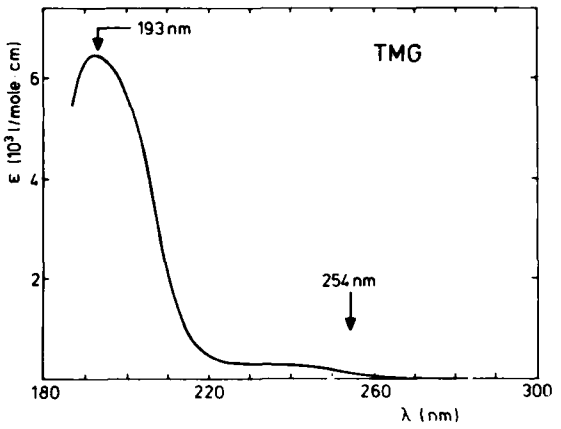

FIG. 4. Extinction coefficient of TMG vs wavelength; arrows indicate wavelengths of stimulation.

are shifted towards slightly larger wavelength. However, the relationship of the three exciting wavelengths to these spectra will be basically the same. With regards to the absorption spectrum of the group V hydride, AsH_3, it may be seen from the data in Fig. 5 [29] that only the 193-nm-ArF wavelength is strongly absorbed. At 254 and 351 nm there is no measurable absorption. It should be noted that the room temperature absorption spectra offer only a first insight into possible interactions with UV radiation taking place in the deposition system. Most likely the position and shape of the spectra will be somewhat different at elevated temperatures.

Deposition of Ga is indeed observed when irradiating TMG with 193 or 254 nm radiation. This is also the case for TEG and TIBG at 254 nm; the effect of 193 nm radiation was not studied in the latter two cases. Further shifts may occur when the molecules are adsorbed at the substrate surface. We have also observed that, as reported earlier,[7] an arsenic deposit is obtained on the quartz walls of the apparatus when irradiating the reactor containing only AsH_3 and H_2 at room temperature with the Hg lamp. This finding suggests that dissociation of adsorbed AsH_3 molecules may take

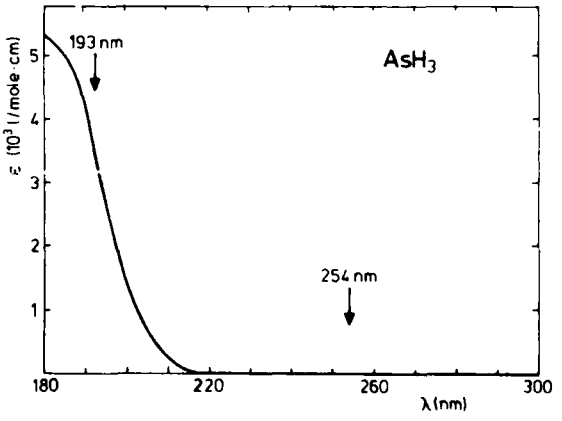

FIG. 5. Extinction coefficient of AsH_3 vs wavelength taken from Ref. 29; arrows indicate wavelengths of stimulation; thickness data from weight measurements.

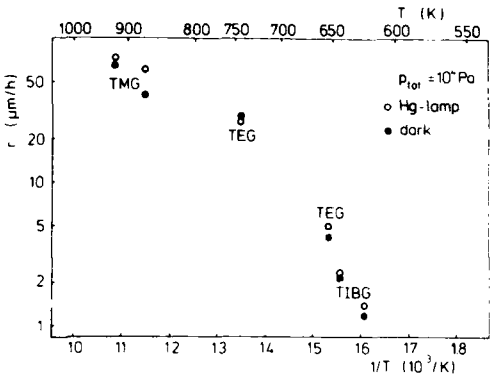

FIG. 6. Growth rate with and without UV stimulation using a Hg lamp ($\lambda = 254$ nm) for TMG, TEG, and TIBG as Ga sources for different parameters. TMG: $p_{TMG} = 42$ Pa, $p_{AsH_3} = 230$ Pa, $v = 8.4$ cm/s; TEG: $p_{TEG} = 25$ Pa, $p_{AsH_3} = 170$ Pa, $v = 10$ cm/s; TIBG $p_{TIBG} = 3$ Pa, $p_{AsH_3} = 17$ Pa, $v = 10$ cm/s; thickness data from weight measurements (Refs. 7 and 24).

place at the walls and is related to a wavelength shifted absorption spectrum. Multiple-photon excitation appears to be a very unlikely process at the relatively low intensities used in our Hg-lamp studies.

IV. RESULTS

A. Hg-lamp stimulation

Typical data obtained with 254 nm radiation from a Hg lamp are shown in Fig. 6.[7,24] The depositions were carried out at a total pressure of 0.1 bar using the three Ga compounds TMG, TEG, and TIBG. For each compound data on UV stimulation are shown for two temperatures, one above and one below the transition point between transport dominated and reaction limited growth. For transport limited conditions, the UV effect is negligible, as expected. It is distinctly visible at lower temperatures, where the growth process is reaction limited. Moreover, the magnitude of the percentage increase in deposition rate upon irradiation decreases with the stability of the metal-organic compound, i.e., in the direction TMG to TEG to TIBG.

In earlier publications[7,23] it was argued, that at reaction limited conditions without illumination the growing surface appears to become covered with alkyl or Ga-alkyl groups. This leads to a saturation of the growth rate with increasing pressure of the metal-organic compound. An example of this behavior is shown in Fig. 7,[7] which shows a clear slowing down of the increase in growth rate with increasing TEG pressure. Similar data were obtained with TMG; in this case the saturation effect is even more pronounced. In both cases the slowdown or saturation of the rate increase is relieved by the UV radiation. It was also shown that this slowdown or saturation is not caused by slow dissociation of the AsH_3, since an increase of the AsH_3 concentration does not affect the rates observed in the dark.

The importance of surface processes in the rate limiting step is further underlined by the effect of irradiation on the morphology of the surface. In all cases a smoother surface

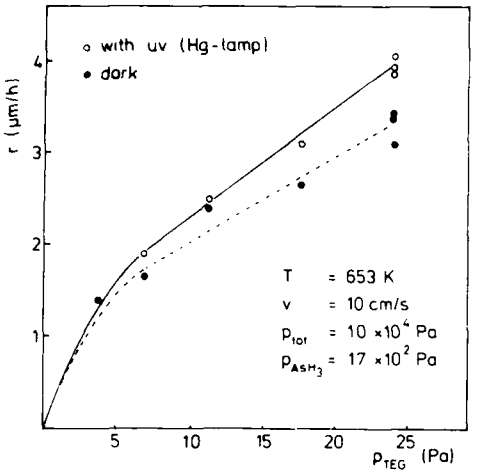

FIG. 7. Dependence of GaAs growth rate on TEG pressure without and with Hg lamp ($\lambda = 254$ nm) stimulation; thickness data from SEM measurements taken from Ref. 7, but using corrected vapor pressures from Ref. 24.

and a reduced growth of pyramids and whiskers was observed with UV.

B. Excimer-laser stimulation

There are two main differences between using UV irradiation from an excimer laser and from a Hg lamp. The laser stimulation is not continuous in time but the energy is applied in ~20-ns pulses at a repetition rate of 10 Hz. Moreover, the average power supplied by the laser is higher by a factor of 700 compared to that in the Hg-lamp experiments. Additionally, the wavelengths are different. In all laser experiments the area of deposition was clearly visible and corresponded roughly to the cross section of the laser beam. Also with laser stimulation a smoother surface was obtained.

The data in Fig. 8 show the temperature dependence of the growth rate at a total pressure of 0.1 bar with and without

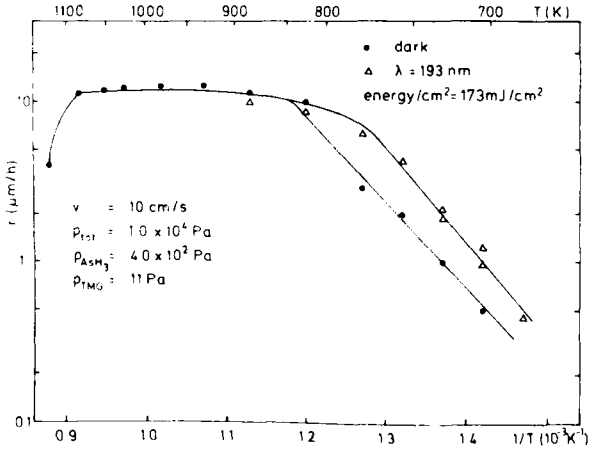

FIG. 8. Temperature dependence of GaAs growth rate with and without excimer laser ($\lambda = 193$ nm) stimulation using TMG; thickness data from optical and weight measurements.

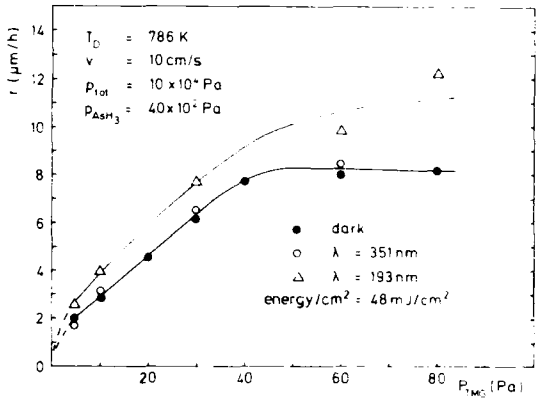

FIG. 9. Dependence of GaAs growth rate on TMG pressure without and with excimer-laser stimulation ($\lambda = 193$ nm); data for excimer laser irradiation at $\lambda = 351$ nm are also shown; data from optical thickness measurements.

laser irradiation at 193 nm. As expected, UV stimulation is only observed in the temperature region below 850 K, where the growth process is kinetically limited. Interestingly, the magnitude of the increase due to irradiation is rather modest (approximately a factor of 2) and the percentage increase roughly constant over the range investigated.

For larger TMG pressures at temperatures in the reaction-limited region the rate tends to saturate (Fig. 9), as observed in the Hg-lamp experiments. The effect of UV irradiation in the lower-TMG pressure region is to raise the rate by 20% to 30%. However, the saturation of the rate at higher pressures is removed, at least in the pressure region investigated. In this case a wider beam was used, so that the illuminated area on the substrate was nearly four times as large as in the case of Fig. 8; consequently, the energy density per cm^2 was lower by the same factor. Whereas at the higher energy density the window remained clean, in the latter case a slight amount of deposition was observed, indicating that the flushing was not completely effective. Thus, the values reported in Fig. 9 for growth with UV irradiation represent a lower boundary.

Also shown in Fig. 9 are data for 351-nm radiation which was applied at the same energy density as the 193-nm radiation. According to the absorption spectrum in Fig. 4 photodissociation at this wavelength does not occur. Thus, only thermal effects could contribute to the rate. From the absence of any effect of the 351 nm radiation on the rate it follows that heating of the substrate does not play a significant role. Consequently, thermal effects can be excluded as an explanation for the stimulation observed with 193 nm irradiation.

At the same conditions as used in the experiments of Fig. 9 and a TMG pressure of 30 Pa the effect of the repetition rate of the laser pulses was explored. Increasing the pulse rate but keeping the energy per pulse constant led to a sublinear increase of the growth rate (increasing the pulse frequency from 10 to 50 Hz resulted in roughly doubling the increase).

The data in Fig. 10 show the influence of the AsH_3 pressure on the growth rate. As in the case of Fig. 3 there is a slight dependence of the growth rate without illumination on

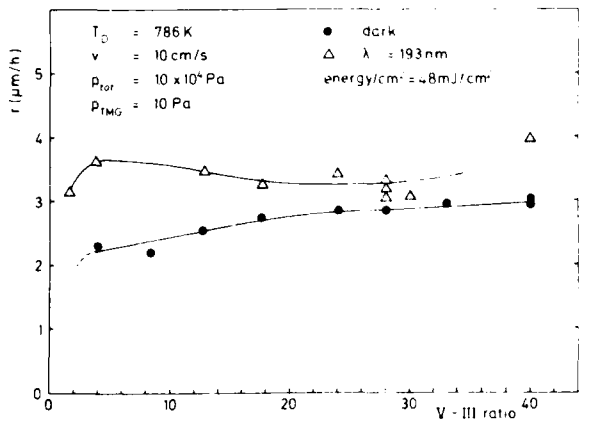

FIG. 10. Dependence of GaAs growth rate on V/III ratio for constant TMG pressure without and with excimer laser stimulation (λ = 193 nm); data from optical thickness measurements.

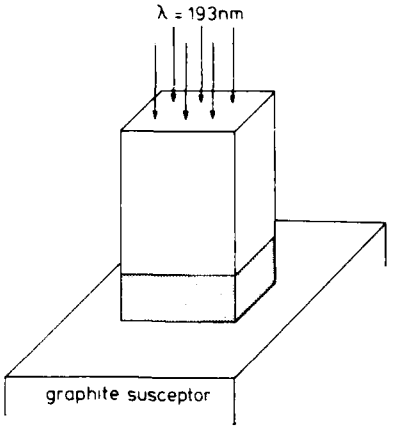

FIG. 11. Schematic of irradiation geometry used in calculations; cross section of beam 1 × 1 cm²; absorption volume of interest near surface is indicated.

the AsH_3 pressure for low values of the pressure, but otherwise the rate is essentially constant. UV radiation generally causes the rate to increase, but the magnitude of the stimulation effect at a given TMG pressure appears to depend on the AsH_3 pressure. At higher pressures the effect on the rate is small. However, it clearly increases for lower pressures.

V. DISCUSSION

One of the surprising features of the data presented above is that the increase of the rate observed in the two cases (Hg lamp and excimer laser) is of comparable magnitude, even though the total energy entering the reactor per unit time is different by a factor of 700. However, when considering the large difference in extinction coefficient at these two wavelengths it turns out that the number of photons available for photodecomposition in the surface region is essentially the same for both cases. The experiments with 351-nm-laser radiation prove that the effect for the two shorter wavelengths must be photochemical in nature. To understand the stimulation process, particularly for application in selective deposition, it would be of crucial importance to be able to distinguish between UV stimulation of reactions occurring in the gas phase and those at the substrate surface. The observation that the laser beam cross section corresponded to the deposited area indicates that processes at the surface or in gas phase regions close to the surface dominate in the enhancement of the growth.

The occurrence of photochemical reactions is therefore important for the growth process if they take place at or near the substrate surface. To this end we have performed some simple model calculations based on Lambert–Beer's law using the extinction data in Figs. 4 and 5 to find out what fraction of the energy reaches the substrate and to what extent the gas phase near the surface is affected by absorption of energy and consequently by photodissociation of the reactants. The radiation was assumed to enter the reactor as a cylindrical beam of 1 cm² cross-sectional area (Fig. 11).

In the case of the 254-nm-Hg lamp irradiation the absorption in the gas phase was nearly negligible, the photodissociation of TMG being at most of the order of 2%. This finding suggests that a stimulation of some processes at the surface must at least play an important role. As mentioned before, the 351 nm radiation is not absorbed in the gas phase and does not lead to surface reactions either, since any effect on the deposition rate was absent.

For the 193 nm radiation the absorption in the gas phase cannot be neglected. The energy density reaching the surface strongly depends on the concentration of the reactants, since these materials may absorb considerable amounts of energy in the upper layers of the gas phase. The increase in growth rate Δr caused by UV irradiation will be discussed from this angle utilizing the following three figures. We will assume that thermally and optically stimulated growth are additive.

The data of Fig. 8 have been replotted to show Δr vs $1/T$ (Fig. 12). It may be seen that Δr increases exponentially towards higher temperatures. This may be explained qualitatively as follows: At higher temperatures an increasing

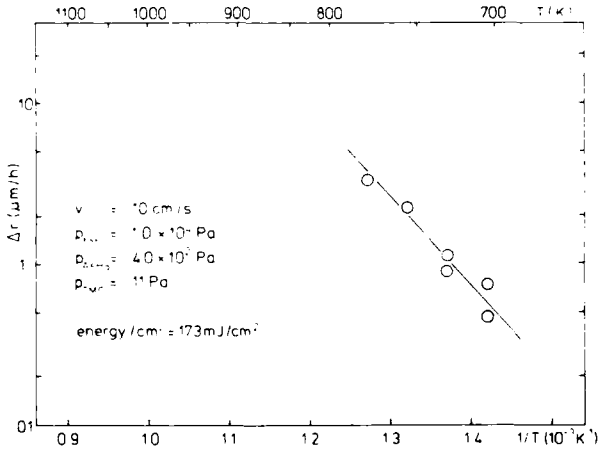

FIG. 12. Temperature dependence of increase in growth rate caused by excimer-laser radiation (λ = 193 nm); data points (open circles) derived from Fig. 8.

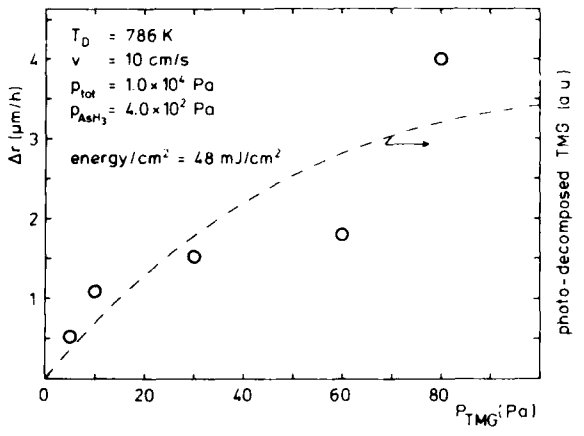

FIG. 13. Dependence of increase in growth rate caused by excimer laser radiation ($\lambda = 193$ nm) radiation on TMG pressure; data points (open circles) derived from Fig. 9; dashed line: calculated density of photodecomposed TMG near substrate surface (see the text).

fraction of the TMG will be thermally dissociated. As a consequence, the absorption will decrease and more photons will reach the surface, which leads to increased photodissociation of the TMG near the surface and thereby to enhanced growth. The exponential behavior directly follows from Lambert–Beer's law.

Figure 13 exhibits experimental data (open circles) taken from Fig. 9 for the increase in growth rate with increasing TMG pressure. The dashed line represents the calculated concentration of photodecomposed TMG in an 0.5-cm-deep area adjoining the substrate (see volume indicated in Fig. 11). The vertical scale was used as a fitting parameter. It may be seen that this simple model indeed roughly represents the experimental data. At low-TMG pressures the rate increases linearly with the TMG pressure since the fraction of photons absorbed in the upper regions of the gas phase is mainly determined by the AsH_3 pressure. At higher-TMG pressures the TMG makes itself more and more felt and finally dominates the absorption behavior. This explains the

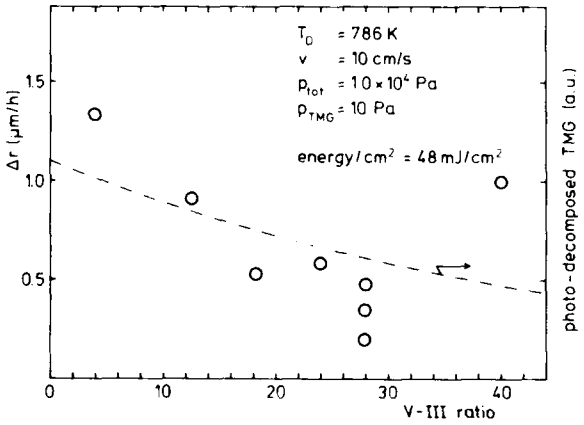

FIG. 14. Dependence of increase in growth rate caused by excimer laser radiation ($\lambda = 193$ nm) on V/III ratio for constant TMG pressure; data points (open circles) derived from Fig. 10; dashed line: calculated density of photodecomposed TMG near substrate surface (see the text).

sublinear increase of the rate in Fig. 13. In fact, at even larger pressures the rate should reach a maximum and decrease again.

The effect of bulk-gas phase absorption, in this case particularly of AsH_3, is also visible in Fig. 14, where the experimental points show the Δr vs V/III-ratio data (at constant TMG pressure) taken from Fig. 10. The dashed line shows again the computed data for the concentration of photodecomposed TMG in the gas phase near the surface. The curve was scaled to fit the experimental points. Since in all cases the gas phase is As rich the increase in the rate caused by UV irradiation is a function of the amount of photodissociated TMG near the substrate. Because of the increasing loss of photons due to absorption by the AsH_3 in the bulk of the gas phase, Δr will decrease with increasing V/III ratio, as found experimentally.

When using a beam with cross section of 1 cm^2 and a pulse rate of 10 Hz, at a linear flow velocity of 10 cm/s the entire gas phase flowing over the sample should be exposed to UV radiation. Higher pulse rates should lead to an increase in the amount of reactants dissociated, but also to an increase in the amount of energy reaching the surface per unit time. The sum of these effects apparently leads to a less than linear increase of the growth rate with pulse rate.

To distinguish between UV assisted reactions at or near the surface will require further experiments. Using incidence parallel to the surface would be helpful in deciding this question, but only if radiation is used of a wavelength where the optical absorption in the gas phase is relatively weak. An alternative is to utilize pulsed injection of the reactants, as done in atomic layer epitaxy,[30] and to apply the irradiation perpendicular to the surface between the reactant injection pulses. These experiments are in progress in our laboratory at the present time.

VI. CONCLUSIONS

From the data and discussion in the foregoing sections some important conclusions may be drawn for the investigated system:

(i) UV-assisted growth only takes place in areas of the substrate which are directly exposed to irradiation.

(ii) The UV-stimulation effect is largest for the most stable metal-organic compounds.

(iii) Loss of photons due to absorption in the gas phase plays an important role in determining the magnitude of UV-assisted growth of GaAs; it requires careful tailoring of the experimental conditions and of the geometry of the reactor.

(iv) The relative importance of gas phase and surface reactions is not completely clear as yet. However, the photochemical processes leading to growth take place very near to the surface.

ACKNOWLEDGMENTS

The authors are indebted to W. Kläui for making his UV spectrometer available for absorption measurements on TMG. Discussions with H. Heinecke, H. Jürgensen, and M. Weyers were helpful in defining conditions for stimulated

growth. M. Heyen made important contributions to the design of the reactor and the gashandling system. The financial support of the VW Foundation for this work is gratefully acknowledged.

[1]K. P. Pande and O. Aina, J. Vac. Sci. Technol. A **4**, 673 (1986).
[2]H. Heinecke, A. Brauers, H. Lüth, and P. Balk, J. Cryst. Growth **77**, 241 (1986).
[3]A. Brauers, F. Grafahrend, H. Heinecke, H. Lüth, and P. Balk, "Advanced Materials for Telecommunications," presented at the European Materials Research Society Proceedings Meeting, Strasbourg, France, 1986, code R **13**, p. 231.
[4]S. Sakai, S. Yomamoto, and M. Umeno, Jpn. J. Appl. Phys. **25**, 1156 (1986).
[5]H. Heinecke, F. Grafahrend, A. Brauers, H. Lüth, and P. Balk, *Photon, Beam and Plasma Stimulated Chemical Processes* (Materials Research Society, Pittsburgh, PA 1987), p. 75.
[6]K. J. Jones, Solid-State Technol. **28**, 151 (1985).
[7]P. Balk, H. Heinecke, C. Plass, N. Pütz, and H. Lüth, J. Vac. Sci. Technol. A **4**, 711 (1986).
[8]V. M. Donnelly, D. Brasen, A. Appelbaum, and M. Geva, J. Appl. Phys. **58**, 2022 (1985).
[9]V. M. Donnelly, D. Brasen, A. Appelbaum, and M. Geva, J. Vac. Sci. Technol. A **4**, 716 (1986).
[10]J. Haigh, J. Vac. Sci. Technol. B **3**, 1456 (1985).
[11]V. M. Donnelly, M. Geva, J. Long, and R. F. Karlicek, Appl. Phys. Lett **44**, 951 (1984).
[12]J. Nishizawa, H. Abe, T. Kurabayashi, and N. Sakurai, J. Vac. Sci. Technol. A **4**, 706 (1986).
[13]F. A. Houle, Appl. Phys. A **41**, 315 (1986).
[14]T. F Deutsch, D. J. Ehrlich, and R. M. Osgood, Jr., Appl. Phys. Lett. **35**, 175 (1979).
[15]S. Y. Tsao and D. J. Ehrlich, Appl. Phys. Lett. **45**, 617 (1984).
[16]T. Motooka, S. Gorbatkin, D. Lubban, and J. E. Greene, J. Appl. Phys. **58**, 4397 (1985).
[17]G. S. Higashi and C. G. Fleming, Appl. Phys. Lett. **48**, 1051 (1986).
[18]M. J. Mayo, Solid-State Technol. **29**, 141 (1986).
[19]J. Takahashi and M. Tabe, Jpn. J. Appl. Phys. **24**, 274 (1985).
[20]M. Okuyama, Y. Toyoda, and Y. Hamkawa, Jpn. J. Appl. Phys. **23**, 297 (1984).
[21]Y. Taroi, J. Hidaka, and K. Hota, Jpn. J. Appl. Phys. **23**, L827 (1984).
[22]Y. Namasawa, K. Yamazaki, and K. Hamano, J. Electron. Mater. **15**, 27 (1986).
[23]N. Pütz, H. Heinecke, E. Veuhoff, G. Arens, M. Heyen, H. Lüth, and P. Balk, J. Cryst. Growth **68**, 194 (1984).
[24]C. Plass, O. Kaiser, H. Heinecke, H. Lüth, and P. Balk (to be published).
[25]N. Pütz, H. Heinecke, M. Weyers, M. Heyen, H. Lüth, and P. Balk, J. Cryst. Growth **74**, 292 (1986).
[26]S. A. Mitchel, D. A. Hackett, D. M. Rayner, and M. R. Humphries, J. *Chem. Phys.* **83**, 5028 (1985).
[27]H. H. Gilgen, C. J. Chen, R. Krchnavek, and R. M. Osgood, Jr., Springer Ser. Chem. Phys. **39**, 225 (1984).
[28]J. Haigh, J. Mater. Sci. **18**, 1072 (1983).
[29]R. F. Karlicek, B. Hammarlund, and J. Ginocchio, J. Appl. Phys. **60**, 795 (1986).
[30]A. Doi, Y. Aoyagi, and S. Namba, Appl. Phys. Lett. **48**, 1787 (1986).

Atomic-layer growth of GaAs by modulated-continuous-wave laser metal-organic vapor-phase epitaxy

Yoshinobu Aoyagi, Atsutoshi Doi, Souhachi Iwai, and Susumu Namba
RIKEN, The Institute of Physical and Chemical Research, Wako-shi, Saitama, 351-01, Japan

(Received 18 March 1987; accepted 8 June 1987)

Atomic-layer epitaxy (ALE) including self-arresting deposition mechanism at 100% surface coverage is realized in GaAs by a modulated-continuous-wave laser metal-organic vapor-phase epitaxy technique. Selective decomposition of trimethylgallium (TMG) or triethylgallium (TEG) on an As-atom layer by laser irradiation is an important mechanism to realize the ALE. The experimental results are well-explained by a calculation based on this selective decomposition mechanism.

I. INTRODUCTION

Recently many researchers have become interested in techniques of thin epitaxial-layer growth controlled in one atomic layer scale to get abrupt heterostructure interfaces and extremely thin layers of a quantum-well structure. Molecular-beam epitaxy (MBE)[1] and metal-organic vapor-phase epitaxy (MOVPE)[2] techniques have recently made it possible to grow such epitaxial layers. However, in both techniques the epitaxial layer is continuously grown and the growth rate is essentially sensitive to growth parameters, such as growtn time, growth temperature, and flux of sources. Therefore, the precise control of these parameters is important to achieve one atomic layer crystal growth in these techniques. On the other hand, an ideal atomic-layer epitaxy (ALE) has a mechanism of self-arresting deposition at 100% surface coverage. Therefore, one atomic layer growth could be easily achieved, even if growth parameters are largely changed. This unique mechanism of ALE is one of attractive points for the growth of the thin layer with one atomic scale preciseness.

After a proposal of ALE by Suntola,[3] several ALE techniques[4–6] have been developed. The main technique to achieve ALE used so far is to control the adsorption and desorption of source elemental atoms and to realize one monolayer adsorption on the surface. In case of II–VI compounds[7] the vapor pressure of group II and VI elemental atoms is very high. Therefore, even if the excess source gas is supplied on the substrate, the condition of one monolayer adsorption can be realized by desorbing the adsobates thermally under a proper condition of the growth temperature. In case of III–V compounds the vapor pressure of group V elements is very high and the same technique done for II–VI compounds is used for growth of group V elements.

However, the vapor pressure of group III elements is very low. Therefore, it is very difficult to control adsorption of the group III element to one monolayer by controlling the adsorption and desorption, which was done for II–VI compounds. Even if we use molecules including the elemental atom of group III to increase the vapor pressure, the method controlling the adsorption and desorption to get the monolayer is not suitable for the adsobates with a size larger than a bond length of atoms of the substrate, because steric hindrance of each adsobate obscures the 100% coverage of adsobates at the surface. Even if trimethylgallium (TMG) is used in case of GaAs, which is one of the small metal-organic compounds with a planer structure,[7] 100% coverage is difficult due to the steric hindrance. Moreover, this method is not suitable for the molecules (e.g., TMG) which adsorb and decompose on the decomposed element itself (Ga in case of GaAs), because the vapor pressure of the decomposed group III element (Ga) is very low and this decomposition violates the ALE requirement of arresting the deposition at 100% coverage of the surface. Therefore, it is very difficult to achieve the ideal growth rate of 1 monolayer/cycle in the metal-organic compounds—AsH_3 system for GaAs.

If the decomposition rate of TMG or triethylgallium (TEG) on the As layer is much larger than that on the Ga layer and the decomposition rate on the Ga layer is small, most of the TMG or TEG is decomposed on the As atom layer. Once the As layer is covered by the Ga atom, the adsorbed TMG or TEG on that layer does not decompose due to the low-decomposition rate of TMG or TEG on the Ga atom layer. Therefore, self-arresting of the deposition of Ga at 100% coverage is achieved and the ideal ALE is realized.

In this paper we describe the new ALE technique (laser ALE) of GaAs by a modulated-cw-laser MOVPE (ML-MOVPE).[8,9] Using this technique the ideal growth rate of one monoatomic layer/cycle is realized. The experimental results are analyzed by a selective decomposition model for the adsorbed TMG on As-atom layer under an Ar-ion laser irradiation.

II. EXPERIMENT

To achieve an ideal ALE crystal growth we developed the modulated-cw laser MOVPE technique. Figure 1(a) shows a schematic diagram of the furnace of the modulated-cw laser MOVPE and typical time sequences of the source gas flow and the laser-light irradiation. In this technique, the source gases of TMG or TEG and AsH_3 are separately introduced into a growth chamber by switching the valves, and the laser is selectively irradiated onto the substrate during a period of the desired gas flows by rapidly switching the shut-

 0734-211X/87/051460-05$01.00 © 1987 American Vacuum Society

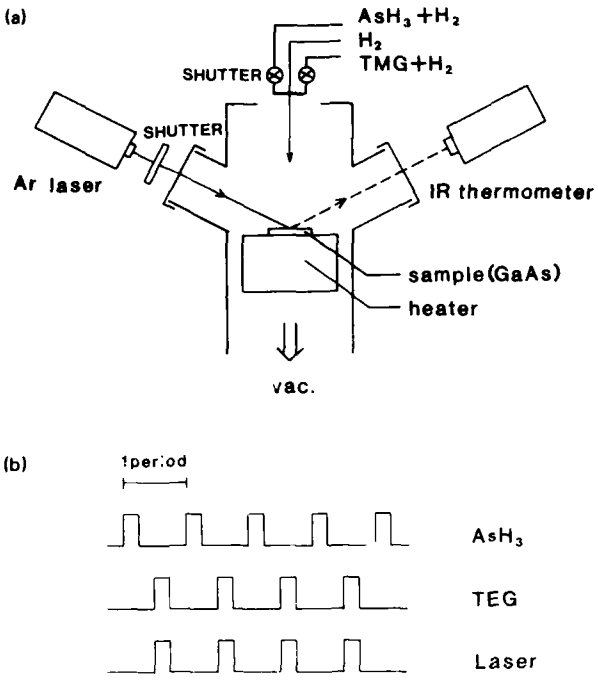

FIG. 1. (a) Schematic diagram of the furnace of the modulated-cw-laser MOVPE and (b) typical time sequences of the source gas flow and the laser irradiation.

ter on and off. In a typical experimental condition, AsH_3 (20% in H_2) with a flow rate of 100 sccm was accumulated for 3 s before switching and was switched on for 1 s with keeping the same flow rate, so that 5×10^{-5} mol/cycle of AsH_3 was fed into the growth chamber. The typical amount of TMG or TEG fed into the chamber by the same method was 6.3×10^{-7} mol/cycle. The H_2 carrier gas was constantly fed into the chamber with a flow rate of 2700 sccm. The gases of TMG or TEG and AsH_3 were alternatively fed into the chamber with an interval of 1 s to prevent mixing of the gases. Since the effective volume of the growth chamber is about 100 cc, a flushing time of 1 s seems to be enough to minimize mixing of the gases. The growth system was operated at a pressure of 100 mb. A typical time sequences of the gases and laser irradiation are shown in Fig. 1 (b). In this case the laser irradiation coincides with the TMG or TEG gas flow. If the laser irradiation coincides with the AsH_3 gas flow, we do not observe any crystal growth of GaAs.

The laser used was the cw-Ar-ion laser with a wavelength of 514.5 nm and a power of 1.2 W typically. An excimer laser is one of candidates of the laser ALE. However, in case of the excimer laser the decomposition of TMG or TEG occurs in the gas phase and the Ga atom decomposed in the gas phase sticks on the substrate and this sticking violates the ALE condition. Therefore, in our experiment the Ar-ion laser is used to promote only the surface-photochemical decomposition[10,11] to realize the ALE. The irradiated area was an ellipse shape with the line of apsides of 1 mm and the minor axis of 0.5 mm.

The epitaxial layer of GaAs was grown on Si-doped ($n=2\times10^{18}$ cm^{-3}) substrates with an orientation of (100) $\pm$ 0.5°.

III. EXPERIMENTAL RESULTS AND DISCUSSION

Figure 2 shows a typical photograph of the crystal grown under the ALE condition of 430 °C for TEG. As shown in this photograph the growth rate of the laser-irradiated part at the center is largely enhanced and has a plateau shape in spite of the Gaussian profile of the intensity of the laser beam shown in the bottom of this figure. No deposition of GaAs is observed in the area without the laser irradiation at this temperature. This growth of the plateau shape is one of the characteristics of the laser ALE.

The temperature dependence of the growth rate is shown in Fig. 3 for TMG and TEG with and without the laser irradiation. In case of TMG the growth rate is independent of the growth temperature between 370 and 430 °C, with a constant value of one monolayer/cycle (0.283 nm/cycle) under the laser irradiation, but any temperature-independent region is not observed without the laser irradiation as shown in the figure by circles in case of TMG. This result suggests that the ALE is achieved by the modulated-cw-laser MOVPE technique in the temperature region of 370–430 °C and the growth mechanism must involve a surface photoreaction. The growth rate is dependent on the temperature above and below this temperature region. In the temperature region more than 430 °C the curves of the temperature dependence of the growth rate under the laser irradiation seems to be shifted about 60 °C from the curves of the temperature dependence without the laser irradiation. In

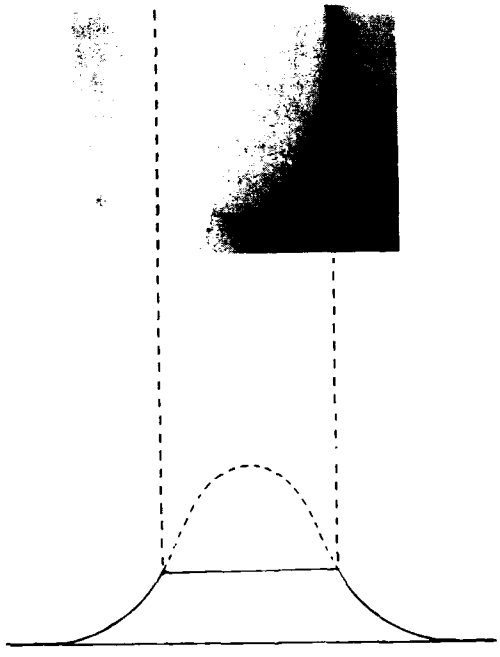

FIG. 2. Typical photograph of the crystal grown under the laser ALE by using TEG.

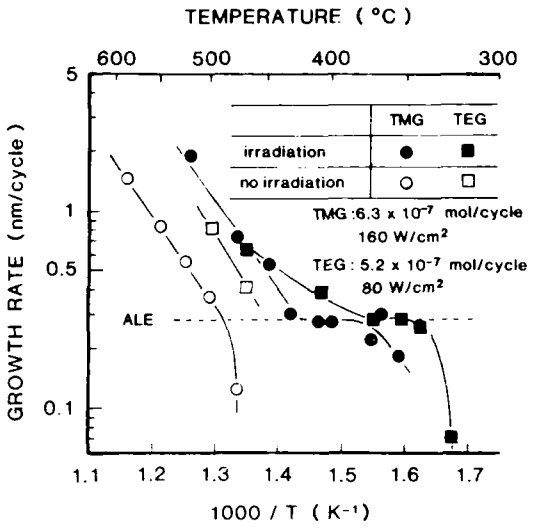

FIG. 3. Temperature dependence of the growth rate with and without the laser irradiation for TMG and TEG.

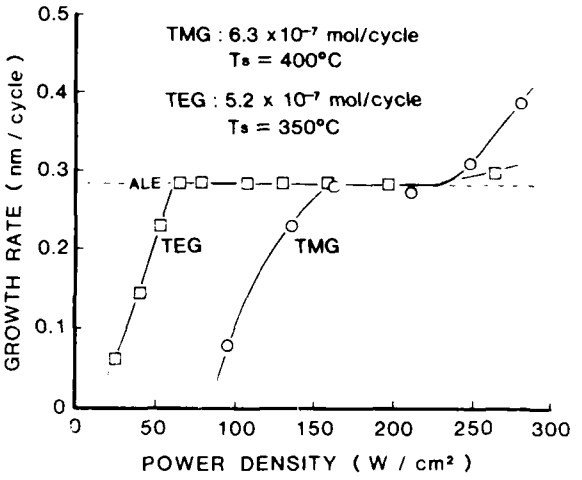

FIG. 4. Growth rate as a function of the laser power for TMG and TEG.

this temperature region the crystal growth is mostly caused by a pyrolytic decomposition of TMG adsorbed onto the substrate surface and the photochemical reaction at the surface is masked by this pyrolytic reaction. The shift of 60 °C is possibly caused by a local-temperature heating of 60 °C during the laser irradiation at 160 W/cm^2. In the lower-temperature region it seems that an enhancement of the growth by the photochemical reaction could not compensate the decrease of the growth rate due to the temperature decrease. Therefore, the growth rate decreases, even if the laser light is irradiated. This result suggests that a temperature-dependent mechanism should be included in a growth mechanism and this temperature dependence is arrested under the laser irradiation for the temperature-independent region from 370 to 430 °C. In case of TEG the temperature-independent region is also observed under the laser irradiation but the temperature region is lower than that of TMG and the lowest limit of the temperature to get the temperature-independent growth rate is 350 °C for TEG. However, the behavior of the temperature dependence of the growth rate is almost same in TMG and TEG.

The growth rate as a function of the laser power is shown in Fig. 4. The growth rate is constant at a value of 1 monolayer/cycle when the laser power is between 150 and 230 W/cm^2 for TMG and 80 to 230 W/cm^2 for TEG. The increase of the growth rate above 230 W/cm^2 is attributed to a local-temperature increase due to the laser irradiation. An estimated temperature increase of 90 °C at 230 W/cm^2 leads to a local-substrate temperature as high as 490 °C for TMG and 440 °C for TEG. This temperature is equal to the critical temperature of 490 °C for TMG and 440 °C for TEG at which decomposition of TMG occurs thermally at the surface. The growth rate decreases when the laser power is $>$150 W/cm^2 for TMG and 60 W/cm^2 for TEG. This decrease is due to the amount of decomposed TMG or TEG is not enough to cover one atomic layer in this laser-power region.

The growth rate of GaAs as a function of a TMG or TEG flux/cycle introduced is shown in Fig. 5. Above the TMG or TEG flux of 1×10^{-7} mol/cycle, the growth rate is independent of the TMG or TEG flux and remains constant at 1 monolayer/cycle up to the highest TMG or TEG flux examined in our experiments. Below the TMG or TEG flux of 1×10^{-7} mol/cycle, the growth rate decreases with decreasing the TMG or TEG flux. However, the growth rate does not show a linear dependence on the TMG or TEG flux as in the case for the conventional MOVPE where the growth rate is limited by a mass transport.

To explain all of data mentioned above, a model schematically shown in Fig. 6 is assumed. That is, the adsorbed TMG or TEG on the Ga atom and on the As atom has a different decomposition lifetime of τ_{Ga} and τ_{As}, respectively, and TMG or TEG does not adsorb on TMG or TEG which has already adsorbed on the GaAs substrate. We also introduce the desorption lifetime of τ_d. Under the laser irradiation, τ_{Ga} and τ_{As} is changed, but the change of τ_{As} is much larger than that of τ_{Ga}. If the decomposition rate of TMG or TEG on the As atom is much higher than that on the Ga atom, the deposition of Ga stops automatically at 100% coverage of

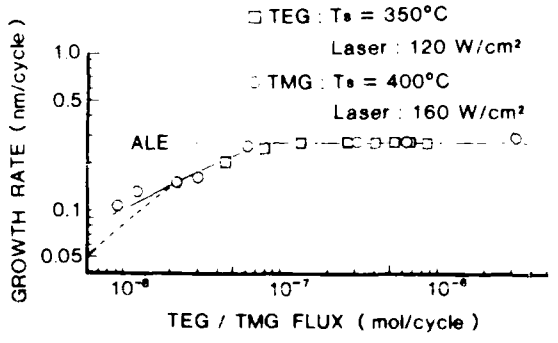

FIG. 5. Growth rate as a function of the flux/cycle for TMG and TEG.

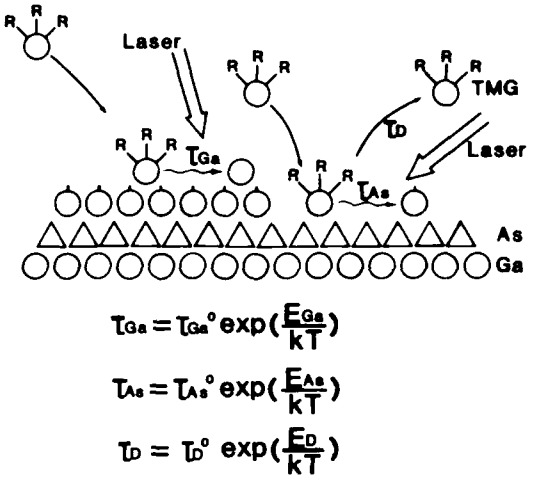

FIG. 6. Schematic diagram of our model in which the selective decomposition of a metal-organic compound at the As surface is assumed.

Ga on the As atom. The ideal ALE is realized under this condition. Concerning the As deposition, AsH_3 is supplied during 1 s with an interval of 3 s in the ML-MOVPE. This time sequence allows the thermal decomposition of the adsorbed AsH_3 and the desorption of the excess As because of the high-vapor pressure of As. Therefore, the monolayer growth of As is automatically achieved. In the calculation discussed in this report, therefore, only the deposition of Ga is considered. This model gives following rate equations:

$$\frac{dX}{dt} = AF(1-X) - X/\tau_{dec} - X/\tau_d , \tag{1}$$

$$1/\tau_{dec} = S/\tau_{Ga} + (1-S)/\tau_{As} \quad \text{for } 0 \le S \le 1 , \tag{2}$$

$$AF = AB(N_{in}/N_{st}) , \tag{3}$$

where A is a rate of the supply of TMG on the substrate, F is a sticking coefficient, X is a density of TMG on the substrate, N_{in} is the feeding rate of TMG into the growth chamber, N_{st} is the surface density of the lattice site, B is a constant depending on the growth system. We estimate AB is 0.025 from the analysis reported in a previous paper.[8,9] S is a surface coverage of Ga on the substrate. When S becomes ~ 1, τ_{dec} is considered to be equal to τ_{Ga}.

The lifetime is considered to have an activation process given by

$$\tau_{Ga} = \tau_{Ga}^{0} \exp(E_{Ga}/kT) , \tag{4}$$

$$\tau_{As} = \tau_{As}^{0} \exp(E_{As}/kT) , \tag{5}$$

$$\tau_{d} = \tau_{d}^{0} \exp(E_{d}/kT) . \tag{6}$$

The thermal process is included through these equations.

Under the laser irradiation the total decomposition rate due to the heating of the substrate and the laser irradiation is given by

$$1/\tau_{As,Ga} \quad 1/\tau'_{As,Ga} + 1/\tau^{l}_{As,Ga} , \tag{7}$$

where τ' and τ^{l} mean the lifetime with and without the laser irradiation, respectively.

Since the deposition yield of Ga for feeding during 1 s is given by

$$Y = \int_0^1 X/\tau_{dec}\, dt , \tag{8}$$

we can calculate the deposition yield of Ga as a function of the temperature, the laser power and the flux, from Eqs. (1)–(8). The parameters used typically are

$$\tau_d = 0.003 \exp[0.2(\text{eV})/kT] , \tag{9}$$

$$\tau'_{Ga} = 4\times 10^{-13} \exp[1.9(\text{eV})/kT] , \tag{10}$$

$$\tau'_{As} = 9\times 10^{-14} \exp[1.9(\text{eV})/kT] , \tag{11}$$

$$\tau^{l}_{Ga} = 3\times 10^{-13} \exp[1.9(\text{eV})/kT] , \tag{12}$$

$$\tau^{l}_{As} = 3\times 10^{-15} \exp[1.9(\text{eV})/kT] . \tag{13}$$

The calculated results well-explain the experimental results of temperature dependence, laser-light intensity dependence and flow-rate dependence of the growth rate with and without laser irradiation by using these parameters. The details of the calculated results are reported elsewhere. A typical example of the calculation is shown in Fig. 7 for the temperature dependence of the growth rate. Solid curves are calculated results for various enhancement factors of the decomposition rate of TMG which is determined as a ratio of the decomposition lifetime of TMG on Ga to that on As under the laser irradiation. By introducing the 40 times enhancement of the decomposition rate of TMG under the laser irradiation, the plateau region and the temperature dependent regions are well-explained in this calculation.

There are several unknown parameters used for fitting the experimental results. Therefore, it is difficult to confirm the validity of the values used for the fitting at this stage. The details of the discussion will be done elsewhere. However, the emphasis of this paper is to demonstrate the possibility to understand the ALE mechanism in the macroscopic view given by the rate equation of Eq (1). We believe that this is a first trial to understand the characteristics of the ALE theoretically.

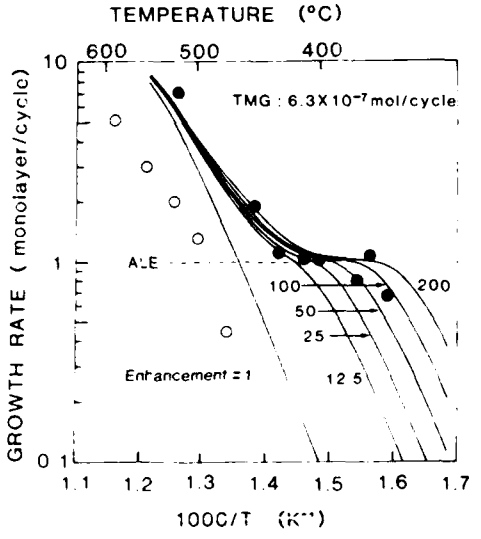

FIG. 7. Typical example of the calculation for the temperature dependence of the growth rate as a function of various enhancement factors. ● and ○ are experimental results with and without the laser irradiation, respectively.

In case of the thermal decomposition, the decomposition rate on the As atom and the Ga atom is almost same. In this case a plateau region would not exist and the straight line shown in the figure for the enhancement factor of 1 is obtained. This result is in good agreement with the temperature dependence of the growth rate without the laser irradiation except the shift of 60 °C, which is due to the local heating of the substrate by the laser irradiation.

It is clear that the effect of the laser irradiation is not the thermal effect but the photochemical reaction. If the thermal effect is dominant, and the increase of the local temperature by the laser-light irradiation is a main mechanism of this ALE, we have to observe the plateau region without the laser irradiation at the growth rate of 1 monolayer/cycle as observed under the laser irradiation. However any plateau region has not observed without the laser irradiation. This result shows that the laser-irradiation effect is not the thermal effect. We find from the calculation that the growth characteristics without the laser irradiation are well-explained by assuming the decomposition rate of TMG or TEG on the As layer and the Ga layer is almost same. These results suggest that the enhancement of the decomposition of TMG or TEG on the As-atom layer by the laser irradiation is essential to get the ALE in the metal-organic–AsH_3 system.

IV. CONCLUSION

We demonstrate the new laser-ALE method by the modulated-cw-laser MOVPE with the self-arresting deposition mechanism at 100% surface coverage. This ALE seems to be achieved by the selective decomposition of the adsorbate of TMG under the laser irradiation. The experimental results are well-explained by the calculation based on this model.

[1] J. H. Neave, B. A. Joyce, and P. J. Dobson, Appl. Phys. A **31**, 1 (1983).
[2] A. Ishibashi, Y. Mori, M. Itabashi, and N. Watanabe, J. Appl. Phys. **58**, 2961 (1985).
[3] T. Suntola and J. Anston, U.S. Patent No. 4058430 (1977).
[4] J. Nishizawa, H. Abe, and T. Kurabayashi, J. Electrochem. Soc. **139**, 1197 (1985).
[5] A. Usui and H. Sunakawa, Jpn. J. Appl. Phys. **25**, L212 (1986).
[6] S. M. Bedair, J. K. Whisnant, N. H. Karam, M. A. Tischler, and T. Katsuyama, Appl. Phys. Lett. **47**, 174 (1986).
[7] B. Beagley and D. G. Schmidling, J. Mol. Struct. **21**, 437 (1974).
[8] A. Doi, Y. Aoyagi, and S. Namba, Appl. Phys. Lett. **48**, 1787 (1986).
[9] A. Doi, Y. Aoyagi, and S. Namba, Appl. Phys. Lett. **49**, 785 (1986).
[10] Y. Aoyagi, S. Masuda, S. Namba, and A. Doi, Appl. Phys. Lett. **47**, 95 (1985).
[11] A. Doi, Y. Aoyagi, and S. Namba, *Gallium Arsenide*, edited by M. Fujimoto (Adam Hilger Ltd., Bristol and Boston, 1985), p. 331.

Summary Abstract: Mass spectral identification of ultraviolet-laser photoablation products from polymers

R. C. Estler[a] and N. S. Nogar
Chemical and Laser Sciences Division, MS G738 LANL, Los Alamos, New Mexico 87545

(Received 27 February 1987; accepted 4 June 1987)

Much attention has been given to the laser photoablation of polymeric films because of applications to etching processes in the microelectronics industry, to eye safety, and to the general topic of laser/materials interactions. Much early work[1-3] indicated that exposure to very short wavelength ($\lambda \lesssim 193$ nm) lasers resulted in very sharp and precise etch features. This is in contrast to the burning and melting usually observed for irradiation with visible lasers. There has been considerable conjecture that the clean etch features are due to a photochemical mechanism, while the rougher features observed at longer wavelengths are controlled by photothermal processes. Extensive modeling of both photochemical and photothermal processes[4,5] has been made.

If the observed process is indeed photolytic, one would expect to observe a variation in the quantum yield(s) as a function of excitation wavelength. We have explored this phenomenon by direct observation,[6] via real-time mass spectrometry, of the volatile photoablation products. We report here on survey mass spectra of tetrafluoroethylene (TFE), polycarbonate (Lexan), polystyrene, and polymethylmethacrylate (PMMA), as well as the wavelength-dependent mass spectra of PMMA.

Our samples were mounted, on a vacuum manipulator, to the side of the normal ionization region of a quadrupole-mass spectrometer, ~3 cm from the central axis. The incident-laser beam passed through the ionization region before striking the polymer surface. Ablated material was spalled back into the ionization region, where it was ionized by 70 eV electrons, and sorted and detected by the quadrupole-mass filter. The photolysis was initiated by the frequency quadrupoled (266 nm) output of a Nd^{+3}:YAG laser, ~10 Hz. The temporal profile is ≈10 ns full width at half-maximum (FWHM), and smooth within the resolution of our electronics (≈2 ns). For wavelength-dependent experiments, coarse tuning was accomplished by Raman shifting in a cell containing molecular hydrogen at high-pressure (200 psi).

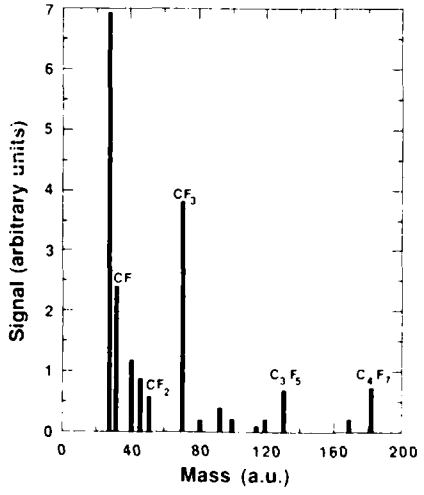

FIG. 1. Electron-impact (70 eV) mass spectrum of material ablated from tetrafluoroethylene (TFE) surface. Laser parameters: 266 nm, 50 mJ/cm², 10-ns pulse. The entire spectrum required ≈10 min (6000 shots) to accumulate.

Photolysis/mass spectrometry of TFE-produced ions of almost every possible combination of C_nF_m, up to mass 200 (the nominal high-mass limit of our scans), see Fig. 1. It is interesting to note, however, that very little signal corresponding to C_2F_m was observed. The dominant peak in the spectrum was due to CF_3, suggesting that either F atom migration in the substrate material, or recombination in the gas-phase plume takes place to an appreciable extent. By far the largest peak observed in the Lexan mass spectrum was due to CO, followed closely by C_2H_2, due in part to the inherent sensitivity of the mass spectrometer for these permanent gases. The next most intense peaks were due to phen-CH_2 (mass 91), Phen (mass 77), and common-hydrocarbon fragments resulting from the photolysis of gas-phase phenyl.[7] Mass analysis of polystyrene exfoliant yielded a large peak due to the monomer (phen-CH = CH_2), and to the various daughters resulting from laser photolysis and cracking due to electron impact. These included Phen, C_1H_n and C_2H_2.

The mass spectrum of PMMA at 266 nm, and a fluence of 50 mJ/cm² showed large amounts of CO and CO_2 (common contaminants in our system), and the monomer (MMA). Also present are the common MMA fragmentation peaks at 69 and 41 a.u. Similar spectra were recorded at 299 and 341 nm. At 240 nm, and the same fluence, the spectrum is quite different. The CO and CO_2 peaks are still evident, but the MMA and daughter peaks have disappeared. A new peak at 60 a.u. and others in the 29–32 a.u. range suggest that the dominant gas-phase product is now methyl formate (HCO_2CH_3). Furthermore, intensity-dependent studies indicate that production of this species is a single-photon event. We compare these results with other mass spectral studies, and propose an explanation for our observed wavelength dependence.

[a] Permanent address: Department of Chemistry, Fort Lewis College, Durango, Colorado 81301.

[1] J. E. Andrew, P. E. Dyer, D. Forster, and P. H. Key, Appl. Phys. Lett. **43**, 717 (1983).
[2] R. Srinivasan and W. J. Leigh, J. Am. Chem. Soc. **104**, 6784 (1982).
[3] J. T. C. Yeh, J. Vac. Sci. Technol. A **4**, 653 (1986).
[4] B. J. Garrison and R. Srinivasan, Appl. Phys. Lett. **44**, 849 (1984).
[5] B. J. Garrison and R. Srinivasan, J. Appl. Phys. **57**, 2909 (1985).
[6] R. C. Estler and N. S. Nogar, Appl. Phys. Lett. **49**, 1175 (1986).
[7] M. Rossi and D. J. Eckstrom, Chem. Phys. Lett. **120**, 118 (1985).

 0734-211X/87/051465-01$01.00 © 1987 American Vacuum Society

Sum-frequency generation on dye-coated surfaces using collinear and noncollinear excitation geometries

R. E. Muenchausen, D. C. Nguyen, R. A. Keller, and N. S. Nogar
Chemical and Laser Sciences Division, Los Alamos National Laboratory, Los Alamos, New Mexico 87545

(Received 1 May 1987; accepted 24 June 1987)

Resonantly enhanced surface second-harmonic generation and sum-frequency generation has been demonstrated on rhodamine 6G coated glass substrates using different excitation geometries. The collinearly excited, doubly-resonant sum-frequency signal is enhanced by more than two orders of magnitude relative to resonantly enhanced second-harmonic generation. For noncollinear excitation, the relative efficiency of nonlinear generation as a function of the angular dependence of the input beams is calculated and compared with experiment.

I. INTRODUCTION

It is well established that the lack of inversion symmetry at interfaces allows the electric-dipole contribution to the second-order susceptibility $\chi^{(2)}$ which is the predominant source of surface second-harmonic (SHG) and sum-frequency generation (SFG).[1] The temporal and spatial coherence of the nonlinear output from smooth surfaces is well established on both theoretical and experimental grounds. Due to its surface specificity, SHG has become an important surface probe.[2,3] It has also been demonstrated that SFG can be a sensitive technique for surface vibrational spectroscopy.[4,5]

In the case of the surface adsorbed dyes, the second harmonic signal is resonantly enhanced when 2ω matches the $S_0 \rightarrow S_2$ electronic transition of the dye. Marowsky *et al.* reported a three order of magnitude increase in the SHG signal of nile blue *A* compared to rhodamine 6G.[6] This increase was attributed to the simultaneous resonance of ω with the $S_0 \rightarrow S_1$ transition and 2ω with the $S_0 \rightarrow S_2$ transition. Generally, this full double-resonance enhancement cannot be realized with SHG for any molecule. For doubly-resonant sum-frequency generation, we expect the output to be enhanced orders of magnitude as was SHG of nile blue *A*, because two different frequencies can be used to address both resonant transitions.

Previous experimental studies of SHG and SFG from surfaces have used a collinear or a coplanar[4,5] excitation geometry. For surface generation the propagation distance of the fundamental beams through the nonlinear medium will be much less than their wavelength. The stringent phase-matching conditions for nonlinear generation in bulk media, which usually require collinear propagation of the input beams, can be relaxed for surface generation.[7]

These considerations suggest that it should be possible to use a noncollinear excitation geometry for the input beams to exploit the directional property of the output beam by spatially filtering the output. Spatial separation of the nonlinear output beam from the reflected fundamental beams will simplify the experimental setup and increase sensitivity relative to a collinear excitation geometry by reducing or eliminating the need for color filters or a monochromator.

II. EXPERIMENT

The experimental details of collinear SHG[8–10] and SFG[10] from rhodamine 6G coated substrates have been reported previously. The experimental setup used to accommodate a noncollinear excitation geometry is shown in Fig. 1.

For SHG a Nd·YAG pumped, tunable dye laser was operated at the peak of the SHG excitation curve at 695 nm. For SFG the tunable dye laser was used to provide ω_1 between 490 and 550 nm. The second laser beam at ω_2, 4% of the Nd:YAG IR fundamental, was delayed to synchronize the arrival times of both beams.

For collinear excitation the dye laser and IR beams were combined and directed onto the sample at an angle of incidence, $\theta \sim 60°$. For noncollinear excitation, the parallel input beams are focused onto the sample at $\theta \sim 60°$ using a $f/1.8$ focal-length lens. The angle between the projection of the input beams onto the surface ϕ could be varied between 3°–15° by adjusting the separation of the input beams on the focusing lens by moving mirrors M2 and M3 conjointly. The

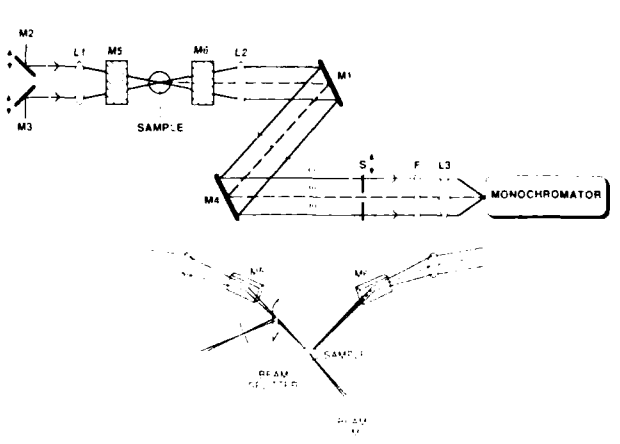

FIG. 1. Schematic of SHG and SFG optical components for noncollinear excitation geometry. M1–M6, mirrors; *F*, color filter; L1, 18-cm focal-length lens; L2, 15-cm focal-length lens; L3, 7.5-cm focal-length lens; *S*, scannable slit.

 0734-211X/87/051466-04$01.00 © 1987 American Vacuum Society

reflected beams were collimated with a 15-cm focal-length lens. A slit was scanned across the collimated output beams in order to spatially resolve the nonlinear output and reflected pump beams.

The transmitted light, which passed through a color filter, was focused onto the slit of a monochromator and detected by a photomultiplier tube. The PMT output was amplified and detected by a gated integrator/boxcar. Spin coated samples[8] were prepared from a 3×10^{-3} M ethanolic rhodamine 6G solution deposited on microscope cover slides yielding coverages ranging from 0.2–30 monolayers. All observed signals were verified to be coherent SHG or SFG based on their monochromaticity at the sum frequency, laser power dependence and spatial profile as discussed previously.[9,10]

III. RESULTS AND DISCUSSION

A. Collinear excitation

The magnitude of the SFG signal depends on the square of the complex second-order susceptibility $|\chi^{(2)}|$ which can be expressed in terms denoting the resonant interactions between two input laser frequencies and a three-level system, summed over all excited states,[11]

$$\chi^{(2)}(\omega_1,\omega_2,-\omega_{SF}) = \sum_{b,c}\frac{\mu_{ab}\mu_{bc}\mu_{ac}}{(\omega_{ba}-\omega_1+i\Gamma_{ab})(\omega_{ca}-(\omega_1+\omega_2)+i\Gamma_{ac})}, \quad (1)$$

where $\omega_{1,2}$ = input laser frequencies; $\omega_{SF}=\omega_1+\omega_2$ = output SFG frequency; μ_{ab} = dipole moment of $a\rightarrow b$ transition; ω_{ba} = frequency of $a\rightarrow b$ transition; Γ_{ab} = homogeneous linewidth of $a\rightarrow b$ transition; and a, b, c, denote the ground and excited energy levels.

To a first approximation, our model of rhodamine 6G energy levels consists of two excited singlet S_1 and S_2 levels as zero-vibration bands, overlapped with weaker vibronic bands. Equation (1) then reduces to four terms corresponding to the four resonant pathways $S_0\rightarrow S_1\rightarrow S_2$, $S_0\rightarrow S_1^*\rightarrow S_2$, $S_0\rightarrow S_1\rightarrow S_2^*$ and $S_0\rightarrow S_1^*\rightarrow S_2^*$, where the asterisks denote the vibronic levels.

The theoretical excitation spectra of SFG and SHG were simulated by performing the summation in Eq. (1) at all ω_1, with $\omega_2 = 9360\ \text{cm}^{-1}$ (Nd:YAG 1.064 μ) for SFG, and $\omega_2=\omega_1$ for SHG. Note that for SHG, Eq. (1) must be multiplied by $\frac{1}{2}$ to account for the fact that terms in the summation are counted twice because $\omega_2=\omega_1$.[6] At the peaks of the excitation curves, the ratio of SFG to SHG is calculated to be 220. The peak of the calculated SFG excitation spectrum is shifted to the blue of the $S_0\rightarrow S_1$ absorption maximum by $\sim180\ \text{cm}^{-1}$ because it is a convolution of the $S_0\rightarrow S_1$ and $S_0\rightarrow S_2$ profiles, and because our choice of $\omega_2=9360\ \text{cm}^{-1}$ results in a frequency detuning of $540\ \text{cm}^{-1}$ between ω_2 and the peak of the $S_1\rightarrow S_2$ transition. For rhodamine 6G, the maximum enhancement factor when $\omega_2=\omega_{ca}-\omega_{ba}=9900\ \text{cm}^{-1}$, corresponding to the fully resonant situation, is 320. The shape and peak intensity of the calculated SFG excitation spectrum were found to be insensitive to the vibronic band contributions, i.e., the second, third, and fourth terms in Eq. (1), because the vibronic bands have large frequency offsets with respect to the zero-vibration bands and because the nonlinearity of SFG suppresses contributions from weak transitions.

In Fig. 2, a sum-frequency excitation spectrum of rhodamine 6G taken at low-pulse energies (0.3 mJ) is shown superimposed on the calculated SFG and $S_0\rightarrow S_1$ absorption curves. The error bar is larger on the red side of the excitation spectrum due to a higher background from interferences such as 355 nm scatter from the Nd:YAG and incoherent molecular fluorescence.[12] The agreement between the observed data and the calculated excitation spectrum is well within experimental errors. The blue shift of the observed excitation spectrum with respect to the $S_0\rightarrow S_1$ absorption spectrum and the observed line shape are in good agreement with the theoretical model.

From measurements of the SFG output referenced to the strongly attenuated Nd:YAG 355 nm output, we estimated the number of SFG photons generated from a monolayer sample at the peak of the excitation curve to be 50 000/pulse. A direct comparison of SFG and SHG signals from the same sample under similar experimental conditions showed an enhancement factor, after correcting for different laser powers and irradiated areas, of 170 ± 50, in agreement with the calculated value of 220.[9]

B. Noncollinear excitation

Consider two beams incident upon the surface at azimuthal angles θ_1 and θ_2 whose planes of incidence have a projection angle ϕ in the xy plane. Figure 3 defines the geometry for this situation and directly follows from Bloembergen and Pershan.[13] Their coordinate system is chosen so that k_s is in the xz plane; the projection angles between the reflected nonlinear output beam and the reflected fundamental beams are δ_1 and δ_2, respectively, as measured from the x axis in the xy plane. Noting that $k_{xy}=0$, and from conservation of momentum, we find that

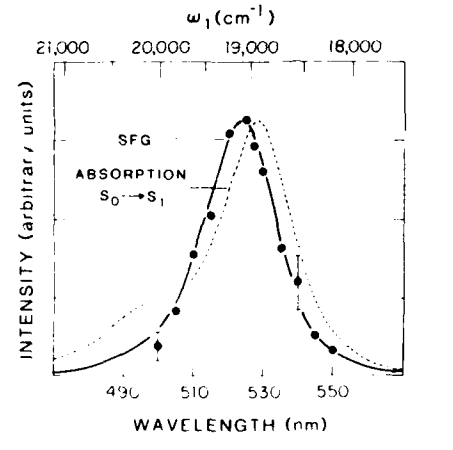

FIG. 2. Sum-frequency excitation spectrum of rhodamine 6G with $\omega_2=9360\ \text{cm}^{-1}$. The calculated spectrum is shown as the solid curve and the points are experimental data. The dotted line is the $S_0\rightarrow S_1$ absorption spectrum

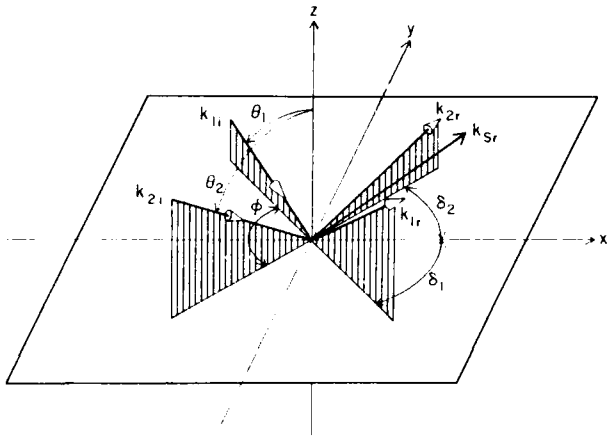

FIG. 3. Simplified coordinate system that defines the noncollinear excitation geometry. The projection angle ϕ is the angle between the input beams in the xy plane. The reflected nonlinear output lies in the xz plane. The transmitted beams have been omitted for clarity.

$$\tan \delta_1 = \frac{k_2 \sin \theta_2 \sin \phi}{k_1 \sin \theta_1 + k_2 \sin \theta_2 \cos \phi} . \quad (2)$$

For input beams with the same azimuthal angle, i.e., $\theta_1 = \theta_2$, this expression reduces to

$$\tan \delta_1 = \frac{k_2 \sin \phi}{k_1 + k_2 \cos \phi} , \quad (3)$$

where now the angular dependence of δ_1 is solely given by the projection angle ϕ. For SHG we have $k_1 = k_2$ and hence Eq. (3) is satisfied for $\delta_1 = \frac{1}{2}\phi$, which fulfills our expectation that the nonlinear output beam simply bisects the reflected fundamental beams.

The angular dependence of surface sum and difference frequency generation for collinear input beams has been given by Dick *et al.*,[14] who determined the efficiency of nonlinear generation as a function of the azimuthal angular dependence (θ) of the linear and nonlinear Fresnel factors. This model may be readily extended to include the projection angle dependence (ϕ) by using the nonlinear law of refraction as given by[13]

$$n_s^2 \omega_s^2 \sin^2 \theta_s = n_{i1}^2 \omega_1^2 \sin^2 \theta_1 + n_{i2}^2 \omega_2^2 \sin^2 \theta_2 + 2 n_{i1} n_{i2} \omega_1 \omega_2 \sin \theta_1 \sin \theta_2 \cos \phi . \quad (4)$$

For input beams where $\phi = 0$ and $\theta_1 = \pm \theta_2$, Eq. (4) reduces to Snell's law.[13]

Figure 4 shows the results of a calculation of the noncollinear, p polarized, reflected SHG intensity for p polarized input beams I_{ppp} as a function of ϕ for azimuthal angles θ of 60° and 50° using the previously reported values of the refractive indices of rhodamine 6G on a fused silica substrate.[14] The inset is an expanded scale of the calculation which shows that for $\phi \leq 15°$, the signal intensity should decrease by less than 10%. Thus, for small projection angles the noncollinear output will not be significantly attenuated.

Figure 5 presents the results for noncollinear SHG of rhodamine 6G for a projection angle of $\phi \sim 8°$. When the input beams are not overlapped, as shown in Fig. 5(b), the two observed SHG peaks are seen to be collinear with the reflect-

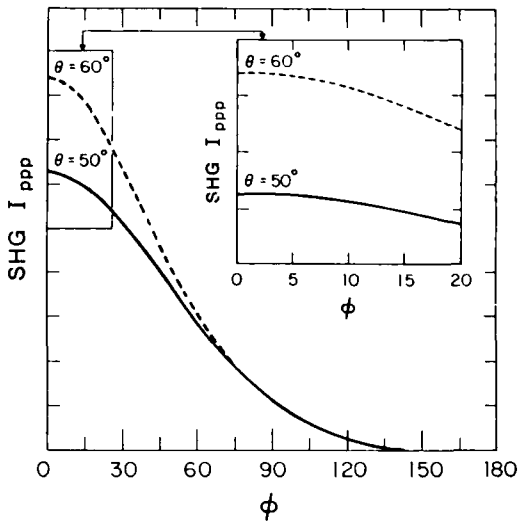

FIG. 4. Calculation of p polarized intensity of reflected SHG, I_{ppp}. For $0 < \phi < 15°$ the calculated intensity decreases by $\sim 10\%$.

ed fundamental peaks, which are shown in Fig. 5(a). When the input beams are spatially overlapped, as shown in Fig. 5(c), the middle peak, corresponding to noncollinear SHG, is clearly evident. From the relative intensities of the three SHG peaks we calculate $\sim 75°$ overlap. This imperfect overlap explains the narrower spatial width of the middle SHG peak relative to the collinear SHG peaks, which have the same width as the input laser beams.

Figure 6 shows the results for noncollinear SFG for a projection angle of $\phi \sim 6°$ that represents the minimum projec-

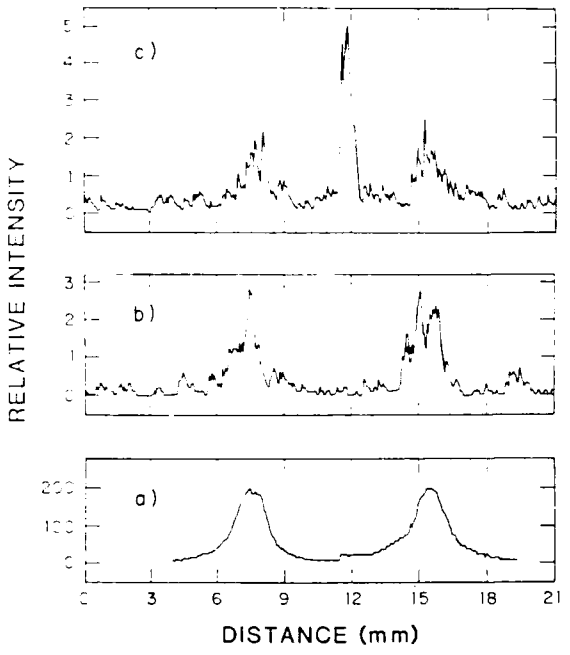

FIG. 5. (a) Spatial scan of the reflected 695-nm pump beams for noncollinear SHG excitation. (b) Spatial scan of SHG with no pump beam overlap. (c) Same as (b) except for overlapped pump beams. Monochromator set at 347 nm.

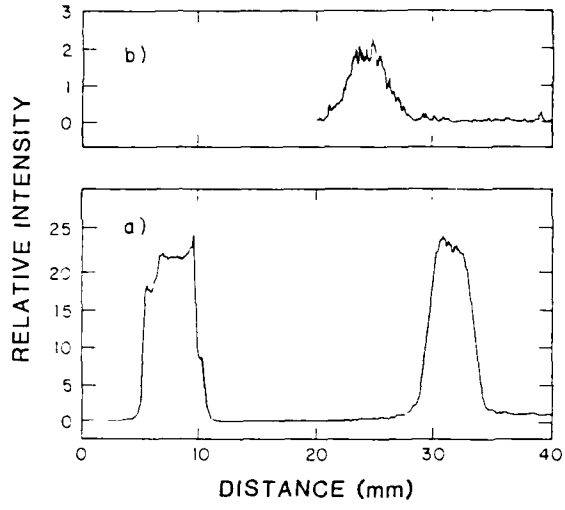

FIG. 6. (a) Spatial scan of IR (left-hand side) and 525-nm reflected light (right-hand side) for noncollinear SFG with no input-beam overlap. (b) Spatial scan of noncollinear SFG with input beams overlapped and the color filter inserted. Monochromator set at 351 nm.

tion angle necessary to achieve good spatial separation under our conditions. Note that the distance between the SFG peak and the 525-nm reflected light peak is about half the distance between the SFG and IR reflected light peaks. This is consistent with the small-angle limit of Eq. (3). From the measured distance between the output beam and the visible beam the output angle δ_1 was measured to be $1.8° \pm 0.3°$, in agreement with the calculated angle of 2°. There was no measureable variation in the noncollinear SHG or SFG intensity over the range in which the projection angle could be varied (3°–15°), within our 15% experimental error. This is consistent with the calculation of I_{ppp} shown in Fig. 4. Furthermore, the measured conversion efficiencies for SHG and SFG agreed to within 30% of those previously obtained using collinear input beams.[10]

IV. CONCLUSIONS

In conclusion, we have demonstrated doubly resonant enhanced sum-frequency generation from monolayers of dye. The SFG excitation spectrum is a convolution of both $S_0 \rightarrow S_1$ and $S_0 \rightarrow S_2$ absorption bands. The use of two input lasers allows the double resonance to be satisfied, resulting in a higher overall signal. Under the same experimental conditions, SFG was enhanced by about 170 over the SHG process.

Additionally, resonantly enhanced surface SHG and SFG using a noncollinear excitation geometry shows that for small projection angles, $\phi \leqslant 15°$, effective separation of the nonlinear output beam from the reflected fundamental beams is achieved without significantly reducing the efficiency of nonlinear generation. Furthermore, the large reductions of detectable scattered light and fluorescence attainable by this technique should increase the sensitivity and versatility of surface SHG and SFG.

[1] N. Bloembergen, R. K. Chang, S. S. Jha, and C. H. Lee, Phys. Rev. **174**, 813 (1968).
[2] Y. R. Shen, J. Vac. Sci. Technol. B **3**, 1464 (1985).
[3] Y. R. Shen, Ann. Rev. Mater. Sci. **16**, 69 (1986).
[4] H. W. K. Tom, Lawrence Berkeley Laboratory Report No. LBL-17820, 1984.
[5] J. H. Hunt, P. Guyot-Sionnest, and Y. R. Shen, Opt. Chem. Phys. Lett. **133**, 189 (1987).
[6] G. Marowsky, A. Gierulski, and B. Dick, Opt. Commun. **52**, 339 (1985).
[7] Y. R. Shen, *The Principles of Nonlinear Optics* (Wiley, New York, 1984).
[8] T. F. Heinz, C. K. Chen, D. Ricard, and Y. R. Shen, Phys. Rev. Lett. **48**, 478 (1982).
[9] D. C. Nguyen, R. E. Muenchausen, R. A. Keller, and N. S. Nogar, Opt. Commun. **60**, 111 (1986).
[10] R. E. Muenchausen, R. A. Keller, and N. S. Nogar, J. Opt. Soc. Am. B **4**, 237 (1987).
[11] B. Dick, A. Gierulski, and G. Marowsky, Ber. Bunsenges. Phys. Chem. **89**, 346 (1985).
[12] G. C. Orner and M. R. Topp, Chem. Phys. Lett. **36**, 295 (1975); H. Lin and M. R. Topp, *ibid.* **47**, 442 (1977).
[13] N. Bloembergen and P. S. Pershan, Phys. Rev. **128**, 606 (1962).
[14] B. Dick, A. Gierulski, G. Marowsky, and G. A. Reider, Appl. Phys. B **38**, 107 (1985).

Surface diffusion measured by laser-induced desorption: Monte Carlo simulation of effects of surface defects on diffusion

Richard B. Hall, Thomas H. Upton, and Eric Herbolzheimer
Exxon Research and Engineering Co., Annandale, New Jersey 08801

(Received 31 March 1987; accepted 8 June 1987)

Recently, pulsed laser-induced desorption (LID) has been used to measure surface diffusion of adsorbed species. Often, however, pulsed-laser excitation leads to stress-induced deformations of the surface. We have found, in the case of a Ni(100) surface, that laser excitation causes a change in the surface morphology that results in an increase in the dissociative sticking coefficient of hydrogen by a factor of more than 3. At the same time, adsorption of other species is not appreciably affected. Based on low-energy electron diffraction (LEED) spot profile analysis, the laser-irradiated surface has $< 10\%$ atomic-step defects. We attempt to estimate the effect that laser-induced surface defects have on the measurement of diffusion by means of a Monte Carlo simulation. Surface defects are introduced into the simulation as trap sites because such defects would have the most pronounced effect on diffusion. We find that $\langle x(t) \rangle$ and $\langle x^2(t) \rangle$ of particles on the defected surface are characteristic of diffusion and obtain an effective diffusion coefficient D from the rate of increase in $\langle x^2 \rangle$ with time. For a $p(2\times 2)$ array of trap sites and noninteracting particles, D decreases with increasing trap site residence time but the magnitude of the decrease is not large. For example, D is decreased only by a factor of roughly 3 when the trap residence time is 3000 times the normal site residence time. The number of particles $N(t)$ that migrate onto the defected portion of the surface under these conditions is reduced by $< 10\%$ relative to a defect-free surface. These variations are within the present experimental uncertainties of the LID technique. Hence, for noninteracting adsorbates such as hydrogen, the reported values of D are representative of the defect-free surface. Using the result that diffusion on the defected portion of the surface can be represented by a single effective diffusion coefficient, we derive an analytic expression for the effects of trap sites on $N(t)$. This analytic expression accurately reproduces the Monte Carlo results.

I. INTRODUCTION

Recently, a number of experiments have been reported in which laser-induced thermal desorption has been used to measure diffusion of adsorbed species.[1–5] Briefly, in this experiment, a laser pulse heats a small area on a surface, producing a rapid temperature jump sufficient to desorb species from that area. After a time delay, a second laser pulse heats the same small area and desorbs adsorbates which have moved into that area from surrounding regions on the surface. The time-dependent signals from the diffusional refilling can then be fit using an equation derived from Fick's second law in order to determine the surface-diffusion coefficient.

There are a number of advantages of this experimental technique. Most notably, surface diffusion can be measured over a wide range of coverage, and adsorbate–adsorbate interaction potentials may be derived from the coverage dependence of the diffusion coefficient.[5–7] Surface-diffusion kinetics and adsorbate–adsorbate interactions are key factors determining the kinetics of surface reactions and laser-induced desorption (LID) has the potential to make a significant contribution to our understanding in this area.

There are some complicating factors that need to be better understood, however. When the surface is not a uniform, two-dimensional lattice, Fick's second law can no longer readily be used to analyze the experimental results. Such a situation arises, for example, when there are defect or trap sites on the surface or when some of the adsorbed species can act as site blocking agents. There are no general, analytic descriptions of these situations, although some special cases, especially for diffusion-mediated surface reactions, have been analyzed.[8–10] An alternative method is to simulate complex-diffusion systems using Monte Carlo techniques.[11,12]

The investigation of diffusion on inhomogeneous surfaces is particularly relevant to LID measurements of surface diffusion. Thermal expansion of the metal, resulting from the laser-induced temperature rise, causes stress in the near-surface region. If this induced stress exceeds the yield stress of the metal (which it almost invariably does), irreversible deformation of the surface occurs. These deformations are typically along the slip planes of the crystal and result in atomic-step defects at the surface. We have found that in the case of Ni(100), the changes in the surface morphology induced by laser excitation result in a significant change in the reactivity of the surface toward hydrogen. We report some of the characteristics of this increased reactivity here and use a Monte Carlo technique to investigate the extent to which these defects might affect the previously reported[2] measurement of the surface mobility of hydrogen on Ni(100).

II. EXPERIMENT

The apparatus used in this experiment has been described previously.[2,13] It is a conventional ultrahigh vacuum appara-

 0734-211X/87/051470-07$01.00 © 1987 American Vacuum Society

tus pumped by a turbomolecular pump and a titanium getter/cryopump. The base pressure of the apparatus is below 2×10^{-10} mbar. The laser used is a Nd-YAG laser operating at a wavelength of 1.06 μm. The laser fluence at the Ni surface is 6 mJ/pulse and the pulse width is 24 ns full width at half-maximum (FWHM). The radius of the laser beam at the surface is determined by a spatial autocorrelation technique[2,14] to be 280 μm. The LID signal is detected by a mass spectrometer located 5 cm from the sample surface. The mass spectrometer is not differentially pumped. Conventional thermal desorption mass spectrometery is used to determine surface coverages. Auger spectroscopy is used to monitor surface cleanliness and a Varian low-energy electron diffraction (LEED) system is used to measure the surface order and to obtain an estimate of the concentration of laser-induced defects by LEED spot profile analysis.

III. RESULTS AND DISCUSSION

During the course of previously reported[2] experiments on the diffusion of hydrogen atoms on Ni(100), we found that the sticking coefficient for hydrogen chemisoprtion on this surface was significantly affected by laser irradiation. This can be easily seen in Fig. 1 in which we show the H_2 LID signal intensity as a function of surface position. In this experiment, one-half of the surface was irradiated prior to dosing the surface with hydrogen. The laser scan pattern was a matrix of 10 spots across the surface by 10 spots down, for a total of 100 spots. The rows were scanned from the top down, starting from left- to right-hand side and alternating directions with each row. The reproducibility of the position of each spot from scan to scan is better than 1 μm. After the first 40 spots were irradiated, the laser was blocked and the surface dosed with 0.5 L of hydrogen. On a normal Ni(100) surface this dose would result in a hydrogen coverage of 0.3×10^{15} H atoms/cm^2.[15] Finally, the LID signals were measured using the same scan pattern. An increase in signal intensity of a factor of 3 is observed from the spots that had been irradiated prior to dosing. The surface temperature was held at 100 K during the entire procedure.

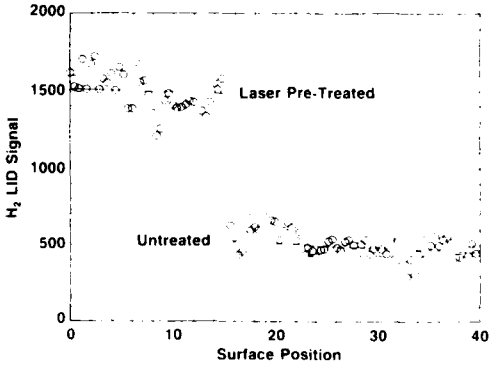

FIG. 1. Effect of laser pretreatment on H_2 LID signal. Following the pretreatment, the surface was exposed to 0.5 L of hydrogen. The LID signal is given in mass-spectrometer counts (at 2 AMU) per laser pulse. (One monolayer of H atoms gives 60 000 counts/pulse.) The surface position of the laser beam, indicated in arbitrary units, is described in text. The surface temperature during irradiation is 100 K.

We have concluded that the increase in LID signal is due to a change in the hydrogen sticking coefficient. There are several reasons for this. Firstly, we find that laser irradiation increases the LID signal of other surface species by $< 10\%$. This includes molecularly adsorbed species such as CO and dissociatively adsorbed species such as methanol.[16] Thus, the laser is not simply increasing the effective surface area by creating many microcracks and microfacets. Secondly, we find that if we irradiate the entire surface and measure the uptake of hydrogen using conventional thermal desorption spectroscopy, we find that for a fixed exposure the uptake is increased by a factor of 3. This is illustrated in Fig. 2. In this case, we change the scan pattern so that the spots overlap (the centers are spaced by a distance roughly equal to the spot radius) and irradiate the entire surface. Shown in Fig. 2 are a H_2 TPD spectrum for an unirradiated surface exposed to a hydrogen dose of 0.62 L and a spectrum for an irradiated surface exposed to 0.28 L. The areas under these curves are identical within experimental error, indicating that despite the difference in exposures, the surface coverage of hydrogen is the same in both cases. There is very little change in the shape or position of the TPD curve for the irradiated surface relative to that of the unirradiated surface. This indicates that the desorption kinetics are not altered sufficiently by laser irradiation to account for the observed differences.

The nature of the damage introduced into metal surfaces by pulsed-laser irradiation has been the subject of a number of previous investigations.[17–20] The defects typically are dislocation networks along slip planes.[18,20] The cause is generally thought to be thermomechanical stress induced by laser heating. The laser-heated volume expands against the rigid boundary of the area of the surface outside the laser radiation, leading to compressive stresses. If this stress exceeds the critical shear stress for dislocation along one of the slip planes of the material, a network of dislocations will result. These dislocations generally result in the formation of atomic steps at the surface.

Some information on the nature of and number of surface defects induced by laser excitation can be obtained from an analysis of the LEED spot profiles.[21–24] Although no LEED spots for facets other than Ni(100) were ever observed, the

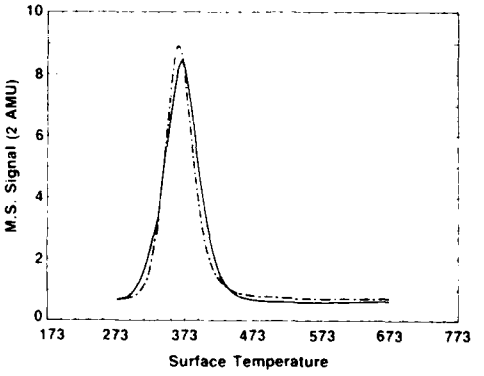

FIG. 2. Thermal-desorption spectra, H_2 from fully preirradiated surface and from unirradiated surface. —is for unirradiated surface exposed to 0.62 L of hydrogen; --- is for preirradiated surface exposed to 0.28 L of hydrogen.

surface disorder induced by the laser resulted in LEED spots that were visually less sharp than the LEED spots for the unirradiated surface. The half-width of the first-order LEED spots from the laser-irradiated surface show an oscillatory dependence on the incident electron energy that is characteristic of the formation of random stepped structures.[21] From the magnitude of the half-width, we estimate that the average distance between these disorders is at least 12 surface lattice units. This suggests that the step or defect density is $< 10\%$.

We find that relatively modest thermal annealing of the surface can entirely reverse the effects described above. Heating the surface to 800 K for 5 min is sufficient to return both the sticking coefficient for adsorption of hydrogen and the half-width of the LEED spots to the values obtained for a Ni(100) surface that has never been irradiated. The dependence on annealing temperature of the relative enhancement in the sticking coefficient, i.e., the ratio of the LID signal from the preirradiated portion of the surface to that from the unirradiated portion, is indicated in Fig. 3. For each data point, one-half of the surface was irradiated at 100 K, the surface was then heated to the indicated temperature for 3 min, recooled to 100 K, dosed with 0.3 L H_2, and the LID signals measured. The time and temperature required to anneal out the effects of laser radiation is typical of that required to anneal out atomic dimension dislocations. It is possible for the laser to introduce more extreme morphological changes than atomic-step dislocations. In fact, scanning-electron microscopy (SEM) pictures of the irradiated surface show craters and dimples with dimensions on the order of microns. These changes in morphology are not annealed out by the temperature treatments described above. We conclude that although laser excitation creates these larger features, they are not the origin of the observed changes in the sticking coefficient or in the broadening of the LEED spots.

The dissociative adsorption of hydrogen on Ni has been the subject of a number of studies.[25-27] On Ni(100), the adsorption is activated with a barrier of ~ 1.2 kcal/mol.[25(a)] This barrier results in a sticking coefficient S_0 that is significantly less than unity. Recent molecular-beam results indicate that S_0 is roughly 0.4,[25(a)] although values ranging from 0.25[25(b)] to 0.6[15] have been reported for H_2 (gas) with a roughly thermal distribution of velocities. Our observation of a factor of 3 increase in the sticking coefficient at low coverages following laser excitation suggests that the sticking coefficient initially should be no greater than 0.33.

The mechanism of the laser enhancement of the dissociative sticking coefficient is not yet fully understood. If laser excitation creates facets with Ni(110) orientation, the probability of dissociative adsorption should increase since S_0 on this surface is roughly 0.96.[26] LEED patterns for the laser-irradiated surface, however, do not exhibit Ni(110) features. If greater than atomic height steps are produced, the step walls are most likely to be a Ni(111) orientation because these have the minimum energy slip planes in Ni. This is not likely to be the cause of the enhanced dissociation since Ni(111) is the least reactive of the Ni surfaces; S_0 is < 0.05.[27] On the other hand, if, as suggested by our LEED results, the defects are atomic-step defects they would probably be reactive. It is likely that the Ni(110) surface is reactive because it has an open structure that exposes the Ni atoms and allows H_2 to achieve a configuration that reduces or eliminates the energy barrier to dissociative adsorption. Atomic step defect atoms are coordinatively more unsaturated than fully coordinated surface atoms are likely to be highly reactive for the same reason. We believe this is the origin of the laser enhancement of the sticking coefficient but additional experiments will be required before this can be confirmed.

That the microscopic sticking coefficient can be altered at a defect density estimated to be $< 10\%$ of the surface suggests the existence of a temporary bound state that allows molecular hydrogen to sample enough of the surface to find these defects. This is contrary to an earlier conclusion[25(a)] that no precursor state to dissociative adsorption exists for this surface, based on the energy and coverage dependence of S_0 in molecular-beam experiments and the angular distribution in thermal desorption. It would be very instructive to perform the same experiments on the laser irradiated surface.

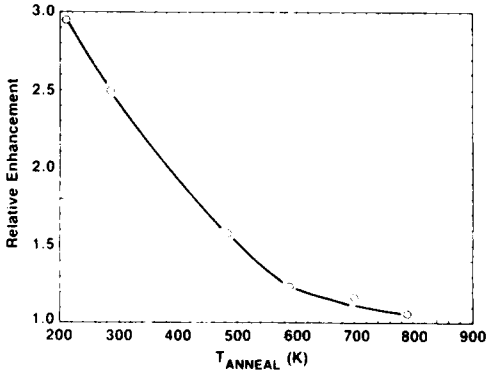

FIG. 3. Thermal annealing of laser-induced surface defects. The relative enhancement is defined to be the ratio of the surface coverage in the preirradiated spots to the surface coverage in the unirradiated spots as measured by the LID signal intensities. The annealing period is 3 min at the indicated temperature.

IV. DIFFUSION SIMULATIONS

In order to estimate the effect that laser-induced surface defects may have on the measurement of adsorbate diffusion, we have used a Monte Carlo method to simulate diffusion on a surface containing trap sites. The computational model used here is related to models published previously.[6] Details of our model will be described in a future publication. In brief, the surface is represented by a two-dimensional array, 100×100 sites. Initially, the top half of the surface has adsorbed "particles" occupying each site and the bottom half is completely empty. Diffusion is simulated by interrogating each site sequentially to determine its occupancy and the occupancy of nearest-neighbor sites. Occupancy of a site by more than one particle is forbidden. Care is taken in the way in which the two-dimensional grid is sampled in order to avoid systematic bias in the results. The array is scanned

vertically and then horizontally, with the direction of scans being chosen randomly between time steps. A scan of the full lattice is taken as a single-time step. In the simulations reported here, a sequence of 150 time steps is repeated 50 times and averaged.

The particle hopping probability per attempt is defined as $p = (n_e/4)\exp(-E/kT)$ where n_e is the number of empty adjacent sites, and E is the energy barrier to hopping from the site. The hopping direction is chosen randomly. Diffusion (and mass transport) occurs on this surface as the particles carry out a random walk from the filled upper region to the empty lower region.

For a uniform surface, the diffusion coefficient is defined as,

$$D = 1/4\ p\,v\,a^2 \tag{1}$$

where v is the hop attempt frequency (s^{-1}) and a is the lattice spacing. With the above definition of the hopping probability, defects can easily be introduced into the empty lattice region by designating certain sites to possess larger hopping energy barriers. In the present work, the density of traps is fixed at 25% with a $p(2\times 2)$ configuration. The hopping barrier for the normal surface site is taken to be 5 kcal/mol, close to the value reported for the hopping barrier for hydrogen on Ni (100).[2,4] In order for the simulation to be run in a reasonable time, each scan must account in an average sense for the integrated effect of a large number of hop attempts, such that there is a good possibility of a hop during each interrogation. Arbitrarily fixing the time step in a simulation to be 4×10^{-10} s, leads to an average hopping probability *per interrogation* of $p' = 0.95$ when $v = 1\times 10^{13}\ s^{-1}$. This value for the time step is used to obtain p' and hence p for other values of E.

Both $\langle x(t)\rangle$ and $\langle x^2(t)\rangle$ (mean and mean-squared displacements, respectively) are computed for the entire ensemble of particles hopping within a 60×100 site array embedded in the larger array. This is done in order to eliminate edge effects in the computation. Diffusion of particles into the initially empty region is, by symmetry, identical to the diffusion of vacancies or "holes" into the initially filled region. Both particles and holes are allowed to hop in each scan to more rigorously maintain the particle-hole symmetry.[28] In the presence of defects, the empty and filled regions of the lattice possess different transport properties so that $\langle x(t)\rangle$ and $\langle x^2(t)\rangle$ are computed separately for particles and holes in each simulation. For the defect-free lattice, we find the expected behavior for both particles and holes. The mean displacement of particles and holes is found to be negligible; the rate at which particles advance into empty region is equal to the rate at which holes advance into the filled region.[29,30]

In Fig. 4, we show the computed $\langle x^2(t)\rangle$ for particles on a uniform lattice. From a solution of Fick's second law for the initial and boundary conditions of our simulation, the evolution of particle and hole concentrations is given by[31]:

$$C_p(x,t) = C_0/2\ \mathrm{erfc}[x/(4Dt)^{1/2}] \quad x>0, \tag{2a}$$

$$C_h(x,t) = C_0/2\ \mathrm{erfc}\,[|x|/(4Dt)^{1/2}] \quad x<0, \tag{2b}$$

where C_0 is the particle concentration at $t = 0$, and at $x < 0$.

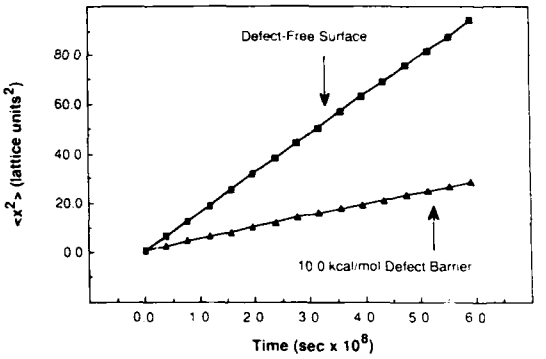

FIG. 4. Mean-square displacement of particles computed in the Monte Carlo simulation for a defect free surface with a hopping energy barrier of 5 kcal/mol, and a partially defected surface containing a $p(2\times 2)$ configuration of trap sites with a hopping energy barrier of 10 kcal/mol. The units are defined in the text.

From these expressions, the mean-square displacement for an ensemble of particles should behave as

$$\langle x_p^{\,2}(t)\rangle = \langle x_h^{\,2}(t)\rangle = 4/3\ Dt. \tag{3}$$

It is clear from Fig. 4 that the computed $\langle x^2(t)\rangle$ values are linear in time. For the defect-free surface, both particle and hole displacements have the same slope. The D values calculated from these results using Eq. (3) agree with those from Eq. (1) over the entire range of hopping barriers studied, validating the simulation procedure.

When trap sites are included in the problem, Eq. (3) is no longer rigorously true and the definition of an effective diffusion coefficient becomes complex. Despite this, we find that the mean-squared displacement of the ensemble of particles (and holes) remains linear in time. In Fig. 4 we show the mean-square displacement for particles for one choice of trap hopping barrier; similar results are obtained for all trap-hopping barriers investigated. This suggests that particle motion on the defected surface, even though it possesses two different hopping barriers, can be characterized by a single, effective diffusion coefficient and we use Eq. (3) to obtain a diffusion coefficient from the simulated results for the defected surface.

In Fig. 5, we show the dependence of D_p on the trap hopping barrier. Although the hole diffusion coefficient D_h is

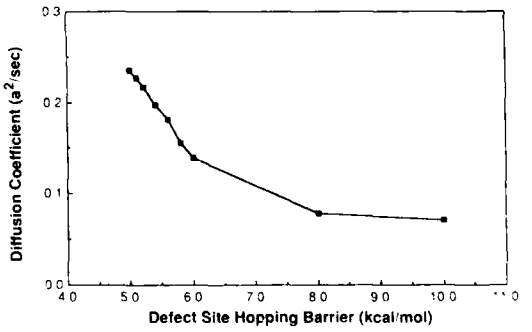

FIG. 5. Effective particle diffusion coefficient for the defected surface as a function of the defect-site hopping barrier.

unaffected, the particle diffusion coefficient D_p decreases as the hopping barrier increases.[32] The magnitude of the decrease is limited, however. For the deepest trap ($E_{tr} = 10$ kcal/mol) considered here, the diffusion coefficient anticipated for *full* coverage of such sites would be 3×10^{-4} times the diffusion coefficient for the reference, undefected surface. The residence time in such sites is roughly 2800 times that of the defect-free surface site and thus particles entering such sites may be viewed as permanently trapped. Nevertheless, the effective D for a surface with 25% concentration of such traps is only a factor of roughly 3 lower than D for the defect-free surface.

Finally, we compute the total number of particles N_p diffusing onto the empty portion of the surface. This is analogous to the experimental observable in an LID measurement of diffusion and we use this computation to estimate the extent to which the measured number of adsorbates which diffuse from the unirradiated portion of the surface into the laser-irradiated area might be affected by creation of laser-induced trap sites. In the inset in Fig. 6, N_p is plotted for the case of a uniform surface with $E = 5$ kcal/mol and for a surface with a $p(2\times2)$ arrangement of traps with $E_{tr} = 10$ kcal/mol. It can be seen that the effect of the traps on N_p is small even though the trap well depth is sufficient to immobilize the trapped particles. Also shown in this figure is the dependence of N_p on the square root of the ratio of D for the defect free portion of the surface on D for the defected portion. As described immediately below, we can derive an analytic expression for this lattice dependence and, as shown by the solid line in Fig. 6, the agreement with the simulation is quite good.

The result from the simulation that diffusion in the presence of trap sites can be described by a single, effective D.

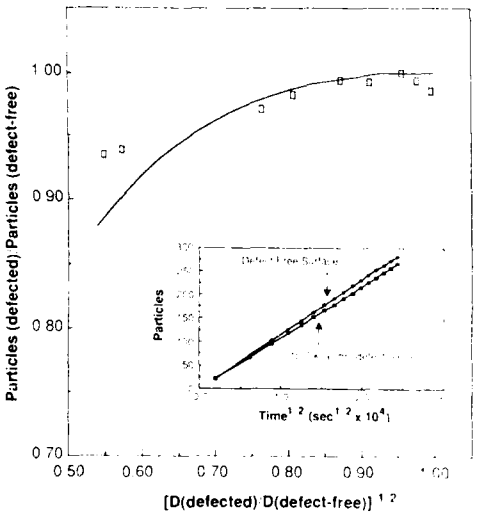

FIG. 6. Effect of trap sites on the number of particles that diffuse into the test area. The inset shows the number of particles N_p in the test area vs the square root of time. The main portion of the figure shows the fraction of the number of particles that diffuse into the defected area relative to the number that would diffuse into a defect-free area vs the square root of the ratio of the diffusion coefficients. The solid line is computed using the analytic expression given in Eq. (8).

allows us to derive an analytic expression for diffusion onto the defected region. For *continuous* media, it may be shown[31] that diffusion from a material having a diffusion coefficient of D_h into a material having a diffusion coefficient D_p can be described by:

$$C_h(x,t) = \frac{kC_0\,(D_p/D_h)^{1/2}\mathrm{erfc}\,\{|x|/[2(D_h t)^{1/2}]\}}{1 + k(D_p/D_h)^{1/2}} \qquad x<0, \tag{4a}$$

$$C_p(x,t) = \frac{kC_0\,\mathrm{erfc}\,\{x/[2(D_p t)^{1/2}]\}}{1 + k\,(D_p/D_h)^{1/2}} \qquad x>0, \tag{4b}$$

where C_0 is the initial concentration in region "h" ($x<0$) and the initial concentration in region "p" ($x>0$) is zero; C_h is the concentration in $x<0$, C_p the concentration in $x>0$, and k is the steady state equilibrium condition at $x=0$. Equilibrium at the interface in our case is defined as the ratio of the forward and reverse hopping rates at $x=0$, i.e.,

$$k = k_f/k_r = \exp\left[-(E_p - E_h)/kT\right] = D_h/D_p. \tag{5}$$

For the general case $k = C_2/C_1$ (at $t=\infty$). Integration over x yields,

$$N_p(t) = 2C_0(\pi)^{-1/2}(D_p t)^{1/2}[k/(1+k^{1/2})]. \tag{6}$$

Equation (5) fails completely to describe the concentration of particles N_p for a discrete two-dimensional lattice in which each site may be occupied by only one particle. It predicts that $N_p(t)$ should *increase* without bound when $D_p < D_h$ for all t. The reason for this is that the boundary conditions given above do not limit the concentration per site to a single particle as is required in the simulation. In order to derive analytic expressions appropriate to our lattice model, we alter the equilibrium to reflect this limitation by setting

$$k = C_p(C_0 - C_h)/C_h(C_0 - C_p). \tag{7}$$

Here, k is an equilibrium constant for the bimolecular reaction between particles and holes at $x=0$. When regions "h" and "p" are homogeneous, we retain Eq. (5). In the case of *ordered* defects as considered here, sites in region "p" are not uniform at the interface (1/2 are traps), so that Eq. (5) is not strictly true. We then *assume* that $k = D_h/D_p$, where D_p is taken to be the effective diffusion coefficient obtained from Fig. 4 and Eq. (3). With this, we obtain the expression given in Eq. (8) for N_p:

$$N_p(t) = C_0(\pi)^{-1/2}(D_h t)^{1/2} \times\left\{\frac{(R+1) - [4R^3 + (R-1)^2]^{1/2}}{(1-R^2)}\right\} \tag{8}$$

where, $R = (D_p/D_h)^{1/2}$. Note that as R approaches 1, the expression in brackets approaches 1 so that we recover the correct expression for a homogeneous surface. In Fig. 6 we plot $N_p(t)$ as a function of R. The solid line in Fig. 6 is calculated using Eq. (8). The agreement between the simulation and the analytic expression is quite good. This supports the use of a single diffusion coefficient to represent diffusion on the defected portion of the surface. The deviation between the simulation and the analytic expression is largest for $D_p \ll D_h$ and comes probably from the assumption that $k = D_h/D_p$, which in the simulation is only ap-

proximately true and is dependent on the geometry of the traps. For an average over numerous random arrangements of traps at a density of 25% rather than a $p(2\times2)$ configuration (which is closer to the experimental situation), the assumption of homogeneity in the defected region is more valid, and the agreement between the simulation and Eq. (8) should improve.

With $(D_p/D_h)^{1/2}=0.54$, as is approximately true for the deepest traps investigated here (see Fig. 5), the number of particles that diffuse onto the defected surface is 87% of the number that would have diffused onto the undefected surface, despite the fact that the traps are sufficiently deep to immobilize the particles. The density of defect sites used in the simulation is significantly greater than the density of defects estimated by LEED spot profile analysis for the Ni(100) surface above. Even with the higher defect density, the simulation indicates that the effect on the value of D extracted from the LID experiment will be small. The value for D is derived from the experimental $N(t)$ data by assuming a $(Dt)^{1/2}$ dependence,[2,27] and is *presumed* to be representative of a defect-free surface. If the number of adsorbates in the laser-irradiated area is actually 87% of what it would be for a defect-free surface, the value of D computed from $N(t)$ versus $t^{1/2}$ would be in error by a factor of 3. This is roughly equal to the experimental uncertainty.

As a final caveat, it is important to recognize that the model used here assumes that normal surface sites are not affected when neighboring trap sites are occupied. If there are long-range particle–particle interactions or if the range of site blocking extends beyond the occupied site, the effect of trap sites on diffusion could be significantly stronger than suggested above. For adsorbed H atoms these effects are not expected to be large. In fact, for the diffusion of H atoms on Ni(100)[2,4] and Ru(100),[33] very little dependence on hydrogen coverage is observed. If adsorbate–adsorbate interactions are significant, they should result in a pronounced dependence of D on coverage.[6] Thus the assumptions made in the current model are likely to be valid for the case of hydrogen diffusion. Hence, we conclude that the values of the diffusion coefficient for hydrogen on Ni(100) reported earlier[2] are not significantly in error due to surface defects induced by the laser excitation. The extension of our results to other adsorbates requires that interadsorbate interactions be carefully considered.

In closing, we note that the measurement of surface diffusion from the total number of laser-desorbed particles is relatively insensitive to traps. Even if particles become immobilized in the trap sites, they are still very likely to be detected by the LID technique. Unless the trapped particles act as barriers to further diffusion, their effect on the net mass transport will be small. The current work indicates that a trap density of 25% is not sufficient to interfere with mass transport as long as nearest-neighbor sites are not affected when the trap becomes occupied. The concentration profile $C_p(x,t)$, on the other hand, is more sensitive to the presence of trap sites. This quantity is more likely to reveal the presence of traps. Although a method to obtain information on $C_p(x,t)$ using LID has been reported,[5] it is unlikely to be of adequate spatial resolution to reveal the presence of trap sites. A number of techniques have been reported[34] that are capable of measuring surface coverage as a function of surface position with sufficient resolution to reveal the asymmetric concentration profiles that result from the presence of traps. We will report on the dependence of $C_p(x,t)$ on trap sites computed with the current model in a future publication.

V. SUMMARY

We observed that pulsed-laser excitation of Ni(100) produces changes in the surface morphology that lead to a threefold increase in the sticking coefficient for the dissociative adsorption of hydrogen. Adsorption of other gases is not significantly affected. LEED spot profile analysis indicates that the laser excitation results in isolated atomic-step defects at a density of roughly 10%. We use a Monte Carlo simulation technique to estimate the extent to which such surface defects might affect the measurement of the surface diffusion of hydrogen using LID. If the defects are trap sites, the effects on the diffusion are most pronounced. Our results indicate that the diffusion coefficient measured in the presence of 25% trap sites arranged in a $p(2\times2)$ configuration is within a factor of 3 of the coefficient that would be obtained in the absence of the traps. This is within the current experimental accuracy of LID measurements of diffusion coefficients and hence we conclude that the values for hydrogen diffusion reported earlier[2] are not seriously in error.

Some useful generalizations come out of the Monte Carlo simulations. We find that the mean square displacement of the ensemble of diffusing particles remain linear in time even when the traps are sufficiently deep to immobilize the particles during the "time" of the simulation. From the computed slopes we obtain effective diffusion coefficients as a function of the trap hopping barrier that are representative of particle transport on the defected surfaces. With values for the effective diffusion coefficients from the simulation, we are able to derive an analytic expression for the number of particles that diffuse into the defected region with time. Good agreement between the simulation and the analytic expression is found for the dependence of this quantity on the ratio of the diffusion coefficient for the defect-free portion of the surface to the diffusion coefficient for the defected portion.

[1] R. Viswanathan, D. R. Burgess, Jr., P. C. Stair, and E. Weitz, J. Vac. Sci. Technol. **20**, 605 (1982).
[2] S. M. George, A. M. DeSantolo, and R. B. Hall, Surf. Sci. **159**, L425 (1985).
[3] C. H. Mak, J. L. Brand, A. A. Deckert, and S. M. George, J. Chem. Phys. **85**, 1676 (1986).
[4] D. A. Mullins, B. Roop, and J. M. White, Chem. Phys. Lett. **129**, 511 (1986); B. Roop, S. A. Costello, D. R. Mullins, and J. M. White, J. Chem. Phys. **86**, 300 (1987).
[5] E. G. Seebauer and L. D. Schmidt, Chem. Phys. Lett. **123**, 129 (1986).
[6] M. Bowker and D. A. King, Surf. Sci. **71**, 583 (1978); A. Sadiq and K. Binder, *ibid.* **128**, 359 (1983); D. A. Reed and G. Ehrlich, Surf. Sci. **105**, 603 (1981).
[7] C. H. Mak and S. M. George, Surf. Sci. **172**, 509 (1986).
[8] S. Prager and H. L. Frisch, J. Chem. Phys. **72**, 2941 (1980).
[9] D. L. Freeman and J. D. Doll, J. Chem. Phys. **78**, 6002 (1983); J. D. Doll and A. F. Voter, Annu. Rev. Phys. Chem. (to be published).

[10]J. J. Fripiat and H. Van Damme, Nato Adv. Sci. Instrum. Ser. B **86**, 493 (1983); V. P. Zhdanov, Surf. Sci. **149**, L13 (1985); S. Sundaresan and K. Rao Kaza, Chem. Eng. Commun. **35**, 1 (1985); J. A. Serri, J. C. Tully, and M. J. Cardillo, J. Chem. Phys. **79**, 1530 (1985); A. B. Doktorov and N. N. Luzken, Chem. Phys. Lett. **79**, 498 (1981); H. H. Kung and M. C. Kung, Chem. Eng. Sci. **33**, 1003 (1978).

[11]M. Silverberg and A. Ben-Shaul, J. Chem. Phys. **83**, 6501 (1985); J. D. Doll and D. L. Freeman, Surf. Sci. **134**, 769 (1983); S. M. Valone, A. F. Voter, and J. D. Doll, J. Chem. Phys. **85**, 7480 (1986), see also Ref. 6.

[12]C. H. Mak, H. C. Anderson, and S. M. George (to be published); X. Jiang and H. I. Metiu (to be published).

[13]R. B. Hall and A. M. DeSantolo, Surf. Sci. **137**, 421 (1984).

[14]S. J. Bares and R. B. Hall, in *Chemistry and Structure at Interfaces: Recent Laser and Optical Investigations*, edited by R. B. Hall and A. B. Ellis (VCH, Deerfield Beach, Florida, 1986).

[15]S. Andersson, Chem. Phys. Lett. **55**, 185 (1978).

[16]R. B. Hall and S. J. Bares, Surf. Sci. **161**, L533 (1985).

[17]A. L. Helms Jr., C. W. Draper, D. C. Jacobsen, J. M. Poate, and S. L. Bernasek, in *Energy Beam-Solid Interactions and Transient Thermal Processing*, edited by D. K. Biegelsen, G. A. Rozgonyi, and C. H. Shank (Elsevier, North-Holland, New York, 1986).

[18]L. Buene, D. C. Jacobson, S. Nakahara, J. M. Poate, C. W. Draper, and J. K. Hirvonen, in *Laser and Electron-Beam Solid Interactions and Materials Processing*, edited by J. F. Gibbons, L. D. Hess, and T. W. Sigmon, (Elsevier, North-Holland, New York, 1981), pp. 583–590.

[19]F. Haessner and W. Seitz, Mater. Sci. **6**, 16 (1971).

[20]H. N. Musal, Jr., NBS Spec. Publ. **568**, 159 (1979).

[21]M. Henzler, Appl. Surf. Sci. **11/12**, 450 (1982).

[22]M. G. Legally, Appl. Surf. Sci. **13**, 260 (1982).

[23]K. D. Gronwald and M. Henzler, Surf. Sci. **117**, 180 (1982).

[24]M. Henzler, in *Electron Spectroscopy for Surface Analysis*, edited by H. Ibach (Springer, Berlin, 1977).

[25](a) A. V. Hamza and R. J. Madix, J. Phys. Chem. **89**, 5381 (1985); (b) K. Christmann, O. Schober, G. Ertl, and M. Neumann, J. Chem. Phys. **60**, 4528 (1974); (c) J. Lapujoulade and K. S. Neil, Surf. Sci. **35**, 288 (1973).

[26]A. Winkler and K. D. Rendulic, Surf. Sci. **118**, 19 (1982).

[27]H. P. Steinruch, K. D. Rendulic, and A. Winkler, Surf. Sci. (to be published).

[28]The probability for a hole hop is taken to be $p = \Sigma_i^{n_j} {}_1 p_i$ where $p_i = 1/4 \exp(-E_i/kT)$, n_j is the number of filled sites surrounding the hole, and E_i is the hopping barrier associated with each filled site. The choice of hopping direction was weighted by the p_i. Since each particle is allowed two hopping attempts in this model, all computed quantities are subsequently divided by 2.

[29]Note that earlier work (Refs. 6 and 30) has shown that for noninteracting particles, there is no difference between random walk and avoided walk diffusion on a *uniform* two-dimensional lattice. That is, site blocking does not influence diffusion of noninteracting particles on a uniform lattice.

[30]R. Kutner, Phys. Lett. A **81**, 239 (1981).

[31]J. Crank, *The Mathematics of Diffusion* (Oxford University, Oxford, 1975).

[32]Diffusion onto the defected surface is a function of reduced flux at the interface (due to interface site blockage by trapped particles) as well as reduced-particle mobility once the particles enter the defected region. We are exploring other trap configurations to isolate geometric effects, however at trap concentrations of 25% and less, geometric effects are not large.

[33]C. H. Mak, J. L. Brand, B. G. Koehler, and S. M. George, Surf. Sci. (to be published).

[34]A. G. Naumovets and Yu. S. Vedula, Surf. Sci. Rep. **4**, 365 (1985); M. Bowker and D. A. King, Surf. Sci. **94**, 564 (1980); D. A. King, J. Vac. Sci. Technol. **17**, 241 (1980).

Ion and neutral atomic and cluster sputtering yields of molybdenum[a)]

M. J. Pellin, W. Husinsky,[b)] W. F. Calaway, J. W. Burnett, E. L. Schweitzer, C. E. Young, B. Jørgensen,[c)] and D. M. Gruen
Materials Science and Chemistry Divisions, Argonne National Laboratory, Argonne, Illinois 60439

(Received 31 March 1987; accepted 22 June 1987)

The yield of neutral and ionized Mo, Mo_2, and Mo_3 sputtered from a Mo target by 4-keV Ar^+ has been measured in the surface analysis by resonance ionization of sputtered atoms (SARISA) machine. Ionization spectroscopy combined with time-of-flight (TOF) secondary ion mass spectrometry (SIMS) allowed us to obtain for the first time absolute sputtering yields and ionization fractions of sputtered atoms and metal clusters. Unlike sputtered atomic species, Mo clusters have been found to be sputtered with large ion fractions. The sputtering yield of Mo clusters is very sensitive to oxygen on the surface, i.e., even small amounts of oxygen on the surface identified by Mo^+ and MoO^+ peaks in the SIMS spectrum, reduce the cluster yield substantially. A broad structureless absorption band was observed for sputtered Mo_2 molecules indicating substantial rovibronic excitation as predicted by theoretical models.

I. INTRODUCTION

Recently, the mechanism by which polyatomic species (particularly metal adsorbate molecules and metal clusters) are ejected following energetic ion bombardment has been extensively studied both theoretically and experimentally.[1-6] Due to the small fraction of sputtered clusters, however, relatively little experimental data is available for these species. Furthermore, most of the measurements performed so far have dealt with sputtered cluster ions. Previous measurements of sputtered neutral clusters fall into two groups: (1) molecules[7(a)] and Van der Waals clusters from insulating solids and frozen gases,[7(b)] and (2) metallic species: Cu_2 and Cu_3,[2] and the dimers of the alkali metals Li, Na, and K.[7(c)] Practically nothing, so far, is known about the ionization probability of clusters during the sputtering event.

In the present work, the yields of neutral and ionized Mo clusters emitted from a Mo surface during ion-beam bombardment were measured. From the well-known sputtering yield for polycrystalline Mo[8(a)] (1.4 for 4-keV Ar^+ primary ion), absolute sputtering yields of sputtered neutral Mo_2 and Mo_3 were determined using resonant and nonresonant ionization spectroscopy (RIS, NRIS). The yields of sputtered Mo^+, Mo_2^+, Mo_3^+, and Mo_4^+ were also determined by time-of-flight (TOF) secondary ion mass spectrometry (SIMS). The relationship between the ion and neutral cluster yields was determined using the known Cu^+ ion yield.[8(b)] In the SARISA[9-11] machine, SIMS, NRIS, and RIS can be performed at the same time and under exactly the same conditions by simply changing the target potential and turning the ionizing lasers on or off. When saturation can be achieved for the laser ionization of the neutral species, absolute sputtering yields can be obtained (since the transmission of the TOF apparatus can be precisely determined).

The internal energy distribution, i.e., the population of rotational and vibrational sublevels of the sputtered clusters, is of particular interest. Recently several authors have published theoretical rovibrational populations.[3,5,12] Snowdon *et al.*[5,12] have demonstrated a good agreement between macroscopic phase space and microscopic Monte Carlo descriptions, with both predicting an extensive rovibrational excitation peaking at low vibrational quantum numbers. In principle, the rovibrational structure of sputtered clusters can be resolved using RIS. Interpretation of the results can be complicated by the low sputtering yields of clusters, power broadening, competition from nonresonant ionization processes and molecular fragmentation.

II. EXPERIMENT

The experiments presented here have been performed in the SARISA III apparatus. A detailed description of the principle of RIS and its experimental realization can be found in previous publications.[9,10] A description of the version of the machine used for these experiments is given in Ref. 11. In previous experiments, the SARISA method has proven to be a sensitive, low-damage technique for the study of sputtered neutral species. For Fe^{54} implanted in Si, a detection limit of 500 ppt has been achieved.[11] This high sensitivity is of particular importance when low ion currents are desired in order to prevent surface damage or when the species of interest is only a small fraction of the total sputtered flux, as is the case for sputtered clusters. The SARISA machine in its present configuration allows measurement in three modes. These are RIS, NRIS, and SIMS, all utilizing TOF mass spectrometry.

For all data presented, a 4-keV Ar^+ beam was used for sputtering. Typical ion beam currents were 2 μA on a spot size with a 200 μm diameter. The ion beam was pulsed to a pulse length of 500 ns. The repetition rate was 20 Hz. The background pressure in the target chamber and the analyzer chamber was $1-2\times10^{-10}$ Torr without the ion beam and increased to a few times 5×10^{-10} Torr during ion bombardment.

For excitation and ionization of the species under investigation, a YAG-pumped dye laser and a XeCl excimer laser have been used. The specific details of the two lasers and the dye used will be discussed in the next section.

 0734-211X/87/051477-05$01.00 © 1987 American Vacuum Society

III. EXPERIMENTAL RESULTS

All the measured sputtering yields described here have been normalized with respect to the sputtering yield of sputtered neutral Mo atoms.[8] Under the UHV conditions in which all the experiments have been performed (below 10^{-10} Torr background pressure), an essentially oxygen free surface was achieved. Since the Mo ground state is ^7S and thus has no spin-orbit splitting, ground state atoms dominate the sputtered flux.[13,14(a)]

Sputtered Mo atoms could be ionized in two ways: (1) by absorption of two nonresonant photons at 308 nm from the excimer laser (NRIS) *or* (2) by simultaneous absorption of one resonant photon from the dye laser at 317.03 nm and one ionizing photon from the excimer laser (RIS). In general, RIS is substantially more efficient than NRIS. For Mo, however, the wavelength of the 308 nm nonresonant photons is sufficiently close to the 317.03 nm resonant transition that effective ionization can be achieved with the excimer laser alone. In Fig. 1 the dependence of the Mo signal is plotted as a function of the excimer laser power. For the RIS signal in Fig. 1, the dye laser was frequency doubled and tuned to 317.03 nm. The energy of the dye laser pulse was ~0.5 mJ in an area of 1×3 mm. For RIS, the Mo signal shows only small increases in signal with increasing laser power for laser energies in excess of 0.1 mJ. The achievement of saturation allows us to determine the transmission of the spectrometer from the known sputtering yield of Mo. The Mo atom RIS signal shown in Fig. 1 is also highly saturated with respect to the resonant dye laser (317.03 nm) intensity.

Furthermore, Fig. 1 demonstrates that NRIS of Mo atoms by two 308 nm photons is not in the saturation regime over the intensity levels studied here. However the signal levels for the NRIS process differ by only an order of magnitude from the saturated RIS signal level. This allows us, once the relation between RIS and NRIS signals is established (Fig. 1), to restrict the measurements to the NRIS case.

Neutral Mo_2 and Mo_3 clusters are also ionized nonresonantly by two 308 nm excimer laser photons. The saturation dependence for Mo_2 is also shown in Fig. 1. In contrast to Mo atoms, the production of Mo_2 photoions is fully saturated by NRIS. For Mo_2, this is most likely due to the presence of a previously observed nearby intermediate resonance state.[16] For molecules and clusters dissociation by the ionizing laser might play an important role. For Mo_2 dissociation seems to be negligible in the power regime shown in Fig. 1 for two reasons. First, no decrease in Mo_2^+ signal is observed even at the highest laser levels. If creation of Mo_2^+ was followed by subsequent dissociative absorption of additional laser photons a decrease in Mo_2^+ signal would be observed at the highest laser fluences. Second, ionization with two separate laser colors (308 and 517 nm) produced essentially the same number of Mo_2^+ photoions. It seems unlikely although not impossible, therefore, that predissociation of Mo_2^+ is occurring.

The different isotopes of Mo and Mo_2 are resolved in SARISA by different flight times. Figure 2(a) shows the

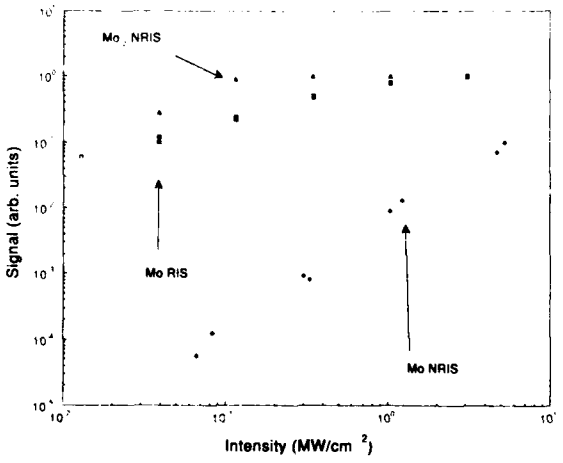

FIG. 1. Dependence of the Mo and Mo_2 signal on excimer laser intensity. For Mo the resonant and nonresonant ionization case is shown. For Mo_2 only the nonresonant case is shown. Note that the signal scale is arbitrary units. Consequently only the slope of each saturation curve is meaningful.

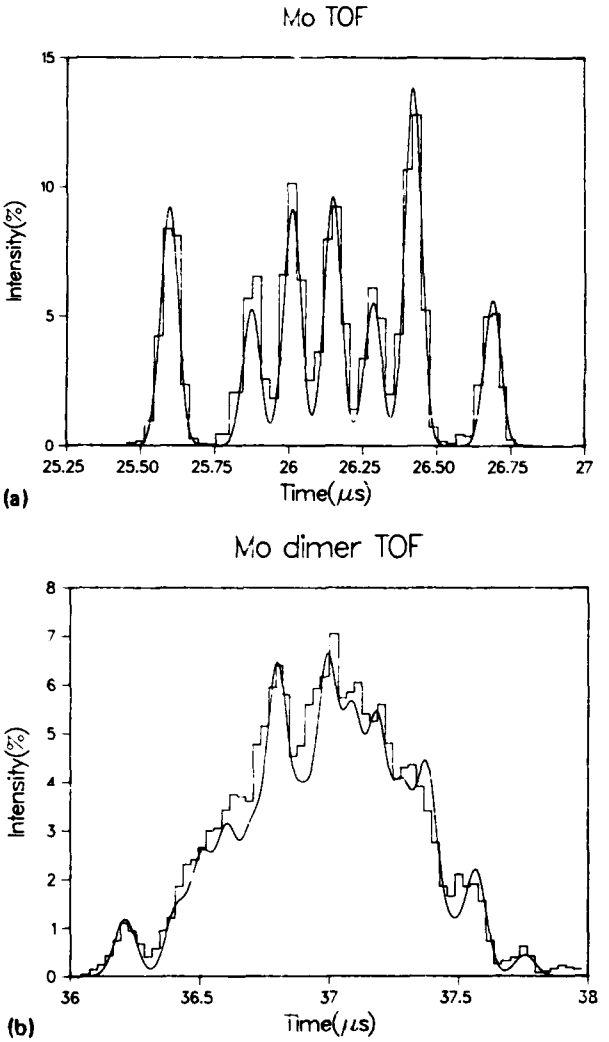

FIG. 2 NRIS time-of-flight spectrum for Mo and Mo_2 sputtered by 4 keV Ar^+ from a clean polycrystalline Mo surface; (a) the histogram is the measured atomic Mo isotope distribution. The smooth curve is the calculated Mo isotope ratio for an instrument with mass resolution ($m/\Delta m$) of 200. (b) The same as Fig. 2(a) but for Mo_2.

time-of-flight spectrum of different atomic Mo isotopes arriving at the channel plate detector. The spectrum is obtained by gating the ion counter. Figure 2(b) shows the isotope distribution of Mo_2. The histogram curve in both figures represents the measured distributions while the smooth curves are calculated time-of-flight distributions using the known Mo isotope ratios and assuming an instrumental mass resolution ($m/\Delta m$) of 200. The shape of the expected distribution corresponds well for both Mo and Mo_2 with the measured spectrum.

A unique feature of SARISA is the possibility of operating the machine in a TOF SIMS mode without changing any of the essential parameters. Thus an absolute $Y_{ion}/Y_{neutral}$ ratio can be measured after accounting for the different instrument transmission factors for ions and neutral particles. These transmission factors were determined using clean polycrystalline Cu targets and the known Cu and Cu^+ sputtering yield.[8] It should be noted that the Cu^+ sputtering yield is critically dependent on the O contamination of the Cu surface. Indeed the Cu^+ increases by a factor of 25 for oxidized Cu substrates.[8(b)] In this experiment the Cu surface was rigorously cleaned and was free of oxygen contamination to $<0.1\%$ of a monolayer. In Table I we have summarized the sputtering yields of neutral and ionized Mo, Mo_2, and Mo_3 relative to Mo atoms. Mo_4^+ has also been detected. The ratio of instrumental transmission factors for secondary neutral particles and secondary ions for SARISA is 0.11. The measured transmission for secondary ions is 70% in good agreement with ion optic calculations for the present SARISA apparatus.[11] Because the Cu ion yield is so critically dependent on surface chemistry we are presently endeavoring to determine a more exact value for the ion to neutral transmission ratio in SARISA. This will be determined by comparing the signal detected for K and K^+ ejected from a polycrystalline Mo surface with the known K ion fraction from a Mo surface.[14(b)] The advantage for this system is that the ratio of the ion and neutral sputter yields is near unity.

The values in Table I are only valid for clean, oxygen-free surfaces. In particular, the yields of the ionized species will be considerably enhanced if the surface is oxygen contaminated. Furthermore, oxygen drastically reduces the total yield of Mo clusters. By oxygen free we mean that MoO and MoO^+ could not be detected in the sputtered flux.

At this point it should be mentioned that even little oxygen contamination of the surface (exposure of the target to the background pressure of $1-2\times10^{-10}$ Torr for several tens of minutes without ion bombardment) resulted in a considerably enhanced Mo ion fraction and the appearance of neutral and ionized MoO in the sputtered flux. This is quite understandable from the findings by Saidoh *et al.*[4] for Mo exposed to oxygen. The appearance of MoO in the sputtered flux, furthermore, is correlated with a strong decrease of cluster emission.

In order to measure the rovibrational distribution of sputtered Mo_2 RIS has been employed. The spectroscopy of the Mo_2 cluster is relatively well studied[15–17] and shows several remarkable features. The 1.94-Å Mo_2 bond distance of the $^1\Sigma_g^+$ ground state is extremely short and several of the low-lying electronic states exhibit nearly the same bond length. The large dissociation energy of 4.2 eV and the high ground state vibrational frequency ω_e of 449 cm^{-1} are, furthermore, remarkable.

Flash photolysis studies by Efremov *et al.*[16] and supersonic beam studies by Hopkins *et al.*[15] of Mo_2 dimers report a $A\,^1\Sigma_u^+ \leftarrow X\,^1\Sigma_g^+$ transition from the Mo_2 ground state at 5180 ± 10 Å. This transition only consists of 0–0, 1–1, 2–2,..., vibrational transitions, due to Franck–Condon factors for the electronic states involved. The rotational structure of the Σ–Σ transition is rather simple with the odd rotational levels of the ground state missing.[15]

Mo_2 could be ionized by two 308-nm photons, by one 517.5-nm photon, and one 308-nm photon or by two 517.5-nm photons. It was rather unexpected that Mo_2 photoions could be produced by absorption of two 517.5-nm photons. From this (and the laser intensiy dependence of the photoion yield) we can conclude that the ionization energy of Mo_2 must be below 4.8 eV. Because of the saturation observed for NRIS of Mo_2 with the excimer laser alone, resonant studies of the vibrational and rotational population had to be performed with two 517.5-nm photons. (See Fig. 3.) This was a considerable disadvantage since the intensity re-

TABLE I. Relative yields of different neutral and ionized particles emitted from a Mo surface under 4-keV-Ar^+ ion bombardment. All data are given in respect to the number for neutral Mo atoms, arbitrarily set to 100 in this table. The data are valid for clean, oxygen free surfaces. Absolute yields of each species can be drawn using the measured sputtering yield of Mo atoms (= 1.4) [Ref. 8(a)] and an ion transmission measurement using the known Cu^+ sputtering yield [Ref. 8(b)].

	Mo	Mo_2	Mo_3	Mo_4
Neutral	100	0.22	4×10^{-4}	...
Ionized	0.89	0.89	0.02	2×10^{-3}
P^+	0.0089	4.05	50	...

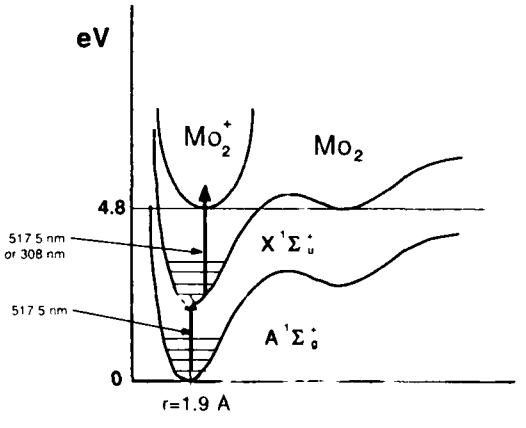

FIG. 3. Resonant excitation scheme used to study sputtered Mo_2. Resonant excitation is achieved by a YAG pumped dye laser at 517.5 ± 10 nm ($A\,^1\Sigma_u^+ \leftarrow X\,^1\Sigma_g^+$ transition). Ionization is obtained by absorption of a second 517.5 nm photon. Ionization could also be achieved by absorption of a 308 nm excimer photon, but the simultaneous absorption of two excimer photons saturates the transition, as shown in the text.

quired to saturate the resonant excitation step and the ionization step of the two-photon process are quite different. The end result is that the resonant step was strongly overdriven in order to obtain reasonable efficiency in the overall two-photon ionization process.

Spectral scans of the 510- and 530-nm spectral region demonstrated a broad structureless absorption band for sputtered Mo_2 molecules. The width of this feature is indicative of significant rovibrational excitation in the sputtered diatomic flux. Due to sensitivity limitations, power broadening of individual rotational lines could not be avoided. The lack of observed structure in the $^1\Sigma_u - {}^1\Sigma_g$ transition may in part be due to this.

IV. DISCUSSION

The contribution of neutral Mo_2 dimers to the sputtered flux is only about 0.22% of the total flux. The contribution of neutral Mo_3 is about three orders of magnitude less. For dimers, the measured ion fraction $P^+ = Y(Mo^+)/Y(Mo)$, is 0.0089, which is a factor of 5 larger than has been previously reported. This difference may be due to detection of high energy neutrals in SARISA which were previously not detected. It may as well be due to residual O contamination present on our surfaces. It is, however, somewhat astonishing that the ion fraction of the sputtered clusters is always > 1 and increases with the number of cluster atoms. The low ionization energy of Mo_2 (< 4.8 eV) might be a possible explanation for this experimental observation.

The electron tunneling model can be used to explain experimental ion fraction in sputtering from clean surfaces.[18] In this model the ion fraction P^+ can be described by

$$P^+ \propto e^{-(I-\phi)/\epsilon_0} \tag{1}$$

as a function of the difference between ionization energy I of the sputtered particle and the work function ϕ of the target. The parameter ϵ_0 is proportional to the velocity of the sputtered ion. In Fig. 4 the measured ion fraction of Mo and Mo_2 have been used in conjunction with Eq. (1). The ionization energy of Mo is 7.2 eV. For Mo_2, a value of 4.8 eV has been used for I although we realize our measurements only determine this as an upper limit on the actual ionization energy. For Mo_3 the ionization energy is not known. However, if we assume that Eq. (1) is valid, we can use the measured ion fraction of 50 to determine an $I = 4.1 \pm 0.5$ eV. This value is 0.5 eV less than the Mo work function of 4.6 eV. Clearly larger clusters must have I's which tend toward ϕ. For many systems however, the I's oscillate toward the large cluster asymptote.

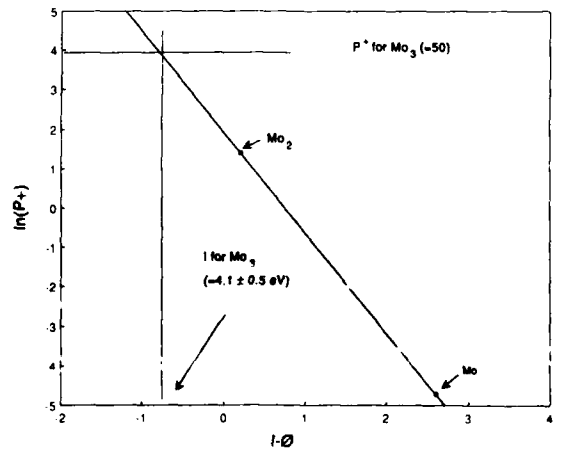

FIG. 4. Ion fraction of sputtered Mo, Mo_2, and Mo_3 from a clean Mo surface. The full curve gives the best fit by Eq. (1) in the text. The ionization energy of Mo_3 is not known but in the basis of the model presented in the text is 4.1 ± 0.5 eV.

A question of substantial importance is the rotational and vibrational population of sputtered molecules and sputtered clusters. If the rovibrational distribution of the sputtered molecules were known, a comparison with theoretical predictions[5,19–24] should yield information about the mechanism of molecule (cluster) emission. Cluster formation via recombination processes over the solid surfaces[19,20] and direct emission from the surface by direct knock on in the collision cascade[5,21–24] have been proposed. The results obtained for Mo_2 and Mo_3 cluster emission from Mo targets favor a direct cluster emission. The strong influence of oxygen on the Mo target surface on the cluster emission intensity suggests the importance of the surface as the source of the emission.

The *single collision mechanism* results in distributions of the rotational and vibrational energy with clear signs of the cascade (E^{-2}) statistics, which means a *non-Boltzmann* character. In the validity regime of the *single collision mechanism*, a substantial population in the first few vibrational levels can be assumed. In addition, rotational levels up to rotational quantum numbers of 100 may have substantially population.

In the Mo target, nearest neighbors have a lattice distance of 3.4 Å. The radius corresponding to the minimum of the Mo_2 ground state potential curve is 1.94 Å. In this case Snowdon[15] has shown that increased population of higher vibrational levels can be expected. In the context of these considerations, a broad spectral feature of the $A\,^1\Sigma_u^+ \leftarrow X\,^1\Sigma_g^+$ transition line might be expected. Due to the low Mo_2 total yield, this broad feature creates a critical burden for detecting the rovibrational structure. The broad structureless spectrum detected may well represent the broadened vibrational and rotational structure theoretically predicted.

[a] Work supported by the U. S. Department of Energy, BES-Materials Sciences, under Contract No. W-31-109-ENG-38.

[b] Permanent address: Institut für Allgemeine Physik, Technische Universität Wien, Karlsplatz 13, 1040 Wien, Austria.

[c] Permanent address: Fysisk Institut, Odense Universitet, Campusvej 55 DK-5230 Odense M, Danmark.

[1] A. Wucherer and H. Oechsner, Nucl. Instrum. Methods B **18**, 458 (1987); W. Gerhard and H. Oechsner, Z. Phys. B **22**, 41 (1975).

[2] W. O. Hofer and H. Gnaser, Nucl. Instrum. Methods B **18**, 605 (1987).

[3] R. Walkup, Ph. Avouris, and D. E. Harrison, Jr., Nucl. Instrum. Methods B **15**, 461 (1986).

[4] M. Saidoh, H. Gnaser, and W. O. Hofer, Appl. Phys. A **40**, 197 (1986).

[5] K. J. Snowdon, B. Willerding, and W. Heiland, Nucl. Instrum. Methods B **14**, 467 (1986).

[6]R. W. Dreyfus, R. Kelly, and R. E. Walkup (to be published).
[7](a) R. de Jonge, T. Baller, M. G. Tenner, A. E. de Vries, and K. J. Snowdon, Nucl. Instrum. Methods B **17**, 213 (1986). (b) For a recent review, see: J. Schou, Nucl. Instrum. Methods B (to be published). (c) A. P. M. Baede, W. F. Jungmann, and J. Los, Physica **54**, 459 (1971).
[8](a) *Energy dependence of the yields of ion-induced sputtering of monoatomic solids*, edited by N. Matsunami, Y. Yamamura, Y. Itikawa, N. Itoh, Y. Kazumata, S. Miyagawa, K. Morita, R. Shimizu, and H. Tawara, IPPJ-AM-32 (Institute of Plasma Physics, Nagoya, Japan, 1983). (b) A. Benninghoven, Surf. Sci. **53**, 596 (1975).
[9]M. J. Pellin, C. E. Young, W. F. Calaway, and D. M. Gruen, Surf. Sci. **144**, 619 (1984).
[10]M. J. Pellin, C. E. Young, W. F. Calaway, and D. M. Gruen, Nucl. Instrum. Methods B **13**, 653 (1986).
[11]M. J. Pellin, C. E. Young, W. F. Calaway, J. Burnett, B. Jørgensen, E. Schweitzer, and D. M. Gruen, Nucl. Instrum. Methods B **18**, 446 (1987); C. E. Young, M. J. Pellin, W. F. Calaway, J. Burnett, B. Jørgensen, E. Schweitzer, and D. M. Gruen, Nucl. Instrum. Methods B **27**, 119 (1987).
[12]K. J. Snowdon and R. A. Haring, Nucl. Instrum. Methods B **18**, 596 (1987).
[13]M. J. Pellin, D. M. Gruen, C. E. Young, and M. D. Wiggins, Nucl. Instrum. Methods **218**, 771 (1983).
[14]W. Husinsky, J. Vac. Sci. Technol. B **3**, 1546 (1985); A. R. Krauss and D. M. Gruen, J. Nucl. Mater. **93/94**, 686 (1980).
[15]J. B. Hopkins, P. R. Langridge-Smith, M. D. Morse, and R. E. Smalley, J. Chem. Phys. **78**, 1627 (1983).
[16]Y. M. Efremov, A. N. Samoilova, V. B. Kozhukhovsky, and L. V. Gurvich, J. Mol. Spectrosc. **73**, 430 (1978).
[17]M. M. Goodgame and W. A. Goddard III, Phys. Rev. Lett. **48**, 135 (1982).
[18]M. L. Yu and N. D. Lang, Nucl. Instrum. Methods B **14**, 403 (1986).
[19]K. Snowdon, R. Hentschke, W. Heiland, and P. Hertel, Z. Phys. A **318**, 261 (1984).
[20]B. Garrison, N. Winograd, and D. E. Harrison, Jr., J. Chem. Phys. **69**, 1440 (1978).
[21]D. E. Harrison, Jr., Nucl. Instrum. Methods B **18**, 349 (1987).
[22]K. Snowdon and W. Heiland, Z. Phys. **318**, 275 (1984).
[23]P. Sigmund, H. M. Urbassek, and D. Matragrano, Nucl. Instrum. Methods B **14**, 495 (1986).
[24]H. M. Urbassek, Nucl. Instrum. Methods B **18**, 587 (1987).

Molecular-beam epitaxy growth mechanisms on GaAs(100) surfaces

H. H. Farrell, J. P. Harbison, and L. D. Peterson[a)]
Bell Communications Research, Red Bank, New Jersey 07701-7020

(Received 27 February 1987; accepted 26 May 1987)

A significant liability in the use of molecular-beam epitaxy (MBE) to grow device grade compound semiconductor materials is the cost entailed by the necessity of using ultrahigh vacuum and high-growth temperatures. The commercial feasibility of this process could be considerably enhanced if growth temperatures could be cut by one-half or more. In addition, lower growth temperatures could make feasible the growth of semiconductor layers by MBE on top of previously processed structures without degrading or destroying those structures from the high temperatures currently needed for semiconductor growth. An understanding of the detailed atomic nature of this growth process would be valuable in tailoring existing, or developing new techniques towards this end. In the previous papers in this series, we have developed atomic models for various structures on the GaAs(100) (and related) surfaces used in MBE growth. In this paper, we combine those models to suggest an actual mechanism whereby molecular-beam epitaxy occurs. This proposed mechanism is highly suggestive in terms of improving growth techniques by, for example, varying the incident flux of the constituent species or by using monochromatic light during the growth process. It is foreseen that the implementation of such variations at specific points during the growth cycle may allow substantial reduction in substrate temperature or otherwise improve MBE growth on compound-semiconductor surfaces.

I. INTRODUCTION

Compound semiconductors appear to be among the most promising materials for the generation and detection of light for photonic communication devices. One of the fabrication processes used for such materials is molecular-beam epitaxy (MBE). GaAs has been the most studied compound semiconductor with MBE and provides a prototype for understanding the detailed nature of that growth process. Currently, the (100) surface is the favored-growth substrate, partially because of the ease with which it may be cleaned and partially because of the difficulty of achieving good MBE growth on other surfaces such as the $(\bar{1}\bar{1}\bar{1})$.

In the MBE growth of compound semiconductors, not only must the purity of starting materials be maintained and the substrate temperature be carefully controlled, but also the *relative* flux of two or more elements must be carefully governed. On GaAs(100) and related III–V (100) surfaces, an optimal-growth region has been established that is characterized by a (2×4) diffraction pattern as observed with reflection high-energy electron-diffraction (RHEED). The growth conditions under which this region occurs involve substrate temperatures between 550 and 700 °C and As_4 pressures in the 10^{-6}–10^{-5} Torr range. Higher As fluxes produce a $c(4\times4)$ structure and lower fluxes a (4×2) structure, neither of which produces as high a quality material as that grown on a (2×4) substrate. These diffraction patterns have also been observed under static, ultrahigh vacuum (UHV) conditions and, on the basis of these UHV studies, the (2×4) stucture is generally assigned a full monolayer of As atoms in the terminating layer.[1,2]

RHEED has proven to be an important technique for studying MBE growth on the GaAs(100) and related surfaces. A detailed monitoring of the intensity of RHEED features shows a cyclical variation which correlates exactly with the epitaxial layer-by-layer growth. Briones, Golmayo, Gonzalez, and de Miguel[3] have used these RHEED oscillations to determine that the initial surface stoichiometry, presumably corresponding to the most As-rich form of the (2×4) structure, varies by one-quarter of a monolayer of Ga atoms before converting into either the (4×2) or $c(4\times4)$ structures. This variation is particularly noteworthy in a structure that is generally considered to be terminated by a complete monolayer of As atoms.[1,2]

On the basis of the results of Briones *et al.*[3] and on other new experimental information[4–6] we have proposed a new model for the (2×4) surface structure.[4–6] In addition, we have expanded upon this and related models[4–6] to develop a coherent growth mechanism for molecular-beam epitaxy on III–V (100) surfaces in general and the GaAs(100) surface in particular.

It is the purpose of this paper to present this growth mechanism, to propose specific experimental approaches for testing it, and, finally, to suggest ways in which the existing growth procedures can be varied to optimize the resulting material.

II. RESULTS

Several assumptions should be noted before beginning a detailed discussion of the various stages in the MBE growth process. The first assumption deals with the nature of the unreacted species. While both As_2 and As_4 may be used in the incident flux, it is generally observed that As_2 is the predominant species desorbed from the surface. Therefore, for

 0734-211X/87/051482-08$01.00 © 1987 American Vacuum Society

simplicity, we will assume that As_2 is the actual diffusing species present on the surface and skip the question as to whether As_4 is cleaved on physisorption or chemisorption. Ga is assumed to be present in a monotonic form prior to actual chemisorption.

A second major assumption is that surface species or complexes with the longest-residence time will tend to be those that are electronically stable, i.e., not in an excited electronic state. While many excited species are expected to form during growth, it is assumed that they will be labile unless stabilized within a relatively short period of time (e.g., some number of vibrational cycles). Therefore, the surface complexes that characterize a particular stage of growth will be those that closely resemble structures seen under static-UHV conditions.

We will first describe the surface structure in the presence of an As flux, but before the Ga flux is turned on to begin the growth process. Growth will then be followed through one full cycle representing the deposition of a complete bilayer. For simplicity, growth will be described in terms of four intermediate stages corresponding to the chemisorption of 0.25, 0.5, 0.75, and 1.0 of a monolayer of Ga. This division is natural as well as formal as it corresponds to stable intermediate species.

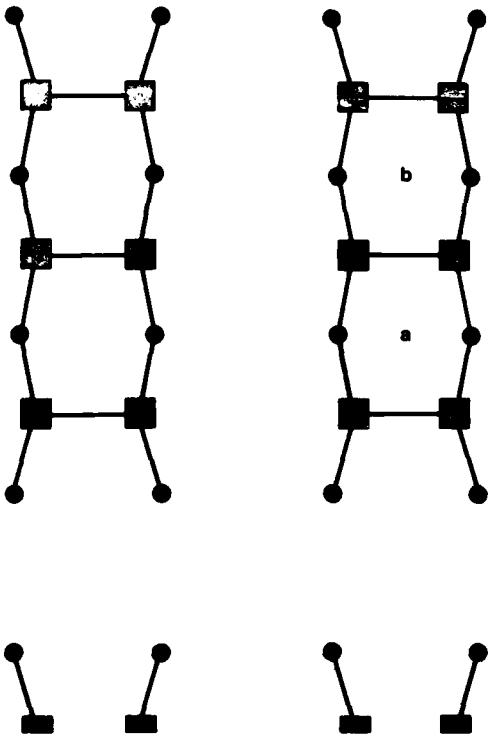

FIG. 1. A planar view of the As-rich GaAs(100)(2 × 4) surface is shown. The As atoms (open squares) form three dimers per unit cell. The dimer vacancy exposes four Ga atoms (solid circles) in the second layer. A Ga dimer can be inserted at either a or b. The size of the symbol indicates the proximity of the layer to the surface.

A. Initial structure

Barring multiple scattering effects, when the RHEED oscillations show their maximum intensity, the surface is most perfect. This is seen when the surface is allowed to reach equilibrium in the presence of an As flux, but in the absence of a Ga flux, prior to the beginning of epitaxial growth. When the As flux is high enough to produce an intensity maximum, but not so high as to change the surface to a $c(4\times4)$ structure, it has previously been assumed that the surface is terminated with a complete monolayer of As atoms,[1,2] presumably in the form of surface dimers.[7] This assumption, however, would result in a surface structure where either the bonding or dangling As orbitals are partially empty.[4–6] As previously discussed, this structure is energetically less favorable than one where these orbitals are completely filled.[4] Such a structure is shown in Fig. 1 and is proposed to have three As dimers and one dimer vacancy per unit cell.[4–6] The dimer vacancy exposes four Ga atoms in the second layer. The bonding of the surface As atoms approaches $s(p)$ rather than sp^3 hybridization as is found in the bulk. [The notation $s(p)$ indicates that the As 4s state splits off from the three As 4p states. Here, the 4p orbitals are the bonding orbitals, being used for the dimer and backbonds, and the 4s orbital is the "nonbonding" orbital, but lies well below the Fermi level.] As a consequence the surface is dilated or relaxed outward slightly, and the dimer bond contracts the dimerized As atoms together to an interatomic distance that is considerably shorter (e.g., 2.6 Å)[8] than the projected bulk positions (4.0 Å).

Because of its importance in defining each step in our proposed growth mechanism, the underlying physical concept of this model will be described in some detail for this structure. The choice of the "initial" structure as being one with three As dimers and one dimer vacancy per unit cell is not in the least arbitrary, but is based on both sound conceptual and experimental considerations.[4–6] As noted above, the physical concept underlying this initial structure (and all of the intermediary structures discussed below) is that, at any point in the bilayer growth, the dominant surface species are those that are *stable* within their specific environment.[4–6] [The real importance of short-lived (e.g., $< 10^{-5}$ s), highly mobile or highly labile species is not disregarded here, but, in general, is outside of the present scope of discussion.] In this context, the relevant stability involves both steric and electronic considerations.[4] Steric considerations require that no *undue* strain is imposed on the covalent bonds of the surface species. Electronic considerations require that all states, both bonding *and nonbonding*, that lie below the Fermi level be filled and all states lying above the Fermi level be empty.[4]

A strong asymmetry exists between the nonbonding orbitals on the surface Ga and As atoms. For Ga, two of the three 4p states are involved in the sp^2 bonding orbitals and the nonbonding or "dangling" orbital has strong p character and lies above the Fermi level; therefore it is empty.[4] However, for As, the nonbonding orbital is strongly s like in character and lies well below the Fermi level; therefore it is filled.[9] These observations are a simple consequence of the relative positions of Ga and As within the Periodic Table,[4] but have profound significance in terms of defining the electronically stable, and hence relatively long-lived, surface species that

occur within the bilayer growth cycle.

For example, if at some point during the cycle, the surface was completely covered with a full monolayer of As *dimers*, and if it was assumed that the bonding orbitals or states were completely filled, then the "dangling orbitals" on each surface As atom would only contain 3/2 of an electron. As these states are strongly *s*-like in character, and therefore well below the Fermi level (e.g., 10–12 eV), this would be a highly unphysical situation. However, if one out of every four surface dimers is removed, the underlying Ga dangling bonds (four, with 3/4 of an electron each) that are nominally above the Fermi level can transfer their unwanted electrons to the remaining As dangling bonds (six, with 3/2 of an electron each) to achieve the ideal situation where all of the Ga dangling bonds are empty and all of the As dangling bonds are filled. Note that this very simplistic electronic argument necessitates a unit cell with a basis of eight atomic sites, and, given the assumption of surface dimers, a twofold periodicity along the $[1\bar{1}0]$ direction. We suggest that it is no accident that the experimentally observed (2×4) unit cell is the simplest of those that meets these requirements. Both our recent high-resolution electron-energy-loss spectroscopy[5] and angle-resolved photoemission spectroscopy[6] results support such a structure. Last, but not least, independent theoretical studies by Chadi[9] indicate that such a "dimer vacancy" or "missing row" structure is expected to have a minimal free energy at the surface.

While a similar one-to-one correspondence does not always exist between all structures observed under static UHV conditions and MBE-growth conditions, similar requirements for electronic stability are imposed in all cases to be discussed below and, for simplicity in reading, will not be pursued in detail.

B. Stage1

When the Ga flux is turned on, the Ga atoms presumably arrive at the surface as monatomic species. A single-Ga atom might attempt to bond to one As atom via an As-dangling orbital, but this would be a rather short-lived species having only one covalent bond and three electrons in the Ga-nonbonding orbitals. (Here, a total of five electrons, two from the As dangling orbital and three from the Ga itself, are shared among one bonding orbital and two dangling orbitals.) A somewhat more stable species is produced, however, when a Ga atom is inserted into an As-dimer bond. Here, two covalent bonds are formed and only one electron is left in a Ga-nonbonding orbital. Both species are expected to be more or less labile, and a given Ga atom may enter into a number of these unstable surface complexes before it reaches its final bonding site.

The insertion of two Ga atoms into two adjacent As-dimer bonds, however, does allow for the formation of a stable Ga species on the surface.[4,5] This is a Ga dimer with five covalent bonds and no electrons in the Ga dangling orbitals. (The two single electrons left in the nonbonding Ga orbitals of each of the two Ga atoms combine to form a covalent bond between the two inserted Ga atoms.) Note that there are two sites per unit cell where such a Ga dimer could form [Fig. 1 site (a) or (b)]. Unlike the As dimer, the Ga dimer has approximately sp^2 bonding with the consequence that it is relaxed inward toward the bulk This will relax the underlying As atoms that it is bonded to back towards, and perhaps even beyond, the projected bulk positions.[4,5] This configuration is shown in Fig. 2 and the relaxation of the As atoms serves an important function in setting up the following stages. (Note that the insertion of either one or a pair of Ga atoms into As-dimer bonds is more stable than chemisorption across As-dangling orbitals at this stage not only on the basis of electronic considerations, but also on the basis of steric considerations as the dimer sites are initially separated by about 2.6 Å while the other sites are about 5.4 Å apart.)

When approximately one-quarter of a monolayer of Ga has been deposited, there will, on the average, be one Ga dimer per unit cell. As there are two sites per unit cell, these Ga dimers may be either next to those in adjacent cells, in Fig. 2, or offset by one atomic spacing as would be the case if the dimer at point a had been inserted at point b instead. Because of the As-stabilized conditions used in MBE growth, while these Ga dimers are being formed there is still an As flux to the surface that greatly exceeds the Ga flux. However, at this stage of growth there are essentially no stable binding sites for As, and short-lived species presumably form and decay with the subsequent diffusion and desorption of As_2.

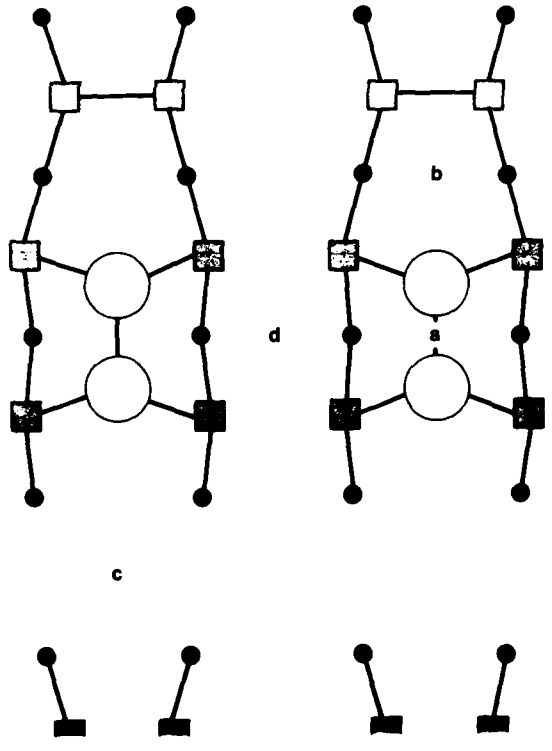

FIG. 2. After the chemisorption of the 1/4 monolayer of Ga (open circles), one Ga dimer per unit cell initiates growth of the second layer. In the right-hand cell the dimer may be aligned with that in the left-hand adjacent cell as shown inserted at a, or staggered if inserted at b. Insertion of a second Ga dimer at point d necessitates the filling of the As vacancy at point c.

C. Stage 2

For the growth process to proceed further, four Ga atoms must be chemisorbed contiguously as two adjacent dimers to provide a bonding site for an As_2 dimer. In addition, the dimer vacancy in the first layer must be filled to provide a basis for the chemisorption of further Ga atoms. As will be seen, these two steps (the chemisorption of an As dimer to fill the vacancy and the chemisorption of a second pair of Ga atoms) must occur essentially simultaneously within a given unit cell to achieve an electronically stable situation. This step, and a similar one near the end of the cycle, appear to be the rate limiting steps for epitaxial growth to occur. In addition, the necessity of having an As_2 dimer (or its monatomic constituents) available for concurrent chemisorption may explain, in part, the requirement of a much larger As than Ga flux to the surface for successful growth to occur.

For the configuration shown in Fig. 2, spatially the only reasonable bonding site for a Ga atom is between four of the As atoms already bonded to Ga dimers, point d. Here is where the lateral relaxation of these As atoms becomes important as it will allow the Ga atom to bridge this position forming two covalent bonds simultaneously (rather than only one as would have been true in the very first stage of Ga chemisorption). However, while this site is geometrically feasible, and even desirable, when only one Ga atom is adsorbed it produces an electronically unstable species with three electrons in the Ga-dangling orbitals. The chemisorption of a second Ga atom in the adjacent site, with the concomitant formation of a dimer bond between the two Ga's, eases the situation only slightly as it reduces the number of electrons in Ga-dangling orbitals to only two per atom. Even so, this species is still expected to be extremely labile as it contributes a total of four electrons to the unit cell that are nominally above the Fermi level and therefore may be considered to be in an excited state. These four extra electrons would seem to present an enormous barrier to the growth process were it not for another chemisorption process that actually requires such an excess.

As noted above, the second difficult step at this stage of growth is the filling of the dimer vacancy in the original surface layer. This vacancy exposes four Ga atoms to which the new As dimer must bond. In the structures shown in Figs. 1 and 2, these Ga atoms have empty dangling orbitals. However, for a physisorbed or gaseous As_2 species to be bonded stably to this site, four extra electrons must be provided by the substrate. The reasons for this are as follows. An unbonded-As_2 molecule (either in the gaseous state or thermally diffusing on the surface) has ten valence electrons, five from each As. A bonded-As dimer requires 14 electrons, two for the dimer bond, eight for the four backbonds, and two each in the two dangling *s*-like orbitals. Therefore, the substrate must provide four additional electrons for the dimer vacancy to be filled in other than an ephemeral fashion.

On this basis, it is eminently plausible that these two chemisorption processes, one producing an excess of four electrons and one requiring four additional electrons, are closely coupled in both time and space. The resulting structure is shown in Fig. 3 for several adjacent unit cells. However, it may now be seen that there are additional binding sites for

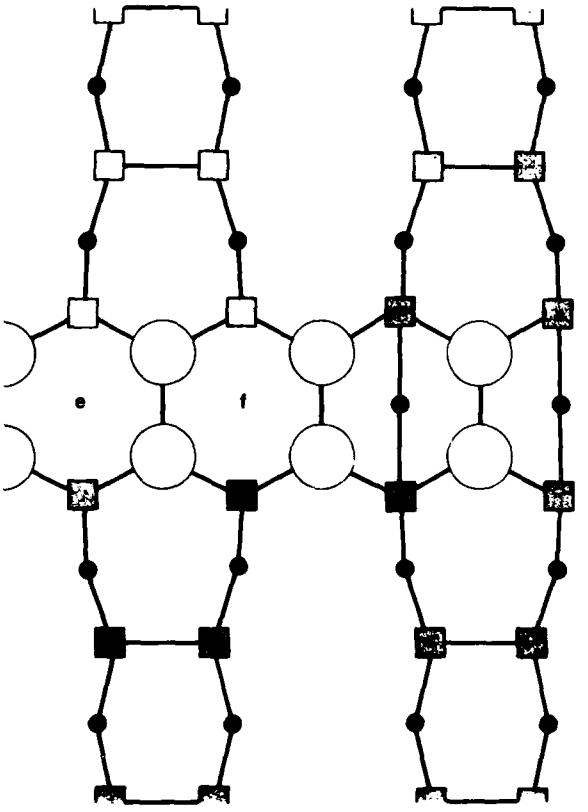

FIG. 3. Coupled with the filling of the As-dimer vacancy in the lower-As layers, the chemisorption of a second Ga dimer per unit cell opens up a new site for the chemisorption of an As dimer centered at either points e or f. Note that island formation is extended along the $[1\bar{1}0]$ direction.

As_2 molecules, shown as positions e and f in Fig. 3. In fact, given the excess As flux, it is probable that almost as soon as two adjacent Ga dimers are formed, a new As-surface dimer will be inserted into the Ga-dimer bonds. This is shown schematically in Fig. 4. This process is expected to be relatively rapid (e.g., <0.1 s) on the time scale of a bilayer growth cycle, but much slower than the residence times of labile-Ga species, (e.g., $<10^{-9}$ s).

The chemisorption of these As dimers initiates the growth of the top of the bilayer. Note that there now is a top or surface layer with one quarter of a monolayer coverage, and a second layer with one-half of a monolayer coverage. This represents the roughest atomic configuration, and, not surprisingly, occurs at the middle of the bilayer growth cycle where the experimentally observed RHEED intensities reach their minimum value. This suggests that one possible method for checking this model is to investigate the curvature of the RHEED intensities in the vicinity of the minima as a function of the incident As flux.

Figure 4 brings us to the middle of the bilayer growth cycle. It is worthwhile to pause at this point and explore some of the tacit assumptions underlying the above model. First, let us consider the question as to whether or not the

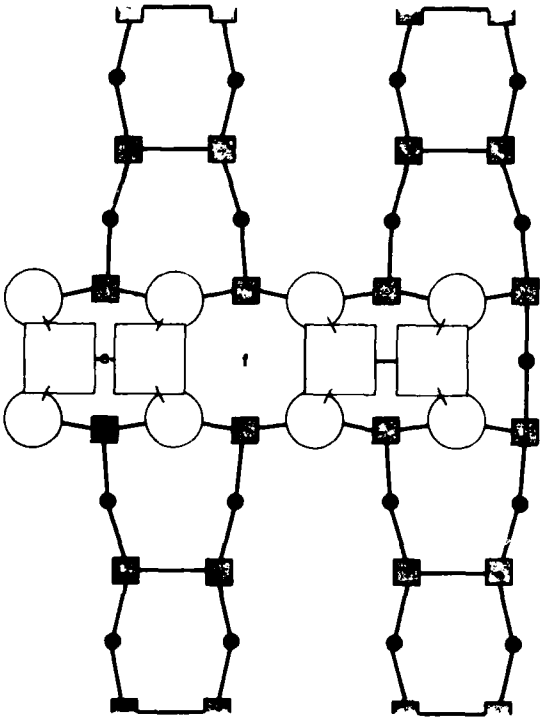

FIG. 4. The chemisorption of an As dimer (large open squares) initiates growth in the top of the surface bilayer and completes the second state of the growth cycle.

first and second steps may be reversed. In the first step, we are inserting a Ga dimer across two As-dimer bonds. Here, the bonding sites are about 2.6 Å apart.[8] In the second step, the Ga dimer is inserted between four As-dangling orbitals. If the step order is inverted, then these dangling orbital sites are unphysically far apart (e.g., 5.4 Å). Therefore, at least for the initial or nucleation step withing a given domain, it seems improbable that step 2 will precede step 1. However, the possibility of spontaneous dimer dissociation at growth temperatures[10] may allow an inversion of step order and the resulting As dimers would be greatly weakened allowing for easy insertion of Ga atoms. It is probable that both processes occur in parallel on the surface.

A second question that needs to be addressed is what happens when the Ga dimers in Fig. 2 are staggered rather than perfectly aligned to enhance the Ga dimer insertion illustrated in Fig. 3? The easy answer, that growth only proceeds within a domain of properly aligned Ga dimers, is confounded by two facts. The first is that as there are two apparently equivalent sites per unit cell, these domains would be quite small. The second is that growth is apparently characterized by the development of long islands or plateaus along the [1$\bar{1}$0] direction (as shown schematically in Figs. 3, 4, and following). This indicates that the growth process in contiguous unit cells is correlated and points to the possibility that either atomic rearrangement occurs at domain boundaries during the development of the Ga half-monolayer (presumably a strongly exothermic process that could power either surface diffusion or rearrangement reactions), or that the first and second stages, as simplisitically outlined above, may occur in a coherent fashion to extend growth along the [1$\bar{1}$0] direction after the initial, nucleation stage. (In the former case, thermally activated exchange of the Ga dimer between points a and b may be important.) The latter case could be envisioned as, for example, the insertion of two Ga dimers across As-dimer bonds, followed by the second stage, where the initial dimer vacancy is filled and a Ga dimer is inserted across the "dangling bond positions" and culminating in a "domino theory" extension where laterally contiguous unit cells experience rearrangement of their initial Ga chemisorption under the influence of previously reacted sites. This picture, while conceptually more complicated than the relatively simple one Ga dimer than one Ga plus one As dimer model leading to Fig. 3, may actually describe what occurs on the surface.

D. Stage 3

In any event, the surface structure at the midpoint of the growth cycle is expected to resemble that shown in Fig. 4 after the subsequent chemisorption of the first quarter-monolayer of As. Note that there are no As-bonding sites within this simple picture. Here again, we are faced with a large incident flux of As atoms with no place to go. There is, however, a site for chemisorbing a Ga dimer. As in the first stage, this presumably does not occur with the instantaneous chemisorption of a molecular Ga_2 species, but as a stepwise processes involving two Ga atoms that may have to make a number of attempts via unstable absorption sites before achieving stable pairing as is shown in Fig. 5.

E. Stage 4

We are now a full three-quarters of the way through the growth cycle but are again faced with a double dilemma; on the average, there are no available sites for As chemisorption in the top layer, and one dimer vacancy per unit cell must be filled in the next-to-last layer. As before, these two separate processes necessitate in one case (the insertion of an As dimer across four unoccupied Ga dangling orbitals) the provision by the substrate of four extra electrons per unit cell and in the second case (the filling of the Ga dimer vacancy) the development of four unwanted electrons for unit cell. This is the second rate-limiting step in the growth process. As before, it is proposed that these two steps occur essentially simultaneously with a variety of intermediates being formed and then dissociating until, statistically, a stable electronic situation results. Referring to Fig. 5, it can be seen that there is one site per unit cell g that corresponds to a Ga dimer vacancy. There are, however, four alternative sites per unit cell for the essentially simultaneous chemisorption of an As dimer (positions h, i, k, l in Fig. 5). The occupation of one such site, however, rules out the occupation of other sites within a given unit cell (e.g., h rules out i or k rules out l, Fig. 6). Furthermore, the completion of the bottom, Ga half of the bilayer opens up one additional As dimer binding site per unit cell. As in the second stage, this fourth or last stage of bilayer growth is proposed to involve the incorporation of a

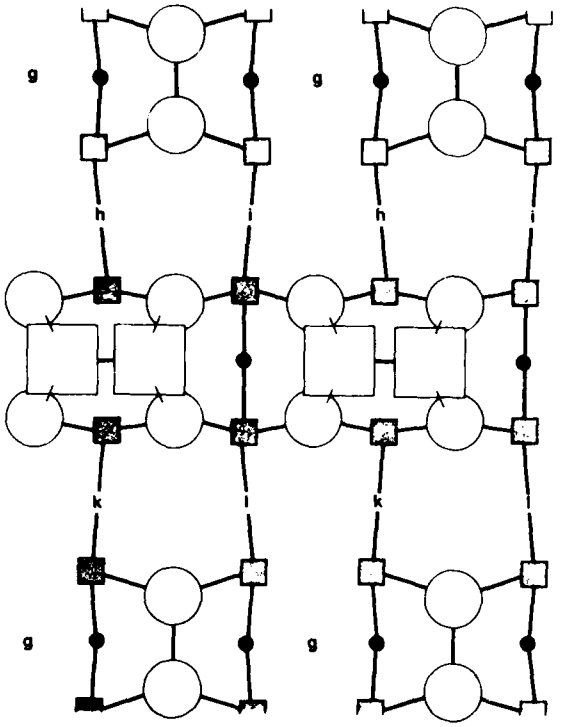

FIG. 5. The chemisorption of a third Ga dimer per unit cell completes the third stage of the growth cycle. Note that this structure is stabilized relative to a (4×2) unit cell by presence of 1/4 of a monolayer of As in the outermost layer. Further growth necessitates the simultaneous filling of the Ga-dimer vacancy site at point g and the chemisorption of one As dimer per unit cell at either points h or i or at points k or l.

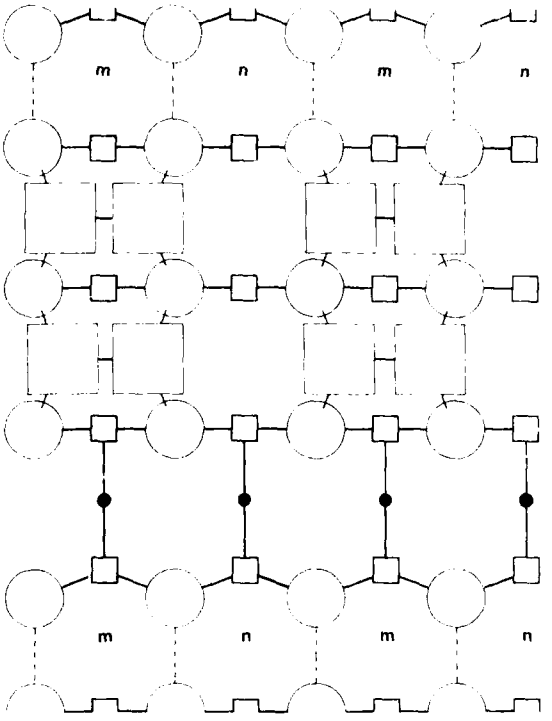

FIG. 6. Here, the correlated chemisorption of a Ga dimer at point g and an As dimer at point h is shown. This opens up one additional site for the adsorption of an As dimer. Site m is favored over site n on the basis of backbonding.

second As_2 unit still keeping all As dangling bonds filled and all Ga ones empty. While intermediate structures may occur, backbonding requirements indicate that the new structure within a given domain will be that shown in Fig. 6. There again, we find three As dimers and one dimer vacancy per unit cell. For variety, a $c(2\times8)$ rather than a (2×4) domain is shown (Fig. 7).[4,5] Note that otherwise, the atomic configurations is essentially that shown in Fig. 1, and we have recapitulated the bilayer growth cycle.

III. DISCUSSION

It is appropriate to note a few words here on the basic $(2\times4)/c(2\times8)$ unit cell. The first point is one that may not be obvious from a casual perusal of Figs. 1 and 6. That is, that there is very little difference in free energy between these two structures. Given the presence of the dimer vacancy, and the covalent nature of the GaAs bonds, adjacent As dimer triplets are only connected via the third layer. In a sense, this may be regarded as a fifth nearest-neighbor interaction which is rather weak even in a directionally bonded system. Both unit cells involve three-aligned As dimers per unit cell. Backbonding strain is minimized by having the dimers aligned along the [110] direction for any given tri-

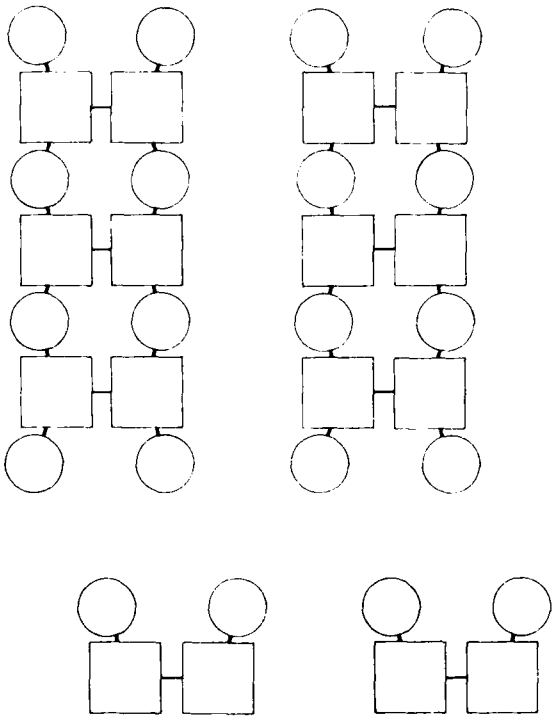

FIG. 7. The growth cycle is complete and the As-rich structure shown in Fig. 1 is recovered. This occurs when an As dimer and a Ga dimer are simultaneously chemisorbed on the structure shown in Fig. 5 followed by the chemisorption of a final As dimer. Here, for variety, a $c(2\times8)$ unit cell is shown.

plet. The dimers are contracted along the $[1\bar{1}0]$ direction, and as the As bonding approaches $s(p)$ hybridization, the underlying Ga atoms are also displaced primarily along the $[1\bar{1}0]$ direction.[4,6] This picture is in contrast to that proposed by Larsen *et al.*,[1,2] where the second layer Ga atoms are at their projected bulk positions and with the As dimers asymmetrically bonded (with partially filled orbitals). The structure shown in Figs. 1 and 6 produces significantly less backbonding strain on the underlying Ga atoms by not pulling them in two directions at once and allows the preferred $s(p)$ bonding of the As surface dimers.

Another interesting point to note is that the (2×4) structure is apparently preserved, albeit in a somewhat diffuse form, throughout the growth cycle. This is particularly interesting near the third stage where approximately 3/4 of a monolayer of Ga atoms has been chemisorbed. Our earlier work under static UHV, or nongrowth, conditions indicates that the stable structure in this region is the (4×2) or $c(8\times2)$ unit cell that is characterized by three parallel Ga dimers and one dimer vacancy, per unit cell, in a fashion somewhat analogous to the As-rich (2×4) or $c(2\times8)$ unit cells shown in Figs. 1 and 6 (though orthogonally oriented and with rather different surface relaxation).[4-6] Under MBE growth conditions, however, the (2×4) structure is locked-in at the second stage by the chemisorption of an As dimer on top of the Ga atoms (Fig. 4). This chemisorption step prevents reconstruction at the 3/4 monolayer level (Fig. 5) and preserves the general nature of the $(2\times4)/c(2\times8)$ unit cell throughout the growth cycle. Hence one does not observe an oscillation back and forth between (2×4) and (4×2) as one successively adds monolayers of As then Ga then As and so forth; as one might at first expect. This is of course in agreement with what one finds experimentally.

One of the purposes of this paper is to suggest experimental tests for checking this model mechanism. Given restrictions on experimental geometry imposed by incident molecular beams, grazing incidence techniques such as RHEED are the most appropriate for *in situ* measurements. One possibility, mentioned earlier, is to measure the detailed nature of the RHEED intensity as a function of the stage in the growth cycle (e.g., the curvature at the minimum). However, accurate evaluation of the data would need model calculations, possibly involving the inclusion of multiple scattering. Presently, model calculations are being done by several groups.[11] Though to the best of our knowledge, none to date have included surface reconstruction effects. A more empirical approach might be to halt the growth process at various points during the cycle and monitor the diffraction pattern as a function of incident As flux. With zero flux, presumably all intermediates would eventually revert to a Ga-stabilized structure. However, the rate at which this revision occurs should depend upon the relative Ga and As concentrations at the surface. If these concentrations vary at different stages during the growth cycle, as suggested by this model, different relaxation times should be observed. Similar experiments in the presence of an As flux of varying intensities are logical elaborations on the above suggestion.

Another purpose of this paper, and pragmatically the most important, is to suggest specific modifications of existing experimental procedures to facilitate the growth process. One obvious suggestion is to vary the incident flux of one or more species during the growth cycle. For example, within this simple model, no As uptake occurs at the first and third steps, but an excess of As is crucial at the second and fourth stages. Therefore, it might be reasonable to pulse the As source (or the Ga) synchronously with the monolayer growth cycle. Careful experimental investigation is needed, however, to refine such an approach. A simple variation on this idea has already been attempted via the sequential deposition of a full monolayer of As followed by a full monolayer of Ga.[12] This led to good quality epitaxial growth even at temperatures below 200°. Obviously, this line of investigation provides very attractive possibilities and needs further study.

A second suggestion for facilitating the growth process involves the use of monochromatic light to selectively break certain bonds at specific stages during the growth process. For example, the initial stage involves the breaking of As-dimer bonds on the surface and the insertion of Ga atoms. If these dimer bonds could be broken photonically rather than thermally, lower-reaction temperatures might be usable. Considerable information exists in the literature about the relative position of the dimer associated surface states and the valence-band maximum (VBM).[1,2] Some of these states lie within 1 eV of the VBM and excitation from these states to above the gap, particularly to the appropriate, quasilocalized antibonding states, might be feasible. The use of polarized light to select between Ga and As dimers also opens up interesting possibilities. While many questions need to be investigated along this line, it is important to note that recent experiments with II–VI compounds show that the use of light allows for the growth of materials with previously unobtainable doping characteristics.[13] Therefore, we suggest that this approach also opens up a potentially valuable area for further investigation.

ACKNOWLEDGMENTS

The authors wish to acknowledge the many valuable discussions with D. E. Aspnes, J. L. de Miguel, J. Ihm, J. Levkoff, E. O. Kane, and M. C. Tamargo.

[a] Present address: Department of Physics, University of Oregon, Eugene, OR 97403.

[1] P. J. Dobson, J. H. Neave, and B.A. Joyce, Surf. Sci. **119**, L339 (1982).
[2] P. K. Larsen, J. H. Neave, J. F. Van der Veen, P. J. Dobson, and B. A Joyce, Phys. Rev. B **27**, 4966 (1983).
[3] F. Briones, D. Golmayo, L. Gonzalez, and J. L. de Miguel, Jpn. J. Appl. Phys. **24**, L478 (1985).
[4] H. H. Farrell, J. P. Harbison, D. J. Frankel, C. Yu, Y. Chiang, and N. Tache (to be published).
[5] D. J. Frankel, C. Yu, J. P. Harbison, and H. H. Farrell, J. Vac. Sci. Technol B **5**, 1113 (1987).
[6] H. H. Farrell, J. P. Harbison, Y. Chiang, and N. Tache (to be published).
[7] A. Y. Cho, J. Appl. Phys. **47**, 2841 (1976).
[8] R. I. G. Uhrberg, R. D. Bringans, R. Z. Bachrach, and J. E. Northrup, Phys. Rev. Lett. **56**, 520 (1986).

[9]D. J. Chadi, J. Vac. Sci. Technol. A **5**, 834 (1987).
[10]H. H. Farrell, F. Stucki, and G. J. Lapeyre (to be published).
[11]See, for example, J. M. Van Hove, C. S. Lent, P. R. Pukite, and P. I. Cohen, J. Vac. Sci. Technol. B **1**, 741 (1983); and A. Madhukar and S. V. Ghaisas, Appl. Phys. Lett. **47**, 247 (1985).
[12]Y. Horikoshi, presented at the 4th International Molecular Beam Epitaxy Conference, York, England, 7–10 September 1986.
[13]R. N. Bicknell, N. C. Giles, and J. F. Schetzina, presented at Seventh Molecular Beam Epitaxy Workshop, Cambridge, MA, 20–22 October 1986; Appl. Phys. Lett. **49**, 1095, 1735 (1986).

A study of the mechanism of metal deposition by the laser-induced forward transfer process[a)]

F. J. Adrian, J. Bohandy, B. F. Kim, and A. N. Jette
Milton S. Eisenhower Research Center, Applied Physics Laboratory, The Johns Hopkins University, Laurel, Maryland 20707

P. Thompson
Department of Physics, The Johns Hopkins University, Baltimore, Maryland 21218

(Received 12 March 1987; accepted 22 June 1987)

The mechanism of the laser-induced forward transfer (LIFT) technique for transferring metal features from a film to a substrate is examined by using the one-dimensional thermal diffusion equation with a moving solid-melt boundary to model the heating, melting, and vaporization of the metal film by the laser. For typical LIFT conditions the calculations show that the back of the film (i.e., the part exposed to the laser) will reach the boiling point before the film melts through, which supports the qualitative picture that the LIFT process involves vapor-driven propulsion of metal from the film onto the target.

I. INTRODUCTION

Recently, it has been shown that metal features can be written from a metal film to a target substrate in close proximity to the film by a laser pulse focused on the obverse interface (i.e., opposite the film–target interface) between a transparent support and the metal film.[1] The general features of this method, which is denoted laser-induced forward transfer (LIFT), are readily perceived from the diagram of the LIFT apparatus shown in Fig. 1. The process has the advantages of simplicity and cleanliness in comparison with other metal deposition methods such as ultraviolet (UV) photolysis of gas phase metallo-organic precursors[2–4] and methods involving liquid phases.[5–7] Although the spatial resolution of the LIFT process is at present somewhat less than that of other methods, it appears likely the resolution can be improved by improving the laser focus, and in any event, the inherent advantages of the method warrant its further investigation.

The characteristics of the metal deposits obtained by this process,[1] in particular the fact that the size of the written metal features correspond closely to the size of the laser focal spot, suggest that the LIFT mechanism is thermal ablation of the source film in the laser irradiated region combined with propulsion of this material onto the target by metal vapor that is trapped between the source film and its support and is released the instant the film ruptures. Clearly, if this mechanism is to be operative it is necessary that the laser pulse energy be sufficient to produce simultaneous melting of the film in the irradiated region and a substantial vapor pressure at the laser-irradiated side of the film. This hypothesis and other features of the LIFT process are examined here by calculations of the laser-induced heating, melting, and vaporization of the metal film using the one-dimensional heat transfer equation with a moving solid-melt boundary. The calculations will show that the aforementioned conditions of melting and vaporization occur for nearly all the combinations of laser energy (30–100 mJ deposited in 15 ns) and film thickness (0.12–1.2 μm) used in the experiments, with the notable exception of the thickest films at low-laser power, in which case the laser energy at which metal transfer ceases is comparable to that at which the calculations predict incomplete melting of the film.

II. THEORETICAL MODEL

The model is based on a calculation of the heating and accompanying melting of a rectangular area of a metal film by a focused laser beam. The heated area is determined by the focal area of the laser and is 2.5 cm by 50 μm. Since these dimensions are much larger than the film thickness ($\lesssim 1$ μm) a one-dimensional geometry will be a good approximation. Furthermore, even though the temperature will considerably exceed the boiling point of the metal in many cases, radiation effects are negligible because of the small area of laser focus combined with the smallness of the Stefan–Boltzmann radiation constant.

Thus, the model requires solutions to the one-dimensional heat transfer equation with a penetrating heat source and a moving boundary between the solid and molten phases of the metal film. This boundary condition, known in mathematics literature as the Stefan or the moving boundary value problem,[8] is not only what makes the problem a nontrivial one

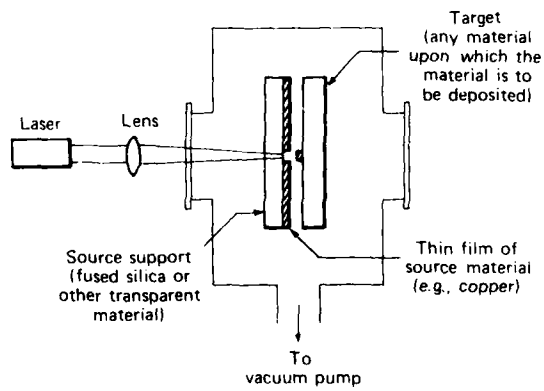

FIG. 1. Schematic illustration of the apparatus for metal deposition from a solid-phase precursor. The source material and target are in contact during an actual experiment.

 0734-211X/87/051490-05$01.00 © 1987 American Vacuum Society

but is a key feature of the model. This boundary between the two phases propagates through the material until either melt through occurs or laser heating stops. The position of the boundary as a function of time, whether melt through occurs, and the temperature profile at melt through are key points for interpretation of the LIFT results.

The one-dimensional heat equation is[9]

$$\frac{\partial U^{(i)}(x,t)}{\partial t} = \sigma_i \frac{\partial^2 U^{(i)}(x,t)}{\partial t^2} + \frac{\sigma_i}{K_i T_o} S_i(x,t), \quad (1)$$

where $i = 1$ refers to the solid phase and $i = 2$ refers to the molten state. $U^{(i)}(x,t)$ is the normalized temperature

$$T_i(x,t) = T_o \cdot U^{(i)}(x,t), \quad (2)$$

where T_o is the melting temperature of the film and $T_i(x,t)$ is the temperature of the film at position x and time t (K). K_i is the thermal conductivity of the metallic film (W/m K) and σ_i is

$$\sigma_i = K_i/\rho_i C_i, \quad (3)$$

where ρ_i is the film density (kgm/m^3) and C_i its specific heat (J/kgm K). The source term is

$$S_i(x,t) = A f(t)(1 - R_i)\alpha_i e^{-\alpha_i x}, \quad (4)$$

where $A f(t)$ is the heat flux as a function of time (J/m^2 s), R_i is the reflectivity of the film and α_i is the attenuation constant into the film (m^{-1}). In all cases the integral of $f(t)$ over time is unity so A in Eq. (5) is the total laser energy incident on the film. The computer code will accommodate pulse shapes that are rectangular (constant heat input), triangular, and Gaussian. The Gaussian and triangular pulse shapes gave very similar results. The solution to Eq. (1) is obtained subject to the following boundary conditions at the front and back surfaces:

$$\frac{\partial Ux^{(1)}(0,t)}{\partial x} = -(1 - R_1)\frac{Af(t)}{K_1 T_0}; \quad y(t) = 0, \quad (5a)$$

$$\frac{\partial Ux^{(2)}(0,t)}{\partial x} = -(1 - R_2)\frac{Af(t)}{K_2 T_0}; \quad y(t) > 0, \quad (5b)$$

and

$$\frac{\partial U^{(i)}(B,t)}{\partial x} = 0, \quad (5c)$$

where B is the thickness of the film and $y(t)$ equals the position of the interface between phases (1) and (2) at time t. In addition to the boundary conditions at the front and back surfaces, the boundary conditions on the moving interface must be satisfied

$$U^{(1)}[y(t),t] = U^{(2)}[y(t),t] = 1 \quad (6a)$$

and

$$K_1 \frac{\partial U^{(1)}(y,t)}{\partial x} - K_2 \frac{\partial U^{(2)}(y,t)}{\partial x} = \frac{\rho_1 L}{T_0}\frac{dy}{dt}, \quad (6b)$$

where L is the latent heat of fusion of the metallic film (J/kgm). Initially at $t = 0$ the temperature of the material is

$$U^{(1)}(x,0) = C'/T_o = C. \quad (7)$$

Because of the moving boundary Eq. (1) is solved numerically. The finite difference technique developed by Ehrlich[10] for the melting solid was selected to determine the solutions of this equation which is a variation of the Crank–Nicolson method.[11] This theory was generalized to include a penetrating heat source and is, with this modification, essentially the same as detailed by Ehrlich. Hence, the procedure will only be briefly outlined.

A grid is imposed on the (x,t) plane such that $U_{i,j} = U(i\,\Delta x, j\,\Delta t)$. The values of $U_{i,j+1}$ on the $j+1$ time step are given in terms of the known $U_{i,j}$ on the j time step using the standard Crank–Nicolson method noting that $U_{i,0} = C$ by Eq. (7). This method is straightforward except at the front and back surfaces where minor modifications must be made. The calculation proceeds until such a time that $U_{0,j+1} \geqslant 1$ while $U_{0,j} < 1$. Then a new base line is established using the scaling

$$\Delta t' = \frac{(1 - U_{0,j})}{U_{0,j+1} - U_{0,j}}\Delta t,$$

and the molten phase is entered. From Eq. (6b) the slope of the melt front is determined with various initial approximations and an iterative procedure. In this way the melt front position at the next succeeding time step is located.[10] On the molten side of the melt front, the solutions to Eq. (1) are obtained using thermal and physical parameters appropriate for the liquid phase ($i = 2$) while on the solid side the constants pertaining to the solid phase are employed. These constants are tabulated in Table I for Cu. Strictly, these parameters are a function of temperature as well as phase,[12] but for metals this dependence is unimportant for our applications.

The calculations were done on an IBM PC with computer code written in Fortran. The resulting melt front versus time curves are shown in Fig. 2 for copper films ranging in thickness from 0.12 to 1.2 μm and at pulse energies comparable to those used in the experiments with a triangular pulse shape being used for $f(t)$ in Eq. (4). The calculations stop when the liquid phase reaches the back surface of the film (melt through) or at the end of the laser pulse (15 ns). Figure 3

TABLE I. Copper thermal constants.

Constant	Solid	Liquid
Thermal conductivity K[W/(MK)]	388	170
Specific heat C[J/(kgmK)]	385	494
Density ρ[(kgm/M^3)]	8.895×10^3	7.97×10^3
Reflectivity R	0.329	0.329[a]
Attenuation coefficient α[M^{-1}]	8.92×10^7	8.92×10^7
Latent heat of fusion L[J/kgm]	2.05×10^5	
Melting temperature T_o[K]	1356.15	

[a] Assumed to be the same as the solid phase.

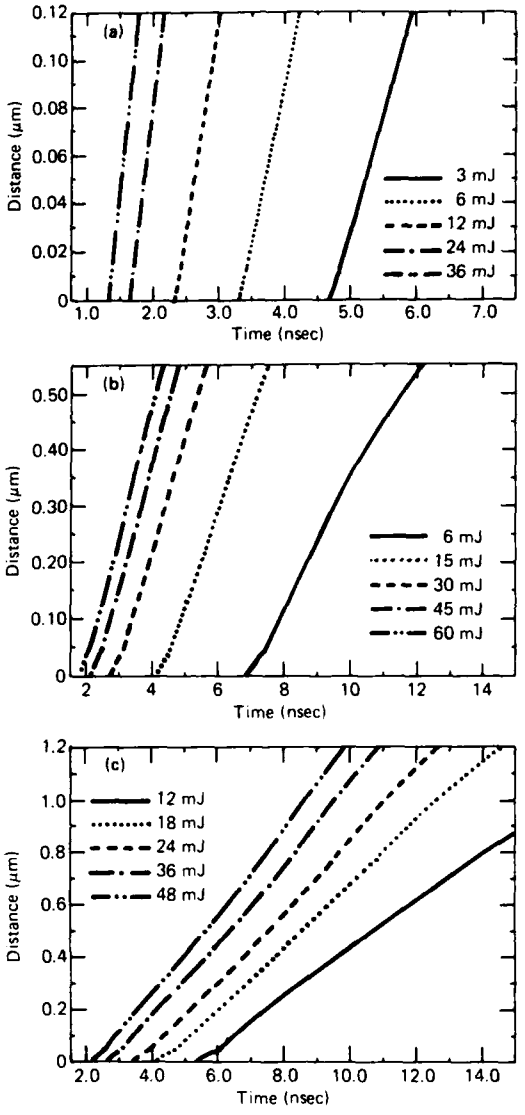

FIG. 2. Theoretical melt front propagation curves for (a) 0.12; (b) 0.55, and (c) 1.20-μm-thick Cu films.

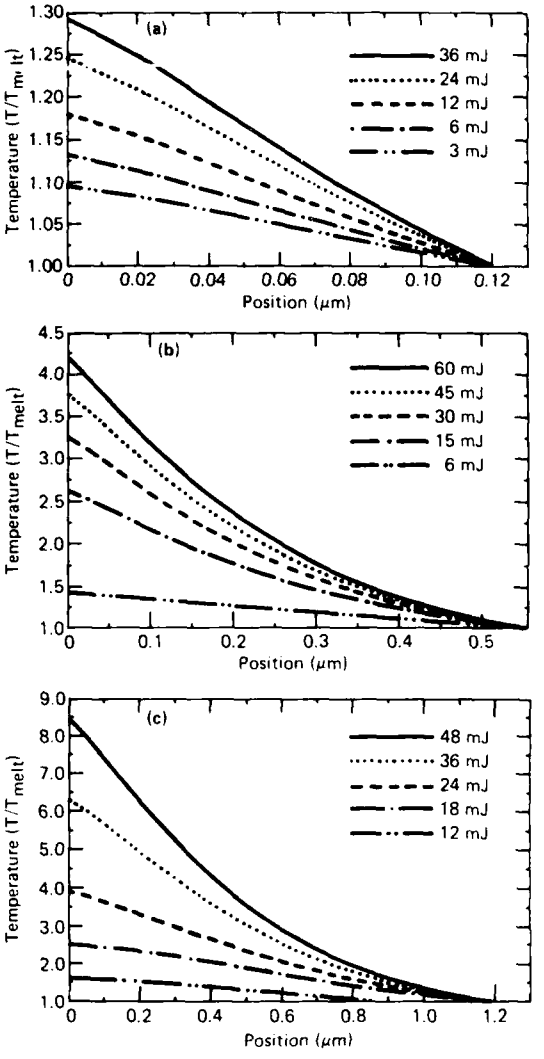

FIG. 3. Temperature profile curves after melt through for (a) 0.12; (b) 0.55, and (c) 1.20-μm-thick Cu films.

gives the corresponding temperature profile at melt through for these films where the boiling point of copper at the standard pressure of 760 Torr corresponds to the normalized temperature $U(x,t) = 2.1$. The temperature profiles at melt through in Fig. 3 show that for the thickest films (0.55 and 1.2 μm) the front (i.e., laser-irradiated surface) is well above the boiling temperature at melt through, provided that melt through occurs. For the thinnest film (0.12 μm) melt through occurs before the front surface reaches the boiling point; however, it should be noted that the thin films melt through much more rapidly and vaporization is virtually certain before the end of the laser pulse.

The slopes of the melt front propagation versus time curves decrease with film thickness as consequence of the boundary condition on the back surface, Eq. (6c). As heat diffuses to the back surface it has nowhere to go (except lateral diffusion) and builds up rapidly increasing the temperature. Thus the slopes are very steep for the thinner films.

III. DISCUSSION: COMPARISON WITH EXPERIMENT

Figure 4 shows electron micrographs and film thickness profiles (obtained with a DEKTAK profilometer) of metal lines deposited using the apparatus shown in Fig. 1 for various film thicknesses and laser energies. The details of the process have been given previously,[1] so the process need be described only briefly here. The light source is a Lambda Physik EMG 102E pulsed excimer laser operating in the stable resonator configuration at 193 nm. It produces a light pulse of ~15-ns duration which is focused by a cylindrical-fused silica lens onto a copper film deposited on a transparent silica support to yield a focal line 2.5 cm by 50 μm. The laser energies were determined by measuring the energy of a known fraction of the beam reflected off a beam splitter with a GENTEC model PRJ-M power meter. The laser energy actually reaching the film was then determined from this energy and appropriate loss factors of 10% (determined from data on the Suprasil silica used by its manufacturer

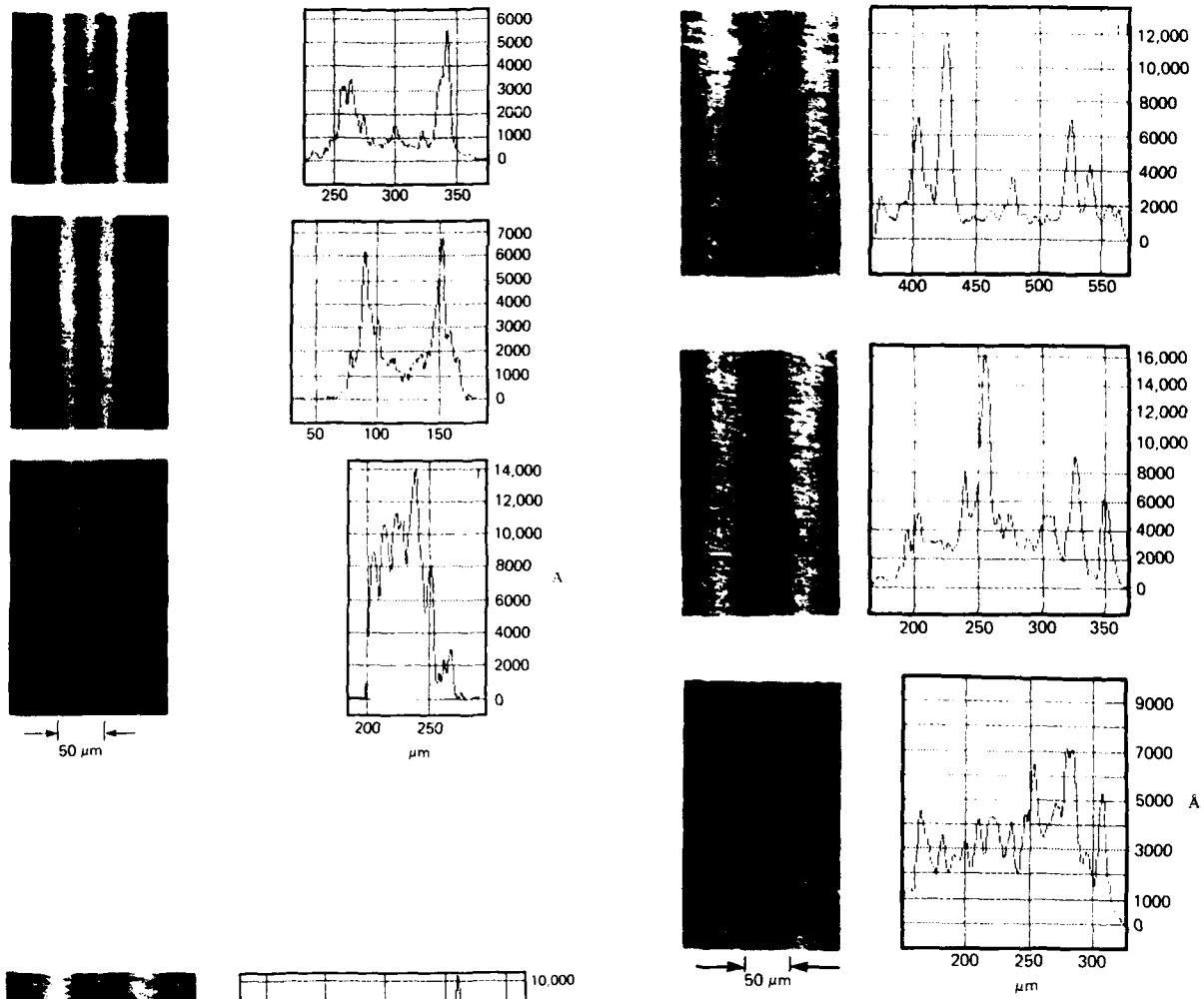

FIG. 4. Cu depositions on a silica substrate and DEKTAK profilometer curves for varying film thicknesses and laser pulse energies. Upper left: film thickness is 0.12 μm and the top, middle, and bottom sections are for laser energies of 41, 27, and 22 mJ, respectively. Lower left: Film thickness is 0.55 mm and the top, middle, and bottom sections are for laser energies of 101, 67, and 35 mJ, respectively. Right: Film thickness is 1.0 μm and the top, middle, and bottom sections are for laser energies of 90, 61, and 43 mJ, respectively.

Heraeus Amersil) for each of the silica optics traversed by the beam before reaching the sample.

Comparison of these experimental results with the calculated melting curves and temperature profiles in Figs. 2 and 3 show that in all cases the laser energy is sufficient to melt and partially vaporize the film, and, consequently, the observed metal transfer is expected to occur. In fact the laser energies in these cases are usually considerably in excess of the threshold energy for melt through, and at these higher energies it appears that the deposits are considerably thicker at the edges of the deposited line than in its center. This may result from the deposited metal being very hot initially, and being heated even further by the laser beam after deposition, in which case it is reasonable to expect that the metal would tend to accumulate and solidify primarily at the edges of the deposition line.

Of particular note is the fact that for a 1.2-μm-thick film a laser pulse of 60-mJ energy yielded a deposit but a 30-mJ pulse did not. This result is qualitatively and even semiquantitatively consistent with the calculations which show that a 1.2-μm-thick film does not melt through at 12-mJ laser energy and just barely melts through at 18 mJ.

This experiment and the theoretical model suggest the following sequence of events for the LIFT process: (1) The laser pulse heats the front surface of the film until it melts; (2) the melt front propagates through the film until it reaches the back surface; (3) at this time or shortly before the melt through occurs, the front surface is superheated or close to the boiling point; and (4) at or close to melt through the metal vapor pressure at the back surface propels the molten liquid to the target substrate where it solidifies as a metal feature. The theoretical model also suggests that the LIFT process is often completed before the laser pulse attains its maximum intensity and generally establishes an approximate time scale for the process. This time could be checked experimentally by measuring the reflectance of the laser beam from the metal film, which should change markedly at melt through. Further work is continuing to investigate different metal films on other substrates and the effect of laser-pulse wavelength on the LIFT phenomenon.

[a] This work was supported by the Department of the Navy, Space and Naval Warfare Systems Command under Contract No. N00039-87-C-5301.

[1] J. Bohandy, B. F. Kim, and F. J. Adrian, J. Appl. Phys. **60**, 1538 (1986).
[2] T. F. Deutsch, D. J. Ehrlich, and R. M. Osgood, Jr., Appl. Phys. Lett. **35**, 175 (1979).
[3] D. J. Ehrlich, R. M. Osgood, Jr., and T. F. Deutsch, Appl. Phys. Lett. **38**, 946 (1981).
[4] D. J. Ehrlich, R. M. Osgood, Jr., and T. F. Deutsch, J. Vac. Sci. Technol. **21**, 23 (1982).
[5] R. F. Karlicek, V. M. Donnelly, and G. J. Collins, J. Appl. Phys. **53**, 1084 (1982).
[6] S. Tamir and J. Zahavi, J. Vac. Sci. Technol. A **3**, 2312 (1985).
[7] R. K. Montgomery and T. D. Mantei, Appl. Phys. Lett. **48**, 493 (1986).
[8] J. R. Cannon, *The One-Dimensional Heat Equation*, Vol. 23 in Encyclopedia of Mathematics and its Applications (Addison–Wesley, Menlo Park, CA, 1984).
[9] H. S. Carslaw and J. C. Jaeger, *Conduction of Heat in Solids*, 2nd ed. (Oxford, England, 1959).
[10] L. W. Ehrlich, J. Assoc. Comput. Mach. **5**, 161 (1958).
[11] J. Crank and P. Nicolson, Proc. Cambridge Philos. Soc. **45**, 50 (1947).
[12] R. F. Wood and G. E. Giles, Phys. Rev. B **23**, 2923 (1981).

Chemical processes involved in the etching of silicon by xenon difluoride

J. A. Dagata,[a] D. W. Squire,[a),b)] C. S. Dulcey,[b)] D. S. Y. Hsu, and M. C. Lin
Chemistry Division, Code 6105, Naval Research Laboratory, Washington, D. C., 20375-5000

(Received 6 February 1987; accepted 7 May 1987)

The spontaneous etching of silicon by xenon difluoride has been investigated under single collision conditions using multiphoton ionization mass spectrometry for the detection of radical products. SiF_2 is the only gas phase radical observed with an apparent activation energy of 6.7 ± 0.5 kcal/mol. Electron ionization techniques were used to determine an apparent activation energy for gas phase production of SiF_4 of 5.6 ± 0.8 kcal/mol. The identification of SiF_2 as the sole reactive desorbing species during the steady-state etching process is useful for understanding many aspects of primary surface processes and secondary gas phase reactions in etching.

I. INTRODUCTION

The spontaneous etching of silicon at room temperature by xenon difluoride (XeF_2) has been proposed as a model system for studying the silicon etching mechanism in fluorine-containing plasmas.[1-3] XeF_2 is used as a means of delivering fluorine atoms to a silicon surface at low ambient temperatures and pressures. This model system removes many of the difficulties associated with studying the etch process in a plasma environment.

The first step in the study of the reaction mechanism is the identification of the products which desorb from the surface during steady-state etching.[1-8] The product distribution reveals valuable information about physical and chemical processes occurring in the active etch zone on the surface. This information, combined with activation energies for the appearance of the various species may allow identification of the elementary steps controlling the etch process. A better understanding of the spontaneous etching mechanism of silicon is of obvious technological interest.

Previously, the principal method used to determine product distributions was electron ionization mass spectrometry (EI/MS).[1-3,7,8] However, electron impact ionization may cause fragmentation of the nascent product molecule and create difficulties in product identification, particularly when the fragments are possible reaction products. Therefore application of a species-selective detection technique is desirable.

Recently, we have employed multiphoton ionization mass spectrometry (MPI/MS) to investigate radical species desorbing from silicon single-crystal surfaces etched by F_2 and NF_3.[9,10] This technique allows selective ionization and sensitive detection of gas-phase radicals. In this paper, results for the thermal etching of silicon by XeF_2 are reported for surface temperatures in the range of 300–1200 K and for XeF_2 gas pressures between 1.0×10^{-6} and 2.0×10^{-4} Torr. SiF_2 is the only radical product that has been detected in the gas phase. MPI/MS results have been combined with EI/MS results for SiF_4 production obtained under identical conditions to determine apparent activation energies and estimate relative product distributions.

The present results conform to a model for the etching process under steady-state conditions in which the overall etch rate is determined by the rate at which fluorine atoms are formed on the surface and diffuse through the fluorosilyl etch layer[3,11,12] to the underlying silicon substrate. Temperature studies indicate that the fluorosilyl layer undergoes a disordering at about 800 K which alters the relative contribution of competing surface processes and the SiF_2/SiF_4 product distribution.

II. EXPERIMENT

The experimental apparatus has been described in detail elsewhere.[9,10] Briefly, it consists of a differentially pumped vacuum system in which a *p*-doped (110) silicon sample (20–30 Ω cm, Virginia Semiconductor) was mounted, an excimer-pumped dye laser (Lambda Physik) and a quadrupole mass spectrometer (Extrel) modified for both laser and electron ionization.

The silicon sample ($10\times10\times2.5$ mm) was resistively heated by tungsten filaments placed into 1×1 mm channels machined along the edges of the crystal. The sample temperature was measured by spot welding a thermocouple to a tantalum spring which was then inserted into a 1-mm-diam hole drilled into a third edge of the crystal. Temperatures up to 1200 K could be achieved with this arrangement. The sample face was mounted about 50 mm from the ion region of the mass spectrometer and normal to the quadrupole axis. A 4.0-mm-diam skimmer separated the source region from the mass spectrometer.

The XeF_2 reagent (SCM Specialty Chemicals) was stored in a stainless-steel bulb and purified by a freeze–thaw cycle. A continuous flow of gas was directed at the silicon surface through a 1.6-mm stainless-steel tube positioned about 15 mm from the sample. Pressure in the source region was monitored with a Bayard–Alpert ionization gauge and pressures in the range of 5.0×10^{-6} to 2.0×10^{-5} Torr were typically used. (Base pressures in the system were 3.0×10^{-7} Torr in the source region and 7.0×10^{-8} Torr in the mass spectrometer region.)

Detection of SiF_2 was carried out in the 320–322 nm region using Rhodamine 640 and doubling with a KDP crystal. Laser energy was typically about 600 μJ/pulse in a 10-ns pulse and was focused by a 25-cm lens into the mass spectrometer ionization region. A two-photon resonance

 0734-211X/87/051495-06$01.00 © 1987 American Vacuum Society

with the $\tilde{B}\ ^1B_2$ state of SiF_2 enhances the three-photon ionization process in this wavelength region.[9] The MPI spectroscopy of SiF has been previously characterized.[9,13] An unusually strong enhancement of the ion signal at 437.6 nm has been identified as being both one-photon resonant with the A $^2\Sigma^+$ state and two-photon resonant with the $v = 1$ level of the $C''\ ^2\Sigma^+$ state of this radical. The fundamental of Coumarin 440 (average energy of 1–2 mJ per pulse) was used in an attempt to detect this species.

Electron ionization with 70-eV electrons was performed to obtain cracking patterns and product distributions. A channeltron electron multiplier was used for ion detection. Signal measurement was handled somewhat differently for (pulsed) laser and (continuous) electron ionization. For the laser ionization experiments (repetition rate = 10 Hz, pulse width = 10 ns), the signal was amplified, sampled by boxcar integrator and computer averaged (typically 400 shots per measurement). For EI measurements, an ORTEC pulse counting system monitored the signal from the continuous electron impact current. The pulse counter output was sampled, digitized and computer averaged. Thus the EI measurements have a significant duty cycle advantage ($\sim 10^7$) over the pulsed laser measurements.

III. RESULTS

A. Laser ionization

SiF_2 was detected by MPI/MS as a significant volatile product of the etching of silicon (110) by XeF_2. Wavelength spectra from 320 to 322 nm at surface temperatures of 310 and 1000 K and with an ambient pressure of 7.0×10^{-6} Torr are presented in Fig. 1. As noted, the ionization enhancement in this spectral region arises from two-photon resonance with the $\tilde{B}\ ^1B_2$ state of the radical. The partially resolved features in the spectrum were previously assigned as sequence bands of the bending vibration.[9]

Mass spectra taken at the 320.9 nm SiF_2 resonance peak with an ambient pressure of 6.0×10^{-6} Torr at substrate temperatures of 320 and 1000 K are shown in Fig. 2. The figure demonstrates that SiF_2^+ ions (m/z 66) alone are produced by laser ionization at this wavelength and do not undergo further fragmentation. The SiF_2^+ ion signal displays a linear pressure dependence from 1.0×10^{-6} to 5.0×10^{-5} Torr. A typical plot of ion signal versus pressure is shown in Fig. 3. The linearity of the signal as a function of pressure indicates that secondary gas-phase reactions are negligible in this pressure regime.

The temperature dependence of the SiF_2^+ ion signal is shown in Fig. 4. An apparent activation energy for the gas phase production of SiF_2, $E_a(SiF_2) = 6.7 \pm 0.5$ kcal/mol, was determined by a least-squares fit to an Arrhenius form, $I = A\exp(-E_a/kT)$. Data from different experimental runs are indicated by distinct symbols in the figure. Individual data sets show a noticeable break in their temperature dependence curves between 700 and 900 K. Their effect on fitting the activation energy has been neglected. The physical significance of this break will be considered in the Discussion.

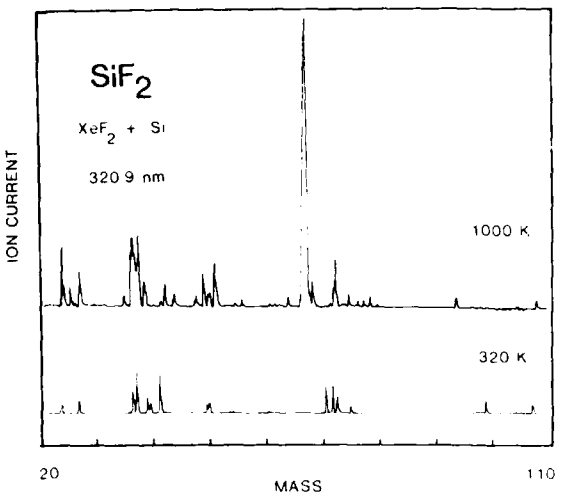

FIG. 2. Ion signal vs mass at a fixed laser wavelength of 320.9 nm for the reaction products of XeF_2 and p-doped silicon (110). The ambient pressure was 6.0×10^{-6} Torr XeF_2 and the surface temperature was 320 and 1000 K.

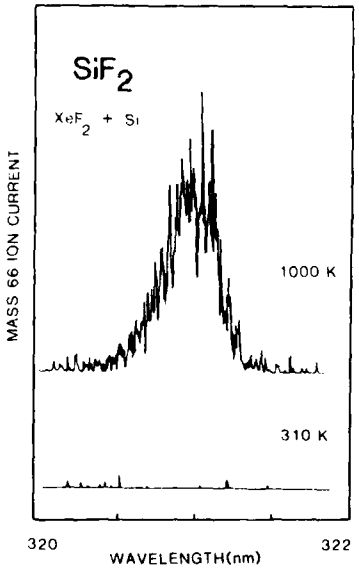

FIG. 1. Mass 66 ion signal vs wavelength for the reaction of XeF_2 and p-doped silicon (110) at 7.0×10^{-6} Torr XeF_2 and surface temperatures of 310 and 1000 K. Excitation is two-photon resonant through the $\tilde{B}\ ^1B_2$ state of SiF_2.

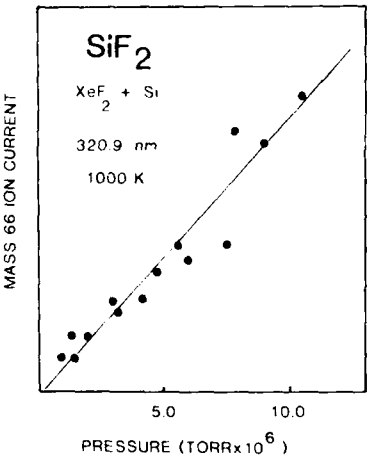

FIG. 3. Mass 66 ion signal vs XeF_2 pressure at a laser wavelength of 320.9 nm and surface temperature of 1000 K.

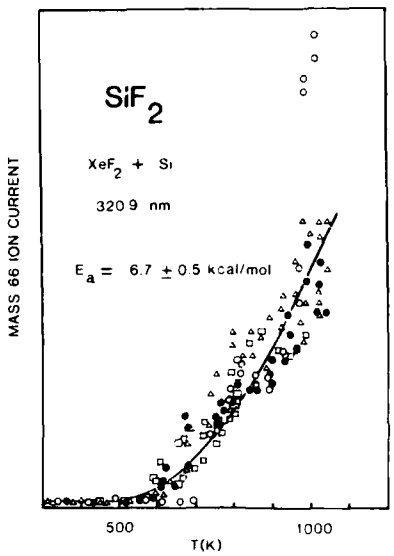

FIG. 4. Mass 66 ion signal vs temperature at a fixed laser wavelength of 320.9 nm over the range of 300–1200 K for the reaction of XeF_2 and *p*-doped silicon (110). Data points from four separate runs are distinguished by different symbols in the figure. The curve is a least-squares fit of the data to a simple Arrhenius form yielding $E_a(SiF_2) = 6.7 \pm 0.5$ kcal/mol.

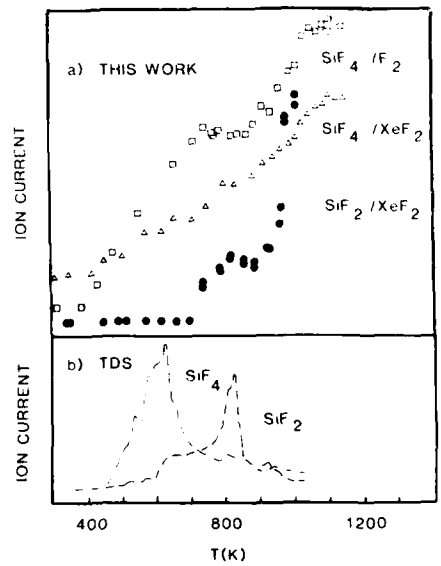

FIG. 5. (a) The temperature dependence of the SiF_4 and SiF_2 etch products from the etching of Si(110) by XeF_2 (ΔSiF_4, from m/z 85 electron ionization signal at 70 eV; and, ●, SiF_2, from laser ionization at 320.9 nm) and etching of Si(110) by F_2 (□, SiF_4, from m/z 85 electron ionization signal at 70 eV as reported in Ref. 10). The data points for the SiF_2 temperature dependence are replotted from Fig. 4 and represent a single scan. The signal intensities are not corrected for differences between the partial pressure of the etch gas used. (b) Thermal desorption spectra for SiF_2 (dashed curve) and SiF_4 (dot–dashed curve) from XeF_2 etching of Si(111). TDS results are redrawn from Fig. 1 of Ref. 11.

As alluded to earlier, the SiF radical has a strong MPI resonance at 437.6 nm. An extensive search for gas phase SiF at this wavelength failed to detect this species between 300 and 1200 K using various XeF_2 gas pressures from 5.0×10^{-6} to 2.0×10^{-4} Torr. In our preliminary work[9] on the MPI spectroscopy of SiF, this radical was generated in a flow reactor by passing F_2 and NF_3 over heated silicon chips. The extremely high temperature required to detect this radical suggested that it is the product of a reaction of gas-phase silicon atoms with the fluorinating agent. This technique was found to be a highly inefficient method of producing gas phase SiF (the major product is always SiF_2). Studies of single crystal silicon etching by F_2 and NF_3[10] also show that the SiF/SiF_2 product ratio is essentially zero.

No MPI or LIF spectrum of SiF_3 has been observed to date. In the absence of any further spectroscopic diagnostic, it was assumed that an MPI spectrum of SiF_3 might resemble the known MPI spectrum of the carbon analog CF_3.[14] An extensive search for this radical using F_2 as an etchant and scanning over the wavelength region from 416 to 510 nm failed to detect SiF_3 desorbing from the surface.[10] Further work to establish an MPI diagnostic for SiF_3 is planned.

B. Electron ionization

EI techniques were employed to determine the temperature dependence of the stable product SiF_4. The apparent activation energy for the gas phase production of SiF_4, from the SiF_3^+ ion signal, is 5.6 ± 0.8 kcal/mol. The present investigation failed to detect any silicon-containing species above mass 104, specifically Si_2F_6, which has been suggested as a possible volatile etch product.[12,15] The ion signal from SiF_3^+, the major daughter ion of SiF_4 ionization, is plotted as a function of temperature in Fig. 5(a). Substantial etching at room temperature is evident. There is also a slight apparent discontinuity in rate of increase near 800–900 K.

Our EI measurements of the ion signal of SiF^+, the major daughter ion of SiF_2 ionization, showed the presence of room temperature SiF_2 above the signal contributed from ionization of higher mass species. SiF_2 was not detected by laser ionization at low temperatures (see Figs. 1 and 4). This discrepancy is probably due to the limits of our detection efficiency at the low XeF_2 pressures used in the present experiment ($< 10^{-5}$ Torr) and by the duty cycle mentioned earlier (also see below).

The mass spectrometer used in the present experiments has an ion transmission tuned for maximum efficiency around the SiF_2 mass, with decreasing detection efficiency toward higher masses. The SiF_4 fragmentation pattern at 70 eV obtained with the present spectrometer is compared to published values in Table I. To establish that the transmission efficiency of our instrument did not cause distortions in the EI data, our results are compared to the results of Winters and Houle for the room temperature etching of silicon by XeF_2.[8] Their results were obtained by EI/MS with an electron energy of 30 eV, and must be adjusted to reflect differences in ionization efficiency and fragmentation pattern. A crude estimate of the SiF_2 contribution to the m/z 47 ion signal at room temperature may be obtained by including in the 30 eV data (column D) a contribution from SiF_4 fragmentation and by correcting for the transmission bias differences between columns A and B of Table I. The result (column E), is in reasonable agreement with the present data obtained at 70 eV (column F). This result demonstrates that the EI mass sensitivity of our instrument does not lead to unreasonable values for the mass distributions.

TABLE I. Mass fragmentation patterns observed from electron ionization of SiF_4 and $XeF_2(g) + Si(s)$.

	SiF_4		
	A	B	C
	This work	Ref. 8	Ref. 16
m/z	Electron energy = 70 eV		
104	2.46	0.7	1.76
85	100.0	100.0	100.0
66	2.9	2.0	0.68
47	26.9	7.0	3.8
	$XeF_2(g) + Si(s)$ at 300 K		
	D	E	F
	Ref. 8		This work
	Electron energy		
m/z	30 eV	(70 eV calc)	70 eV
85	100	100	100
66	12	20	...
47	20	104	89

IV. DISCUSSION

The most significant result of the present study is the direct observation by MPI/MS of the gaseous SiF_2 radical and the direct elimination of SiF as a gas-phase product in the thermal etching of silicon by XeF_2. The apparent Arrhenius activation energy for gas-phase production of SiF_2, $E_a(SiF_2) = 6.7 \pm 0.5$ kcal/mol, is in reasonable agreement with the apparent activation energy for SiF_4 production determined by EI/MS, $E_a(SiF_4) = 5.6 \pm 0.8$ kcal/mol. The latter value is in close agreement with the activation energy for the overall etch rate reported by Ibbotson *et al.*,[6] $E_a(\text{E.R.}) = 5.7$ kcal/mol for $T > 460$ K. Although SiF_3 cannot be fully eliminated as a gas-phase product at present, indirect evidence[7,8,10] indicates that it is at best a very minor product.

The temperature dependence of the SiF_4 signal from XeF_2 and F_2 etch gases and the SiF_2 MPI signal from XeF_2 for a single data set are plotted in Fig. 5(a). These data are independently scaled to illustrate the temperature behavior of each system. The product ion signals in both the XeF_2 and F_2 systems exhibit discontinuities in the monotonic rise of the signal with increasing temperature in the range of 700–900 K. The apparent breaks in the SiF_2 and SiF_4 temperature profiles (which were neglected in the evaluation of activation energies) suggest that the relative rates of two or more elementary surface processes are changing within this relatively narrow temperature range.

The fact that more than one thermochemical mechanism can be observed under steady-state etching conditions is significant. This information will be used below with data from other studies to help distinguish between alternative models proposed for the surface fluorosilyl layer. This layer is responsible for the efficient propagation of the etch boundary through the silicon substrate.

It is difficult to characterize the fluorosilyl layer during active etching but is is known from quartz microbalance measurements that 2–6 equivalent monolayers are sorbed prior to the onset of etching.[2] Recent analysis of postetched silicon samples by XPS indicates that SiF_3 moieties predominate with few SiF_2 present in the surface layer.[12] The average saturation of the SiF_n (a) groups varied between $n = 2.6$ and 3.3 in that study. The authors of the latter work concluded that the fluorosilyl layer "exhibits poor connectivity" and consists of "small fluorosilane molecules or of molecular radical species mixed together in a disordered homogeneous environment." Earlier models adopted a more ordered structure for the fluorosilyl layer which was believed to be composed of a large fraction of SiF_2 units, $-(SiF_2)_n-$.[5,17]

The notions of an ordered or disordered homogeneous fluorosilyl layer imply certain limits on the number of Si–Si linkages in the fluorosilyl layer, the strength of these bonds and whether or not the topmost layer is fluorinated preferentially to the underlying layer. The sorption of a substantial amount of fluorine prior to the onset of etching suggests that fluorination of SiF_3 is a bottleneck in the etching reaction,[12] or that the underlying substrate must be at least partially fluorinated before saturation of SiF_3 occurs. In the context of steady-state etching, however, the former possibility may be ruled out. The similar values of the activation energies obtained for SiF_2, SiF_4, and the overall etch rate using F atom,[4,5] F_2,[5,10] NF_3,[10] and XeF_2 indicate that SiF_2 and SiF_4 production proceed from a common rate-limiting step along the reaction pathway. If SiF_3 is a "bottleneck" then there would be different activation energies for these products. The breaks in the SiF_2 and SiF_4 product signals at about 700–900 K distinguish low- and high-temperature processes. This point will be discussed later.

These findings for silicon etching by XeF_2 can be rationalized according to the general reaction scheme[1–3]:

(i) initial fluorosilyl layer formation, overlayer formation and dissociative chemisorption,

$$XeF_2(g) + Si(s) \rightarrow XeF_2(a), \quad (1)$$

$$XeF_2(a) \rightarrow 2F(a) + Xe(g); \quad (2)$$

(ii) propagation of the fluorosilyl layer and product formation,

$$nF(a) + Si(s) \rightarrow SiF_n(a), \quad n = 1\text{–}3, \quad (3)$$

$$F(a) + SiF_3(a) \rightarrow SiF_4(a); \quad (4)$$

(iii) product desorption,

$$SiF_2(a) \rightarrow SiF_2(g), \quad (5)$$

$$SiF_4(a) \rightarrow SiF_4(g), \quad (6)$$

where a = adsorbed, s = solid, and g = gas phase.

The temperature dependence of these elementary reaction steps is expected to follow a simple exponential form for steps (1), (2), (5), and (6). Steps (3) and (4), on the other hand, may have a complex temperature dependence because multiple thermal processes occurring in the fluorosilyl layer may cause displacement of fluorosilyl moieties and Si–Si bond weakening. The effects of thermal displacements are (i) an increased fluorine uptake deep within the fluorosilyl layer and substrate, and (ii) eventual rupture of Si–Si bonds between partially fluorinated SiF_n species.

Desorption profiles from TDS studies[11] for SiF_4 and SiF_2 products, shown in Fig. 5(b), support this view. The SiF_4 signal exhibits a broad peak at about 600 K. The broadness of this peak, coupled with the fact that the signal could not be saturated even at high XeF_2 dosing levels, indicates that thermal activation of the fluorosilyl layer can lead to saturation of SiF_3 species, i.e., step (4). This reaction was shown to dominate the TDS spectrum until about 800 K at which point the source of surface-bound fluorine responsible for SiF_3 saturation was consumed. SiF_2 species were seen to desorb strongly above this temperature. Whether SiF_2 units exist on the surface and desorb directly into the gas phase or are formed by a reaction of SiF_3 groups, for example, is not known.

The breaks in the SiF_2 and SiF_4 signals under steady-state etching conditions, as shown in Fig. 5(a), do occur in roughly the same temperature region where SiF_2 desorption is observed in the TDS experiment. This correlation between reactions leading to SiF_2 desorption [Fig. 5(b)], the sudden falloff in the product signals and the subsequent rapid increase in the SiF_2/SiF_4 product ratio [Fig. 5(a)] suggest that a significant change in the nature of the fluorosilyl layer occurs between 700 and 900 K. Within the generalized context of the fluorosilyl layer presented above, this change can be plausibly related to thermal activation of SiF_n groups and the breakup of Si–Si bonds in the etch layer. The consequences of "disordering" are that (i) at higher temperatures, more active sites are exposed, which enhances the fluorination of subsurface silicon, and (ii) the amount of fluorine relative to silicon bonds available for SiF_2 and SiF_4 product formation decreases.

To summarize, two processes have been identified in the present work which depend critically on the substrate temperature. Previous studies of silicon etching reactions were restricted to temperatures below 600 K and therefore only probed the low temperature regime. The low-temperature process is dominated by chemical attack by F(a), i.e.,

$$F(a) + -(SiF_2)_n- \rightarrow SiF_3(a) + SiF_2(a) + -(SiF_2)_{n-2}-, \quad (7)$$

with subsequent product formation, i.e.,

$$F(a) + SiF_3(a) \rightarrow SiF_4(a), \quad (4)$$

$$SiF_2(a) \rightarrow SiF_2(g), \quad (5)$$

$$SiF_4(a) \rightarrow SiF_4(g). \quad (6)$$

This behavior is very different from the high temperature process, dominated by thermal cleavage of Si–Si bonds via decomposition reactions such as,

$$-(SiF_2)_n- \rightarrow mSiF_2(g) + -(SiF_2)_{n-m}-, \quad (8)$$

which requires substantial thermal activation. This process produces more active sites which further enhance the chemical attack of the substrate by fluorinating agents. It should be noted that the reaction step given in step (7), the reaction of fluorine with surface and/or subsurface fluorosilyl groups, is not specific to $-(SiF_2)_n-$ units but can occur just as well with a more general structure with mixed SiF_n species, such as $-SiF-(SiF_2)_n-SiF_3$.

The observation of SiF_2 and SiF_4 as the only gas phase products of etching reaction is not inconsistent with the detection of large amounts of SiF_3 on postetched surfaces by XPS.[12] At high temperature, the $SiF_3(a)$ surface species may undergo a thermal decomposition reaction analogous to that of gas phase Si_2F_6 which decomposes by disproportionation to SiF_2 and SiF_4 rather than into SiF_3 radicals.[18] On the surface, this step can be described as

$$\equiv Si - SiF_3(a) \rightarrow \equiv SiF(a) + SiF_2(g), \quad (9)$$

or

$$- SiF_2 - SiF_3(a) \rightarrow - SiF_3(a) + SiF_2(g), \quad (10)$$

depending on desorption site.

Conclusions about the surface obtained from experiments which analyze the surface after etching has ceased may nevertheless underestimate the importance of SiF_2 and SiF_4 surface species. A simple calculation of the maximum residence time for these products, using $\tau = k^{-1} = A^{-1}\exp(E_a/RT)$, with a typical unimolecular desorption value of $A \sim 10^{13}\ s^{-1}$ and the activation energies given above, shows that τ is < 1 ns at room temperature and thus these species, if present on the surface, would not be detected by a postetch analysis.

Ibbotson *et al.*[6] have interpreted the difference between chemiluminescence and etch-rate data for the XeF_2 and F atom etching systems as indicating that the XeF_2 surface etching mechanism may be different from the F atom mechanism. Their experiments were performed at relatively higher pressures ($2–10^{-2}$ Torr) where a substantial XeF_2 overlayer is formed. The present results for silicon etching by XeF_2 were obtained at much lower pressures ($< 10^{-6}$ Torr) which minimizes the formation of a significant physisorbed XeF_2 overlayer.[6] The negative activation energy for low temperature etching, which was attributed by Ibbotson *et al.* to overlayer formation below 460 K, is not evident in our data. Evidently at low pressures the etch process is not strongly influenced by the formation of XeF_2 multilayers.

V. CONCLUSION

SiF_2 is the dominant reactive species which desorbs during steady-state etching of silicon by XeF_2. The primary surface reactions lead almost exclusively to SiF_2 and SiF_4 gas phase products. Apparent Arrhenius activation energies of $E_a(SiF_2) = 6.7 \pm 0.5$ kcal/mol and $E_a(SiF_4) = 5.6 \pm 0.8$ kcal/mol have been determined. The SiF_2/SiF_4 product distribution and activation energies for the XeF_2–Si system are in reasonable agreement with results in the literature.

The present results support a model of the etch process under steady-state conditions in which the fluorosilyl layer has some "ordered" character, as suggested previously.[1–6,10] No evidence was obtained which would support an alternative picture of the layer as a disordered homogeneous mixture at low temperatures. In the proposed model, production of F atoms represents an upper limit to the reaction rate at low temperatures. At these temperatures the flux of F atoms and the competition between chemisorption and saturation to SiF_4 determine the actual etch rate. At high temperatures the etch rate is governed by the breakup of the fluorosilyl layer.

ACKNOWLEDGMENTS

The authors would like to thank Professor L. C. Lee (San Diego State University) for providing an initial supply of XeF_2 for these experiments and the results of his UV - visible chemiluminescence studies prior to publication. This research was supported in part by the Office of Naval Research. JAD and DWS would like to thank the National Research Council for Cooperative Research Associateships.

[a] NRC/NRL Cooperative Research Associate.
[b] Geo-Centers, Inc., 4710 Auth Place, Suitland, Md 20746.

[1]H. F. Winters and J. W. Coburn, Appl. Phys. Lett. **34**, 70 (1979).
[2]H. F. Winters, J. W. Coburn, and T. J. Chuang, J. Vac. Sci. Technol. B **1**, 469 (1983).
[3]H. F. Winters and J. W. Coburn, J. Vac. Sci. Technol. B **3**, 1376 (1985).
[4]V. M. Donnelly and D. L. Flamm, J. Appl. Phys. **51**, 5273 (1980).
[5]D. L. Flamm, V. M. Donnelly, and J. A. Mucha, J. Appl. Phys. **52**, 3633 (1981).
[6]D. E. Ibbotson, D. L. Flamm, J. A. Mucha, and V. M. Donnelly, Appl. Phys. Lett. **44**, 1129 (1984).
[7]M. J. Vasile and F. A. Stevie, J. Appl. Phys. **53**, 3799 (1982).
[8]H. F. Winters and F. A Houle, J. Appl. Phys. **54**, 1218 (1983).
[9]J. A. Dagata, D. W. Squire, C. S. Dulcey, D. S. Y. Hsu, and M. C. Lin, Chem. Phys. Lett. **134**, 151 (1987).
[10]D. W. Squire, J. A. Dagata, D. S. Y. Hsu, C. S. Dulcey, and M. C. Lin, J. Phys. Chem. (submitted).
[11]B. Roop, S. Joyce, G. Schultz, N. D. Shinn, and J. I. Steinfeld, Appl. Phys. Lett. **46**, 1187 (1985).
[12]F. R. McFeely, J. F. Morar, and F. J. Himpsel, Surf. Sci. **165**, 277 (1986).
[13]C. S. Dulcey and J. W. Hudgens, Chem. Phys. Lett. **118**, 444 (1985).
[14]M. T. Duignan, J. W. Hudgens, and J. R. Wyatt, J. Phys. Chem. **86**, 4156 (1982).
[15]F. A. Houle, J. Appl. Phys. **60**, 3018 (1986); J. Chem. Phys. **80**, 4851 (1984).
[16]V. H. Dibeler and F. L. Mohler, J. Res. Natl. Bur. Stand. **10**, 25 (1948).
[17]T. J. Chuang, J. Appl. Phys. **51**, 2614 (1980).
[18]S. K. Bains, P. N. Noble, and R. Walsh, J. Chem. Soc. Faraday Trans. 2 **82**, 837 (1986).

Summary Abstract: Adsorbate interactions and poisoning on Cr(110)

Neal D. Shinn
Sandia National Laboratories, Division 1134, Albuquerque, New Mexico 87185

(Received 12 March 1987; accepted 7 May 1987)

Understanding the energetics of adsorbate interactions at surfaces is a necessary prerequisite to the elucidation of the mechanisms of chemical processes occurring at surfaces. Although adsorbate:adsorbate interactions are frequently manifested in the kinetics of surface reactions (e.g., via the promotion or poisoning of a specific reaction step by a coadsorbate[1]), it is less common to observe spectroscopic changes in the adsorbate:surface bonding that can be correlated to the measured kinetic changes.[2,3] This paper summarizes earlier vibrational[4,5] and more recent photoemission data[6] for the CO and oxygen chemisorption systems on the close-packed Cr(110) surface. High-resolution electron-energy loss spectroscopic (EELS) and ultraviolet photoemission data for the mixed CO/O overlayer provide unambiguous evidence for coadsorbate interactions that block the formation of a stable CO dissociation intermediate and, consequently, inhibit the dissociation of carbon monoxide.[7,8] Although steric effects and direct competition for surface adsorption sites can account for reduced sticking probabilities and subsequent variations in reaction kinetics, the stoichiometry of the CO/O interaction on Cr(110) and the low-oxygen coverages involved suggest that electronic interactions are responsible, at least in part, for these observations.

Figure 1 shows representative vibrational (EELS) spectra of the two molecular CO binding states that are sequentially populated below ~150 K. The α_1 CO molecular binding state (lower curve) is a surface-stabilized CO dissociation intermediate, which is the only molecular-binding state for coverages up to 0.25 monolayer (ML). [One monolayer is defined as the surface atomic density of the ideal Cr(110) plane, 1.705×10^{15} cm^{-2}.] The arrow identifies the Cr–O stretch, at 600 cm^{-1}, due to the residual 2%–3% of a monolayer of surface oxygen.[5] Carbon monoxide stretching frequencies are found in the range 1150–1330 cm^{-1}, indicative of (1) substantial C–O bond weakening and (2) Cr–CO bonding inconsistent with the conventional Blyholder description[9] involving CO 5σ electron donation to the metal and synergistic electron backdonation from the metal *d* states to the antibonding CO $2\pi^*$ orbitals, analogous to the bonding in transition metal carbonyl complexes.[10] Further insights into the details of the CO–metal bonding are provided by recent theoretical[11-13] and experimental[14] work, but these studies all involve cases where the CO valence orbitals are much less perturbed—and the C–O stretching frequency is nearer to the gas phase value of 2143 cm^{-1}—than in the case of α_1 CO on Cr(110). At 0.25 ML coverage, a $c(4\times2)$ α_1 CO ordered overlayer is observed by low-energy electron diffraction (LEED), at which point the α_1 CO binding state is saturated. Subsequent addition of carbon monoxide results in the disordering of the overlayer and the onset of three new vibrational features in the EELS data (Fig. 1, upper curve): two C–O stretching frequencies at 1865 and 1975 cm^{-1} and a Cr–CO stretching mode at 495 cm^{-1}. These vibrational modes are indicative of terminally bonded CO molecules on Cr(110), analogous to CO chemisorption states on all other transition and noble metals studied to date.[15] Annealing studies have shown that molecules in the α_1 CO state dissociate at a lower surface temperature than those in the terminally bonded α_2 CO state, further supporting the designation of the α_1 CO state as a surface-stabilized dissociation intermediate.

Oxygen dissociatively adsorbs at temperatures above 120 K until diffusion of the atomic oxygen into the lattice becomes rate limiting and surface oxygen blocks adsorption sites. Only one vibrational feature, at 605 cm^{-1}, is found for dissociative adsorption, corresponding to the Cr–O stretching mode, and an ordered overlayer is formed at a coverage of ~1/8 ML. At surface temperatures below 150 K, a minority molecular O_2(ads) state is seen in the EELS data (ν_{O_2} = 1020 cm^{-1}) as well as by electron stimulated desorption[5].

Because the α_1 CO state is a stable dissociation intermediate, it is an excellent candidate for detecting surface electronic changes by electronegative adatoms which inhibit dissociation or "poison" the surface.[1] A series of vibrational spectra were recorded with increasing CO exposures for various precoverages of atomic oxygen. Figure 2 illustrates one such series where the initially clean surface has been predosed with oxygen at 300 K to slightly poison the surface [Fig. 2(a)]. Note that even after very low-CO doses, the

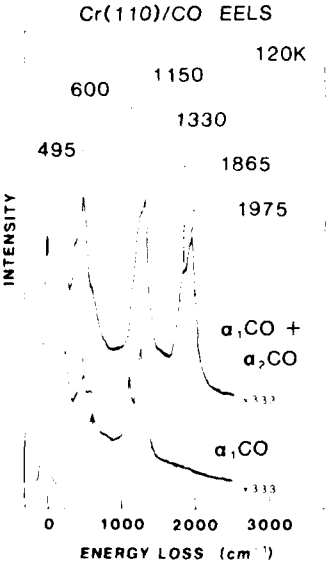

FIG. 1. High-resolution electron-energy loss spectra of molecular CO adsorbed on Cr(110) at low coverage ($\theta_{CO}<0.25$) and at high coverage ($\theta_{CO}>0.25$).

 0734-211X/87/051501-03$01.00 © 1987 American Vacuum Society

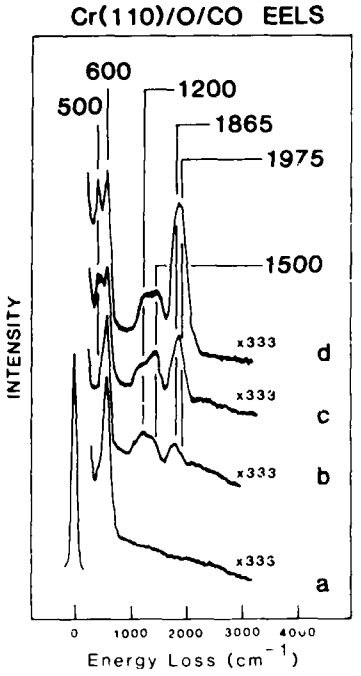

FIG. 2. Vibrational spectra illustrating the blocking of α_1CO by the preadsorption of atomic oxygen. Gas exposures are: (a) 0.3 L of oxygen at 300 K, followed by CO exposures at 120 K of (b) 0.15 L; (c) 0.30 L, and (d) 0.45 L.

terminally bonded α_2CO state (ν_{CO} = 1865 and 1975 cm^{-1}, ν_{Cr-CO} = 500 cm^{-1}) appears along with the expected α_1CO state (ν_{CO} = 1200 cm^{-1}) [Figs. 2(b)–2(d)]. (The 1500 cm^{-1} peak has been attributed to the presence of a surface carbonate due to the reaction of adsorbed CO and oxygen.[4]) This result could be due to the preadsorbed oxygen simply blocking the adsorption sites (e.g., surface hollow sites) or a more subtle electronic interaction. Evidence for the latter is seen in Fig. 3 where the α_1CO intermediate state is adsorbed *first* [Fig. 3(b)] and then subsequently converted to the terminally bonded α_2CO state by the subsequent addition of atomic oxygen [Figs. 3(c) and 3(e)]. This experiment, which assumes that the vibrational cross section for the α_1CO molecules is independent of the nature of the mixed surface adlayer, suggests that each oxygen atom strongly perturbs two nearby CO molecules; this stoichiometry is inconsistent with a site-blocking explanation alone.

The dependence upon vibrational cross sections for quantitative interaction measurements is avoided by using photoemission spectroscopy to demonstrate the oxygen-induced α_1CO→α_2CO binding state conversion at low temperatures. The same experiment, repeated at 90 K using angle-integrated ultraviolet photoemission with synchrotron radiation,[8] is shown in Fig. 4. The most notable spectroscopic change is in the CO 4σ peak region. The α_1CO 4σ peak is weak and centered at 11.6 eV binding energy, whereas the α_2CO 4σ peak is intense and at a lower binding energy of 10.8 eV.[6] Starting with the ~0.25 ML of α_1CO [Fig. 4(a)], the addition of oxygen [Figs. 4(b) and 4(f)] results in the changes described above as well as the obvious addition of the oxygen 2*p* photoemission peak at 6 eV. Subsequent addition of more carbon monoxide for comparison [Fig. 4(g)] confirms that the CO 4σ peak changes are due to the binding state conversion, as expected. Just as was seen in the EELS experiments of Figs. 2 and 3, the ultraviolet photoemission spectroscopy (UPS) data of Fig. 4 clearly show that (1) the preadsorbed oxygen blocks only the α_1CO dissociation intermediate and not the conventional terminally bonded α_2CO state, and (2) the subsequent addition of oxygen to an α_1CO overlayer causes the α_1CO→α_2CO binding state conversion.

These experimental results illustrate that in the case of CO dissociation on Cr(110), the presence of the electronegative adatom, i.e., oxygen, not only sterically inhibits but also electronically alters the Cr(110) surface as to prevent the stabili-

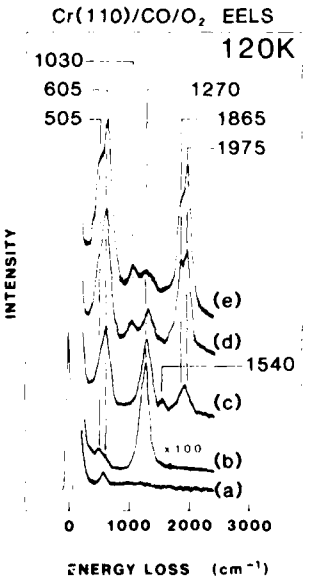

FIG. 3. Vibrational data highlighting the conversion of α_1CO to α_2CO by the addition of oxygen at 120 K: (a) 0.6 L CO, plus subsequent oxygen exposures of (b) 0.2 L; (c) 0.4 L, and (d) 0.5 L.

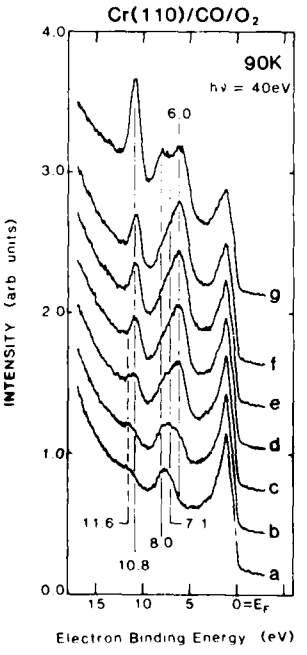

FIG. 4. Angle-integrated UPS data for the oxygen-induced CO binding state conversion at 90 K. Exposures for the spectra shown are: (a) 0.7 L CO followed by oxygen exposures of (b) 0.1 L; (c) 0.2 L; (d) 0.3 L; (e) 0.4 L, and (f) 0.5 L. Finally, (g) 3.0 L of CO is added to the mixed CO/O overlayer to saturate the surface with α_2CO after the oxygen exposures.

zation of the dissociation intermediate, α_1CO. On other metals where such an intermediate may be a short-lived transition state, these spectroscopic observations would be considerably more difficult. Finally, although the presence of oxygen on Cr(110) does block the stabilization of the intermediate, CO still dissociates, but at a higher temperature. On other metals where the dissociation is not self-poisoning (via stable oxide formation), the manifestation of the CO/O results seen here would be an increase in the activation energy barrier for the $CO \rightarrow C(ads) + O(ads)$ reaction. Thus this work may serve as a model for the processes underlying surface "poisoning" on transition metals of greater catalytic interest.

ACKNOWLEDGMENTS

The portion of this work performed while a Visiting Scientist at the National Bureau of Standards (1985) was supported by the Department of Energy, Office of Basic Energy Sciences, Division of Material Science under Contract No. DE-ACO4-76DP00789 with Sandia National Laboratories. Partial support was received by NBS from the Department of Energy, Office of Chemical Sciences and from the Office of Naval Research. The author also acknowledges the support of an NBS-NRC Postdoctoral Research Associateship in 1984–85.

[1]D. W. Goodman, in *Chemistry and Physics of Solid Surfaces*, edited by R. Vanselow and R. Howe (Springer, Heidelberg, New York, 1986).
[2]J. L. Gland, R. J. Madix, R. W. McCabe, and C. DeMaggio, Surf. Sci. **143**, 46 (1984).
[3]M. Trenary, K. J. Uram, and J. T. Yates, Jr., Surf. Sci. **157**, 512 (1985).
[4]N. D. Shinn and T. E. Madey, Phys. Rev. Lett. **53**, 2481 (1984); J. Chem. Phys. **83**, 5928 (1985).
[5]N. D. Shinn and T. E. Madey, Surf. Sci. **173**, 379 (1986); **176**, 635 (1986).
[6]N. D. Shinn and T. E. Madey, Phys. Rev. B **33**, 1464 (1986); N. D. Shinn, *ibid.* (submitted).
[7]N. D. Shinn and T. E. Madey, J. Vac. Sci. Technol. A **3**, 1673 (1985).
[8]N. D. Shinn, Langmuir (submitted).
[9]G. Blyholder, J. Phys. Chem. **68**, 2772 (1964).
[10]S.-S. Sung and R. Hoffmann, J. Am. Chem. Soc. **107**, 578 (1985).
[11]P. S. Bagus, C. J. Nelin, and C. W. Bauschlicher, Jr., Phys. Rev. B **28**, 5423 (1983).
[12]R. P. Messmer, Surf. Sci. **158**, 40 (1985).
[13]C. M. Kao and R. P. Messmer, Phys. Rev. B **31**, 4835 (1985).
[14]J. E. Houston, C. H. F. Peden, P. J. Feibelman, and D. R. Hamann, Surf. Sci. (submitted).
[15]J. T. Yates, Jr., T. E. Madey, and J. C. Campuzano, in *The Chemical Physics of Solid Surfaces and Heterogeneous Catalysis*, edited by D. A. King and D. P. Woodruff (Elsevier, Amsterdam, 1986).

Formation of TiN on Si and SiO_2 by rapid processing using a large area electron beam

Die-chi Sun, Zeng-qi Yu, and Fu-ming Li
Department of Physics, Fudan University, Shanghai, China

Yuan-cheng Du, Hai Wang, and Guo-bao Jiang
Department of Electrical Engineering, Fudan University, Shanghai, China

(Received 6 February 1987; accepted 7 May 1987)

Rapid nitridation of Ti film evaporated on a Si and SiO_2/Si wafer using a large area electron beam has been described. A predominant enhanced processing of an e-beam should be considered. The film structure of the sample processed by an e-beam has been characterized by Rutherford backscattering (RBS) and secondary ion mass spectrometry (SIMS) analysis. after rapid processing. Identification of the chemical composition of the film was performed with x-ray diffraction. The minimum sheet resistance of TiN was about 0.6 and 14.2 Ω/□ for Si and SiO_2/Si substrate, respectively. A ratio of 0.96% ± 5% (N/Ti), the stoichiometric composition of the sample characterized by RBS, has been obtained.

I. INTRODUCTION

The increasing challenge is reducing the vertical dimensions in modern very large scale integrated (VLSI) fabrications. A multilayer metallization system has been used conventionally. It comprises three parts: (1) aluminum used as a last layer to offer electrical interconnects; (2) the metalloid silicide chosen as an Ohmic contact to the Si, and (3) an intermediate layer inserted between them as a diffusion barrier. The nitride of transition metal may be suggested as a suitable diffusion barrier.[1-4] A TiN film is preferred because of its chemical stability, and thermodynamic and electrical properties. Moreover, it has been used as a gate electrode in the metal–oxide–semiconductor (MOS) transistors and as a low-barrier Schottky diode potential. In the last several years, the formation of TiN and its properties have been investigated. Different methods of preparing TiN film, such as by reactive sputtering or evaporation,[1] nitrogen ion-implanted into evaporated Ti film and formed during nitrogen annealing of magnetron-sputtered Ti film,[2,3] or N_2 ion-implanted annealed TiN film by thermal treating or an electron-beam, have been reported.[4] However, for a suitable TiN diffusion barrier layer, as most previous papers have reported, either a relatively high annealing temperature or a long enough treating time was required.

We present here a method of TiN formation by rapid nitridation processing of evaporated Ti film on the Si and SiO_2/Si substrate using a large area electron beam. It is found to be quite effective in forming homogeneous TiN on both Si and SiO_2/Si substrates in 5–60 s. In this paper the properties of TiN film and the characteristics of the film have been evaluated after rapid nitridation processing by sheet resistivity measurement, Rutherford backscattering spectrometry (RBS) and secondary ion spectrometry (SIMS) analysis (ISM-3F, made in France). The formation of the silicide $TiSi_2$ obtained simultaneously using an e-beam on Si has been discussed. The x-ray diffraction (XRD) analysis was performed with a XD-3A x-ray diffractometer (manufactured by Shimadzu, Japan).

II. EXPERIMENT

A. The preparation of specimens

The substrate of the specimen was (111)-oriented *p*-type 10 Ω cm polished Si wafer. The SiO_2 film on the Si wafer was formed in a furnace oxidation system, the thickness of the SiO_2 film was about 1000 Å. Before Ti-film deposition, the Si substrates were subjected to a dip in BHF for 5–15 s owing to residual native oxide, Ti film over the Si and SiO_2/Si wafer was deposited in a standard vacuum system (the pressure of the vacuum system was typically down to 1×10^{-6} Torr) with the conventional evaporation technique from a filament. After as-evaporated Ti film, the thickness of Ti film checked by a Tencor-200 α-step profiler was about 600–1000 Å.

B. The rapid nitridation processing

The rapid nitridation processing was performed by a large area electron beam,[5,6] the apparatus used in our experiments is shown in Fig. 1. The e-beam was created from the cold

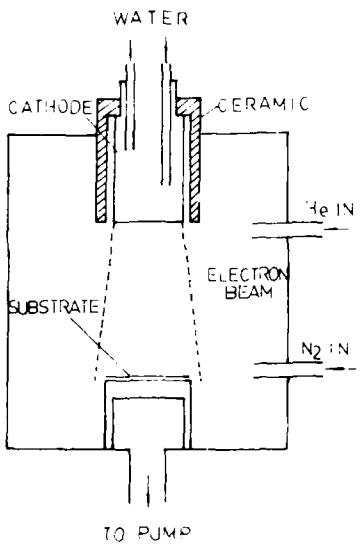

FIG. 1. Schematic diagram of an e-beam rapid nitridation processing system.

 0734-211X/87/051504-04$01.00 © 1987 American Vacuum Society

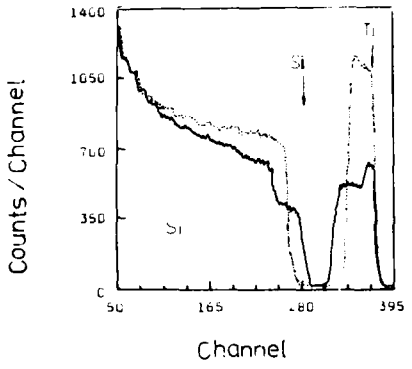

FIG. 2. Backscatter spectra of 2 MeV $^4He^+$ from a specimen processed with a 3:1 ratio of N_2/He and an e-beam power density of 30 W/cm^2 for a processing time of 20 s (solid line) and from an as-evaporated Ti film an Si (dotted line).

cathode glow-discharge electron gun, aluminum was used as the cathode material covered by a thin oxide laver. It is based on the secondary electron emission and a beam can be generated efficiently in helium discharge. The cross section of the e-beam was 50 mm in diameter and the uniformity over the cross section was better than 4%. The e-beam cross section was able to increase to more than 100 cm^2. In the nitridation processing the e-beam was operated in both helium and nitrogen gas surroundings, the ratio of N_2 and He in the mixture, the pressure and the flow rate of the gas were varied with the operation conditions. The power density of the e-beam was controlled by both voltage (1.8–2.2 kV) and current (200–400 mA). After 5–60 s of nitridation processing, TiN was formed; the surface of the thin film turned a gold-like color.

III. RESULTS AND DISCUSSION

A. Ti on single crystal Si

The stoichiometric composition of the sample processed by the e-beam and the as-deposited Ti film were characterized by RBS. The analysis was performed by scattering 2 MeV $^4He^+$, the result is shown in Fig. 2. The results of the XRD analysis of the processed samples (including TiN/SiO_2/Si sample) were shown in Fig. 3. Three diffraction lines of TiN (111), (200), and (220) were observed after rapid processing with the e-beam, for the Ti on single crystal Si sample in Fig. 3(a). The diffraction pattern of $TiSi_2$ was also observed along with the pattern of TiN. These patterns are similar to results reported by Ting.[7] It proved that there is evidence of TiN composition in the specimen after 20 s of rapid e-beam processing with a power density of the e-beam kept at 30 W/cm^2, under a ratio of 3:1 (N_2/He) and a mixture flow rate of 30 cm^3/min. Figure 2 shows both spectra for as-deposited Ti on the Si wafer and the processed specimen from variations of Si and Ti signals in the corresponding RBS spectra, there appears to be no information on nitrogen because of the large silicon background signal which is superimposed on the nitrogen peak.[8] It is worth noting that the formation of $TiSi_2$ phase silicide can be simultaneous with sample nitridation by e-beam rapid treating, in addition to obtaining TiN on the surface.

The sheet resistance was measured by the conventional four-probe technique. Figure 4 shows the sheet resistance as a function of processing time at the same power density of the e-beam, ratio of nitrogen and helium, and flow rate of the mixture. As is evident in Fig. 4, as-deposited film exhibits a sheet resistance of 18 Ω/□. During e-beam processing, the sheet resistance will decrease with time; at 20 s it is down to a minimum of 0.6 Ω/□; after the minimum the sheet resistance increases again. It is likely to be similar to other techniques[2], but before the minimum, the sheet resistance seems to have no maximum. It can be compared with previous techniques.[2] The decrease in sheet resistance is due to both TiN on the surface and $TiSi_2$ silicide; the increase of sheet resistance depends on the dominant formation of TiN on the surface. The explanation seems to be that compounds such as nitrides and silicides, when we discuss their similarities in variation of resistance, show the dominant role of the outmost electrons (most probably the *d*- electron) of the transition metal; they appear to donate electrons, i.e., they belong to so-called metalloids.[9]

Furthermore, the dependence of the N,Ti, and Si distribution on the depth from the surface is shown in Fig. 5. Data from the SIMS profile with an argon sputtering beam are evidence of the effectiveness of e-beam rapid nitridation processing for Ti films on Si wafers. The formation of TiN film

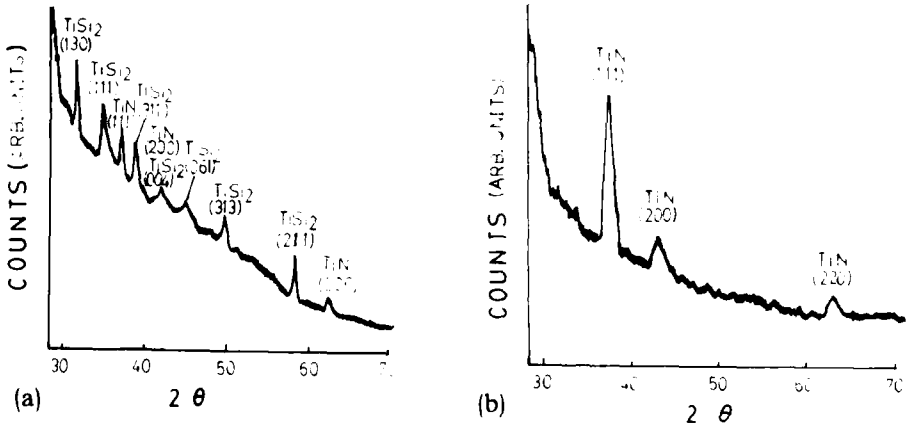

FIG. 3. X-ray diffraction spectrum: (a) for a TiN/Ti/Si sample after 20 s of nitridation processing of EB; (b) for a TiN/SiO_2/Si sample after 40 s of nitridation processing of EB.

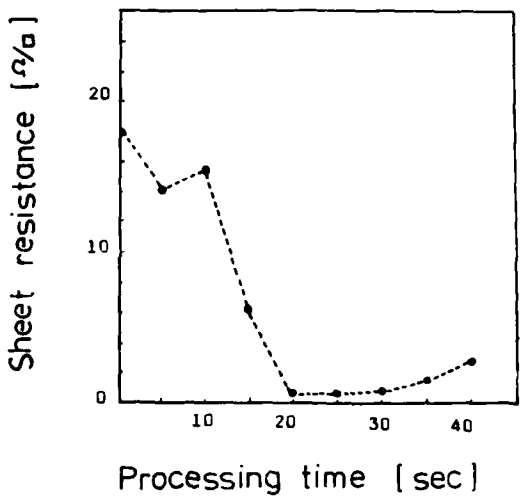

FIG. 4. Sheet resistance as a function of processing time. Specimen with Ti evaporated on Si wafer processed with e-beam power density of 30 W/cm^2 and a 3:1 (N_2/He) ratio at a flow rate of 30 cm^3/min.

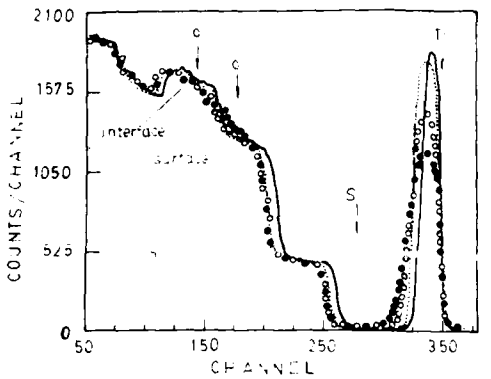

FIG. 6. Backscatter spectra with a 1:1 ratio (N_2/He) and an e-beam power density of 35 W/cm^2 for 10 s, (dash line); 30 s (open circle); 60 s (solid) processing time. Also, as-evaporated Ti film on SiO_2/Si (solid line).

may not only be deduced from XRD but also from SIMS analysis. The TiN film on the surface can be obtained in 5 s of processing with a rapid driving e-beam. It is indicated that the formation of the TiN film prepared by this e-beam is very rapid in comparison with other techniques,[2] we propose that the e-beam plays an important role in the nitridation processing; it may increase electron-stimulated surface reaction between nitrogen and Ti; the e-beam may be a source for heating the sample and dissociating the interface between Ti film and Si substrate. It suggests that enhanced or induced reaction by e-beam treating be regarded as a predominant driving mechanism for rapid nitridation processing.

B. Ti on SiO_2/Si

The nitridation processing of the Ti film deposited on the SiO_2/Si substrate was performed in the same manner as the Ti deposited on Si. The TiN film was formed in 10–60 s. The RBS spectra of these samples are shown in Fig. 6. In RBS analysis, because of the large silicon background signal which is superimposed on the nitrogen peak the ratio of nitrogen to titanium can be determined by comparing the titanium peak from a TiN film with the peak from an as-deposited sample,[8] as calculated with RBS, a ratio of 0.96% ± 5% (N/Ti) for TiN/SiO_2/Si sample can be obtained. According to Chu *et al.*,[10] a TiN thickness of the nitridated sample for Ti/SiO_2/Si by e-beam may be achieved with RBS data, the width of TiN film thickness is about 1077 Å. From the trailing and leading edge of the Ti peak (in the TiN) we conclude that the Ti signal is well-separated from the Si signal, the slight shift of the Si background towards lower energy for the e-beam treated sample is due to a variation in TiN film thickness. As indicated by RBS data, the oxygen signal is superimposed on the Si signal, the spectra for both as-deposited sample (solid line) and the sample (dash line) processed by the shorter processing time, the Ti signal is somewhat broad, the height of Ti signal has no obvious change, with 30 s nitridation processing, the height of Ti signal (open circle) has dropped and the width of Ti signal increase significently. After 60 s (solid) of processing with the e-beam, besides the variation of both the height and the width of Ti signal, a second oxygen peak near the surface position of oxygen occurred. It indicates that a significant amount of oxygen has to be dissolved in the TiN film. The Si did not diffuse into the Ti film at even longer processing time; this was different from previous studies.[11] It is shown that the silicide was not formed in our experiment for the Ti on the SiO_2/Si sample, as shown in Fig. 3(b), the XRD lines only give information on TiN. On the other hand, the nitridation processing of Ti on SiO_2/Si by the e-beam seems that

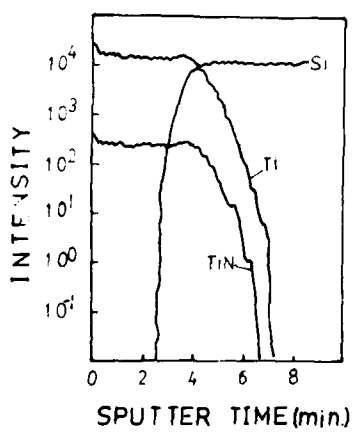

FIG. 5. SIMS profiles of N, Ti, and Si for same specimen as in Fig. 3.

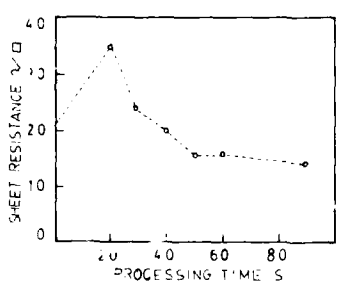

FIG. 7. Sheet resistance as a function of processing time. Specimen with Ti evaporated on SiO_2/Si wafer processed with an e-beam power density of 35 W/cm^2 and an 1:1 ratio of N_2/He at a flow rate of 30 cm^3/min.

the SiO_2 was easily broken down. Previous studies[11] have shown that Ti atoms at the interface have a strong tendency to reduce neighboring Si–O bonds and to form new Ti–O and Ti–Si bonds, from our data, it is not obvious that the silicide begins to be formed by the e-beam driving due to the processing time being shorter than that of other studies.[2]

The dependence of the sheet resistance on the processing time for Ti on SiO_2/Si by the e-beam is shown in Fig. 7. The value increases to a maximum before it begins to decrease. The resistance increase results from the impurity diffusion into Ti layer as mentioned above. With respect to the decrease of the sheet resistance at the longer processing time, it is due to the TiN formed on the surface. The behavior of the sheet resistance variation is also similar to the results for TiN/SiO_2/Si sample reported by Adams *et al.*[2]

IV. CONCLUSION

We have used a rapid electron-beam processing to form TiN of an evaporated Ti film on both Si and SiO_2/Si wafer. The RBS and XRD spectra indicate that the surface film structures, include both TiN and $TiSi_2$ on Si and TiN on SiO_2/Si wafer. In comparison with the results obtained by conventional methods, a predominant e-beam enhanced mechanism should be considered. The rapid nitridation processing using large area e-beam does not appear to meet some problems under the influence of a residual gas such as O_2, which cannot be avoided in conventional reactive sputtering, reactive evaporation, and furnace annealing. Moreover, it does not cause the shallow junction degradation of integrated circuits because of the rapid nitridation driving. It is obvious that the e-beam rapid nitridation process might lead to applications of the results of electrical characteristics used as a diffusion barrier.

ACKNOWLEDGMENTS

The authors wish to acknowledge H. S. Cheng at the Department of Nuclear Physics, Fudan University for RBS measurement and helpful discussion, Y. M. Zhao for SIMS analysis at Department of Material Science Fudan University, and L. Sun for XRD analysis.

[1] M. Wittmer, J. Vac. Sci. Technol. A **3**, 1997 (1985).
[2] E. D. Adams, K. Y. Ahn, and S. B. Brodsky, J. Vac. Sci. Technol. A **3**, 2264 (1985).
[3] I. Suni, M. Blomberg, and I. Saarilahti, J. Vac. Sci. Technol. A **3**, 2233 (1985).
[4] A. Armigliato, M. Finetti, and J. Carrido, S. Guerri, P. Ostoja, and A. Scorzoni, J. Vac. Sci. Technol. A **3**, 2237 (1985).
[5] Y. C. Du, Z. Lu, Z. Q. Yu, D. C. Sun, F. M. Li, and G. J. Collins, Chin. Phys. **6**, 208 (1986); or Chin. J. Semicond. **6**, 159 (1985) (in Chinese).
[6] C. A. Moore, J. J. Rocca, and G. J. Collins, Appl. Phys. Lett. **45**, 169 (1984).
[7] C. Y. Ting, J. Vac. Sci. Technol. **21**, 14 (1982).
[8] R. J. Schutz, paper presented at the Symposium on Interfaces and Contacts, Boston, MA, 2–4 Nov. 1982.
[9] S. P. Murarka, M. H. Reed, C. J. Doherty, and D. B. Fraser, J. Electrochem. Soc. **129**, 293 (1982).
[10] W. K. Chu, J. W. Mayer, and M. A. Nicolet, *Backscattering Spectrometry* (Academic, New York, 1978).
[11] C. Y. Ting, M. Wittmer, S. S. Iyer, and S. B. Brodsky, J. Electrochem. Soc. **131**, 2934 (1984).

Tunneling spectroscopy study of aniline adsorbed on aluminum oxide

R. J. Graves and C. B. Wallace
The BDM Corporation, Albuquerque, New Mexico 87106

R. Ellialtioglu
Marmara Scientific and Industrial Research Institute, P. O. Box 74, Gebze, Kocaeli, Turkey

H. W. White[a)]
University of Missouri-Columbia, Columbia, Missouri 65211

(Received 27 February 1987; accepted 26 May 1987)

Aniline has been studied using tunneling spectroscopy. Detailed comparisons of the spectrum with infrared data of aniline adsorbed on iron oxide, other tunneling data, and infrared and Raman spectra of aniline in the gas, liquid, and solid phases are presented. Large shifts (> 100 cm^{-1}) to lower frequencies were seen for the two aniline N–H stretching bands, the NH_2 deformation mode, and the C–N stretching mode. Smaller shifts were also seen in the aromatic ring stretching mode frequencies. Comparisons of a' with a'' vibrational modes and of out of the benzene plane with in-plane bending modes indicated that the a'' modes and the in-plane bending modes had lower intensities and appeared less frequently than did the a' and the out-of-plane modes in the spectrum. The shifts in N–H frequencies and the dominance of the a' and the out-of-plane modes indicated that the orientation of aniline on aluminum oxide is one in which aniline is bonded to the surface via the N atom with the benzene group primarily parallel to the surface, though slightly tilted away from the surface, and the NH_2 H atoms undergo some degree of hydrogen bonding with surface O atoms or hydroxyls. This orientation is consistent with the results of Busca *et al.* as discussed in the text.

I. INTRODUCTION

Recent work on the aniline and amino–pyridine/α–Fe_2O_3 adsorbate systems by Busca, Cerisola, and Lorenzelli[1] has lead to a re-examination of aniline on aluminum–oxide using tunneling spectroscopy at the University of Missouri-Columbia. A tunneling spectrum of aniline has been published previously by Jaklevic[2-4]; however, no assignments of its vibrational modes nor any listing of its frequencies has been published along with that spectrum.[5,6] Indeed, attempts by our laboratory to analyze the tunneling spectrum of aniline presented here prior to the work of Busca *et al.* met with failure. With the orientation of adsorbed aniline postulated by Busca *et al.* (indicated in Fig. 1) a re-examination of the tunneling spectrum of aniline has been undertaken.

Because the thickness of the metal–adsorbate interface region is of the order of 5 to 10 Å, information on the types and orientations of molecular species in the region is generally very difficult to obtain. Tunneling spectroscopy can provide information on the bonding of these species and, to a limited extent, provide information on their orientations with respect to the oxide. The results reported here were originally part of a series of studies on chemicals that either corrode aluminum oxide or that inhibit corrosion. These studies included the corrosion agents carbon tetrachloride[7] and trichloroethylene,[8] their inhibitor formamide,[9] and acridine[10] and thiourea[11,12] which are inhibitors of aluminum oxide corrosion by hydrochloric acid.[13,14]

Aniline presents a unique opportunity to determine the orientation of its adsorbed species by tunneling spectroscopy because of the group theoretical representation of its vibrational modes. While tunneling has no symmetry selection rules as do infrared and Raman spectroscopies, it does have an "orientational" selection rule in that molecular bonds oriented perpendicular to the junction oxide surface will have molecular vibrations that couple more strongly with the electron flow (i.e., parallel to it) than will the vibrations of bonds oriented parallel to the surface (i.e., perpendicular to the electron flow). Aniline, with fourteen atoms, belongs to the C_s point group. It has 36 fundamental vibrations classified as follows[15-17]:

$$\Gamma = 20a' + 16a''.$$

All of these vibrations are Raman and infrared active. The plane of symmetry is normal to the benzene plane and passes through the N atom. The molecular transition moments are either in the plane of symmetry (a') or normal to it (a''). These symmetry species mix the transition moments of C_{2v} which occur along the x (perpendicular to the benzene plane), y and z axes.[18] Thus aniline modes in a tunneling spectrum can be examined from two standpoints: in or out of the plane of symmetry (i.e., a' vs a''); in or out of the plane of the benzene ring [i.e., in-plane (IP) a' and a'' vs out-of-plane (OP) a' and a'']. If the orientation of aniline on aluminum oxide is the same as that determined by Busca *et al.* for aniline on iron oxide, the most intense tunneling spectral peaks would be expected to be the a' (in the plane of symmetry) modes that are out of the plane of the benzene ring (and thus perpendicular to the surface) and a'' (though fewer) modes that are also out of the benzene ring. IP a' and a'' modes would not be excluded, however.

The infrared and Raman spectra of molecular aniline have been studied by a number of investigators. The most recent investigation of aniline has been conducted by Niu, Dunn, and Boggs[19] (1985) who calculated the infrared frequencies

 0734-211X/87/051508-06$01.00 © 1987 American Vacuum Society

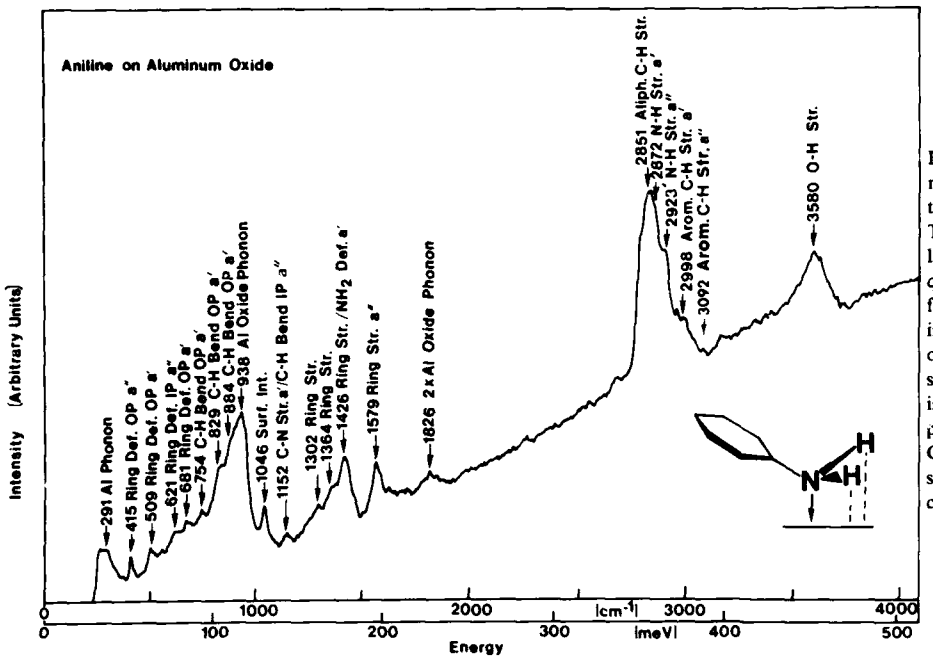

FIG. 1. Tunneling spectrum of aluminum/aluminum oxide/lead tunnel junctions doped with aniline ($C_6H_5NH_2$). The locations of significant structures are labeled in units of cm^{-1}. Peak position frequencies have been compensated for the frequency shifts due to the superconducting lead overlayer. The inset indicates the orientation for aniline indicated by this spectrum (the symmetry plane of aniline is the plane passing through the C–N bond perpendicular to the plane formed by the C_6H_5N group). This orientation is consistent with that of Busca *et al.* as discussed in the text.

and relative intensities of aniline, aniline–NHD, and aniline–ND_2 and compared them with those measured by Evans.[15] The spectra of crystalline (infrared and Raman) and liquid phase aniline (Raman) have been measured by Tripathi[18] (1980), of gaseous, solution (both infrared), and liquid (infrared and Raman) aniline, aniline–NHD, and aniline–ND_2 by Evans[15] (1960), and of solutions of aniline (infrared) to study N^{15} isotope effects by Tsuboi[20] (1960). Earlier investigations were conducted by Califano and Moccia[21] (1957), Orville–Thomas[22] (1957), Fuson *et al.*[23] (1952), Flett[24] (1948), Venkateswaren and Pandya[25] (1941), Kohlrausch and Wittek[26] (1941), and Williams *et al.*[27] (1939). Far infrared investigations of the vapor phase spectrum of aniline have been conducted by Larsen *et al.*[28] (1976) and Kydd and Krueger[29] (1977). The structure of aniline was determined by Lister *et al.*[30] (1974) from microwave spectral data with the angle between the NH_2 and the C_6H_5N planes determined to be $37°29' \pm 2°$, ending the debate over the symmetry group of aniline.

II. TUNNELING SPECTROSCOPY AND EXPERIMENT DISCUSSIONS

Tunneling spectroscopy involves the measurement of the electrical current (I) associated with electrons which tunnel through an oxide film having an adsorbed molecular layer on its surface. The electrons which inelastically tunnel through the oxide excite the characteristic vibrations of the adsorbed molecules. Graphs of the second derivative of the current with respect to the voltage d^2I/dV^2 versus the bias voltage V display large peaks centered at the voltage $V_m = h\nu_m/e$, where h is Planck's constant, e is the electronic charge, and ν_m is a molecular vibrational frequency. These graphs show peaks which can be associated with the presence of infrared, Raman, and optically forbidden vibrational modes. Tunneling "selection" rules are essentially orientational in nature in that vibrational modes with a large component perpendicular to the surface (and parallel to the electron current flow) have greater intensities than modes oriented essentially parallel to the surface. The spectra can be used to identify molecular species on the oxide layer, estimate molecular orientation, and detect chemisorption bonding to the oxide layer.

A general review of tunneling spectroscopy and of junction preparation has been given by Hansma.[2] Aluminum/aluminum oxide/dopant/lead tunnel junctions were fabricated in a manner described earlier.[7,31] The aluminum electrode was evaporated to a thickness of about 1000 Å in an ion-pumped vacuum system. This step was followed immediately by the growth of a "barrier" oxide layer about 20 Å thick using a glow discharge in a partial pressure of oxygen. The junctions were liquid-doped by placing several drops of aniline on the electrode and spinning off the excess. The doped substrate was quickly returned to the vacuum chamber and a lead counter electrode evaporated over the molecules. While tunnel junctions prepared with a top electrode of aluminum, chromium, or most of the transition metals will have tunneling spectra that bear little or no resemblance to infrared or Raman spectra of the original molecules adsorbed without overlayers (presumably because the top metal electrode has "damaged" the dopant molecules),[2] this does not seem to be the case for lead, thallium, and under some conditions, indium, tin, silver, and gold.[2] For these metals tunneling spectra that closely resemble the infrared and Raman spectra of the surface-adsorbed molecules without a top electrode are obtained. Frequency shifts of ~6–8 cm^{-1} due to the lead electrode are accounted for before comparison of tunneling frequencies with infrared and Raman spectral frequencies.[2]

To obtain spectra the junctions were connected to the tunneling spectrometer and cooled to 4.2 K. A dc bias across the

junction was swept slowly from 30 to 500 mV (~ 300 to 4000 cm^{-1}). An ac modulation signal of 1000 Hz and about 1 mV (rms) was applied continuously. The amplitude of the second harmonic signal d^2V/dI^2 generated by the tunnel junction was recorded as a function of the vibrational dc bias. The energies of the vibrational modes were determined by measuring the bias voltage at which peaks occurred.

III. RESULTS

Our aniline tunneling spectrum is shown in Fig. 1, and its frequency assignments are listed in Table I. The frequencies of the various modes are essentially the same as those of the Jaklevic data[6] (frequencies taken from the spectra of Jaklevic[6] or Busca *et al.*[1] are indicated as, for example, ~1397). Our spectrum and the Jaklevic results will be discussed in Sec. IV.

In the frequency range of 300 to 700 cm^{-1} ring deformations are assigned to three peaks and a shoulder at 415 (OP *a"*), 509 (OP *a'*), 681 (OP *a'*), and 621 (IP *a"*), respectively. An Al–N stretching mode might be expected from the Busca *et al.* orientation near 500 cm^{-1} as seen in tunneling spectra of formamide[9] and phenazine.[10] Aniline, however, has a vibrational mode at 509 cm^{-1} which would be superimposed on and obscure such a stretching mode.

In the frequency range 700–1000 cm^{-1} three C–H OP *a'* bends are assigned. The shoulder at 884 cm^{-1} is difficult to assign because the aluminum oxide phonon occurs at 938 cm^{-1} and dominates this portion of the spectrum; however, a clearly resolved peak occurs near this frequency in the Jaklevic[2-4] *aniline tunneling spectrum*, so the assignment is made.

In the range of 1000 to 1200 cm^{-1} two peaks are assigned. The peak at 1046 cm^{-1} is assigned to a surface interaction and is discussed with the background structures below. The peak at 1152 cm^{-1} is assigned as a C–N stretch *a'* and/or to a C–H IP bend *a"*. Busca *et al.* noted the disappearance of the C–N stretching frequency of the free aniline molecule at 1280 cm^{-1} from their adsorbed infrared spectra and stated that the mode was superimposed on the α-Fe_2O_3 background near 1200 cm^{-1}. Careful examination of their spectra would allow an assignment to ~1150 cm^{-1} or to ~1250 cm^{-1}. The C–N stretching frequency is assigned here to 1152 cm^{-1} because bonding to aluminum oxide rather than iron oxide could shift this mode to a lower energy as seen in the tunneling spectrum of phenazine.[10] This spectral region is normally expected to contain IP C–H bending modes, and such a possibility is acknowledged; however, if the Busca *et al.* orientation is correct, these modes would not have large intensities because they would be almost entirely parallel to the oxide surface.

In the region of 1300 to 1800 cm^{-1} three peaks and a shoulder are assigned, at least partially, as ring stretching modes—1302, 1426, 1579, and 1364 cm^{-1}, respectively. The 1302 cm^{-1} peak also may correspond to a C–H IP bend *a"* noted by both Evans and Tripathi (it should be so noted in Fig. 1). The 1364 cm^{-1} shoulder may correspond to a shoulder at ~1374 cm^{-1} on a peak at ~1397 cm^{-1} in the Jaklevic data. Three small peaks appear in the Busca *et al.* data at ~1343, ~1357, and ~1373 cm^{-1} but are not discussed. These peaks seem to shift up in frequency from the solution data. The 1426 cm^{-1} peak does not correspond well to optical data although this is approximately the region where ring stretching modes occur in aniline. Busca *et al.* discuss the downshifting of the NH_2 *a'* deformation mode from 1623 to 1445 cm^{-1}. This mode could be represented by a shoulder on the 1426 cm^{-1} peak about 1438 cm^{-1}; thus, the double assignment may be warranted rather than a single assignment to NH_2 deformation alone. The Jaklevic data show two peaks—~1454 and ~1485 cm^{-1} [NH_2 deformation and an overtone band[15] (1480 cm^{-1}) or a ring stretching *a'* mode (1500)[15,18]]. The ring stretching mode at 1579 cm^{-1} is *a"* in the optical literature.[15,18] Thus only one peak in this region may unequivocally be assigned according

TABLE I. The tunneling vibrational frequencies and mode assignments as determined by this study are shown for aniline. Frequency units are cm^{-1}. The parentheses about footnote e indicate the presence of this mode in the tunneling spectra data of Jaklevic; no assignments for the modes of aniline were given by Jaklevic. While the reference for Niu *et al.* (footnote b) is included, their data were taken from Evans (footnote d).

Tunneling Frequency	Assignment	Footnote
291	Al Phonon	a
415	Ring Def. OP *a"*	b,c,d(e)
509	Ring Def. OP *a'*	b,c,d(e)
621	Ring Def. IP *a"*	b,c,d(e)
681	Ring Def. OP *a'*	b,d(e)
754	C–H Bend OP *a'*	b,c,d(e)
829	C–H Bend OP *a'*	b,c,d(e)
938	Al Oxide Phonon	a
1046	Surface Interaction	f,g,(e)
1152	C–N Str. *a'*/C–H Bend IP *a"*	g,h/b,c,d(e)
1302	Ring Str./C–H Bend IP *a"*	i/d(e)
1364	Ring Str.	i(e)
1426	Ring Str./NH_2 Def. *a'*	i/h,i(e)
1579	Ring Str. *a"*	c,d(e)
1826	2 × Al Oxide Phonon	a,i
2851	Aliph. C–H Str.	a,g,i
2872	N–H Str. *a'*	h,i,(e)
2923	N–H Str. *a"*	h,i(e)
2998	Arom. C–H Str. *a'*	c,d,g,h(e)
3092	Arom. C–H Str. *a"*	b,c,d
3580	O–H Str.	h,i,j,k(e)

[a] R. M. Ellialtioglu, H. W. White, L. M. Godwin, and T. Wolfram, J. Chem. Phys. **72**, 5291 (1980).
[b] Z. Niu, K. M. Dunn, and J. E. Boggs, Mol. Phys. **5**, 421 (1985).
[c] G. N. R. Tripathi, J. Chem. Phys. **73**, 5521 (1980).
[d] J. C. Evans, Spectrochim. Acta **16**, 428 (1960).
[e] R. C. Jaklevic, in *Tunneling Spectroscopy Capabilities, Applications, and New Techniques*, edited by P. K. Hansma (Plenum, New York, 1982), Chap. 15, pp. 451–473.
[f] C. S. Korman, J. C. Lau, A. M. Johnson, and R. V. Coleman, Phys. Rev. B **19**, 994 (1979).
[g] R. J. Graves and H. W. White, Spectrochim. Acta Part A **43**, 107 (1987).
[h] G. Busca, G. Cerisola, and V. Lorenzelli, Corros. Sci. **23**, 789 (1983).
[i] This work.
[j] C. Morterra, S. Coluccia, E. Garrone, and G. Ghiotti, J. Chem. Soc. Faraday Trans. 1, **75**, 271 (1979).
[k] N. M. D. Brown, R. B. Floyd, W. J. Nelson, and D. G. Walmsley, J. Chem. Soc. Faraday Trans. 1 **76**, 2335 (1980).

to data from the optical literature.

The Jaklevic tunneling spectrum also contains peaks at ~1251 and ~1397 cm^{-1} and a shoulder at ~1334 cm^{-1}. A shoulder in our spectrum about 1253 cm^{-1} seems to correspond to the ~1251 cm^{-1} Jaklevic peak. No such mode has been seen in optical spectra of the free molecule, but as noted previously, such a mode could correspond to the C–N stretching mode. This mode could also be a C–H IP bend or a ring stretching mode. A mode about 1390 cm − 1 was noted by both Tripathi,[18] who did not assign it, and Evans,[15] who assigned it as a combination band.

The spectral region of 2700 to 3500 cm^{-1} contains a number of different stretching modes. This frequency region most examined extensively by Busca *et al.* Their infrared spectra of aniline on α-Fe_2O_3 indicated that the two N–H stretching frequencies shifted from 3480 and 3395 cm^{-1} to 2910 and 2860 cm^{-1}, respectively. Such shifts in the tunneling spectrum would superimpose the N–H stretching frequencies onto the C–H aliphatic contamination stretches that are considered to be background structures in tunneling spectra. No clear structures are seen in our tunneling spectrum of aniline in the 3400 to 3500 cm^{-1} region (i.e., where N–H stretching would normally be expected). C–H stretching modes associated with the aromatic ring occur in the range of 3000 to 3100 cm^{-1} for free aniline. These stretches are indicated in the tunneling spectrum at 2998 (a') and 3092 cm^{-1} (a''). The Jaklevic data in this region contain a peak at ~2829 cm^{-1} (aliphatic C–H stretching), two shoulders about ~2873 and ~2913 cm^{-1} (N–H stretching a' and a'', respectively), a peak at ~3004 cm^{-1} (aromatic C–H stretching a'), and shoulders about ~3027, ~3072, and ~3088 cm^{-1} (aromatic C–H stretching, a'', a', and a'', respectively). The Jaklevic data also contain a broad, low-intensity peak at ~3326 cm^{-1} which was assigned as N–H stretching. Such a mode is not present in our spectrum. This peak will be discussed in Sec. IV.

The background tunneling spectral features include the aluminum phonon at 291 cm^{-1}, the aluminum oxide phonon at 938 cm^{-1}, the 1046 cm^{-1} peak, the broad-aluminum oxide phonon overtone from 1826 to 1866 cm^{-1} (indicative of less than monolayer coverage), the aliphatic C–H stretching mode at 2851 cm^{-1},[10] and the broad-O–H stretching region at approximately 3580 cm^{-1} (normally about 3620 cm^{-1}). A peak in the tunneling spectra of aromatic compounds from 1050 to 1070 cm^{-1} has been seen previously.[10,32,33] This mode has been described as being associated with a surface reaction of an aromatic molecule rather than a C–H IP bend by Korman *et al.*[32,33] The O–H region, associated with surface-bound hydroxyl intrinsically present in plasma-grown oxide, in our spectrum is broadened and downshifted from the normal O–H stretching region seen in tunneling. Shifts in the O–H stretching region may indicate hydrogen bonding of the aniline NH_2 H atoms to surface O atoms or hydroxyls as indicated by Busca *et al.* Downshifting of O–H stretching vibrations in infrared spectra of aniline adsorbed on silica has been examined by Kiselev *et al.*[34] and in infrared spectra of pyridine adsorbed on η-Al_2O_3 and Cr_2O_3-I by Morterra *et al.*[35] and Morishige *et al.*[36], respectively.

IV. DISCUSSION

The strongest modes in the low-frequency region of the aniline tunneling spectrum are those modes associated with bending out of the benzene plane of both a' and a'' symmetry types; however, the number of strong a' modes is greater than the number of a'' modes (five to one). The only IP bending mode in this region is assigned to a shoulder about 621 cm^{-1} and is an a'' mode.

The relatively strong intensities of modes associated with C–C and C–H bending out of the benzene plane and their a' (in the symmetry plane and thus essentially perpendicular to the oxide surface) nature gives support to the Busca *et al.* orientation for the benzene group of adsorbed aniline. The tunneling data supports the interpretation that this ring is essentially parallel to the surface although the presence of IP bends implies some degree of tilt to the ring orientation is possible.

The range of the spectrum between 1100 and 1600 cm^{-1} contains several modes displaying frequency shifts. The modes at 1152 and 1426 cm^{-1} are partially assigned to C–N stretching and NH_2 deformation. These two modes were downshifted in the Busca *et al.* data. Aniline also has C–H IP bending modes near 1152 cm^{-1}; however, this mode is an IP bend and a'' so that the intensity of this structure is probably primarily due to C–N stretching as in the tunneling spectrum of phenazine.[10] The 1426 cm^{-1} peak is assigned to both the shifted NH_2 deformation (a vibrational mode that would have a large perpendicular component to the surface in the Busca *et al.* orientation) and a ring stretch although no optical ring stretch occurs near this frequency. The small peak at 1302 cm^{-1} and the shoulder about 1364 cm^{-1} are assigned to ring stretching modes although no optical modes have been assigned to ring stretches in this region. The 1302 cm^{-1} peak could be assigned as a C–H IP bend a'' mode by comparison with Evans[15]; however, the Evans assignment is not confirmed by Niu *et al.*[19] or Tripathi.[18] Careful examination of the Busca *et al.* spectra indicates three small structures in the liquid-aniline spectrum that seem to shift to higher frequencies (that are approximately the same as those seen here) in the adsorbed spectrum but which are not discussed in the text. A final ring stretching mode is seen in this region at 1579 cm^{-1} and corresponds to an a'' ring stretch (1590[15] and 1583[18] cm^{-1}) and may receive intensity contributions from an a' ring stretch at 1600 cm^{-1} in the optical data (here possibly seen as a shoulder on the 1579 cm^{-1} peak).

The frequency shifts discussed in the previous paragraph may arise due to an increase of the electron probability density in the σ bonds of the benzene ring. Such a transfer could cause a "stiffening" of some ring force constants (particularly those associated with bonds near the N atom) and thereby raise the frequencies required to excite some of the ring stretching modes. As noted previously three small peaks in the Busca *et al.* data in the 1300–1400 cm^{-1} range appeared to shift upward in frequency in the adsorbed spectrum from the solution spectrum but no discussion of the possible shifts was given.

The N–H stretching frequencies are not present at their normal frequencies in the tunneling spectrum. They are

downshifted and superimposed on the aliphatic C–H stretching modes as anticipated from the Busca *et al.* data. Comparison of the intensities of the shoulder about 2872 cm^{-1} (N–H stretching a') with the shoulder about 2923 cm^{-1} (N–H stretching a'') and of the peak at 2998 cm^{-1} (aromatic C–H stretching a') with the peak at 3092 cm^{-1} (aromatic C–H stretching a''), although inconclusive, indicates again the dominance of a' modes over a'' modes. This interpretation can also be made based on an examination of the Jaklevic spectra which has much less aliphatic C–H stretching intensity to obscure the intensity of the N–H stretching region. The N–H shifts imply the strong adsorption of aniline in the orientation proposed by Busca *et al.* In order to determine whether the angle between the C_6H_5N and the NH_2 planes has changed from 37.5° (Ref. 30) would require extensive calculations to reproduce the measured intensities.

Of interest is a comparison of our tunneling spectrum with that of Jaklevic.[2-4,6] In the Jaklevic spectrum the intensity of the ~948 cm^{-1} aluminum oxide phonon is reduced in comparison to the other modes of the spectrum indicating that the aniline coverage on the oxide surface is much greater in the Jaklevic data than in our spectrum. This possibility is also implied by the presence in the Jaklevic data of a broad peak attributed to N–H stretching which could encompass one or both of the N–H stretching modes (~3326 cm^{-1}). These modes could indicate the presence of two forms of aniline in the Jaklevic data. For example, there could be a complete monolayer of aniline adsorbed in the Busca *et al.* orientation plus additional, essentially unperturbed, aniline providing the normal N–H stretching frequencies possibly forming a second layer (the sensitivity of tunneling spectroscopy to submonolayer coverages has been demonstrated by Hansma[2]). The presence of unperturbed aniline in the Jaklevic spectrum is also indicated by the presence of a number of additional structures in the ring stretching region. The Jaklevic data largely confirms the structures and assignments in our spectrum in the ring stretching region and helps detail other regions of the spectrum (e.g., the NH_2 deformation occurs at 1445 cm^{-1} in the Busca *et al.* data but has been assigned as part of the 1426 cm^{-1} peak in our spectrum; the Jaklevic spectrum indicates two small peaks, one of which is ~1445 cm^{-1}). In our spectra the O–H stretching region was seen to be broadened and downshifted; however in the Jaklevic data this is not the case. It should be noted that the Jaklevic junctions were infusion doped as opposed to our junctions which were liquid doped. The infusion doping process involves the use of water vapor transport of the dopant molecule through the top metal electrode. This could imply the presence of additional water on the oxide surface and possibly fewer perturbed O–H frequencies would then be expected. The infusion doping process may also allow for greater than monolayer coverages as opposed to the liquid doping process which generally results in monolayer or less coverages.

V. CONCLUSIONS

The tunneling spectrum of aniline on aluminum oxide has been measured. The shifts in frequencies, particularly of NH_2 modes, have been found to agree with those measured by Busca *et al.* for aniline adsorbed on α-Fe_2O_3. Comparison of our data with tunneling spectra infusion doped with aniline by Jaklevic indicates the difference in coverages between the two spectra and possibly indicates at the partial formation of a second aniline layer in the Jaklevic data. a' symmetry modes and modes bending out of the benzene plane were seen to dominate over a'' modes and modes primarily within the benzene plane although all the various types of modes were represented in the data. The orientation of aniline on aluminum oxide indicated by this work is one in which the benzene ring is oriented largely parallel to the oxide surface, though with some degree of tilt possible. The molecule is bonded to the surface via the N atom, and the H atoms are hydrogen-bonded to surface O atoms or hydroxyl groups. This orientation is consistent with that proposed by Busca *et al.* for aniline on α-Fe_2O_3.

ACKNOWLEDGMENT

The authors wish to thank Dr. R. C. Jaklevic for supplying copies of his raw spectral data for examination and for helpful discussions of his work.

[a] Author to whom correspondence should be sent.

[1] G. Busca, G. Cerisola, and V. Lorenzelli, Corros. Sci. **23**, 789 (1983).
[2] R. C. Jaklevic, in *Tunneling Spectroscopy Capabilities, Applications and New Techniques*, edited by P. K. Hansma (Plenum, New York, 1982), Chap. 15, pp. 451–473; P. K. Hansma, *ibid.*, Chap. 1, pp. 1–41.
[3] D. G. Walmsley and J. L. Tomlin, in *Progress in Surface Science*, edited by S. G. Davison (Pergamon, New York, 1985), Vol. 18, pp. 247–447.
[4] R. C. Jaklevic and M. R. Gaerttner, Appl. Surf. Sci. **1**, 479 (1978).
[5] R. C. Jaklevic (private communication).
[6] R. C. Jaklevic (unpublished data).
[7] R. M. Ellialtioglu, H. W. White, L. M. Godwin, and T. Wolfram, J. Chem. Phys. **72**, 5291 (1980).
[8] H. W. White, R. Ellialtioglu, and J. E. Bauman, Jr., J. Chem. Phys. **75**, 3121 (1981).
[9] R. Ellialtioglu, H. W. White, L. M. Godwin, and T. Wolfram, J. Chem. Phys. **75**, 2432 (1981).
[10] R. J. Graves and H. W. White, Spectrochim. Acta Part A **43**, 107 (1987).
[11] C. D. Crowder, G. P. Alldredge, and H. W. White, Phys. Rev. B **31**, 6676 (1985).
[12] C. D. Crowder, H. W. White, and G. P. Alldredge, Phys. Rev. B **31**, 6685 (1985).
[13] V. E. Jenckel and F. Woltmann, Z. Anorg. Chem. **233**, 236 (1937).
[14] J. Sundararajan and T. L. Rama Char, J. Sci. Ind. Res. Sect. B **17**, 387 (1958).
[15] J. C. Evans, Spectrochim. Acta **16**, 428 (1960).
[16] K. Nakamoto, in *Infrared and Raman Spectra of Inorganic and Coordination Compounds*, 4th ed. (Wiley, New York, 1986), p. 458.
[17] G. Herzberg, in *Molecular Spectra and Molecular Structure* (Van Nostrand, Princeton, 1945), Vol. 2.
[18] G. N. R. Tripathi, J. Chem. Phys. **73**, 5521 (1980).
[19] Z. Niu, K. M. Dunn, and J. E. Boggs, Mol. Phys. **55**, 421 (1985).
[20] M. Tsuboi, Spectrochim. Acta **16**, 505 (1960).
[21] S. Califano and R. Moccio, Gazz. Chim. Ital. **87**, 805 (1957).
[22] W. J. Orville-Thomas, Chem. Rev. **57**, 1179 (1957).
[23] N. Fuson, M. L. Josien, R. L. Powell, and E. Utterback, J. Chem. Phys. **20**, 145 (1952).
[24] M. St. C. Flett, Trans. Faraday Soc. **44**, 767 (1948).
[25] C. S. Venkateswaran and N. S. Pandya, Proc. Ind. Acad. Sci. Sect. A **15**, 390 (1942).

[26]K. W. F. Kohlrausch and H. Wittek, Monatsh. Chem. **74**, 1 (1941).
[27]V. Williams, R. Hofstadter, and R. C. Herman, J. Chem. Phys. **7**, 802 (1939).
[28]N. W. Larsen, E. L. Hansen, and F. M. Nicolaisen, Chem. Phys. Lett. **43**, 584 (1976).
[29]R. A. Kydd and P. J. Krueger, Chem. Phys. Lett. **49**, 539 (1977).
[30]D. G. Lister, J. K. Tyler, J. H. Høg, and N. W. Larsen, J. Mol. Struct. **23**, 253 (1974).
[31]H. W. White and R. J. Graves, Am. J. Phys. **50**, 38 (1982).
[32]C. S. Korman, J. C. Lau, A. M. Johnson, and R. V. Coleman, Phys. Rev. B **19**, 994 (1979).
[33]C. S. Korman and R. V. Coleman, Phys. Rev. B **15**, 1877 (1977).
[34]A. V. Kiselev and V. I. Lygin, in *Infrared Spectra of Surface Compounds* (Wiley, New York, 1975), pp. 217–220; A. V. Kiselev, V. I. Lygin, and Z. G. Khlopova, Zh. Fiz. Khim. **59**, 2878 (1985) [Russ. J. Phys. Chem. **59**, 1725 (1985)].
[35]C. Morterra, S. Coluccia, E. Garrone, and G. Ghiotti, J. Chem. Soc. Faraday Trans. 1 **75**, 271 (1979).
[36]K. Morishige, S. Kittaka, and S. Katsuragi, J. Chem. Soc. Faraday Trans. 1 **78**, 2947 (1982).

The role of Farben centers in electron- and photon-stimulated desorption from alkali halides

G. M. Loubriel and T. A. Green
Sandia National Laboratories, Albuquerque, New Mexico 87185

N. H. Tolk and R. F. Haglund, Jr.
Department of Physics and Astronomy, Vanderbilt University, Nashville, Tennessee 37235

(Received 13 March 1987; accepted 7 May 1987)

Measurements of the time history of ground-state neutral lithium desorption from LiF during pulsed electron irradiation have resulted in a new model for the lithium-desorption mechanism. We show that the slow diffusion to the surface of bulk Farben (F) centers created by the electron-beam is the rate-controlling factor responsible for most of the time history of the lithium desorption rather than the thermal evaporation of the metal from the surface. Comparison between theoretical and experimental time dependencies yields values for the F center diffusion constant and its activation energy.

In our recent papers,[1,2] we report measurements of the time dependence of electron-stimulated desorption (ESD) of neutral ground state Li (Li^0) from a LiF(100) surface during electron-beam irradiation.[1] The data presented in these papers, and the latest results presented here all show that under certain conditions, the emission of Li^0 persists for up to seconds after the excitation pulse. By contrast, the neutral excited lithium (Li^*) desorption is extremely fast (< 100 ns). The contrasting time scales suggest that Li^* and Li^0 are produced by completely different mechanisms and led us to a reconsideration of the delay mechanism presented in the literature for metal atom desorption in the alkali halides.[3] We have explained the persistence of the Li^0 emission after a pulse in terms of the slow diffusion of bulk F (Farben) centers (an electron trapped in a halogen vacancy) created by the electron beam. A quantitative model which describes the bulk diffusion of the F centers and their surface conversion to a desorbed Li atom is used to extract from the data the F center diffusion hopping rate and activation energy, as well as an F center surface residence time. This is the first time that F center bulk diffusion has been connected with delays in metal atom desorption from alkali halides and our results contrast with the generally accepted notion that the thermal desorption of the metal atom from the surface is responsible for the delays.[3] While surface effects are also important, especially at very low temperatures, the data show that at high temperatures the delay in the metal atom signal is entirely due to the F center diffusion time.

In order to put the model into a suitable perspective, the current view of electron- and photon-induced halogen desorption must first be summarized. We follow the description of Szymonski[4] and that of Agullo–Lopez and Townsend.[5] These descriptions are based on more than a decade of electron and photon-stimulated desorption research on alkali halides, and Refs. 4 and 5 cite many of the most significant papers. It will be seen from these that, although the mechanism of desorption seems to be well-understood in its main qualitative outlines, there is still much to understand about all the quantitative reaction mechanisms involved. References 4 and 5 are not in complete agreement on some details of the halogen desorption process. Our model is based, however, on ideas common to both descriptions.

Following Refs. 4 and 5, in a typical desorption experiment, the electron or photon beam deposits energy to a depth up to several hundred angstroms, the most important end result of which is the production of electron–hole pairs. The holes are self-trapped within picoseconds, leading to the formation of V_k centers (An F_2 molecular ion replacing two F ions). On a similar time scale the electrons in the system are captured by the V_k centers to form self-trapped excitons (STE), and are also captured by whatever preexisting acceptor defects and impurities are in the crystal at the time of irradiation. The STE also decay in times of the order of a nanosecond[6] and a decay channel of substantial probability leads to the formation of F center–H center pairs, some of which annihilate mutually, and some of which separate to lead independent lives. An F center is an electron occupying the normal place of a negative halogen ion. An H center is an interstitial neutral halogen atom crowded amongst the negative halogen ions along a (110) line to form what is also known as a crowdion.

According to Refs. 4 and 5, the release of the interstitial halogen atoms from H centers arriving at the surface is the source of halogen desorption. The H centers start their travels in a replacement sequence along the 110 directions containing the F center of the F–H pair. If this collision chain intersects the surface, a nonthermal halogen atom can be ejected on a time scale of < 0.0001 seconds.[7] Otherwise, the H center can thermalize and diffuse around the crystal until it is annihilated, trapped in the crystal, or reaches the surface and releases a thermal halogen atom. It is generally agreed that, when the crystal surface has become nonstoichiometric, excess metal atoms are formed; at sufficiently high temperatures the metal atoms desorb.[4,5,7] The electronic mechanism by which the metal atoms form is not understood at present, but the presence of Li metal in the surface region of electron irradiated LiF at temperatures below 588 K appears to be well established; above this temperature, the Li metal signals disappear,[8] probably due to rapid desorption.

In this paper we accept the description of the halogen de-

 0734-211X/87/051514-05$01.00 © 1987 American Vacuum Society

sorption mechanism sketched above but we note that since an H center incorporates an interstitial halogen atom, the release of its atom does not change the stoichiometry of the surface. The lack of stoichiometry resides in the F centers. Therefore, before the surface can become nonstoichiometric, the F centers must diffuse from their place of creation to the surface. Since H centers are very mobile compared to F centers, it is appropriate to consider that the F center diffusion takes place for the most part after the halogen atoms have left the crystal. This is the physical basis of our model. Thus, the model adds a new source of delay to delays occurring at the surface during the desorption step. This is the delay due to F center diffusion. The phenomenon of F center diffusion at high temperatures is not completely understood at present, although several plausible diffusion mechanisms have been developed.[9-11] Radiation-induced F centers, and the coloring they produce in alkali halide crystals, have been a source of fascination for over 50 years. For this reason, it is very pleasing that the new measurements[1] have uncovered their participation in the electron stimulated desorption process.

Our experimental setup has been discussed previously.[12] An electron-beam is incident along the surface normal on a clean, optically transparent LiF target at $\sim 6\times 10^{-10}$ Torr. The beam current ranged from 10^{-6} to 10^{-4} A and the beam cross section was approximately 0.0025 cm.[2] The LiF(100) target surface was cleaved prior to introduction into the vacuum system and then cleaned by repeated cycles of heating to 770 K and electron bombardment. This heating was repeated between spectra so as to keep the total irradiation time to a minimum (the longest spectrum recorded lasted for about 2 h). For the measurement of Li^0 yields, a laser beam was made to impinge from the back of the sample, collinear with the electron gun, with a strength of 85 μW. The Li^0 atoms are excited by the laser and their decay at ~ 2 mm in front of the sample is detected by optical elements. Analysis of the electron pulse shows that it has a slow time rise but that its cutoff is sharp (between 100 and 400 ns). For this reason we will analyze the effects of the sharp turnoff of the beam. Timing of the fluorescence relative to the electron pulse was achieved by using a time to amplitude converter or a multichannel analyzer for dwell times ranging from 10^{-8} to 10^{-5} s. We did not analyze the velocity of the emitted Li^0 particles prior to the timing of their fluorescence. The reason for this is that if we assume a Maxwell–Boltzmann velocity distribution for the Li^0 atoms, as in other alkali halides,[13,14] the velocity spread can be converted to a spread in time which is smaller than our counting dwell times. The experiments reported here were carried out at 628, 699, and 826 K using a 200 eV electron-beam chopped in a square-wave fashion. The high temperatures minimized the effects of charging on the electron-beam energy. The Li^0 yield following electron beam turnoff is shown in Fig. 1 for a sample temperature of 699 K. The square wave pulse repetition rate was 3.74 ms. These data will be compared with theory after the model is introduced and the necessary notation developed. In a separate experiment we completely turned off a 400 eV electron-beam and with the sample at 675 K observed the decay of the Li^0 yield. The time required for the yield to drop to 10% of its maximum value prior to turnoff was 200 s. Finally we have performed several sets of experiments at varying temperatures and beam energies with electron pulses of 1 μs duration.

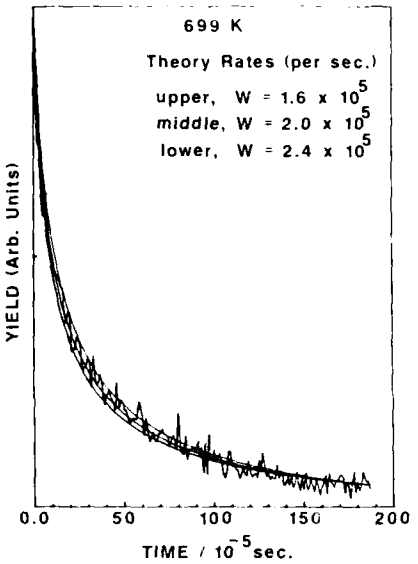

FIG. 1. Time dependence of the drop of the Li^0 yield for a sample temperature of 699 K. The smooth curves correspond to our theoretical fits to the data using different values of the F center hopping rate W and a fixed value of the surface residence time $1/\gamma = 1.67 \cdot 10^{-6}$ s.

The desorption mechanism we propose is illustrated in Fig. 2. First, the electron-beam produces a one-dimensional distribution of F center, H center pairs and the H centers rapidly leave the crystal. Second, each F center diffuses to the surface where it creates a neutral Li atom. Third, the neutral Li atom thermally desorbs. The parameters of the model are a bulk hopping rate W and a surface residence time equal to the inverse of a rate constant γ. The model takes into account the time history of the electron beam. It also uses a depth distribution of defects created in the bulk, previously tested for desorption of halogens,[15] and an experimental range of 61.8 Å for 200 eV electrons.[16] The incorporation of the concepts outlined above into a calculation

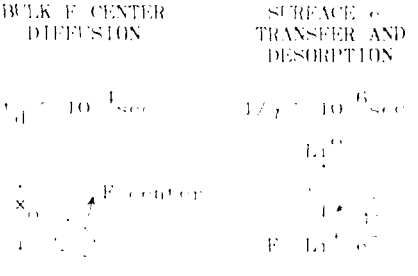

FIG. 2. Mechanism for electron-stimulated desorption of Li^0 from LiF: (1) Electrons penetrate a distance x_0 into the bulk and create F centers that diffuse to the surface in a time t_d. (2) The F center electron is captured by a Li ion. (3) The neutral Li atom desorbs. The time required for steps 2 and 3 is the surface residence time $1/\gamma$, which is much smaller than t_d at the temperatures and electron penetration depths used here.

which can be compared to experiment is somewhat complicated. The method is described at length in Ref. 2. In the following paragraphs we describe the physics of the problem and give a simple example of how the model results in equations that can be compared to experiment.

We will now address the energies involved in our model and, in particular, the energy to desorb Li^0. The calculations we are about to present are very approximate, mainly because most of the required energy levels involved (for example, the binding energy of the F-center electron) are not well-known in the bulk and have never been measured at the surface. The energy required to remove Li^0 has not been measured, but the work of Kawano *et al.*[17] shows that the energy to thermally remove a neutral molecule of LiF from the crystal is 2.91 eV. To remove Li^0 we remove a LiF molecule (2.91 eV), dissociate the molecule (5.95 eV), and replace the F^0 in the crystal (at negligible cost, as first assumed by Mott and Littleton[18]). We have thus expended 8.86 eV to produce Li^0. In order to understand how this energy requirement would change in the presence of an F center, we need to realize that in the case discussed above the electron residing in the desorbed Li atom came from the valence band of the crystal. The cost to remove this electron is the band-gap energy (13.6 eV) plus the electron affinity (~ 1 eV). The energy of the bulk F center's electron in LiF has been estimated to be between 5 and 8 eV.[19] Thus, if the electron that neutralizes the desorbed Li atom starts from an F center we save 8.1 eV, resulting in an energy for desorption of 0.8 ± 1.5 eV. This result shows that it is possible for thermal energies to induce desorption of Li^0 if there are F centers present.

To understand the physics associated with the time dependence of the Li^0 yield, we need to compare the delay caused by the surface residence time $1/\gamma$ to the diffusion time $t_d = (\bar{x}_0)^2/2W$ for the F center to reach the surface from the average penetration depth $\bar{x}_0$, measured in units of the crystal-lattice constant ($\bar{x}_0 = 6$ for 200 eV electrons[2]). Here, W is the bulk F center hopping rate. The importance of $1/\gamma$ and t_d in the time behavior of the desorption can be best illustrated by considering each process independently. If the F center is created in the surface the Li atom can desorb without bulk diffusion and therefore the desorbed Li^0 flux following surface energy deposition decays exponentially with rate γ. For F centers created in the bulk, the surface concentration of F centers is governed by the Green's function for bulk diffusion, that leads to an asymptotic $t^{-3/2}$ power law for the F center concentration. In general we have both surface desorption and bulk diffusion. Intuitively, it is clear that since an exponential decays faster than any given power law, the dependence of the yield at short and long times are mostly governed by surface desorption (γ) and bulk diffusion (W), respectively.

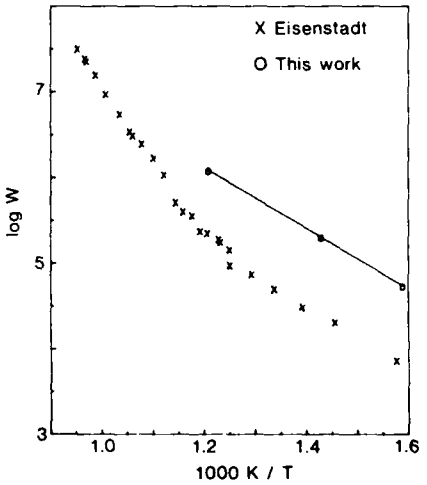

FIG. 3. Arrhenius plot of our best fits for the F center bulk hopping rate W and the data of Eisenstadt (Ref. 21) on the cation vacancy diffusion rate in LiF. As described in the text, the similarity of the activation energies in the low temperature regime (0.7 eV) is consistent with the assignment of an F center as the bulk defect responsible for the desorption.

To illustrate the nature of the solutions to this diffusion problem and their subsequent use in comparing to the data we will assume that the surface desorption time is negligible compared to t_d ($\gamma = \infty$). In this case, for a square electron beam excitation pulse that produces one F center at a depth x_0 between time $t = 0$ and $t = t_0$, the desorbed Li atom flux $\Phi(t)$ is given by

$$\begin{aligned} &\Phi(t) = f(t) \equiv (1/t_0)\mathrm{erfc}\left[(t_d/2t)^{1/2}\right], \quad 0 \leqslant t \leqslant t_0, \\ &\Phi(t) = f(t) - f(t - t_0), \quad t_0 \leqslant t \leqslant \infty, \\ &\Phi(t) \to (t_d/2\pi t^3)^{1/2}, \quad t \to \infty, \end{aligned} \tag{1}$$

where erfc is the co-error function. Equation (1) exhibits the rise and fall of the desorbed Li flux as a result of F center production by the electron beam as well as the asymptotic $t^{-3/2}$ behavior that represents the probability of first arrival[20] at the surface at times $t \gg t_d$. The use of an infinite surface desorption rate in the derivation of Eq. (1) is consistent with the experimental data for the temperatures of 826 and 699 K. At low temperatures (for example, 628 K) $\gamma = \infty$ is incompatible with the experimental data and the full theory is required. Since the electron-beam creates F centers over a distribution of depths x_0, Eq. (1) has to be summed numerically over this distribution in order to compare with the experimental data. For the general case when γ and W are finite, the solutions to the diffusion equation are similar to those in Eq. (1) except that complex error functions are obtained. Also, the asymptotic behavior is identical. The depth distribution of defects and the time history of the electron-beam must again be taken into account.

Returning to Fig. 1, we can now compare the time dependence of the ESD Li^0 yield for a temperature of 699 K, with curves from the model that provide the best-fit value for W and its upper and lower bounds. The fitting is accomplished by adjusting the values of the bulk hopping rate W and the surface desorption rate γ. Since the absolute value of the yield and the background level are not known, the theoretical curves were normalized to the experimental data at the beginning and end of the beam-off period. This constraint does not affect the ability to fit the data since the values of γ and W determine the slopes of the decay at short and long times, respectively (see Ref. 2). We find best fits of $W = 2 \times 10^5\ s^{-1}$ and $\gamma \geqslant 1 \times 10^5\ s^{-1}$ for 699 K. The corresponding delays of $t_d = 0.9 \times 10^{-4}$ s and $\gamma^{-1} < 10^{-5}$ s imply that, at this temperature, bulk diffusion is the rate limit-

ing step. The determination of the best fit is unique within the bounds specified since γ and W mostly affect the yield at short and long times, respectively. In particular, the assumption that the decay is governed solely by surface evaporation of a Li-rich submonolayer surface layer[3] would result in a finite γ of the order of 10^3 s^{-1}, an infinite W, and a consequent exponential behavior that does not fit the data. Also, if during the on part of the beam we had formed many monolayers of a Li-rich layer, the desorption yield in the off period would be roughly independent of time.

Very similar results are obtained at 826 K where we find $W = 1.2\times10^6$ s^{-1} and $\gamma \geqslant 2\times10^5$ s^{-1}. For 699 and 826 K an infinite value of γ is compatible with the data but not at 628 K. At 628 K we find that the surface rates are slow enough to obtain a finite value of $\gamma = 0.7\times10^5$ s^{-1} and $W = 5.4\times10^4$ s^{-1}. Values of γ larger than 3.0×10^5 s^{-1} do not fit the data. This demonstrates that, in general, it is es sential to take the surface processes into account.

The values of W given above result in a temperature dependence given by $W = W_0 \exp(-U/kT)$, where W_0 is a temperature independent preexponential, k is Boltzman's constant, T is the absolute temperature, and $U = 0.7 \pm 0.3$ eV. A plot of $\ln(W)$ vs $1000/T$ is shown in Fig. 3. It is important to compare these results with previous data on LiF. The activation energy for F center diffusion has not been measured directly. To determine if the value of 0.7 eV obtained for the activation energy of the bulk defect is compatible with the assignment of the F center as the bulk defect we will use the model of Kalnin *et al.*[9] This model is designed to explain F center diffusion at temperatures where the number of thermally produced vacancies is smaller than those produced by divalent metal impurity ions (the extrinsic, im-

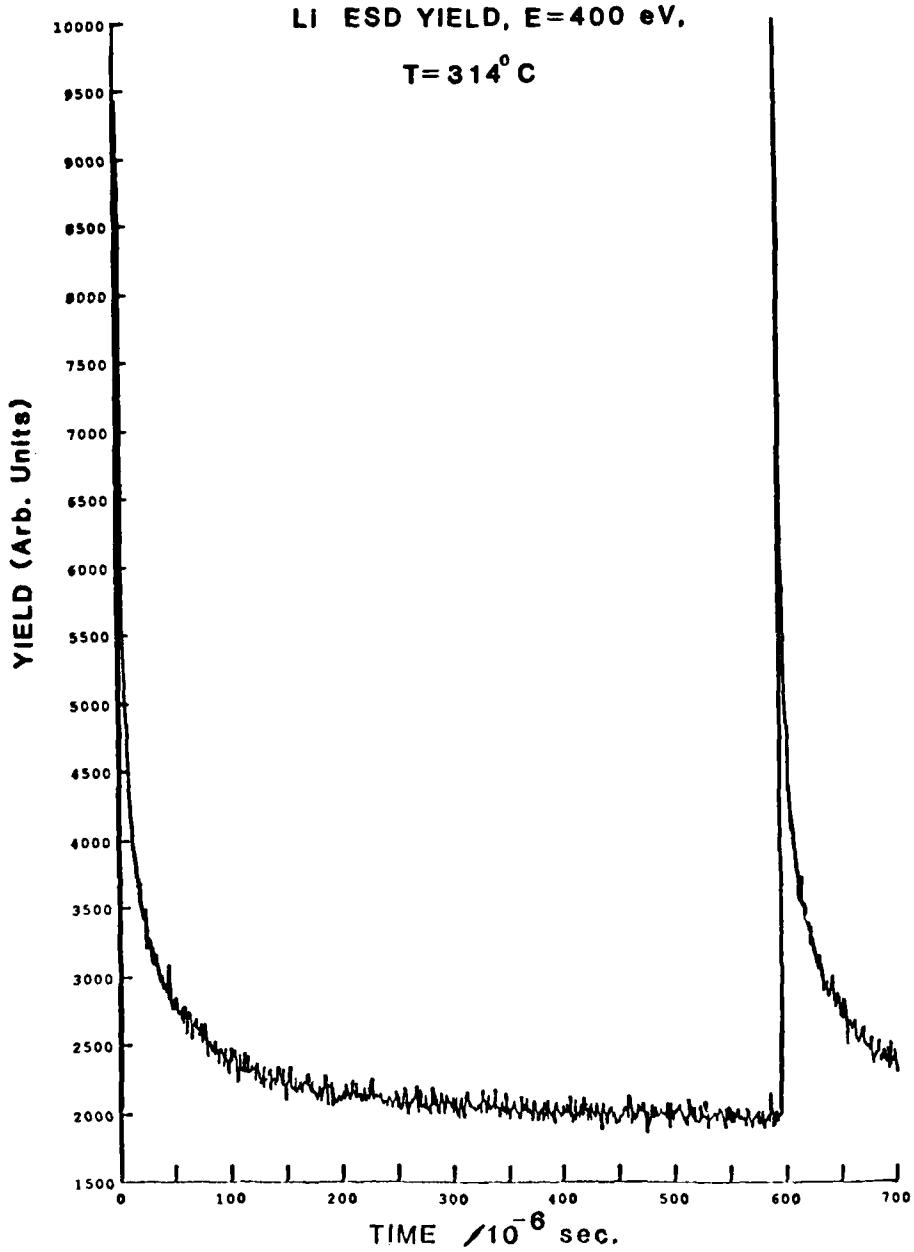

FIG. 4. Time dependence of the Li^+ yield from 1 μs duration electron pulses of 400 eV energy.

purity regime). For low-impurity densities, their model implies that the F center hopping rate is proportional to the product of the density of divalent impurity ions and the cation vacancy hopping rate. For this reason, if the diffusing entity is an F center, the activation energies for W and the cation vacancy diffusion constant should be equal. As is seen from Fig. 3, the activation energy for W and that of the cation vacancy diffusion[21] are the same. We can also test that we are in the impurity regime by using the model of Kalnin and our values of W to obtain the concentration of divalent impurities.[1,2] This concentration we obtain is indeed larger than the concentration of thermally produced anion–cation vacancy pairs.

We have further tested our model by examining the asymptotic behavior of the yield after electron pulses of 1 μs duration. This was achieved at a temperature of 673 K for beam energies of 100, 200, 250, and 400 eV and at a beam energy of 400 eV for temperatures of 587, 624, 673, 697, 721, and 771 K. Figure 4 shows the Li^0 desorption yield that follows these μs duration pulses for a temperature of 587 K and a beam energy of 400 eV. Our fits to this data are as good as the best fit shown in Fig. 1 and hence shows that the model can account for the time behavior and, in particular, the long time decay. The asymptotic $t^{-3/2}$ regime is not yet probed in the first 0.6 ms of the decay, mostly due to the increased penetration of the 400 eV electrons compared to the 200 eV data previously presented, but the important point shown is that the decay is not exponential. The results of desorption of Li^0, following the 1 μs pulses also tests the applicability of the model to cases where the duty cycle of the beam, and the F center damage, is small.

In summary, we have made new time-resolved measurements of ESD of Li^0 from a LiF(100) surface. The time dependence of the flux in the beam-off period is consistent with the delay observed in the metal desorption being primarily due to the diffusion of F centers produced in the bulk by the electron-beam. At the high temperatures discussed here, the surface desorption rate, by contrast, is very fast and only affects the flux at very early times. This new insight into the mechanism for metal atom desorption suggests a number of new directions for experimental and theoretical work.

ACKNOWLEDGMENTS

That portion of the work performed at Sandia National Laboratories was supported by the U.S. Department of Energy under Contract No. DC-ACO4-76DP00789. The work performed at Vanderbilt University was partially supported by Sandia National Laboratories under Contract No. 65-2377.

[1] G. M. Loubriel, T. A. Green, P. M. Richards, R. G. Albridge, D. W. Cherry, R. K. Cole, R. F. Haglund, Jr., L. T. Hudson, M. H. Mendenhall, D. M. Newns, P. M. Savundararaj, K. J. Snowdon, and N. H. Tolk, Phys. Rev. Lett. **57**, 1781 (1986).
[2] T. A. Green, G. M. Loubriel, P. M. Richards, N. H. Tolk, and R. F. Haglund, Jr., Phys. Rev. B **35**, 781 (1987).
[3] Y. Al Jammal and P. D. Townsend, J. Phys. C **6**, 955 (1973).
[4] M. Szymonski, Radiat. Eff. **52**, 9 (1980).
[5] F. Agullo-Lopez and P. D. Townsend, Phys. Status Solidi B **97**, 575 (1980).
[6] R. T. Williams, W. L. Faust, and B. B. Craig, Cryst. Lattice Defects Amorph. Mat. **12**, 127 (1985).
[7] H. Overeijnder, R. R. Tol, and A. E. DeVries, Surf. Sci. **90**, 265 (1979).
[8] G. Singh and T. E. Gallon, Solid State Commun. **51**, 281 (1984).
[9] Yu. Kh. Kalnin and Z. S. Itzkovich, Sov. Phys. Solid State **16**, 1986 (1975).
[10] G. C. Kuczynski and J. J. Byun, Phys. Status Solidi B **50**, 367 (1972).
[11] E. L. Wolf, Phys. Rev. **142**, 555 (1966).
[12] R. F. Haglund, Jr., R. G. Albridge, D. W. Cherry, R. K. Cole, M. H. Mendenhall, W. C. B. Peatman, and N. H. Tolk, Nucl. Instrum. Methods Phys. Res. B **18**, 549 (1987).
[13] H. Overeijnder, M. Szymonski, A. Haring, and A. E. de Vries, Surf. Sci. **90**, 265 (1979).
[14] N. H. Tolk, R. F. Haglund, Jr., M. H. Mendenhall, E. Taglauer, and N. G. Stoffel, *Desorption Induced by Electronic Transitions, DIET II*, edited by W. Brenig and D. Menzel (Springer, New York, 1984), p. 152.
[15] Y. Al Jammal, D. Pooley, and P. D. Townsend, J. Phys. C **6**, 247 (1973).
[16] I. M. Bronshteyn and A. N. Protsenko, Radio Eng. Electron. Phys. **15**, 677 (1970).
[17] H. Kawano, T. Kempo, H. Koga, Y. Hidaka, and M. Suga, Int. J. Mass Spect. Ion Phys. **47**, 265 (1983).
[18] N. F. Mott and M. J. Littleton, Trans. Faraday. Soc. **34**, 455 (1938).
[19] B. S. Gourary and F. J. Adrian, Solid State Phys. **10**, 127 (1960).
[20] W. Feller, *An Introduction to Probability Theory and Its Applications* (Wiley, New York, 1968), Vol. 1.
[21] H. Eisenstadt, Phys. Rev. **132**, 630 (1963), Fig. 4.

Summary Abstract: Laser etching and evaporation of CaF_2 studied by mass spectrometry

R. C. Estler,[a] J. E. Anderson, E. C. Apel, and N. S. Nogar
Chemical and Laser Sciences Division, Los Alamos National Laboratory, Los Alamos, New Mexico 87545

(Received 27 February 1987; accepted 7 May 1987)

Experimental studies of laser etching (sputtering) in optical materials have traditionally concentrated[1] on phenomenology of the process: etching thresholds, and physical and bulk material properties effecting these thresholds. More recently, considerable attention[2,3] has been given to the etching mechanisms and to the molecular phenomena associated with the etching process.

In this work we describe a study of the interaction of relatively high-influence laser pulses ($\phi \geqslant 10$ J/cm^2) with a (nominally) transparent optical medium. We have used both conventional electron impact ionization (with quadrupole mass discrimination) and RIMS (resonance ionization mass spectrometry) with time-of-flight detection as diagnostics for investigating the sputtered material produced from laser–solid interactions. RIMS[4] is a form of laser-ionization mass spectrometry which takes advantage of available laser-based multiphoton ionization schemes for the selective detection of atoms and small molecules. CaF_2 was chosen for this study since it is a common dielectric used in UV and some vis-IR optics, and may be treated as a prototype system for these studies. The objective of this work was to obtain information about the laser–solid interaction through measurement of the chemical and velocity distributions of the particles ejected from the surface during the etched (optical damage) process.

All experiments were monitored by mass spectrometry, using one of two mass spectrometer/ionization systems: a quadrupole apparatus equipped with electron impact ionization, and a time-of-flight apparatus in which multiphoton photoionization was used. Optical damage was initiated by either the fundamental (1.06 μ), or frequency tripled (355 nm) or quadrupled (266 nm) output of a Nd^{+3}:YAG laser (quanta ray/spectra physics model DCR 1A). The laser was equipped with filled-beam optics, and produced a beam whose spatial profile is somewhat more sharply peaked than for a Gaussian beam. The Q-switched output was 10 ns full width at half-maximum (FWHM) in duration, and smooth within the resolution of our electronics ($\approx$2 ns).

For the quadrupole study, primary ions produced in the damaging event were detected by turning off the electron impact ionizer while survey electron impact spectra, indicative of spalled neutrals, were typically acquired at an energy of 75 eV. Spectra were acquired and compared for each of the above conditions. Even allowing for a reduced detection efficiency for ions formed outside the normal ionization region, we estimate the ratio M/M^+ to be $\geqslant 100$.[5]

Among the impurities routinely observed in the electron impact mass spectra are a large peak at 44 a.u., presumably CO_2, a peak at 28 due to CO (or N_2), the water group at 16, 17, and 18 a.u., and a very weak signal at 12 a.u. We have not determined the identity of this last constituent, but it is a frequently observed signal in this apparatus. These results are consistent with the known[6,7] tendency of water to adsorb on CaF_2 surfaces.

Results from the laser damage/laser ionization experiments in the ToF mass spectrometer yield significant additional information. First, since the multiphoton ionization process is resonantly enhanced, the excitation (ionization) spectrum can be used to determine the precursor for a particular ion. And second, by varying the time delay between the damage and interrogation pulses, the velocity distribution of the spalled material can be obtained.

The Ca^+ observed in the laser ionization experiments is produced from atomic Ca by a "2 + 1" (photons to resonance + photons to ionize) process[8] through the enhancing $^1P_0^0$ state at 37 298 cm^{-1}. Similarly, the CaF^+ observed in this set of experiments is derived from CaF by a 2 + 1 ionization process through the F $^2\Pi$ state ($T_0 = 37\,550$ cm^{-1}). These particular ionization paths were chosen so that both species could be detected with the same laser dye. While these results indicate that at least some of the ablated material is directly spalled as Ca and CaF, we have no direct evidence as to what fraction spalls are fragments, and what fraction as CaF_2 molecules. Neither the previously mentioned electron impact spectra, nor the optical ionization currently under discussion is sensitive to CaF_2. We can only infer from thermal vaporization studies[9,10] that a substantial fraction is likely to evaporate as molecules.

Additional information was obtained by measuring both the internal and translational energy distribution of the spalled Ca and CaF. Velocity distributions were measured by varying the time delay between the damage and ionization (probe) lasers. The internal energy content of the CaF radicals was probed by varying the wavelength of the ionization (dye) laser, so that an excitation spectrum was obtained. Damage was initiated at the fundamental (1.06 μ), and frequency tripled (355 nm) and quadrupled (266 nm) wavelengths. The results were found to be dependent on wavelength and may be summarized [8] as follows:

(a) For 1.06 μ irradiation, we observed thermal (850 K) velocity distributions for both Ca and CaF. In addition, the CaF radical exhibited significant amounts of internal (rotational and translational) excitation, consistent with an internal "temperature" of $\approx 10^3$ K.

(b) For both 355 and 266 nm irradiation, the velocity distributions were bimodal, Fig. 1, with a fraction ($\leqslant$50%) of the spalled material exhibiting very high (4000 K) kinetic temperatures, while the remainder exhibited a temperature

 0734-211X/87/051519-02$01.00 © 1987 American Vacuum Society

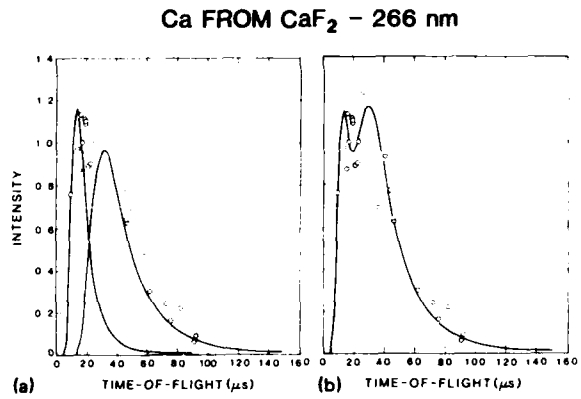

FIG. 1. Optical time-of-flight distribution (O) for Ca spalled from CaF_2 surface at 266 nm, 15 J/cm^2: (a) shows individual fast (4000 K) and slow (850 K) components for comparison with data; (b) shows overall composite fit of fast (33%) and slow (67%) components.

similar (800–1000 K) to that observed for the 1.06 μ experiments. Note that the flight times exhibited in Fig. 1 are for optical time-of-flight (from CaF_2 surface to interrogation zone) and *not* the flight time in the mass spectrometer flight tube. In addition, both the vibrational and rotational temperatures of the CaF radicals decreased with decreasing damage wavelength.

In conclusion, our observations indicate that in the damage event the overwhelming majority material is ablated as neutrals ($M/M + > 100$). In addition, our results do not necessarily point to a single mechanism in the initiation of the breakdown event, but are significant from the standpoint that a change in mechanism, i.e., an opening of a second channel at high photon energy, is indicated. The kinetic temperatures and qualitatively similar estimates of the CaF internal energies observed at 1.06 μ argue for a thermal or sonic mechanism, possibly initiated by avalanche breakdown. In addition, it is tempting to speculate that absorption at this long wavelength is due to a physical or chemical defect in the substrate, since direct excitation of the crystal would imply simultaneous absorption of a large number of photons. The results at shorter wavelengths suggest a more direct photophysical interaction, where rapid energy deposition is followed by nonadiabatic transitions of the fragments to antibonding states.[11,12] Such a mechanism can lead to the nonequilibrium of the various degrees of freedom observed here and also to a nonisotropic angular distribution of products.

[a] Permanent Address: Department of Chemistry, Fort Lewis College, Durango, Colorado 81301

[1] J. F. Ready, *Effects of High-Power Laser Radiation* (Academic, New York, 1971).
[2] W. L. Smith, Opt. Eng. **17**, 489 (1978).
[3] R. Kelly, J. T. Cuomo, P. A. Leary, J. E. Rothenberg, B. E. Braren, and C. F. Aliotta, Nucl. Instrum. Methods B **9**, 329 (1985).
[4] N. S. Nogar, R. C. Estler, and C. M. Miller, Anal. Chem. **57**, 2441 (1985).
[5] R. C. Estler, E. C. Apel, and N. S. Nogar, in Proceedings of the Symposium Laser Induced Damage in Optical Materials, Boulder, CO, 1986.
[6] E. D. Palik, J. W. Gibson, and R. T. Holm, Surf. Sci. **84**, 164 (1979).
[7] S. D. Allen, J. O. Porteus, W. N. Faith, and J. B. Franck, Appl. Phys. Lett. **45**, 997 (1984).
[8] R. C. Estler, E. C. Apel, and N. S. Nogar, J. Opt. Soc. Am. B **4**, 281 (1987).
[9] F. J. Himpsel, U. O. Karlsson, J. F. Morar, D. Rieger, and J. A. Yarmoff, Phys. Rev. Lett. **56**, 1497 (1986); U. O. Karlsson, J. F. Morar, F. R. McFeely, D. Rieger, and J. A. Yarmoff, *ibid.* **57**, 1247 (1986).
[10] G. D. Blue, J. W. Green, R. G. Bautista, and J. L. Margrave, J. Phys. Chem. **67**, 877 (1963).
[11] E. B. D. Bjourdon, J. P. Cowin, I. Harrison, J. C. Polanyi, J. Segner, C. D. Stanners, and P. A. Young, J. Phys. Chem. **88**, 6100 (1984).
[12] B. Jost, B. Schueler, and F. R. Krueger, Z. Naturforsch. Teil A **37**, 18 (1982).

Energy deposition at insulator surfaces below the ultraviolet photoablation threshold

R. W. Dreyfus, F. A. McDonald, and R. J. von Gutfeld
IBM T. J. Watson Research Center, P. O. Box 218, Yorktown Heights, New York 10598

(Received 14 February 1987; accepted 7 May 1987)

A surface deformation technique measures the energy deposited in sapphire and other surfaces upon irradiation by focused excimer laser light. For sapphire, the thermal deformation indicates a linear dependence of absorbed energy on excimer fluence with about 3% of the incident light absorbed per surface at 193 nm. Just below etching threshold this absorbed energy should raise the surface temperature to about 430 K, an insufficient temperature for ablation of Al_2O_3 by thermal vaporization. In contrast the absorbed energy creates $\lesssim 3$ electron–hole pairs/oxygen atom, consistent with a photochemical (electronic type) etching process.

I. INTRODUCTION

One of the basic problems in understanding laser etching is knowing the amount of energy deposited (absorbed) on the surface and the resulting surface temperature. For temperatures sufficiently high to generate vapor pressures $\gtrsim 1$ bar, etching can proceed as a purely thermal process. On the other hand, if the temperature during etching barely exceeds room temperature, direct photochemical decomposition is responsible.[1] The studies of the etching mechanisms of sapphire and polymers are particularly interesting since these two materials have low-vapor pressures but nevertheless require only relatively low UV fluences to bring about etching. In this respect, it is of interest to understand why essentially transparent materials like sapphire are so easily etched by short wavelength UV irradiation.

While there has been an extensive number of techniques applied to surface temperature determinations, the majority of these suffer from interference caused by the dynamical and irreversible nature of laser etching. Untoward dynamical effects that have repeatedly appeared include excimer or probe beam interactions with the etch plume. A second area of complication is knowledge of the relevant physical parameters, e.g., thermal conductivity or optical absorption, which are often in question during large dynamical excursions in both temperature and free electron density.

One of the techniques which avoids the above complications is laser-induced fluoresence (LIF): LIF measures the energies (temperatures) of diatomic species in the etch plume after expansion.[2] It is a basic premise of this approach that the population distribution among high-lying vibrational and rotational states correctly reflects the energies of these species as ejected from the surface. While these internal energies appear to give valid numbers for the surface temperature (as proven by the photothermal etching of graphite),[3] temperatures determined from internal energies do not complete the picture in two areas: collisional effects for dipolar diatomics can only be deduced (not proven conclusively) to be insignificant, and optical energy absorption mechanisms which lead to etching cannot be identified from these experiments, as measurements within the etch are obviously an above-threshold observation.

The present work describes the use of a pulsed photothermal deformation (PPTD) technique to obtain values for surface energy deposition by measuring the thermal deformation of thin samples under pulsed irradiation from an excimer laser.[4,5] In Sec. II we describe three-dimensional thermoelastic calculations from which we obtain the surface deformation corresponding to a given energy deposition, as a function of time. In the PPTD technique (detailed in Sec. III) the surface deformation is detected through the angular displacement of a HeNe laser beam reflected from the sample surface near the edge of the irradiated area.

The results of Secs. II and III are summarized as follows: essentially coincident with the UV laser pulse, local thermal expansion produces direct surface displacement over the optical absorption depth. This can be viewed as a perpendicular (to the surface plane) dilation with fast response due to its compressional nature and small dimensions within the sample. This is immediately followed by (usually small) surface distortions due to (tangentially) propagating bulk and surface waves. The maximum signal, however, is obtained in the time regime (typically 0.1–10 μs) in which bending of the thin sample as a whole ("plate motion") occurs.[6] This latter motion can be compared to flexural bending (if one were dealing with a barlike sample in two dimensions) and hence this motion displays the slow response times associated with flexure.

In Sec. IV A we describe initial experiments used to maximize the large platelike bending deformation, validate the theoretical analysis, and evaluate edge effects. This signal has the advantage of being primarily sensitive to surface absorption relative to small bulk absorption. In addition to the fluence leading to ablation and the energy actually deposited in the surface, one determines whether one or multiphoton absorption in the surface region dominates, as shown in Sec. IV B. It is also possible to correlate the present subthreshold conditions with results[2] that have been previously obtained at fluences just above threshold, as discussed in the case of sapphire samples (Sec. V). The ultimate objective is to obtain a detailed model of the near-threshold etching physics.

II. THEORY

The theoretical model for pulsed photothermal deformation[7] applies standard three-dimensional thermoelastic the-

 0734-211X/87/051521-07$01.00 © 1987 American Vacuum Society

ory for isotropic solids[8] to the case of an infinite plate of finite thickness, having stress-free boundaries and no thermal conduction to the surrounding gas. Laplace and Hankel transform techniques are used with numerical inversion to minimize simplifying assumptions. In particular, the exciting laser pulse has an assumed temporal variation typical of such pulses, with a 5 ns rise to peak and a somewhat slower decay time; the spatial variation of the pulse intensity is taken as Gaussian with a radius of 0.5 mm (the numerical values are those for the present calculations). The model calculations have been shown to agree quite well with experimental data (see Sec. IV A and Ref. 4).

The characteristics of the PPTD signal which are important in the present application are its time variation, its dependence on sample thickness and its relatively large sensitivity to surface absorption vis-a-vis bulk absorption. The first two characteristics are illustrated in Fig. 1, for polymer samples having the following material properties: thermal conductivity equal to 1.6×10^{-3} W/cm °C, thermal diffusivity equal to 1×10^{-3} cm^2/s, longitudinal and shear acoustic velocities of 2×10^5 and 1×10^5 cm/s, respectively, thermal expansion of 4×10^{-5} °C^{-1}, and optical absorption coefficient equal to 2×10^5 cm^{-1} (the laser pulse central fluence is assumed to be 1×10^{-2} J/cm^2). The calculated surface slope (to which the signal is proportional) is shown in log–log form, in order to display both early and later time behavior. At early times the surface deformation is dominated by local thermoelastic expansion, viz., expansion due to local heating of the sample. In this regime the signal is clearly independent of sample thickness. At later times, however, a much larger deformation occurs as a result of bending of the sample as a whole, caused by differential thermal stresses resulting from heating of the sample primarily near the front surface. This deformation decays very slowly because of the inherent slowness of thermal diffusion. The magnitude of the "plateau" signal is inversely related to sample thickness. Also, Fig. 1 demonstrates why the plateau signal is used to characterize absorption: this signal is one-to-two orders of magnitude greater than the local expansion signal, it can be increased by using thin samples, and it is stable over a considerable time. (Small perturbations of the signal occur at intermediate times, due to propagating surface and bulk deformations.)

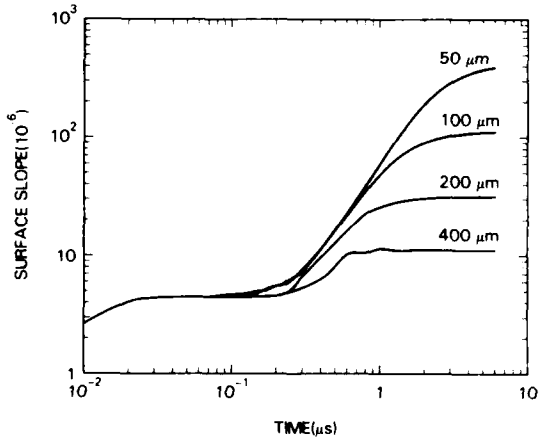

FIG. 1. Calculated surface slope of polymer samples with various thicknesses (as labeled) and subjected to 1×10^{-2} J/cm^2 laser fluence.

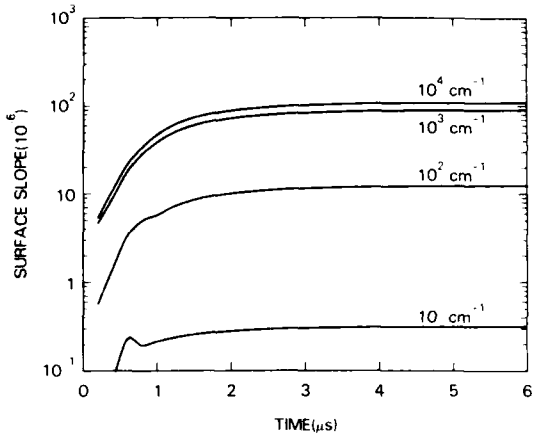

FIG. 2. Similar to Fig. 1; however, for polymer samples of 125-μm thickness, but having various optical absorption coefficients (as labeled).

The sensitivity of PPTD to absorption at or near the surface is suggested by Fig. 2. The plateau signal increases with the absorption coefficient, since the heating is more localized near the front surface, and the differential thermal stress is thus greater. In the direction of decreasing absorption constant, symmetry arguments imply that the PPTD signal from plate bending approaches zero as the heating becomes uniform in the thickness direction, even for a laterally nonuniform beam. This is evident in Fig. 2 as the deformation drops more rapidly than linearly for small bulk absorption, cf. the 10 cm^{-1} curve. Hence a small surface absorption can dominate the signal when the bulk absorption coefficient is small.

The energy absorbed "at" a surface of an otherwise weakly absorbing sample can be inferred by using a strongly absorbing sample of the same thickness for calibration. The model calculations enable a comparison between the signals for "surface" absorption of all the incident energy by the two samples (viz., accounting for the differences in thermal and elastic properties). A comparison of such calculated signals for four different materials is given in Table I. From these data the fraction of the incident energy actually absorbed can be deduced, assuming that the contribution from bulk absorption is small. In the present application, a silicon sample, strongly absorbing in the ultraviolet, is used to calibrate the surface absorption of sapphire, which has a very small bulk absorption coefficient in this same wavelength range.

TABLE I. Calculated PPTD peak signals (surface slope) for 125-μm-thick samples of four materials assuming surface absorption and 1×10^{-2} J/cm^2 laser fluence.

Silicon	5.2×10^{-6}
Sapphire	7.5×10^{-6}
Polymer	7.0×10^{-5}
Glass	1.1×10^{-5}

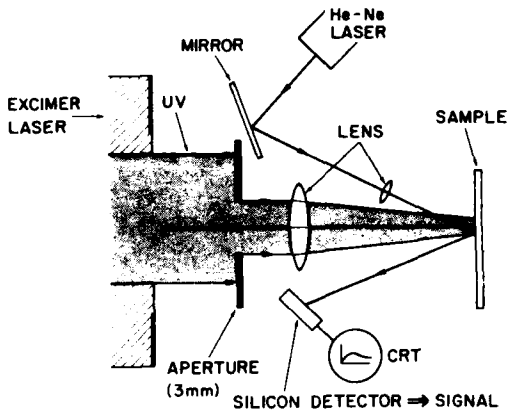

FIG. 3. Schematic illustration of the optical arrangement for detecting pulsed photothermal deformation (PPTD) of surfaces. The HeNe lens has a focal length of 60 cm; the Suprasil™ excimer lens has a focal length of 20 cm at 248 nm. The silicon detector is ~ 1 m from the surface.

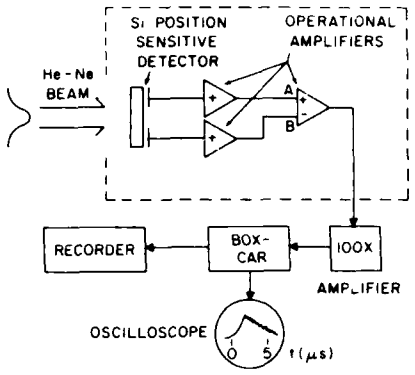

FIG. 4. Schematic illustration of the signal processing electronics for the PPTD measurement. The oscilloscope trace indicates a maximum in the (plate bending mode) deflection near 1 μs; the exact time dependence is a function of sample thickness and elastic and thermal properties.

III. EXPERIMENTAL ARRANGEMENT

The optical portion of the experimental arrangement is shown in Fig. 3. Light from the etching laser (5 ns rise, ~ 15 ns fall times) is directed through a 3-mm aperture and Suprasil™ focusing lens onto the samples. Sets of calibrated attenuators control the excitation fluence. The excimer wavelength is shifted by altering the gas mixture:ArF(193 nm), KrF(248 nm), and XeF(351 nm). A cw HeNe laser beam (4 mW) is focused onto the samples and positioned onto the shoulder of the UV-irradiated area (ranging from 9×10^{-4} to 3×10^{-2} cm^2 and slightly elliptical in shape). The HeNe-probe-beam diameter is about 200 μm. Angular deflection of the probe beam senses the thermal deformation of the sample surface. The theory given in the previous section is used to provide a value for the *relative* sensitivity of different materials (commonly silicon versus sapphire). Experimentally one compares the unknown absorption of sapphire to the results for silicon under similar experimental conditions. In this way one obtains a quantitative result for the UV absorbed in the sapphire (whose characteristics are unknown).

As shown in Fig. 4, the PPTD signal is processed in the following steps. First, the HeNe probe beam is detected with a position-sensitive detector[4] in order to minimize noise from the HeNe laser while retaining high quantum efficiency, and to minimize shot noise. After amplification and substraction of the two PPTD signals, the net value is recorded using a boxcar amplifier set to average over the time period (typical window of $\lesssim 1$ to $\sim 6\,\mu$s) during which the bending mode is maxium. Between 10^2 and 10^3 UV laser pulses are averaged for one datum point. In doing so, no hysteresis is observed involving the sequence of deformation versus fluence data points so long as the etching threshold is not exceeded. Etching is quite evident in the TV monitor displaying an enlarged image of the excitation and probe beam positions on the sample surface. The background noise signal is equivalent to ~ 20 nJ absorbed in the case of 250 μm silicon samples and ~ 50 nJ for sapphire (due to the lower HeNe-beam reflectivity).

While the differences in magnitude between silicon and sapphire PPTD responses have been calculated (Sec. II) and hence compensated, there exist two other sources of uncertainty that are not easily evaluated. The first involves (possible) coherence effects of the excimer laser with the sapphire sample. As noted in Fig. 5, we attribute the surface sensitivity to asymmetry in the optical electric field, E,

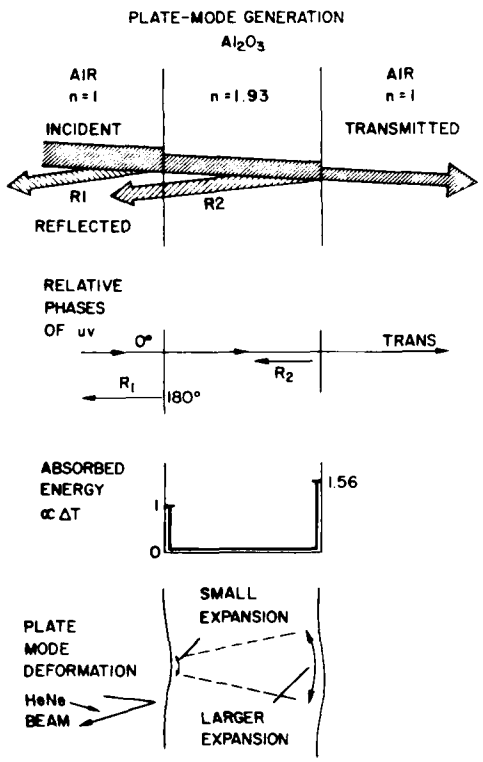

FIG. 5. Schematic of the excimer-beam interaction with a sapphire sample. Primarily it is to be noted that a maximum in the optical E field occurs just inside the exit face, see also Ref. 7. The result is that the maximum surface optical absorption is at the exit face, and hence the sample becomes convex to the right-hand side.

whose magnitude depends on whether an air→sapphire or sapphire→air interface is encountered. That there exists a maximum in E at the exit face has been recognized for some time.[9] Referring again to Fig. 5, this asymmetry does not completely answer the question of the phase of the second surface reflection when it returns to the first surface. We make the assumption that phase coherence is lost or averaged out by the time the reflected excimer beam has reached the front surface. Following this assumption, we calculate the back surface energy absorption to be 56% greater than that of the front surface.[10] As mentioned before, it is this asymmetry between the surfaces that drives the plate-bending mode of deformation. In using this macroscopic E field model, it is also implicit that we assume the surface absorbing species is imbedded in a homogeneous medium with the bulk index of refraction. Because we do not at this stage have a microscopic model for a sapphire surface, we shall ignore the fact that the index of refraction may be depth dependent. If the index variation involves depths $\ll \lambda/4$ the effect on the relative surface absorption is negligible. Interference effects on the HeNe probe beam are much less of a problem as the long optical path to the silicon detector allows one to separate the images of the front and back surfaces. Overall, in consideration of the coherence effects, we estimate that the absolute absorbed energy calibration has an uncertainty of about a factor of 2. The relative absorbed energy points have much less uncertainty, $\sim \pm 10\%$, since here one deals with a specific sample area and any coherence interference effects will be constant. As will become apparent, however, an absolute calibration to within a factor of 2 and a relative calibration for one run of $\pm 10\%$ are more than sufficient to answer our basic questions. The $\pm$ 10% accuracy arises from HeNe intensity fluctuations, shot noise, and limitations in the calibration of the filters used to attenuate the incident UV fluence.

The samples are as follows: The silicon samples are standard ⟨111⟩ orientation, 250 μm thick, electrochemically polished wafers. The sapphire samples were 250 or 100-μm-thick sapphire (Insaco Co.) with the c axis oriented in or near the surface plane. Standard preparation for the sapphire was a 3 h anneal in air at 1500 K, cf. Ref. 11. Chemical etching was utilized as noted; the chemical etchant was a hot phosphoric/chromic acid mixture.[12] Data were normally obtained with the samples in ambient air. An argon atmosphere, however, produced no change in the data, thus showing that the chemical reactivity of the gas environment has no direct influence on the PPTD signal. The polymer samples were free standing polyimide films ranging from ~12 to 125-μm thickness (Kapton H, Dupont Co., Wilmington, DE). Thick glass samples were also compared to the polyimide samples.

IV. EXPERIMENTAL RESULTS

A. Deformation modes of polymer and glass samples

A typical oscilloscope trace for a free standing thin polyimide sample, 125 μ thick, attached to a frame at its periphery is shown in Fig. 6(a). The detected signal changes immediately (to within the rise time of the system) upon absorption of the UV radiation (absorption depth approximately 400

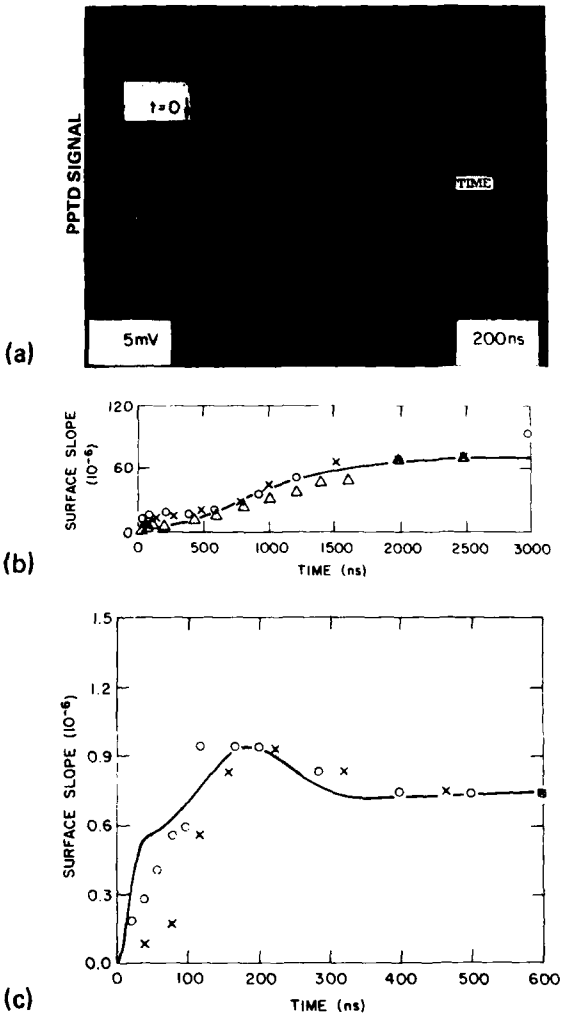

FIG. 6. (a) Oscilloscope traces of the PPTD signal from a 125-μm-thick polyimide sample excited by a UV pulse with fluence of ~8 mJ/cm^2. The probe beam is positioned on opposite sides of the UV beam for the two traces, thereby reversing the sign of the signal. (b) Experimental data for free standing polyimide of 50-μm thickness. The symbols represent data for runs made with different samples. The data is normalized to the theoretical value at $t = 2.0$ μs. (c) Similar to (b) but for a 3-mm-thick Pyrex and normalized at $t = 0.6$ μs.

Å) and corresponds to local thermal expansion of the sample. The signal remains nearly constant for a time much longer than the pulse width of the excitation beam because only lateral heat leak or cooling by the ambient atmosphere will lead to a decrease in the expansion. The second regime, i.e., the effect of surface and bulk waves, is not readily visible here because the third regime, bending of the front and back surface in parallel, is so large that the latter effect dominates. The signal rises to values at least one to two orders of magnitude higher than that due to the initial thermoelastic expansion. In Fig. 6(b) we show the results of experimental data, again for the 125-μm-thick sample normalized to fit the calculated results at a particular time, $t = 2.0$ μs. From the close fit we see that theory and experiment are in good agree-

ment over this range of time scales. For contrast we show the PPTD data plotted with the theoretical results for a 3-mm-thick Pyrex sample. We see the maximum signal obtained is much smaller because no plate mode can occur. Instead only regimes 1 and 2 occur and good agreement with the theory is again evident. To illustrate in greater detail the effects of thickness we swaged a thin polyimide sample onto a thick polymer block and found the photoacoustic behavior to be very much like that observed for the thick pyrex sample, Fig. 6(c). Measurements on several polyimide samples of varying thickness indicate an approximately inverse linear dependence over the range measured shown in Fig. 7.

To study the effect of acoustic waves reflected from physical boundaries we designed a special sample holder which could be moved to permit a variable distance between the optical excitation spot and reflecting boundary. Figure 8 shows two sets of data, one for the excitation located 1 cm from the nearest boundary, the other for a spacing of only 0.15 cm. It is clear that reflected waves are observed in the decay of the latter, not found in Fig. 8(a). These perturbations in the decay signal of Fig. 8(b) are noted only after ~ 3 μs and correspond to reflected acoustic waves traveling at $\sim 1 \times 10^5$ cm/s and certainly do not interfere with any of the early part of the signals such as those shown in Fig. 6.

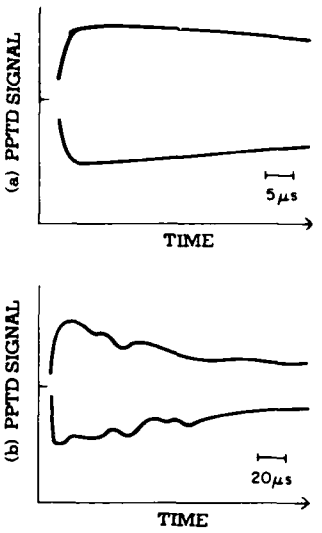

FIG. 8. (a) and (b) Oscilloscope traces showing the absence of edge effects 1 cm from an edge [see (a)] and effect of edge [in (b)] when 0.15 cm from an edge.

B. Sapphire samples

The PPTD signal in Fig. 9 shows a significant absorption (up to 3% of the incident energy) on the sapphire surfaces. To understand the origin of this relatively large absorption requires answers to the following: is this a surface absorption, what is the wavelength and power dependence of the absorbed energy and can the UV absorption be altered by sample treatment?

Figure 9 shows a decrease in absorption as the wavelength increases from 193 to 248 nm and then to 351 nm. Note that the fraction of incident energy absorbed at any wavelength remains constant regardless of fluence. The data thus clearly indicate the signal to be a *linear* function of laser power (below power densities giving rise to ablation), see also Table II. The observed linear dependence is typical for a primarily one-photon absorption process. Figure 10 and Table II show that the large absorption characterizing the as-received and annealed-only samples can be significantly reduced by etching, particularly when long-etch times are involved. This reduction in absorbed energy with etching did not require sample annealing; nevertheless annealing plus etching resulted in the largest decreases.

The observed dependence of the PPTD signal on surface condition is one factor in proving that the signal arises from a surface absorption; other factors are as follows: First, the sign of the sapphire deformation was opposite that of silicon under similar probe beam positioning with respect to the excimer beam (Fig. 3). This reversal in polarity is expected for an absorption located predominately on the back surface (Fig. 5). Second, the thin (100 μm) sapphire samples exhib-

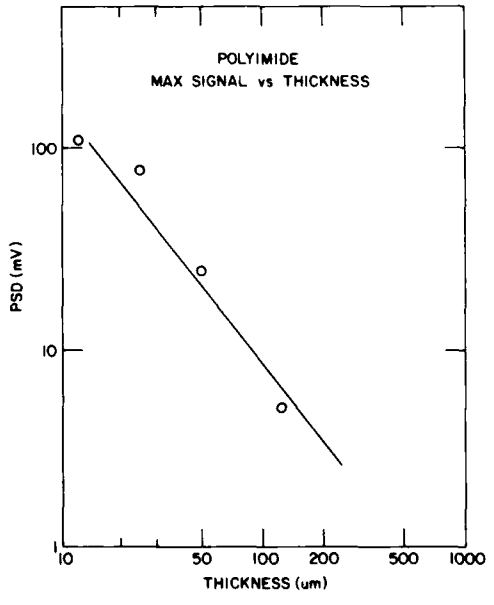

FIG. 7. PPTD signal vs thickness for polyimide.

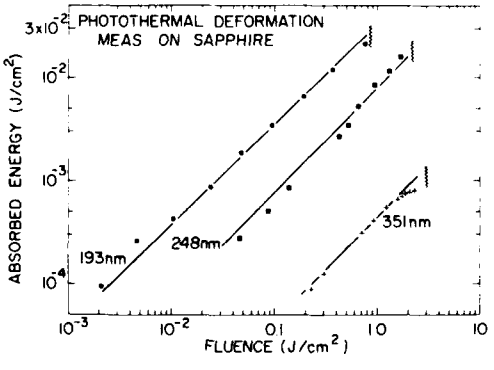

FIG. 9. Energy absorption from PPTD measurement vs fluence for three excimer wavelengths. Note that the percentage of energy absorbed is independent of fluence. The absorption at 193 nm is noted to correspond to a 3% absorption.

TABLE II. Energy absorption and etching threshold for sapphire.

Condition	Fractional surface absorbed energy	Etching threshold (J/cm^2)
193 nm:		
As-received	$\sim 2.2\times10^{-2}$	~ 0.5
10-min etch[a]	1.6×10^{-2}	...
1-h etch	1×10^{-2}	...
Annealed[b]	3×10^{-2}	0.8
Annealed and etched	3×10^{-3}	>1.8
248 nm:		
Annealed	8×10^{-3}	2.1
Annealed and etched	2×10^{-3}	3.6
351 nm:		
Annealed	4×10^{-4}	>1.5

[a] Chemical etching as per Ref. 5.
[b] 1500 K in air for 3 h.

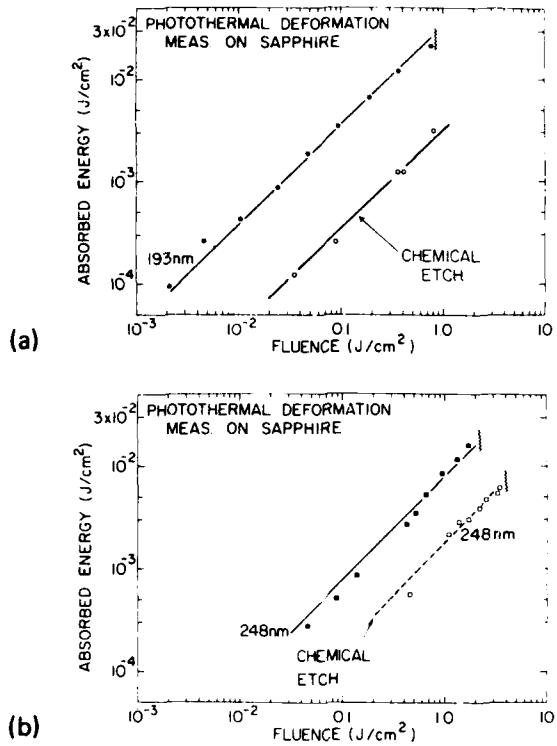

FIG. 10. (a) and (b) Decrease in absorbed energy due to chemical etching as observed at the two shorter UV wavelengths.

it ~ 3 times the deformation as the 250 μm samples. Third, the temporal dependence is quite similar to the calculated rise times for a surface-expansion driven plate mode. This feature contrasts with any possible changes in surface reflectivity due to the excimer radiation. While a *gradient* of reflectivity change would be sensed by the split silicon detector, it is reasonable to presume such changes in reflectivity would be on a nanosecond (or less) and not μs time scale. Taken as a whole, it appears quite probable that the present PPTD signal correctly measures the surface energy absorption and not bulk absorption or other spurious effects. In fact, to duplicate the present signals would require a bulk absorption of 50 cm^{-1} at 193 nm, a value which appears inappropriate for sapphire.[13]

V. DISCUSSION

A primary result of our work is that a platelike deformation gives a large, surface-sensitive signal for thin ($\lesssim 250$ μm) samples. The signal rise time is $\lesssim 1$ μs, with a much longer fall time. The above theoretical results were checked by measurements on polymers and glass of varying thickness. The conclusions concerning the time dependence and (inverse) dependence on thickness were confirmed. Furthermore, edge effects were shown not to be a detrimental influence with reasonable (>3 mm) edge distances. Having a general understanding of the quantitative behavior of PPTD, we can turn now to a detailed consideration of the sapphire results (as normalized from calibrations using silicon wafers).

The primary results for sapphire are summarized in two observations: there exists a large (up to 3% at 193 nm) surface absorption[14] and the percentage is independent of fluence. It is also of interest to note that in going to short UV wavelengths the threshold for etching sapphire drops from $\geqslant 10$ J/cm^2 at 1.06μ (Ref. 15) and >1.5 J/cm at 351 nm, to only 0.6 J/cm^2 at 193 nm. The observation of an absorption independent of fluence rules out a "true" multiphoton absorption process. Stepwise excitation with two or more photons contributing would still agree with the present results so long as one particular step exhibited the controlling absorption cross section. Since the present excimer fluences extend as high as 80% or 90% of threshold, it is highly unlikely that some completely undetected process suddenly sets in and gives rise to sapphire etching. We take the view that the present constant absorption is a direct link in the accumulation of near surface energy, which can, at sufficiently high density, give rise to the surface etching of sapphire. It is interesting to note that F and F$^+$ centers in neutron-bombarded sapphire have optical absorptions[13] quite near the present 193 and 248 nm wavelengths, although a specific correlation between neutron damage and surface defects does not appear practical at this time.

The present PPTD results agree well with earlier, LIF, observations on the UV etching of sapphire. Using a thermal diffusivity of 0.08 cm^2/s and hence an effective heated layer of 0.57 μm, we estimate that a 3% surface absorption is equivalent to a temperature increase of 130 K (just *below* ablation). This value extrapolates smoothly to the 200 to 300 K rises found with LIF measurements on diatomics in the etch plume and futhermore confirms the previous conclusion that collisions in the etch plume do not alter internal energies. The LIF results are, of course, derived from *above* threshold measurements and involve about 60% greater fluences (~ 1 to 1.2 J/cm^2) than those utilized here at 193 nm.[2] The fact that all these temperatures are grossly insufficient to cause thermal vaporization reinforces the previous conclusion,[2] namely, that UV etching of sapphire takes place primarily by a photochemical process.

A determination of the value for the energy deposited in the surface region makes it possible to set an *upper limit* for the density of electrons excited into the conduction band. The 3% absorption amounts to 18 mJ/cm^2 at etching threshold. For the aforementioned two-photon sequential absorption and assuming at least 12.8 eV($= 2\ h\nu$) are required to form an electron–hole (or exciton) (e–h) pair, the above energy density represents $\lesssim 2.2\times10^{23}$ e–h pairs/cm^3. The least certain quantities in the calculation are the depth over which the pairs are distributed and the (additional) energy required per pair when their density becomes large. We use a depth which is only an order of magnitude estimate, namely 0.4 nm, i.e., about 2 monolayers (ML) and neglect the dependence of excitation energy or e–h density. The above numbers imply (neglecting recombination) $\lesssim 10$ electron–hole pairs/Al_2O_3 molecules or $\lesssim 3$ pairs/O atom. Even though recombination and other losses in the excitation energy also undoubtedly occur, a density of even one e–h pairs/anion still appears sufficient to produce a chemically rebonded solid and hence photochemical etching.

ACKNOWLEDGMENTS

We are grateful to R. Walkup for the use of his differential amplifier. In addition, we had the helpful assistance with the sample etching and annealing from M. Shafer, M. Berkenblit, R. Figat, and D. R. Vigliotti.

[1]Photochemical etching includes those cases where chemical bonding or stoichiometric changes in surface species result in a repulsive or at least greatly reduced binding energy state. The separation of predominantly photochemical from thermal processes is a primary question when etching monolayers (not microns) of samples. We do not presently consider processes such as exfoliation or hydrodynamical sputtering which lead to macroscopic material removal, cf. R. Kelly, J. J. Cuomo, P. A. Leary, R. E. Rothenberg, B. E. Braren, and C. F. Aliotta, Nucl. Instrum. Methods B **9**, 329 (1985).

[2]R. W. Dreyfus, R. Kelly, R. E. Walkup, and R. Srinivasan, Proc. Soc. Photo. Opt. Instrum. Eng. **710**, 46 (1987); R. W. Dreyfus, R. Kelly, and R. E. Walkup, Appl. Phys. Lett. **49**, 1478 (1986).

[3]R. W. Dreyfus, R. Kelly, and R. E. Walkup, Nucl. Instrum. Methods B.

[4]R. J. von Gutfeld, F. A. McDonald, and R. W. Dreyfus, Appl. Phys. Lett. **49**, 1059 (1986).

[5]Photoacoustic and photothermal techniques have been used for some time to determine thermal and material properties of condensed matter. Detection of the surface displacement has been made by interferometric means while the surface slope has been detected through the deflection of a probe beam incident on the sample surface. Some of the works utilizing thermal deformation techniques are: M. A. Olmstead, N. M. Amer, S. Kohn, D. Fournier, and A. C. Boccara, Appl. Phys. A **32**, 141 (1983); A Rosencwaig, J. Opsal, and D. L. Willenborg, Appl. Phys. Lett. **43**, 166 (1983); G. Rousset, F. Lepoutre, and L. Bertrand, J. Appl. Phys. **54**, 2383 (1983); G. Rousset, L. Bertrand, and P. Cielo, *ibid.* **57**, 4396 (1985); H. Sontag and A. C. Tam, Appl. Phys. Lett. **48**, 725 (1985); C. Karner, A. Mandel, and F. Trager, Appl. Phys. A **38**, 19 (1985); G. C. Wetsel, Jr., F. A. McDonald, G. E. Jamieson, and J. B. Spicer, in Proceedings of Ultrasonic '85, London, July 1985; S. Ameri, E. A. Ash, B. Neuman, and C. R. Petts, Electron. Lett. **17**, 337 (1981), and Y. Martin, H. D. Wickramasinghe, and E. A. Ash, in Proceedings of the IEEE Ultrasonic Symposium, New York, 1982, p. 563.

[6]P. M. Morse, *Vibrations and Sound*, 2nd ed. (McGraw–Hill, New York, 1948), p. 208.

[7]F. A. McDonald, R. J. von Gutfeld, and R. W. Dreyfus, in Proceedings of the IEEE Ultrasonic Symposium, New York, 1983, p. 403.

[8]W. Nowacki, *Thermoelasticity* (Addison–Wesley, Reading, MA, 1962).

[9]N. L. Boling, M. D. Crisp, and G. Dute, Appl. Opt. **12**, 650 (1973); and Appl. Phys. Lett. **21**, 364 (1972).

[10]G. Hass, *American Institute of Physics Handbook*, 3rd ed., edited by D. E. Gray (McGraw–Hill, New York, 1972), pp. 36–120, Eq. 6(g)-3 to 7.

[11]A. Reisman, M. Berkenblit, J. J. Cuomo, and S. A. Chan, J. Electrochem. Soc. **118**, 1653 (1971).

[12]J. A. Davies, J. Friesen, and J. D. McIntyre, Can. J. Phys. **38**, 1526 (1960).

[13]J. H. Crawford, Jr., Nucl. Instrum. Methods B **1**, 159 (1984); and B. D. Evans and M. Stapelbrock, Phys. Rev. B **18**, 7089 (1978).

[14]An effect of surface condition on sapphire restrahlen bands has been observed previously. A. S. Barker, Jr., Phys. Rev. **132**, 1474 (1963).

[15]*D. W. Fradin and M. Bass, Appl. Phys. Lett.* **22**, 206 (1973).

Summary Abstract: Imaging of surface atoms and their wave functions with the scanning tunneling microscope[a)]

J. E. Demuth, R. J. Hamers, and R. M. Tromp
IBM Thomas J. Watson Research Center, Yorktown Heights, New York 10598

(Received 27 February 1987; accepted 7 May 1987)

The scanning tunneling microscope (STM) was invented less than five years ago by Binnig and Rohrer at the IBM Research Laboratory in Zurich, Switzerland.[1] Their STM image of the Si(111) 7×7 surface three years ago[2] provided a major breakthrough in our understanding of the 7×7 surface and has since stimulated much more STM work on semiconductor surfaces. On 16 October 1986, Binnig and Rohrer were honored for their work with the Nobel Prize in Physics together with Ernst Ruska, the inventor of the electron microscope in 1933. The STM with its ability to study surfaces in real space has from the beginning changed our perception of surfaces. We can now see not only the periodic part of the surface but also the local irregularities, defects, and imperfections at surfaces that have been elusive to most other surface science methods. Another important aspect of STM is that since the electron tunneling process depends on the density of surface electronic states, it ultimately conveys information about the local surface electronic structure.

Two types of electronic information are available in STM. The first is the barrier height for tunneling which can be obtained by modulating the tip to sample distance.[1] In the macroscopic limit, and for large structures, this is equivalent to the average work function of the sample and tip. This barrier height also reflects the response of all the electrons and implicitly does not have any dependence on electron energy. The other electronic information available from STM is spectroscopic information derived from the energy structure of surface charge densities of the sample and tip.[3-6] Here, one measures the tunneling current as a function of bias voltage and observes stepwise increases in the tunnel current whenever the bias voltage is sufficient to allow tunneling into a new set of states.[5] In principle, both the tip and surface may contribute to produce features in I–V measurements. However, for all cases studied to date, measured I–V features appear to be dominated by states on the sample.[5-8] This may arise if the electronic structure of the tip produces a broad structureless resonance about the Fermi level. However, it has also been found that the filled and empty states of the very sharpest tips are slightly displaced (1–2 Å) which becomes an important consideration when comparing I/V images of the filled and empty states of the sample.[9]

While many current surface spectroscopic methods allow one to probe the energy states at the surface, only STM can permit one to spatially resolve these states. Namely, I–V measurements performed at different points on the surface allow one to determine the spatially dependent local density of states on the sample and relate atomic scale structural features to these localized states. Modulation of the bias voltage as performed for fixed metal oxide tunnel barriers can be used to obtain dI/dV.[3-5] However when performed in a constant current model while scanning this method contains two contributions—one from the density of states and one from the surface topography which usually dominates such dI/dV images.[10]

In order to obtain I/V type of data in a scanning mode we have developed a new method, called CITS, for operating the feedback control while scanning.[6,7] Essentially, CITS introduces a timing sequence to the tunneling measurement so that the feedback control can operate independent of the I–V measurements. This is achieved by repetitively ramping the sample bias over some energy range at 2.2 kHz and sampling the tunneling current at particular bias voltages, or in reality at different times during the voltage ramp. One of the bias voltages is selected to control the feedback and maintains an essentially constant barrier height for the other I–V measurements made during the duration of the ramp. We thus can obtain 50 point, 12 bit I–V spectra for each pixel element of a 100×100 pixel image together with a simultaneously obtained topograph *all* in 5 min. The choice of bias voltage for the feedback control during CITS measurements has important implications to readily interpreting such spectroscopic images and is discussed elsewhere.[7,9] Another advantage of such a multiplexed mode for controlling the feedback, is that it provides a large fraction of the duty cycle to perform other functions. Here we use this to make I–V measurements but, for example, one could choose to increase the bias voltage momentarily to decompose molecules near the tip to drive the tip into the surface to modify surface atoms.

We have used the CITS method to atomically resolve and image the surface state charge densities on Si(111) 7×7,[6,7] Si(100) 2×1,[7] and $\sqrt{3}\times\sqrt{3}$ Ag Si(111)[9-11] surfaces. In all cases the onsets we observe in I/V spectra agree very well with the surface state energies found in photoemission and inverse photoemission experiments.[6,7,9] In addition we are able to directly correlate these surface states with specific atomic features in the surface structure. For example, for Si(111) 7×7 we observed a filled surface state close to the Fermi level associated with the dangling bond orbitals of 12 adatoms (atoms adsorbed on a surface) in the Si(111) (7×7) unit cell. In addition we found 7 orbitals 0.8 eV below the Fermi level associated with broken bonds on the threefold coordinated silicon atoms in the underlying surface layers. The location of these states directly correspond to atomic features of the model proposed for the 7×7 surface.[12] Recent theoretical work by Northrup on small subunits of the (7×7) cell is in good agreement with these results and allow one to understand how these surface bonds stabilize the 7×7 surface.[13] The location of the rest atoms states also provide direct, real space evidence from the pres-

 0734-211X/87/051528-02$01.00 © 1987 American Vacuum Society

ence of a stacking fault in the double layer directly underneath the adatoms in one-half of the (7×7) unit cell.[6]

The Si(001)-(2×1) surface reconstructs by forming dimer bonds between adjacent surface atoms, thus reducing the number of broken bonds by a factor of 2. We have observed both the bonding state, located on and between the dimer atoms, and the antibonding orbitals, located on the outer ends of the dimers. Some of the dimers are buckled. On these we find that the bonding state is strongly localized on the "up" side of the dimer, whereas the antibonding state is found on the "down" side. This spatial separation of bonding and antibonding orbitals is strong evidence for charge transfer from the down to the up atom. These experimental findings are in good agrement with the filled and empty states calculated by Ihm *et al.*[14]

Many structural models for the $\sqrt{3}\times\sqrt{3}$ structure of Ag on Si(111) have been previously proposed. Our STM studies together with the $\sqrt{3}\times\sqrt{3}$ Ag coverage determined by medium energy ion scattering and our CITS measurements lead us to derive a structural model consistent with the spatial electronic structures we observed.[9,11] Here we propose an embedded Ag-trimer model where the trimer occupies a vacancy of an otherwise ideal Si(111)-1×1 top layer. Such a structural model while not quantitative, agrees with many previous measurements including bond distances derived by x-ray absorption fine structure (EXAFS).[15] The spatial location of the filled and empty states together with the structural model one derives, by necessity, allows a model of bonding that stabilize the surface. We propose that the Ag cluster acts as a donor to satisfy the Si dangling bonds formed by the vacancy and allows the remaining top Si atom dangling bonds to form bonding–antibonding combinations which reduce the total energy. Unlike Si(111) 7×7 or Si(100) 2×1 where different Si atomic environments lead to charge transfer between Si atoms, the Ag provides the extra electrons to satisfy these dangling bonds, while the vacancy allows a new symmetry to provide covalent bonding between the surface Si atoms.

In summary, the STM can provide both geometric and spatially resolved electronic structure information. Such information may allow one to directly investigate and hopefully understand electron bonding and the geometric structure of surfaces on the atomic level. This information on larger scales, i.e., nanometers, may also provide new insight to numerous microphysics problems where small scale features may be important. This includes, for example, nucleation and growth phenomena, Schottky barrier formation as well as surface reactions at particular sites of the surface.

[a] Work supported in part by the Office of Naval Research.

[1] G. Binnig and H. Rohrer, Helv. Phys. Acta **55**, 726 (1982).
[2] G. Binnig, H. Rohrer, Ch. Gerber, and E. Weibel, Phys. Rev. Lett. **50**, 120 (1983).
[3] G. Binnig, K. H. Frank, H. Fuchs, N. Garcia, B. Riehl, H. Rohrer, F. Salvan, and A. R. Williams, Phys. Rev. Lett. **55**, 991 (1985).
[4] R. S. Becker, J. A. Golovchenko, D. R. Hamann, and B. S. Swartzentruber, Phys. Rev. Lett. **55**, 2032 (1985).
[5] W. J. Kaiser and R. C. Jaklevic, IBM J. Res. Dev. **30**, 411 (1986).
[6] R. J. Hamers, R. M. Tromp, and J. E. Demuth, Phys. Rev. Lett. **56**, 1972 (1986).
[7] R. M. Tromp, R. J. Hamers, and J. E. Demuth, Science **234**, 304 (1986).
[8] R. M. Feenstra, W. A. Thompson, and A. P. Fein, Phys. Rev. Lett. **56**, 608 (1986) and (to be published).
[9] J. E. Demuth, E. J. van Loenen, R. M. Tromp, and R. J. Hamers, Proceedings of the Physics and Chemistry of Semiconductor Interfaces Meeting, January, 1987.
[10] G. Binnig and H. Rohrer, IBM J. Res. Dev. **30**, 355 (1986).
[11] E. J. van Loenen, J. E. Demuth, R. M. Tromp, and R. J. Hamers, Phys. Rev. Lett. **58**, 373 (1987).
[12] K. Takayanagi, Y. Tanishiro, M. Takahashi, and S. Takahashi, J. Vac. Sci. Technol. A **3**, 1502 (1985).
[13] J. E. Northrup, Phys. Rev. Lett. **57**, 154 (1986).
[14] J. Ihm, M. L. Cohen, and D. J. Chadi, Phys. Rev. B **21**, 4592 (1980).
[15] J. Stohr, R. Jaeger, G. Rossi, T. Kendelewicz and J. Lindau, Surf. Sci. **134**, 813 (1983).

Pulsed-laser atom-probe and field-ion microscope study of solid surfaces

T. T. Tsong, H. M. Liu, Q. J. Gao, D. M. Ren, and Y. Liou
Department of Physics, The Pennsylvania State University, University Park, Pennsylvania 16802

(Received 6 February 1987; accepted 7 May 1987)

The atomic structure of a solid surface can be imaged with the field-ion microscope and the chemical species of surface atoms can be identified by time-of-flight atom probe. By incorporating a pulsed-laser technique to field-ion miscroscopy, atomic structures and atomic steps in a surface reconstruction can be studied with a spatial resolution of ~2.5 Å and a time resolution of a few nanoseconds. The mass resolution and material applicability of a pulsed-laser atom probe are greatly improved, and it is also an ion energy analyzer of 5 parts in 10^5 accuracy and resolution, and an ion reaction and dissociation time analyzer of 20 fs time resolution. Some interesting phenomena such as formation of multiple charge cluster ions and dissociation of compound ions by atomic tunneling can be studied with excellent mass, energy, and time resolution for the first time.

I. INTRODUCTION

There are two different aspects of field-ion microscopy, namely the atomic imaging aspect and the chemical identification aspect.[1] Using the field-ion microscope (FIM), the atomic structure of a solid surface can be revealed. The time-of-flight (ToF) atom probe can provide the chemical identity of surface atoms one by one and the composition of surface layers one by one also. Atomic resolution is no longer unique to field ion microscopy. Scanning tunneling microscopes (STM) and electron microscopes, both TEM and STM, have now also achieved atomic resolution. The single atom chemical identification aspect, however, is still unique to field-ion microscopy. Here we will describe how, by combining a pulsed-laser technique to an atomic resolution microscopy, not necessarily restricted to the FIM, the atomic structures of transition states and atomic steps involved in a phase transition can be revealed with ns time resolution.[2] We have also used pulsed-laser stimulated field desorption for ToF atom-probe operation.[3] This results in greatly expanded capability and greatly improved resolution of the atom probe.[4] The ToF atom probe is now capable of mass analyzing materials of good and poor conductivity with a mass resolution as high as 6000. In addition, it is an ion energy analyzer with an accuracy of 5 parts in 10^5, and an ion reaction and dissociation time analyzer of 20 fs time resolution.[5,6] We will illustrate with a few recent studies of surface and ion physics with the FIM and the atom probe.

II. ATOMIC RECONSTRUCTION OF Pt AND Ir SURFACES BY PULSED-LASER HEATING

There are two main objectives of this study. First, we are interested in surface atomic reconstruction by rapid heating and quenching of a solid induced by pulsed-laser heating. Depending on the duration and the power of the laser pulses, the heating rate can be as high as 10^{17} K/s, and the quenching rate can be as high as 10^{11} K/s.[7] Thus, atomic structures of transition states can be quenched for microscopic observations.[2] Second, we are interested in the detail atomic steps involved in the reconstruction and the atomic structure of the reconstructed surfaces.[2] Atomic structures of reconstructed surfaces have been very extensively investigated with diffraction techniques such as low-energy electron diffraction (LEED), but the reciprocal space information is often difficult to provide a unique real-space atomic structure.[8,9] Atomic resolution real-space imaging of solid surfaces can complement diffraction techniques, and are currently actively pursued.[2,10–12] For our first study, we focus on the reconstruction of the Pt and Ir(110) and (001) surfaces.

For the Pt and Ir (110) planes, the equilibrium structure is (1×2) with missing rows of atoms.[9] There are a few possible variations of the "missing row model." The "simple" missing row model is a (1×1) surface with every other [110] atom row missing from the surface. To transform a (1×1) surface into a (1×2) of this structure, long distance, on the order of the size of the plane, diffusion of surface atoms is needed, which is inconsistent with mass surface diffusion data at the transition temperature.[13] An alternative "sawtooth" missing row model has been proposed to overcome this difficulty. In the FIM, we are able to distinguish these two models. The former one gives rise to a (1×2) structure only for the top surface layer, whereas the sawtooth model will show two layers with the (1×2) structure. As shown in Fig. 1, a field evaporation sequence of a pulsed-laser heating reconstructed (1×2) surface shows only one layer of (1×2) structure; thus our result for the Pt and Ir(110) plane is consistent with the simple missing row model of the (1×2) reconstructed surface. FI images show that atom transport tends to occur by cross channel jumps of the entire "plane edge" [110] atom rows as shown in Fig. 2. For a larger plane where such jumps are restricted by available terrace space, we find that [110] atom rows are broken up into small fragments of two to a few atoms by both lateral jumps and cross channel jumps. Single-atom fragments are rarely found. Based on consideration of probabilities of observing different cluster configuations and the relatively strong nearest-neighbor bond strength of surface atoms, we believe that in the (1×1) to (1×2) atomic reconstruction, atoms in these small [110] atom-row fragments jump simultaneously, possibly assisted by phonon waves of soliton nature propagating in the [110] and [001] directions. This is

 0734-211X/87/051530-05$01.00 © 1987 American Vacuum Society

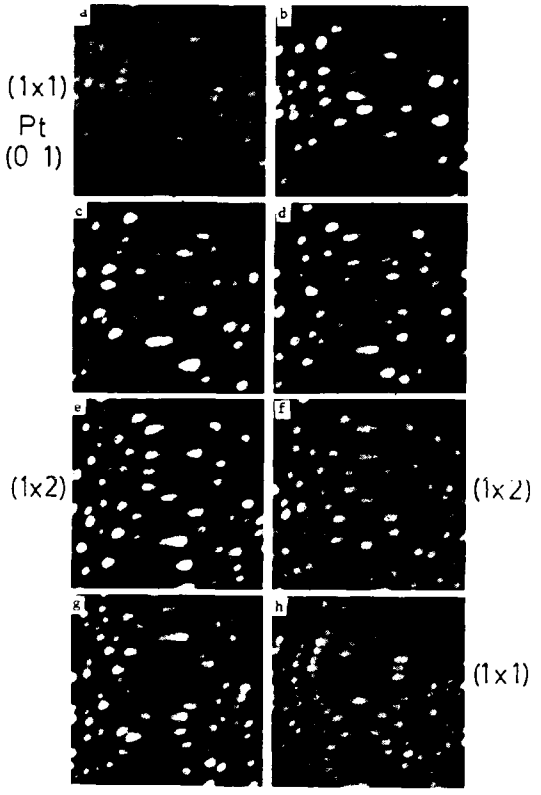

FIG. 1. (a) A (1 × 1) (110) surface of a Pt tip. (b) to (e) Steps in (1 × 1) to (1 × 2) reconstruction. Between two photographs is the heating of a 5 ns laser pulse to ~ 500 K. A complete (1 × 2) structure is seen in (e). (f) to (h). Gradual field evaporation reveals the underneath layer to be (1 × 1).

in great contrast to other observations and computer simulations where atom transport occurs by jumps of single atoms.

Another surface we have studied recently is the (1 × 1) to (1 × 5) reconstruction of the Ir (001) plane. A quasihexagonal model proposed from LEED and other studies basically can be described by squeezing six [110] atom rows of the top layer together to form a closely packed "hexagonal" structure to occupy five [110] atom row widths of the underlying (1 × 1) layer, resulting in a few different buckling heights of these atom rows.[8] FIM images of reconstructed surfaces induced by pulsed-laser heating at ~ 900 K, indeed show [110] atom rows of different image intensities. These atom rows of slightly different heights field evaporate separately. By mapping of the position of atoms in these atom rows, the hexagonal arrangement of these atoms in the reconstructed (1 × 5) layer is confirmed. Figure 3 gives an example of a reconstructed (1 × 5) surface and a map of the atom positions derived from this surface. Although the buckling of the (1 × 5) surface of Au (001) has been directly observed in STM and TEM,[14] no direct observation of the hexagonal arrangement of atoms has been reported before. When the heating temperature is around 500 K or lower, no reconstruction is observed. Instead a nearly circular plane will change to a square shape by diffusion of plane edge atoms along the edge.

FIG. 2. (a) A (1 × 1) Pt (110) surface prepared by low-temperature field evaporation. (b) By irradiation of one laser pulse, two atoms jump together to the next surface channel to form an (1 × 2) structure. (c) Another pulse causes the other [110] atom row of six atoms to jump to the next surface channel.

III. MASS ANALYSIS OF SURFACE ATOMS AND SURFACE LAYERS

The ToF atom probe is capable of mass analyzing surface atoms one by one and surface layers one by one for metals and alloys. For covalent bond materials such as Si, a truly atomic layer by atomic layer compositional analysis is still difficult. For metals and alloys field evaporation occurs at plane edges. For semiconductors due to the large field penetration depth and the covalent bonding, field evaporation tends to be sporadic and the atomic structure appears irregular. However, by annealing the field-evaporated surface, thermally equilibrated atomic structures of high index planes of Si can be revealed as shown in Fig. 4. This is the first time well-ordered atomic images of Si have been obtained by FIM despite continuous attempts by many people over the last 25 yrs. The sporadic field evaporation behavior of Si is removed when a very thin layer of silicide is grown on the surface, and well-ordered atomic structures of silicide have been obtained.[15]

An example of the quantitative atomic layer by atomic layer compositional analysis of a surface is our study of surface segregation and cosegregation with impurities of alloys.[16] It is well-known that for an alloy in thermodynamic equilibrium, the composition of surface layers may not be the same as that of the bulk. One species may segregate to the surface. Also the segregation behavior may be changed by the presence of a small amount of impurities in the alloy, which may also segregate to the surface to form an overlayer. In PtRh alloys, we find the segregation species to be Pt in the top layer, while the second layer is enriched with Rh. From

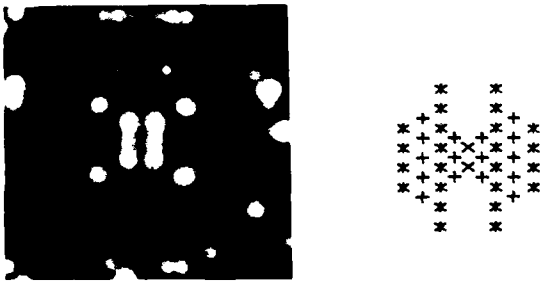

FIG. 3. He field-ion image of a (1 × 5) reconstructed Ir (001) surface and a map of the position of atoms in this layer. Hexagonal arrangements of these atoms are revealed for the first time. Atoms in + positions have the largest buckling height, and in × positions, have the lowest buckling height.

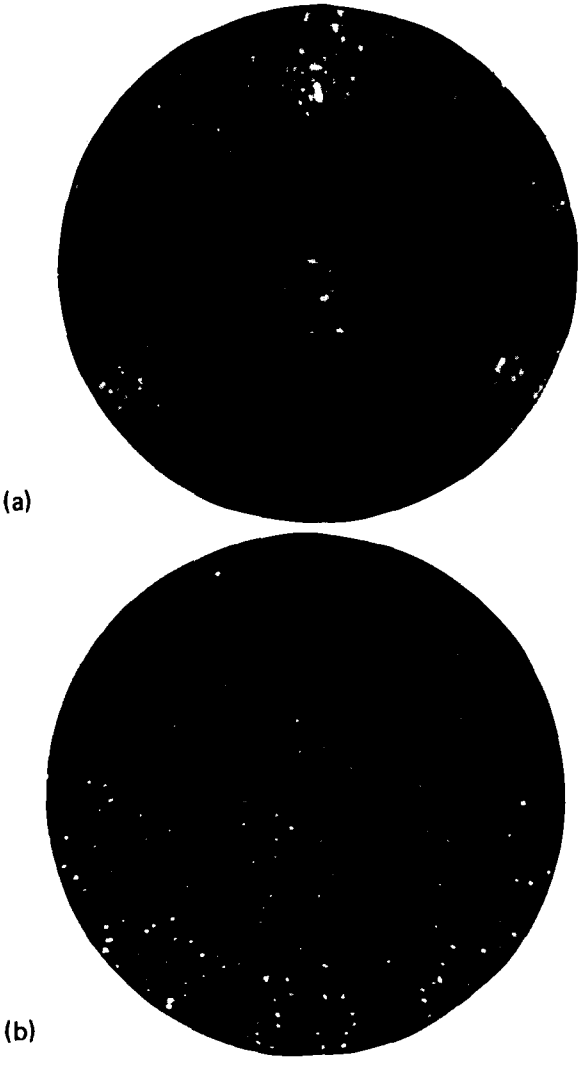

FIG. 4. (a) He-ion image of the field-evaporated surface of an [111] oriented Si tip. (b) Ne-ion image of the same Si surface after annealing to 800 °C for 5 min. Atom-probe analyses show no impurities are present on the surface. The central lane is the (111) surface, and the planes at 1, 2.5, 5, 7, 10, 11.5 o'clock positions are the {230} surfaces.

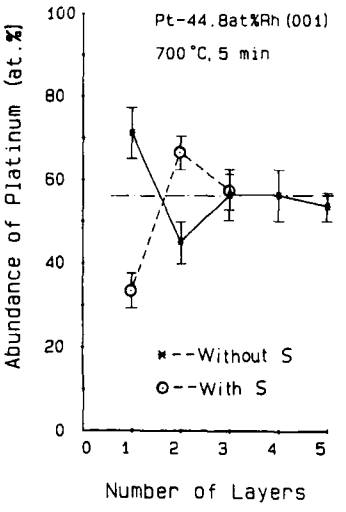

FIG. 5. Absolute composition depth profiles of Pt–44.8 at. % Rh (001) plane showing a reversed segregation behavior by the presence of impurity S. Note also the nonmonotonic depth dependence of the composition depth profiles.

the third layer on, the composition returns to the bulk value. When the alloy contains about 50 ppm of sulfur, the segregation behavior is reversed. Now the top layer is enriched with Rh, and the second layer is enriched with Pt. Also an overlayer of S is found. Figure 5 is composition depth profiles showing this reversed segregation behavior. We also find that the coverage of the sulfur overlayer is linearly proportional to concentration of Rh, approximately with the ratio of 1:1, in the top surface layer, signifying that Rh atoms are drawn to the surface by sulfur atoms because of a strong attractive interaction between Rh and S atoms in the alloy.

The segregant concentration may approach the bulk value either monotonically or nonmonotonically, and the segregation may extend to only one atomic layer or a few atomic layers. Table I summarizes the atom probe result. At the present time, atom probe is the only instrument capable of deriving such detailed information on surface segregation. Such information is important in our endeavor to understand interface segregation phenomena at the fundamental level, particularly the dynamical aspect.

IV. ION ENERGY AND ION REACTION TIME ANALYSIS

In field ion emission there are several phenomena of basic interest. Field ionization refers to ionization of an atom in high-electric field by tunneling of an electron out of the atom. Field desorption refers to desorption of adsorbed species on surfaces by high-electric field, whereas field evaporation refers to desorption in high field of substrate surface atoms. Field dissociation refers to dissociation of compound ions in high-electric field by tunneling of an atom. In general ion-physics terminology, dissociation is considered an ion reaction. Mechanisms of all these physical processes can be best studied by measuring ion kinetic-energy distributions.

The time-of-flight of an ion is directly related to its kinetic energy. With an elaborate calibration scheme, based on the very accurate data of isotope masses available and the 1 ns time resolution of the electronic timer we have, our pulsed-laser time-of-flight atom probe is capable of measuring ion energy with an absolute accuracy of five parts in 10^5.[4] Thus we are able to study mechanisms of ion formation in field desorption and evaporation with an accuracy unachievable before. For example, we find that ions in field desorption are formed in a zone of width $\sim$0.4 Å or less.[17] The spatial resolution of these measurements is about 0.1 Å. Here field-

TABLE I. Surface and impurity cosegregation of alloys.

Alloy system	Segregating Species		Nature of Convergence
Ni–5%Cu	Cu	(1 layer)	nonmonotonic
Pt–5%Au	Au	(4 layers)	monotonic
2 Pt–Rh	Pt	(1 layer)	nonmonotonic
Pt–21%Ir(S)	Pt(s)	(1 layer)	monotonic
5 Pt–Rh(S)	Rh(s)	(1 layer)	nonmonotonic

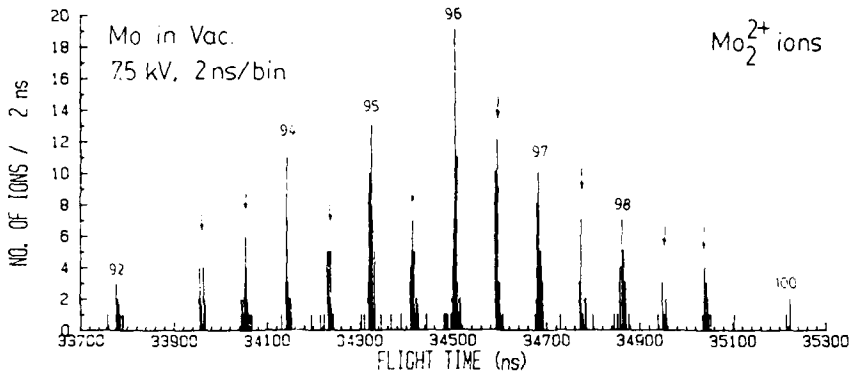

FIG. 6. A pulsed-laser ToF spectrum of Mo showing formation of Mo_2^{2+} ions. The 15 mass lines come from mixing of 7 Mo isotopes. The height distribution of these lines agrees with a random combination of these 7 Mo isotopes to form Mo_2.

ion emission will not be discussed. Instead, two subjects of interest to basic ion physics, will be focused on, namely the smallest stable multiple charge cluster ions and dissociation of compound ions.

In pulsed-laser field evaporation and desorption, if the temperature of the surface is high and the field is low, then cluster ions can be formed. These cluster ions can be moderately large for semiconductors, but otherwise are fairly small. They are often doubly charged, thus unique among different methods of producing cluster ions. Also cluster ions, once formed, have no more chance of interacting with other particles, thus the abundance of different ion species observed reflects the desorption process itself while the ion energy distribution reflects the absolute stability (in many other studies, cluster ions of different sizes can interact with one another before detection; thus only relative stability of cluster ions of different sizes is studied) and the ion reaction rates of these cluster ions. In pulsed-laser stimulated field evaporation of silicon, the most abundant cluster ions found are Si_4^{2+}, Si_6^{2+}, and Si_5^{2+}. Four, five, and six are the magic numbers of the desorption process which are related to the atomic structure and bonding of the Si(111) surface, but may also be related to the fragmentation energy of silicon clusters. A calculation by Raghavachari[18] indicates that Si_4 and Si_6 are most stable with respect to fragmentation. This is in fact consistent with our observation of greatest abundance of Si_4^{2+} and Si_6^{2+} cluster ions.

The smallest sizes of multiple charge cluster ions are called critical numbers. For 2 + ions, this number is usually derived to be on the order of ten although in field-ion emission, it is found to be much smaller. Usually it is as small as three. The difference arises from the fact that in the latter case, it reflects the absolute stability in "Coulomb repulsive dissociation" and in the former case, it reflects the relative stability of all cluster ions present in the experiment and the method used for ionizing clusters. The smallest 2 + cluster ions we have observed are Mo_2^{2+}, as shown in Fig. 6. Thus the critical number for Mo_n^{2+} is as small as two. A detailed analysis of this spectrum shows that few Mo^+ exist, and the energy distributions are very sharp.[17] Thus Mo_2^{2+} has a lifetime much longer than the flight time of the ions in the acceleration region which is ~ 15 ns, or $> \sim 100$ ns. Since these ions are formed at ~ 1000 K, the barrier height for Coulomb repulsive dissociation is at least $kT \ln(100 \times 10^{-9}\ \text{s} / 1 \times 10^{-13}\ \text{s}) \approx 1.2$ eV. This is a very high potential barrier and Mo_2^{2+} must be considered stable. The stability arises from an effective shielding of the two positive charges by the rest of electrons in Mo_2^{2+}.

Ion reaction rates are often reflected in the ion energy distributions, or the shape of the mass lines. We illustrate

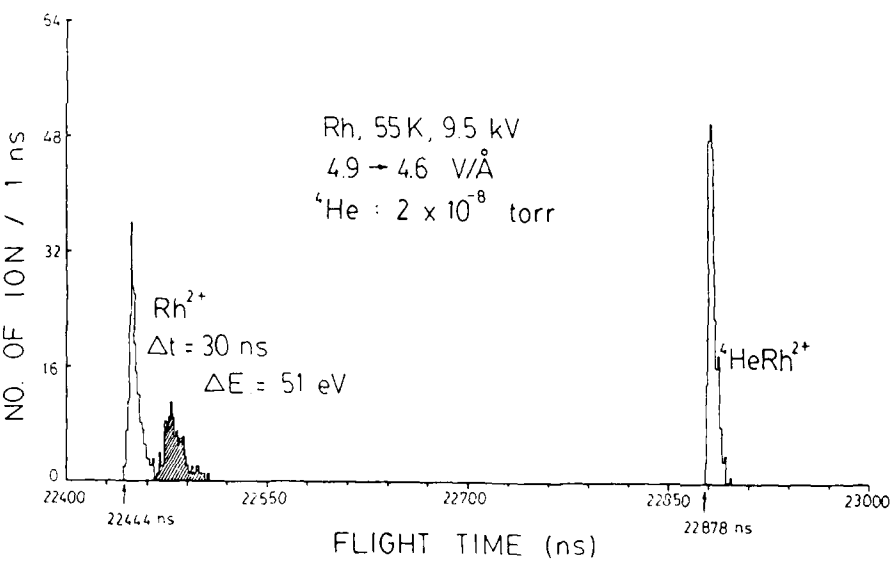

FIG. 7. A pulsed-laser ToF spectrum of Rh in 1×10^{-8} Torr of ^4He, showing a $^4HeRh^{2+}$ line and a Rh^{2+} line with a secondary peak.

here, with an example, dissociation of compound ions, $HeRh^{2+}$, in high electric field by an atomic tunneling effect.[5,6] This ion species can be produced by low temperature (< 100 K) field evaporation of a Rh tip in He of 10^{-8} Torr or higher in a field between 4.5 to 5.0 V/A. Under this field each surface Rh atom in the more protruding position is field adsorbed with a He atom. When the field evaporation is done with a weak stimulation (heat effect) of laser pulses of 300 ps width, a ToF spectrum shown in Fig. 7 is obtained. It contains a He^+ line (not shown), a Rh^{2+} line with a secondary peak with ~ 51 eV additional energy deficit, and a $HeRh^{2+}$ line. The He^+ line and the main Rh^{2+} peak are identical to those of pulsed-laser field desorbed He^+ without field evaporation and of Rh^{2+} produced by field evaporation in ultrahigh vacuum (UHV). The secondary Rh^{2+} peak is produced by field dissociation of $^4HeRh^{2+}$ into a Rh^{2+} and a neutral ^4He by atomic tunneling. With use of the field distribution of the tip geometry one finds that Rh^{2+} in the secondary peak is formed in a spatial zone of 150 Å width centered at ~ 220 Å above the emitter surface as shown in Fig. 8. $^4HeRh^{2+}$ field dissociates in a well defined spatial zone for reason that the dissociation rate is ion orientation dependent. In the as desorbed orientation A, $^4HeRh^{2+}$ cannot field dissociate. As the ion is accelerated away it also rotates. As it rotates by 180° to orientation B, it is most easily field dissociated. The flight time of $^4HeRh^{2+}$ in the field distribution over a distance of 220 Å is 790 fs, which is also the dissociation time and the time for the ion to rotate 180°. The experimental uncertainty in this determination is ± 21 fs. The tunneling effect is confirmed with a strong isotope effect observed when ^4He is replaced with ^3He, the dissociation ceases to occur. Since ^3He is lighter than ^4He, one would expect $^3HeRh^{2+}$ to field dissociate easier. This peculiar isotope effect is the result of a center of mass transformation and a mass ratio dependent barrier height for the atomic tunneling, and can be satisfactorily explained with a theoretical model.[6] This is the most direct experimental evidence of field dissociation by atomic tunneling, which was theoretically discussed by Hiskes in 1961.[19] It is interesting to note field ionization as an electron tunneling phenomenon as proposed by Oppenheimer in 1928,[20] which occurs in a spatial zone of width ~ 0.2 Å and about 4 Å above the field-ion emitter surface,[21] whereas field dissociation as an atomic tunneling phenomenon occurs in a spatial of width ~ 220 Å and about 150 Å above the field emitter surface.[6]

In summary, we have briefly described some of the significant new developments in field ion microscopy, particularly with the pulsed-laser technique. Atomic resolution is no longer unique to field-ion microscopy. However, field evaporation/desorption is still unique. With this process, surface atoms and surface layers can be mass analyzed one by one and deeper surface layers can be reached. It is with these

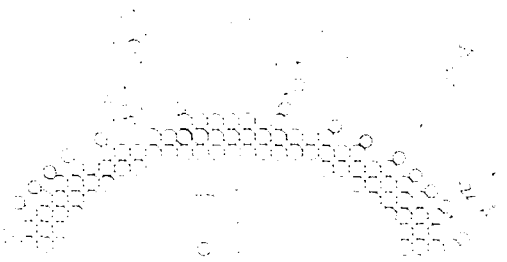

FIG. 8. A model used for explaining the orientational effect of field dissociation of $^4HeRh^{2+}$.

capabilities that the FIM can make unique contributions. We are particularly encouraged by our recent success in obtaining well-ordered atomic images of silicon surfaces, and we hope that in the next few years good progress can be made in this direction.

The works reported here were supported by NSF. The author is grateful to his many co-workers, particularly S. B. McLane, for their help in the experiments reported here.

[1]See for example, E. W. Muller and T. T. Tsong, Progr. Surf. Sci. **4**, 1 (1973); T. T. Tsong, *ibid.* **10**, 165 (1980).
[2]Q. J. Gao and T. T. Tsong, Phys. Rev. Lett. **57**, 452 (1986); Phys. Lett. A **117**, 132 (1986).
[3]G. L. Kellogg and T. T. Tsong, J. Appl. Phys. **51**, 1184 (1980).
[4]T. T. Tsong, Y. Liou, and S. B. McLane, Rev. Sci. Instrum. **55**, 1246 (1984).
[5]T. T. Tsong and Y. Liou, Phys. Rev. Lett. **55**, 2180 (1985).
[6]T. T. Tsong, Phys. Rev. Lett. **55**, 2826 (1985); T. T. Tsong and M. W. Cole, Phys. Rev. B **35**, 66 (1987).
[7]See, for example, *Laser Solid Interactions and Transition Thermal Processing of Materials*, edited by J. Narayan, W. L. Brown, and R. A. Lomons (North-Holland, New York, 1983); Mater. Res. Soc. Proc. **13** (1983).
[8]M. A. van Hove, R. J. Koestner, P. C. Stair, J. P. Biberian, L. L. Kesmodel, I. Bartos, and G. A. Somorjai, Surf. Sci. **103**, 189 (1981).
[9]C. M. Chan, M. A. van Hove, W. H. Weinberg, and E. D. Williams, Surf. Sci. **91**, 440 (1980).
[10]G. Binnig, H. Rohrer, Ch. Gerber, and E. Weibel, Surf. Sci. **131**, L379 (1983).
[11]L. D. Marks, Phys. Rev. Lett. **51**, 1000 (1983).
[12]G. L. Kellogg, Phys. Rev. Lett. **55**, 2168 (1985).
[13]H. P. Bonzel and S. Ferrer, Surf. Sci. **118**, L263 (1982).
[14]G. K. Binnig, H. Rohrer, Ch. Gerber, and E. Stoll, Surf. Sci. **144**, 321 (1984); T. Hasegawa, N. Ikarashi, K. Kobayashi, K. Takayanagi, and Y. Yagi, Jpn. J. Appl. Phys. **25**, L366 (1986).
[15]H. M. Liu, H. F. Liu, and T. T. Tsong, Surf. Sci. (to be published).
[16]M. Ahmad and T. T. Tsong, J. Chem. Phys. **83**, 388 (1985); D. Ren and T. T. Tsong (to be published).
[17]T. T. Tsong, Phys. Rev. B **30**, 4946 (1984); J. Chem. Phys. **85**, 639 (1986).
[18]K. Raghavachari, J. Chem. Phys. **84**, 5672 (1986).
[19]J. R. Hiskes, Phys. Rev. **122**, 1207 (1961).
[20]J. R. Oppenheimer, Phys. Rev. **31**, 67 (1928).
[21]T. T. Tsong and E. W. Müller, J. Chem. Phys. **41**, 3279 (1964).

AUTHOR INDEX

To papers presented at the Second Topical Meeting on the Microphysics of Surfaces, Beams, and Adsorbates

Abrefah, J. – (5) 1404
Adrian, F. J. – (5) 1490
Allen, T. E. – (5) 1427
Anderson, J. E. – (5) 1519
Aoyagi, Yoshinobu – (5) 1460
Apel, E. C. – (5) 1519
Avouris, Ph. – (5) 1387, 1423

Balk, P. – (5) 1453
Balooch, M. – (5) 1404
Blonder, G. E. – (5) 1441
Bohandy, J. – (5) 1490
Bozso, F. – (5) 1387
Brannon, James H. – (5) 1399
Burnett, J. W. – (5) 1477

Calaway, W. F. – (5) 1477
Chuang, T. J. – (5) 1444
Claassen, W. C. M. – (5) 1450

Dagata, J. A. – (5) 1495
Demuth, J. E. – (5) 1528
Dieleman, J. – (5) 1410, 1450
Dodson, Brian W. – (5) 1393
Doi, Atsutoshi – (5) 1460
Donnelly, V. M. – (5) 1441
Dreyfus, R. W. – (5) 1521
Du, Yuan-cheng – (5) 1504
Dubner, A. D. – (5) 1434
Dulcey, C. S. – (5) 1495

Ehrlich, D. J. – (5) 1400
Ellialtioglu, R. – (5) 1508

Estler, R. C. – (5) 1465, 1519

Farrell, H. H. – (5) 1482
Fischer, M. – (5) 1453
Fleming, C. G. – (5) 1441

Gao, Q. J. – (5) 1530
Ghosh, A. P. – (5) 1423
Graves, R. J. – (5) 1508
Green, T. A. – (5) 1514
Gruen, D. M. – (5) 1477
Grundmann, D. – (5) 1453

Haglund, R. F., Jr. – (5) 1514
Hall, Richard B. – (5) 1470
Hamers, R. J. – (5) 1387, 1528
Hanabusa, M. – (5) 1432
Harbison, J. P. – (5) 1482
Herbolzheimer, Eric – (5) 1470
Higashi, G. S. – (5) 1441
Hsu, D. S. Y. – (5) 1495
Husinsky, W. – (5) 1477

Iwai, Souhachi – (5) 1460

Jette, A. N. – (5) 1490
Jiang, Guo-bao – (5) 1504
Jørgensen, B. – (5) 1477

Kaneoka, T. – (5) 1432
Keller, R. A. – (5) 1466
Kim, B. F. – (5) 1490
Kolfschoten, A. W. – (5) 1410

Kunz, R. R. – (5) 1427
Kyuragi, Hakaru – (5) 1436

Lee, L. C. – (5) 1444
Lezec, H. – (5) 1434
Li, Fu-ming – (5) 1504
Lin, M. C. – (5) 1495
Liou, Y. – (5) 1530
Liu, H. M. – (5) 1530
Loubriel, G. M. – (5) 1514
Lückerath, R. – (5) 1453
Lüth, H. – (5) 1453

Matthias, E. – (5) 1415
Mayer, T. M. – (5) 1427
McCrary, V. R. – (5) 1441
McDonald, F. A. – (5) 1521
Melngailis, J. – (5) 1434
Mitchell, M. J. – (5) 1444
Muenchausen, R. E. – (5) 1466

Namba, Susumu – (5) 1460
Nguyen, D. C. – (5) 1466
Nielsen, H. B. – (5) 1415
Nogar, N. S. – (5) 1465, 1466, 1519

Olander, D. R. – (5) 1404

Pellin, M. J. – (5) 1477
Peterson, L. D. – (5) 1482

Reif, J. – (5) 1415
Ren, D. M. – (5) 1530

Richter, W. – (5) 1453
Rosén, A. – (5) 1415
Rothschild, M. – (5) 1400

Schweitzer, E. L. – (5) 1477
Sedlacek, J. H. C. – (5) 1400
Shedd, G. M. – (5) 1434
Shinn, Neal D. – (5) 1501
Siekhaus, W. J. – (5) 1404
Squire, D. W. – (5) 1495
Sun, Die-chi – (5) 1504
Suto, M. – (5) 1444

Thompson, P. – (5) 1490
Tok, N. H. – (5) 1514
Tromp, R. M. – (5) 1528
Tsong, T. T. – (5) 1530

Upton, Thomas H. – (5) 1470
Urisu, Tsuneo – (5) 1436

van Laar, J. – (5) 1410
van Zwol, J. – (5) 1410
von Gutfeld, R. J. – (5) 1521

Walkup, R. E. – (5) 1423
Wallace, C. B. – (5) 1508
Wang, Hai – (5) 1504
Westin, E. – (5) 1415
White, H. W. – (5) 1508

Young, C. E. – (5) 1477
Yu, Zeng-qi – (5) 1504

 © 1987 American Vacuum Society

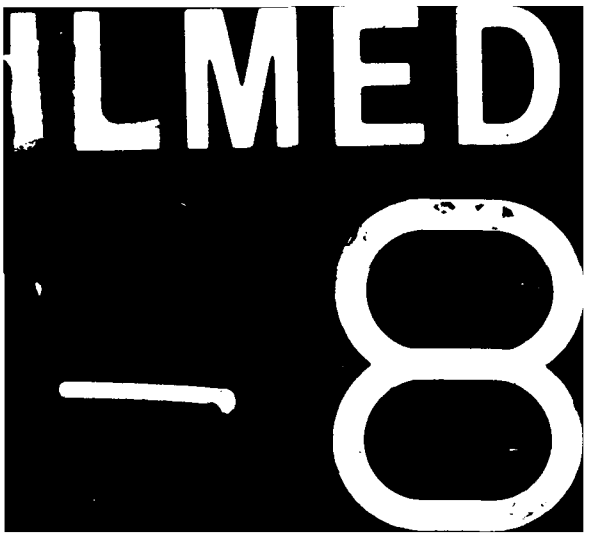
ILMED
8